Modeling of hydraulic fracturing in rocks:

A multiscale and fluid-solid coupling approach

Marina Sousani

Submitted in accordance with the requirements for the degree of
Doctor of Philosophy

The University of Leeds
School of Chemical and Process Engineering & School of Civil Engineering

July, 2015

The candidate confirms that the work submitted is her own, except where work which has formed part of jointly authored publications has been included. The contribution of the candidate and the other authors to this work has been explicitly indicated below. The candidate confirms that appropriate credit has been given within the thesis where reference has been made to the work of others.

Publication list

Publications appearing in Peer-Reviewed Scientific Journals

Chapter 3 & Chapter 4

Sousani M, Eshiet K I-I, Ingham D, Pourkashanian M, Sheng Y (2014). *Modelling of hydraulic fracturing process by coupled discrete element and fluid dynamic methods.* Environ Earth Sci:1-17 doi: 10.1007/s12665-014-3244-3

Chapter 5

Sousani M, Ingham D, Pourkashanian M, Sheng Y, Eshiet K I-I (2015). *Simulation of the Hydraulic Fracturing Process of Fractured Rocks by the Discrete Element Method.* Environ Earth Sci:1-19 doi:10.1007/s12665-014-4005-z

Publications appearing in Conference proceedings

Chapter 3 & Chapter 4

Sousani M *Modelling of the Hydraulic Fracturing of Rocks: A Multi Scale and a Multiphase Approach*. In: Papanikos GT (ed) 1st Annual International Conference on Earth and Environmental Sciences, Athens, 14-17 July 2014.

Publications submitted in Peer-Reviewed Scientific Journals

Chapter 1

Sheng Y, **Sousani M** (2014). *Recent Developments in Multi scale and Multi phase modelling of hydraulic fracturing process.* Submitted: Mathematical Problems in Engneering.

The work contained within these publications is my own primary research. The other authors were my supervisors who acted in an advisory role and gave suggestions regarding the research direction and analysis methods. The author Eshiet Kenneth Imo-Imo has provided part of the text and the laboratory results for Chapter 4, section 4.3.

Acknowledgements

Foremost, I would like to express my sincere gratitude to my supervisors Prof. Derek Ingham, Prof. Mohamed Pourkashanian and Dr. Yong Sheng for their constant support during my Ph.D research, for their guidance, motivation and immense knowledge. Their supervision helped me stay on track with the writing of this thesis and prevent me from deviating from my research. I would like to give my special thanks to Prof. Derek Ingham for his critical reading and good comments for improvements of the publication manuscripts and thesis, as well as his kindly advice throughout the preparation of this thesis. I could not have imagined having better supervision and mentoring for my Ph.D study.

Besides my supervisors, I would like to thank Dr. Kenneth Imo-Imo Eshiet for his contribution to one of my publications and his insightful reading and scientific advise.

My sincere gratitude also is due to Mr. Alexios Alexandropoulos for the sleepless nights we were working together, helping me learn and build appropriate coding and for his exhausting role of listening to me translating my results. Specifically I would like to thank him for his moral support, his daily patience and the encouragement he gave me on difficult times. I would not have managed otherwise.

Last but not the least, I would like to express my gratitude to my family and especially my beloved father Vasili Sousani, for supporting my career choices, guiding me scientifically during my studies and contributing to this thesis by sharing his engineering experience.

Abstract

This dissertation investigates the implications of the fluid flow on the behaviour of the particle-scale structure of a porous hard rock, based on the Discrete Element Method (DEM). This project is driven by the need to contribute towards a better understanding of the mechanical behaviour of porous rock formations under intense injection conditions and the influence of natural pre-existing rock damage to the hydraulic fracturing mechanism. The proposed numerical scheme incorporates different methods for computing both the solid and co-existing fluid phases. The solid phase (rock sample) has been characterized as a collection of discrete interacting particles, bound by spring-like contacts according to the DEM. Meanwhile, the fluid phase has been modelled by discretising the Navier-Stokes equations for porous media, utilising the fluid coupling algorithm embedded in the Particle Flow Code (PFC3D) software by Itasca.

The outcome of this dissertation suggests that the DEM approach is an advanced computational method that can reproduce accurate rock models, adequately describe the inter-particle dynamics and thus contribute towards direct numerical and experimental comparisons, and interpret the geo-mechanical behaviour of the rock materials. Furthermore, this study identifies the importance of shear cracking in the hydraulic fracturing models, whereas conventional theory relates hydraulic fracturing with tensile cracking. Finally, this study focuses on the influences of various parameters, such as the external stress regime, fluid viscosity and pre-existing fractures, on the mechanical behaviour of the rock material in the particle-scale and the hydraulic fracturing process as a whole.

This work is in an early stage and it aims to simulate hydraulic fracturing experiments with the use of a 3D modelling and the DEM approach, and to investigate the micromechanical response of the rock. Further research may include areas such as the 3D modelling of pre-cracked rocks using a larger variety of fracture angles.

Table of Contents

List of Tables

List of Figures

Nomenclature

Acronyms

AE	Accoustic Emissions
BPM	Bonded Particle Model
CCS	Carbon Capture and Storage
CFD	Computational Fluid Dynamics
DDA	Discontinuus Deformation Analysis
DDM	Displacement Discontinuity Method
DEM	Discrete Element Method
DFN	Discrete Fracture Network
DNS	Direct Numerical Solution
EDEM	Expanded Distinct Element Method
EGR	Enhanced Gas Recovery
ELFEN	Finite Element/Discrete Element system
EOR	Enhanced Oil Recovery
FDEM	Finite Discrete Element Method
FEM	Finite Element Method
FLAC	Continuum modelling for non-linear material behaviour
NORM	Naturally Occuring Radioactive Material
PFC	Particle Flow Code
RFPA	Rock Failure Process Analysis
SENB	Single Edge Notch Bending
SJM	Smooth Joint contact Model
SRM	Synthetic Rock Mass
UCS	Uniaxial compressive simulation

UDEC	Universal Distinct Element Code
UFM	Unconventional Fracture Model
XFEM	Extended Finite Elemement Method
YADE	Open source discrete numerical modelling

Variables

k	Absolute permeability
$\dot{\omega}$	Angular acceleration
$\bar{\sigma}_{kk}$	Average direct stresses
$\bar{\sigma}_{ij}$	Average stress in a measurement region
σ_a	Axial stress
$f_{\vec{\beta}}$	Body force per unit volume
σ_t^B	Brazilian tensile strength
a_ρ	Calibration factor for density
a_μ	Calibration factor for viscosity
A	Constant
B	Constant
μ	Correlation factor
A_b	Cross-sectional area of bond
$\acute{A}$	Cross-sectional area of flow
F	Current average force

α	Damping constant
F_i^d	Damping force
$\varepsilon\vec{u}$	Darcy velocity
C_2	Density multiplication factor
ρ	Density of the fluid
B	Depth of the virtual sample
n	Desired porosity
μ_D	Dynamic viscosity of the fluid
z	Elevation of flow
P_0	External pressure
r_0	External radius
P_f	Fluid pressure
F_j	Force acting on particle
i	Free index
F_i	Generalised force
N	Generated particles
D	Grain diameter of real rock
g	Gravitational acceleration
L	Height of granular solid bed
n_0	Initial porosity of virtual sample
P_i	Internal pressure

r_i	Internal radius
u_0	Interstitial velocity
P	Load for SENB test
x_i	Location of particle centroid
σ_L	Longitudinal stress
F_{max}	Max average force
$\sigma_{\alpha_{max}}$	Max axial stress
τ_{max}	Max shear stress of bond
σ_{max}	Max tensile stress of bond
$\bar{R}$	Mean particle radius
K_I	Mode I Stress Intensity factor
m	Multiplication factor
a	Non-dimensional constant
β	Non-dimensional constant
F_i^n	Normal force vector
M_i^n	Normal moment vector
ΔU^n	Normal overlap
k^n	Normal parallel bond stiffness
$\acute{\sigma}_t$	Normal strength of parallel bond
B_N	Notch depth
α_N	Notch length

N_p	Number of particles in a measurement region
U_i	Particle generalised velocity
m_p	Particle mass
ω	Particle rotational velocity
$\ddot{x}_i$	Particle translational acceleration
$\dot{x}_i$	Particle translational velocity
u_p	Platen velocity
v	Poisson ratio
J	Polar moment of inertia of parallel bond
ε	Porosity of granular solids
Δ_p	Pressure difference
r	Radial distance
σ_r	Radial stress
R	Radius of Brazilian disc
V_i	Relevant velocity at contact
σ_o	Required isotropic stress
S	Span of the virtual sample
τ_B	Thickness of Brazilian disc
F_i^T	Total force vector
M_i^T	Total moment vector
q_{UCS}	Uniaxial compressive strength

q	Velocity of liquid
V	Vessel of the virtual sample
C_1	Viscosity multiplication factor
$V^{(p)}$	Volume of particle
W	Width of the virtual sample
E	Young's modulus
$\overline{E}_C$	Young's modulus of parallel bond
E_C	Young's modulus of particles

Chapter 1 Introduction

1.1 Background

Hydraulic fracturing, or fracking, is a technique used in the mining industry and involves the controlled cracking of the rock formation with the use of high pressure liquid fluids (Howard and Fast, 1970). The technique of hydraulically fracturing the rocks has been well known since it has been widely used for Enhanced Oil Recovery (EOR) and Enhanced Gas Recovery (EGR) in the oil and gas industries, especially in the US, to extract more oil/gas through the deep rock formations (Economides, 2007;Kasza and Wilk, 2012). Hydraulic fracturing is a combination of processes, such as the deformation of the formation due to an external mechanical load (i.e. fluid pressure), the fluid flow through pre-existing cracks of the formation and the propagation of cracks (Adachi, 2007; Eshiet and Sheng, 2010). While the technology behind these processes has been used for more than 30 years in the name of energy exploitation, underground formations constitute a complex system of variables (both rock and well properties) that are not fully understood and thus are still under investigation (Economides, 2000;Smith, 2012).

Scientists over the years have concluded that there is a clear relationship between the increase of CO_2 and human activities (IPCC, 2007a;Mikkelsen, 2010). Figure 1.1 demonstrates the average temperatures globally from the mid-19th century until the present. It can be observed that the temperatures continue to rise and the period between 2000 and 2010 was the warmest decade since at least the 1850s.

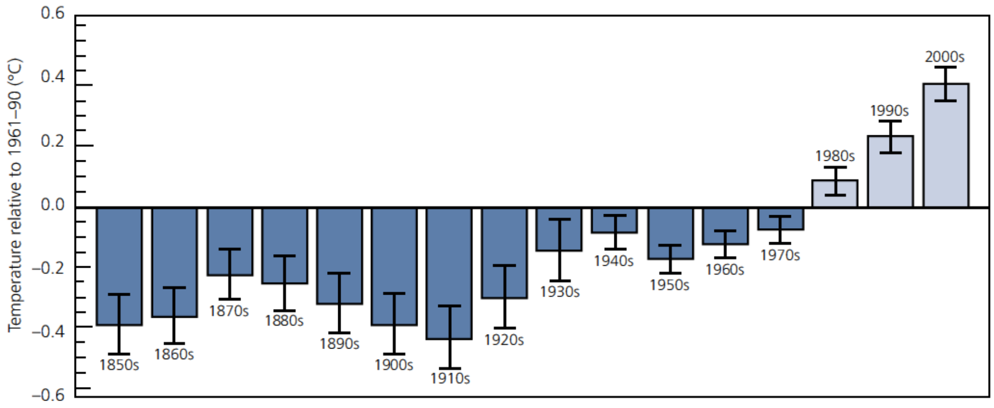

Figure 1.1 Plot of the global average temperatures between the period 1850 and 2010 (DECC, 2011).

Overpopulation, and therefore extensive industrial activities, contribute greatly to the increase of greenhouse gas emissions and countries have agreed to a common mitigation plan in order to reduce the CO_2 emissions to acceptable levels and achieve a low carbon energy future (IPCC, 2007a,b;European Commission, 2011a,b;IEA, 2013). Carbon Capture and Storage (CCS) is a promising method that plays a central role as part of the mitigation plan (Gibbins, 2008;IEA, 2009;DECC, 2011;Global CCS Institute, 2014;IPCC, 2014). CCS is a five step procedure which embraces all stages of industrial production (IPCC, 2005). Specifically, it involves the capture of high amounts of CO_2 produced from industrial facilities before they are released into the atmosphere, its liquefaction and pipeline transport into the site (oil and gas reservoirs, saline formations), injection under high pressure and storage in deep underground formations (Holloway, 2007). The hydraulic fracturing technique on porous media has become part of the injection and storage stage of CCS (Howard and Fast, 1970; Eshiet and Sheng, 2014a) and therefore it is essential to understand the mechanisms that involve permanent storage and reduction of CO_2.

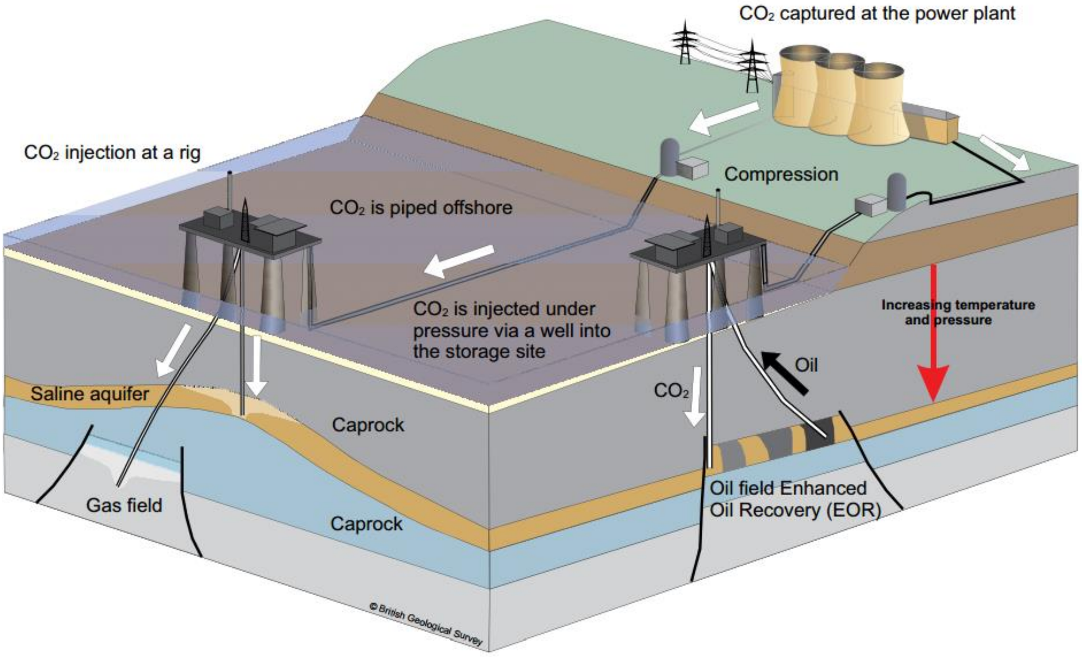

Figure 1.2 Schematic of CCS infrastructure showing the geological media of storage (SCCS, 2009).

The economic benefits from energy exploitation, and especially the extraction of natural gas from shale gas formations, through hydraulic fracturing methods are estimated to be considerable. The US has already moved towards extensive shale gas exploitation, making Europe the next to follow in the search of energy production and economy growth. Specifically, in the UK there are some promising estimations of the amount of shale gas from numerous formations throughout the nation. According to the British Geological Survey (BGS), and the Department of Energy and Climate Change (DECC), the Bowland shale formation is estimated to contain about 1300trillion cubic feet of shale gas, with about 10 per cent recoverable (BGS and DECC, 2013). The scenario for UK shale gas production approaches to be encouraging, according to the Institute of Directors (IoD) (2012; 2013), thus suggesting high investments and numerous jobs (Taylor and Lewis, 2013), and considerable reductions of imported gas (about 37 per cent) in terms of consumption until 2030, which may lead to further reductions in the import costs, assisting towards a more balanced economy and energy security (Economic Affairs Committee, 2014). However, it is important to add that the economic implications are under speculation since they are based mostly on estimations, inferred from the US experience, and not on actual production.

The following sections of this introductory chapter include the current status of research on hydraulic fracturing and computational modelling, the objectives and the outline of this thesis.

1.2 Literature Review

Enhanced Oil Recovery (EOR) and/or Enhanced Gas Recovery (EGR) are regarded as the most effective schemes for a low-carbon energy future, since CO_2 injection and oil/gas extraction from hydrocarbon reservoirs can be performed concurrently (Parker *et al.*, 2009). During this process, fluids are injected under high pressure into porous formations, with the aim of storing the liquefied CO_2 under an impermeable cap-rock, and cause controlled cracking to improve reservoir productivity (Economides, 2000). Figure 1.2 illustrates a hydraulic fracturing technique in a shale gas formation, where the fracturing fluid is injected within the shale under high injection pressure to reactivate or open new fractures in the formation. The fractures stay open with the use of shale-proppants (sand or ceramics) so that the shale gas can travel towards the well (Deng *et al.*, 2014).

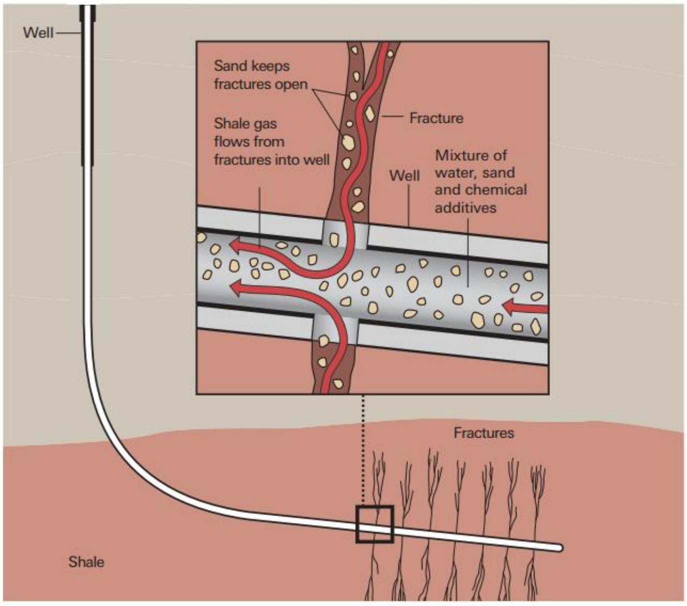

Figure 1.3 Schematic of the hydraulic fracturing technique in a shale gas formation (Royal Society, 2012).

The basic intention of the fracking process is to maximise the reservoir's permeability, but the permeability of a fractured formation is highly affected by the openings of the fractures. However, the fractures tend to close after a hydraulic fracturing operation and thus suitable proppants have to be selected, blend in a certain ratio with the fracturing fluid, fill the fractures and keep them open after fluid injection (Economides, 2007). Therefore estimation of the residual openings (Papanastasiou, 2000; van Dam et al., 2000a; Bortolan Neto and Kotousov, 2012) or the permeability of the fracture openings (Khanna et al., 2012), which are filled with proppants, as well as the optimisation of the used proppants (Vincent, 2002) are of great significance for EGR/EOR applications. A number of studies have focused on the transport of suspended proppant particles within the fracture and the interaction between the formation and the proppant. Specifically, Deng et al., (2014) investigated the shale-proppant interactions and evaluated the fracture aperture under the influence of different pressure levels, proppant sizes and Young's modulus of the shale. According to his findings, the combination that provides soft shale particles, high pressure and large proppant size, suggests small crack openings and large plastic zone for other given conditions (loading rates, shale modulus). Furthermore, the aforementioned three parameters increase the smaller fracture aperture.

Between the two methods of oil and gas extraction, EGR is relatively new and is still under investigation. The main reason is the concerns for degrading gas production due to the mixture between the initial gas in place and the injected CO_2 (van der Meer, 2005). Furthermore, ongoing research aims to provide further insight into such matters, focusing on investigating the factors that affect the process of EGR and storage. Such an example is the work done by Khan *et al.* (2013), who replicated a 3-dimensional reservoir sandstone model using actual experimental data and simulated an EGR process, while sequestrating CO_2. His findings refer to the specific sandstone reservoir and can confirm that the CO_2 injection is applicable in increasing natural gas recovery and storing high amounts of CO_2 at the same time. The conventional procedure of oil extraction involves the injection of water. However a large amount of oil stays trapped within the pores of the formation (about 50 per cent) after the primary production, and further recovery can be achieved by injecting liquefied carbon dioxide (Blunt, 1993). The latter exists in a supercritical state (dense phase fluid), with reduced viscosity (0.04-0.08Cp) and surface tension, which means that the vapour and liquid forms of the CO_2 coexist. The component acts like a gas and a compressible fluid at the same time, and can take the shape of its vessel, while having a density (about 600-800kg/m3) like a fluid (van der Meer, 2005). This supercritical state is achieved at depths above 800-850m, pressures beyond 7.38MPa and temperatures higher than 31^{o}C (Parker *et al.*., 2009). Due to the dense phase and the fact that it is easily miscible with other oils, helps dissolve and relocate the oil. This technique is a key technology to reduce the anthropogenic emissions produced from overpopulated regions, such as China, while satisfying the extensive demands on electricity (Jin *et al.*, 2012). Although hydraulic fracturing is part of the technology used for gas/oil extraction, and thus widely used, it is still lacking the development of appropriate regulations for environmental safety and sustainability.

Regardless of the choice of liquid (water or liquefied CO_2), the hydraulic fracturing process requires the use of a considerable fluid pressure in order to introduce the liquid into the rock formation, until it exceeds the overall strength of the rock (both compressive and tensile) (Fjaer *et al.*, 2008). Therefore, valid estimates of the mechanical behaviour of the rock material under intense injection conditions are crucial to the efficient planning and operation of hydrocarbon reservoirs. This constant increase in the fluid pressure during injection causes redistribution of the in-situ effective stresses within the reservoir. Although in this process the controlled fracturing of the reservoir is desirable, such stress changes may induce irreversible effects into the rock strata (Benson et al., 2008), thus causing possible reactivation of the existing faults. Moreover, the effects of active faults on the process of leakage is a topic where more research has to be performed and scientists generally suggest that the existence of seismogenic faults affects the permeability structure of the zone enhancing fluid transport (Wilkins and Naruk, 2007). In the process of hydraulic fracturing, the latter may lead to possible leakage of liquefied CO_2 (IEAGHG, 2011b) or flowback water, thus resulting in potential hazards. Moving towards a bigger picture, the major effects are the possible contamination of shallow groundwater layers by the migration of the toxic components of the flowback fluids as well as the leakage of methane, which acts as a greenhouse gas, into the atmosphere (Kissinger *et al.*, 2013).

1.2.1 Flowback fluid

Flowback fluid is the recovered fracturing fluid after the pressure release and the extraction phase and it mainly consists of a formation fluid, hydraulic fracturing fluid (water, sand, proppants, and chemical additives) and naturally occurring radioactive material (NORM) of varying concentrations (Edmiston et al., 2011). The key point is that the flowback fluid differs from the initial fracking fluid that was used during injection, in terms of composition. The majority of the volume of sand and proppants stays trapped within the pores of the formation, while the chemical additives react due to intense injection conditions, such as high temperature, resulting in reaction products. Therefore there is a potential risk of contamination of freshwater resources if flowback fluid is allowed to flow freely. The exposure of the chemicals of the fracking fluid and the risk to groundwater reserves is linked to several factors, including underground or above-ground accidents during the transport and the concentration/handling of the possible hazardous substances (Gordalla et al., 2013). Currently, the issue of potential implications on the quality of water is a matter of debate. This is due to the lack of available information on the composition of the chemicals used in the hydraulic fracturing procedures, and therefore scientists are focusing on this research topic aiming to shed more light on the effect of the chemicals used in hydraulic fracturing on water. Recent studies of dealing with the ecotoxicological assessment of undiluted fracturing fluids indicating a hazardous effect on aquatic life. These studies are based on component-based prognostic models rather than measuring the ecotoxicological effect of a fracturing fluid as a whole (Riedl et al., 2013). This provides better accuracy of the overall results, allowing the prognosis of the effect of the mixture components individually. Generally, flowback fluids contain a mixture of hydraulic fracturing fluid and formation water. The potency of flowback fluid depends on the mix ratio of the formation water and fracturing fluid. Although a high proportion of the fracturing fluid may be retained in the formation, there is a high tendency for flowback to take place as a result of imposed fracturing operations (Olsson et al., 2013). At present, very limited studies have dealt with the chemical composition of flowback or its potential pollutants, and there are no studies investigating the difference between fracturing fluid from formation water that contains no fracturing fluid in flowback. The work performed by Olsson et al., (2013) aims to bridge the knowledge gap by analysing the composition and volumes of flowback from different sites in Germany. This research has revealed that no single technology can meet the criteria for the overall treatment of flowback, thus they categorized the flowback fluid into groups and suggested some treatment methods. Furthermore, the accidental penetration of the fracturing and flowback fluids into the water aquifers and their impact on the human-health becomes critical and recently it has been addressed. Such an example is the work by Gordalla et al., (2013) who focused on the assessment of the ingredients of the fracturing fluids on the human-toxicological point of view, the influence of the flowback, the possible hazards of freshwater reserves and suggested methods for minimising the environmental impact. In addition the presence of NORMs in the fracking fluid has been increasingly investigated recently. Even though there are very few shale gas wells drilled in Europe, compared to the US where the disposal of flowback water by injecting it deep underground has become routine (in America in 2008, 1600 wells were in operation, while in Europe there were only about 100) (The Economist, 2011), there is always a concern of how best to dispose of the flowback fluid in Europe. Many sedimentary shale formations can contain high concentrations of NORM, such as radium, uranium and thorium, with radium as the most soluble in the hydraulic fracturing fluid and therefore the most dangerous to flow back to the surface (Abdeen and Khalil, 1995; Edmiston et al., 2011). However, our knowledge is limited and thus ongoing research aims to provide further insights. ReFINE is one of the institutes that is investigating the volume of flowback fluid and the flux of radioactivity, should Europe decide to move ahead with extensive shale gas exploitation. Their recent work (Almond et al., 2014) focuses on the changing levels of radioactivity in the flowback fluid using three different geological locations; i) the Bowland shale formation (UK), ii) the Silurian shale (Poland) and iii) the Barnett shale (USA). Moreover, apart from the importance of extending the available information on the chemical composition of fracturing fluids, or the environmental impact of the flowback and its proposed treating methods, it is of equal importance to investigate the underground formations and their interaction with the potential migrating fracturing fluids or methane. Such an example is the work by Lange et al., (2013) who aimed to identify fault zones as preferential pathways that facilitate the movement of fracturing fluids/methane in unconventional gas reservoirs and analysed the effectiveness of the different layers of overburden.

1.2.2 Risk of contamination of aquifers

The extensive use of unconventional fracking (horizontal drilling and high volume hydraulic fracturing), especially in the US, has triggered a public debate regarding possible health issues related to drinking water. Although industry claims that shale gas fracking is safe with minimum environmental impacts, the European Commission states that the extraction of unconventional hydrocarbons (shale gas) generally imposes a larger environmental footprint than conventional gas extraction (COM, 2014). Risks from ongoing operations may include surface and ground water contamination, water resource depletion, air and noise emissions, land take, disturbance to biodiversity and impacts related to traffic. People’s concern, especially in European countries where groundwater is their main resource of drinking water, has forced countries to seek expert opinions. A typical example is Germany and the ExxonMobil initiative (Panel of Experts, 2012). The latter has formed a multidisciplinary working group in order to identify the possible environmental risks for the Lower Saxony Basin. Their main task is to assess the available technology (drilling and technical processes) and develop a strategy that fits the requirements for safe hydraulic fracturing operations. Part of this assessment is the ‘’*Information and Dialogue process on hydraulic fracturing*’’, focusing on the characterization of the hydrogeological system, the chemical reactions under which leakage may occur, the possible leakage pathways, the development of suitable models and their results (Kissinger et al., 2013; Lange et al., 2013).

1.2.3 Numerical modelling for engineering problems

Moreover, the numerical analysis of rock engineering problems is a challenging and necessary task to investigate the fundamental mechanisms occurring in the rocks and help towards better rock engineering design. Reviews of the available numerical methods, their imitations and enhancements, as well as the developments in modelling the hydrofracturing process, have been presented in (Jing and Hudson, 2002; Adachi, 2007; Lisjak and Grasselli, 2014). The rapid growth in computer power and modelling techniques has resulted in the development of a large number of software packages used for the numerical analysis of complex engineering problems, such as the modelling of fracture in thin structures (Shie, 2014), or the identification of problematic (low bond strength) material parameters in masonry structures (Sarhosis and Sheng, 2014). In cases of pre-cracked rock formations, the numerical model needs to describe numerous discontinuities within the rock's matrix. There are examples of studies dealing with the modelling of rocks with pre-existing fractures, estimating the properties (strength and stiffness), deformations and stress distribution of jointed rock masses around excavations with the use of equivalent continuum models (Sitharam et al., 2001; 2002). However, the effect of sliding and detachment along these fractures is difficult to be described accurately by continuum models. Specifically in the case of hydrofracturing, it is very difficult for the analytical modelling to measure and describe accurately the complex problems associated with fracturing and therefore advanced numerical modelling has been created. In subsurface investigations in particular, where heterogeneity and a wide range of complex inner mechanisms coexist, numerical modelling is necessary to represent real life scenarios. Numerous mathematical solutions have been applied to look into the critical mechanical parameters, such as the stress envelope, the porosity and permeability of the material, the effect of layering within the rock, or the way that these are influenced by the external mechanical load (Hanson et al., 1980), as well as the micromechanical failure process in brittle rocks that controls strain localization in the macroscale (Lockner et al., 1991). However, studies that employ modelling and simulation of rocks at the micro-scale (Potyondy and Cundall, 2004; Eshiet et al., 2013; 2014; Sousani et al., 2014) are fewer and their focus is on the complex interplay between the micro-properties and their corresponding effect on the material’s behaviour during the calibration procedure provides, at best a general guidance.

1.2.4 Modelling of rock fragmentation with DEMs

The available numerical techniques for describing the rock behaviour fall into two basic categories of continuum (Finite Element Method-FEM) and/or discontinuum (DEM) based approaches. The continuum approaches utilise two techniques in order to describe rock discontinuity problems due to the presence of pre-existing fractures. The volume of the fractures is the key factor that determines which method, within the continuum approaches, fits best. If the number of discontinuities is small then the continuum-combined interface method is employed, which uses joint/interface elements to describe the discontinuity behaviour and simulate large deformations/displacements and rotational movements, (Ghaboussi et al., 1973; Goodman, 1976; Bfer, 1985; Riahi et al., 2012), whereas if the number of the discontinuities is relatively large then homogenization techniques are employed. During homogenization, the complex material is replaced by an equivalent model with reduced deformation modulus and strength parameters (Hoek and Diederichs, 2006). The *effective* properties of the homogenized material are calculated and the analysis of the boundary values is performed (Jing and Stephansson, 1997; Hassani and Hinton, 1998). However, each technique and hence the concept of the continuum approach face its own limitations, such as the fact that the rotational movement, slip, complete detachment of blocks and the size effects (due to the presence of discontinuities) cannot be completely described (Hammah et al., 2008), or that the accuracy of the results is compromised by non-negligible changes in the interface elements' edge contacts and the fact that new contacts between solids and joints during the simulation cannot be recognised (Cundall and Hart, 1992).

The DEM is an alternative approach to the Finite Element Method (FEM), which has been widely utilised (Donzé et al., 2008) that aims to describes the macroscopic mechanical behaviour and the cracking behaviour of materials (Kim et al., 2012) as the result of the interaction of its constitutive individual elements. This method allows for the properties of the discontinuities to be considered and thus the overall behaviour of the fractured rocks is captured more accurately. With respect to the simulation of large scale rock formations, such as fractured rock masses, they are usually modelled as a continuous rock which is then divided into sub-blocks separated by faults or joints. A number of fundamental properties and external boundary conditions are assigned to the joints and the assembly, respectively. The internal boundary conditions of the individual blocks are calculated from their interactions at their contacts as the simulation progresses. This method has been applied in several engineering fields, such as slope stability and mining, where large-scale rocks have to be modelled in order to investigate their stability, strength

(Stefanou and Vardoulakis, 2005) and stress field (McKinnon and Garrido de la Barra, 2003; Baird and McKinnon, 2007). Moreover, in the micro or mesoscale of DEM models, the material is described as a discontinuum, consisting of numerous distinct particles which represents the inhomogeneities within the material (fractures or faults) in the particle scale (Potyondy and Cundall, 2004; Bortolan Neto and Kotousov, 2012; Tarokh and Fakhimi, 2014). The DEM approach allows displacements, rotations and complete separation of the discrete elements, and recognizes any new contacts that are developed during the simulation. Initially models, which were based on the particle-scale, were developed in order to simulate the micromechanical behaviour of soils and sands (non-cohesive materials) (Cundall and Strack, 1979). Moreover, the concept of the DEM methodology can be divided into the explicit and implicit approaches. The explicit approach solves the equation of motion of the particles with the use of a time-domain scheme (Cundall and Strack, 1979). Characteristic examples of the explicit approach of the DEMs include the particle flow code (PFC) (Itasca Consulting Group, 2008d), the YADE (V. Šmilauer et al., 2010), and the universal distinct element code (UDEC) (Itasca Consulting Group Inc, 2013). Furthermore, an example of the implicit approach is the discontinuous deformation analysis (DDA) (Shi and Goodman, 1988). Each of the discrete explicit and implicit approaches is based on the DEMs governing formulations with its own limitations, which are discussed below.

1.2.5 Bonded Particle Model (BPM) and implementation in the Particle Flow Code (PFC)

The transition from the aforementioned modelling of soils and sands to the one that simulates the micromechanical behaviour of solid rocks is commonly known as the bonded-particle model (BPM) for rock (Potyondy and Cundall, 2004). In a BPM, the breakage of inter-particle bonds simulates the nucleation of a micro-crack, while micro-cracking is achieved by coalescence of multiple bond breakages. The BPM model has been proven to be a valuable tool to analyse a variety of difficult engineering problems, such as the damaged zones in tunnelling (Potyondy and Cundall, 1998), or the initiation of cracks and their propagation patterns from pre-cracked rock-like materials. The work performed by Zhang and Wong (2012, 2013) is a characteristic example of the use of the BPM model simulating a rock-like material which contains a single and two coplanar flaws, respectively, and is under uniaxial compressive loading. The purpose of this study was to investigate the crack initiation and coalescence processes within the material. Another application of the BPM model is presented by Manouchehrian and Majri (2012), who have employed the BPM model to study the influence of lateral confinement on the cracking mechanism of rock samples containing pre-existing single flaws, or the work performed by Diederichs, (2003), who investigated the effect of the tensile damage and the sensitivity to reduced confinement on the failure mechanism of hard rock masses.

As a result, PFC also utilises the BPM model, since it has been widely used to simulate the fracturing mechanism in brittle rocks. However, initial versions of PFC suffered from limitations on duplicating the micromechanical behaviour of hard rocks with complex shapes and highly interlocked grains using circular (2D version) and spherical (3D version) elements. Specifically, the BPM model produced unrealistic ratios between the obtained tensile and unconfined compressive strength (about 0.25) (Diederichs, 1999; Potyondy and Cundall, 2004; Cho et al., 2007), compared with typical rocks, where the ratio is reported about 0.05-0.1 (Hoek and Brown, 1997), the low non-linear failure envelopes in terms of triaxial tests (Hoek et al., 2000), or the problematic modelling of the interfaces due to the inherent roughness of the interface surfaces (Lisjak and Grasselli, 2014). To tackle these limitations of PFC, a number of enhancement measures have been developed with the aim to provide a more accurate non-linear mechanical behaviour, strength ratios and friction coefficients. The basic concepts include the; "cluster logic" (bonded particles packed together to form angular shapes or blocks that resemble natural grain structures, Figure 1.4(**a**)), performed by Potyondy and Cundall, (2004); the "clump logic" (bonded particles that behave collectively as a single unbreakable rigid body, Figure 1.4(**b**)) from Cho et al., (2007); the flat-joint contact model (a more efficient contact formulation, where disk-shaped particle contacts simulate a finite-length interface and the relative rotation, even upon bond breakage, Figure 1.4(**c**)) from Potyondy, (2012) and finally the; smooth-joint contact model (SJM) and the synthetic rock mass approach (SRM), respectively, from Mas Ivars (2010; 2011). The SJM model (Figure 1.5) simulates the behaviour of an interface disregarding the particle contact orientations locally alongside the interface, while the SRM model is a combination between the BPM and the SJM models that describes the mechanical behaviour of jointed rock masses, including anisotropy, brittleness and scaling effects which cannot be achieved by empirical methods.

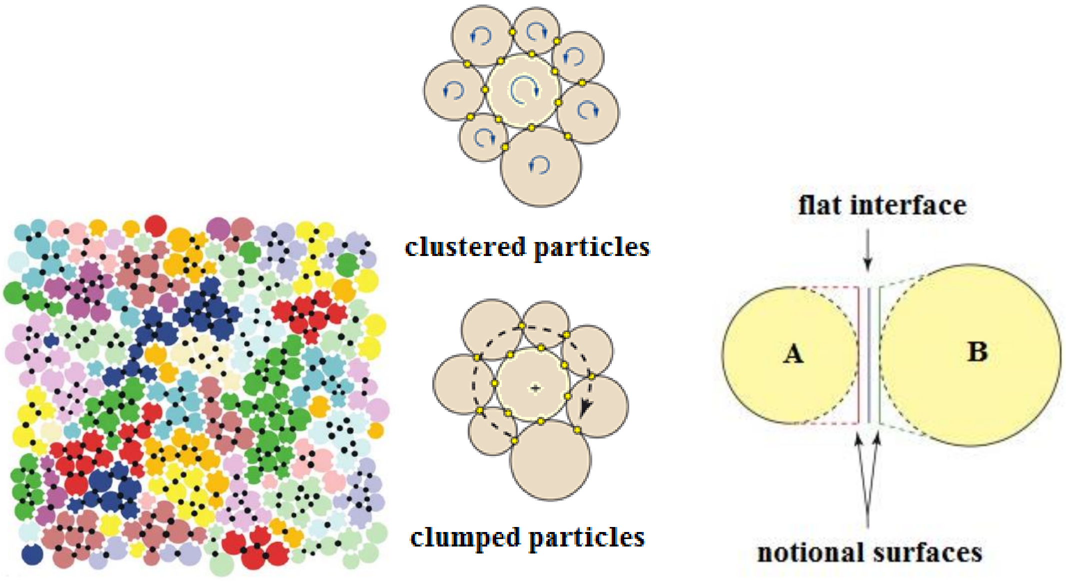

(**a**) (**b**) (**c**)

Figure 1.4 Developments on the BPM model for better representation of the non-linear behaviour of hard rock and more realistic values of the ratio between tensile and unconfined compressive strength. (**a**) The "cluster" logic (Potyondy and Cundall, 2004), (**b**) the "clump" logic versus the "cluster" logic (Cho et al., 2007), and (**c**) the flat-joint contact model (Potyondy, 2012).

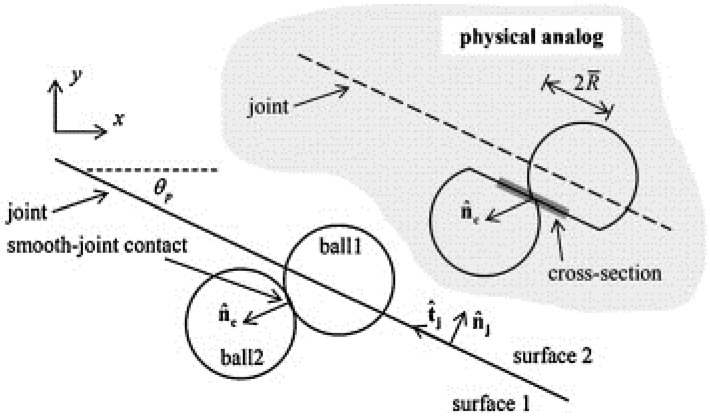

Figure 1.5 Schematic of the smooth-joint contact model (SJM) (Itasca Consulting Group, 2008f).

1.2.6 Applications of PFC

PFC is a well-known commercial code for simulating the fracturing of brittle rocks and has been widely used over many years. The work performed by

Potyondy *et al.* (1996) presents the first PFC synthetic model which can simulate the elasticity of the Lac du Bonnet Granite, its unconfined compressive stress and the crack initiation stress, while in Potyondy and Cundall, (2004) the extended results of the initial work are presented. PFC can also provide a better understanding of the crack initiation and propagation within rocks when combined with indirect observation techniques, such as acoustic emissions (AE). The work presented by Hazzard and Young (2000; 2002, 2004) focuses on the application of PFC on AE in order to provide seismic source information, induced by the bond breakage and hence damage. Their initial work aimed to investigate the micromechanics behind the recorded seismicity and focused on the cracking patterns as well as on the release of energy during damage, while their extended results introduced moment tensors (obtained from the sum of the contact forces upon particle contact breakage) and moment magnitudes (obtained from the eigenvalues of the moment tensor) for specific seismic events. They also developed a three-dimensional PFC model that estimates the locations, magnitudes and moment tensors of seismic events. The obtained numerical PFC models and algorithms were further applied to the simulation of a mine-by excavation of a tunnel that produced microseismic event. In comparison with the actual seismicity on site, the results appeared to produce reasonable realistic information on the source mechanisms. Further applications of PFC include the analysis of various factors controlling the stability of underground excavations in hard rock formations (Diederichs, 2003), or the calculation of fracture toughness of a rock sample with non-uniform size particles in order to understand difficult engineering applications, such as rock cutting and explosive engineering operations (Moon et al., 2007). Similarly, a PFC2D model was developed by Potyondy and Cundall (2000) in order to predict excavation-induced damage (information on the intensity, location, orientation and the progressive development of the cracks in the microscale) in an gneissic tonatile, under compressive loading, from the Olkiluoto formation.

1.2.7 Discrete Element and Finite Element Techniques

Recently, another particle-based code has been developed, called YADE, as an alternative approach to the well-known commercial PFC code as previously described (Kozicki and Donzé, 2008; 2009). YADE aims to be more flexible, by adding new modelling capabilities, several simulation methods (e.g. DEM, FEM) can be coupled within the same framework and also the scientific community can provide direct feedback for improvement of the code with the use of an open-source platform. The fundamental principles of YADE are similar to those of PFC with respect to small deformations and fracturing (linear elastic inter-particle forces and bond breakage, respectively) but new features of simulating rock discontinuities and ensuring frictional behaviour regardless of the inherent roughness have been implemented as an alternative approach to the SJM and SRM models (Scholtès and Donzé, 2012). In addition, the use of YADE in studying the failure of brittle rocks has led to the creation of additional features, such as the interaction range coefficient, that helps to accurately simulate high ratios of compressive to tensile strengths as well as non-linear failure envelopes (Scholtès and Donzé, 2013). However, YADE as well as many of the open-source software packages appear to suffer when compared to commercial products such as PFC, mainly due to the complexity of the user's interface and the lack of user-friendliness. Moreover, open-source software solutions tend to develop mainly in-line with their designers, and also rely on their pool of users and scientistic communities to help discover problems and bugs. Some applications of the YADE code include three-dimensional simulations of the progressive damage in fractured rock masses (Scholtès and Donzé, 2012), or the effect of pre-existing fractures of brittle materials, under triaxial loading, on their mechanical behaviour (Scholtès et al., 2011; Harthong et al., 2012). In the aforementioned simulations the open-source code YADE has been collaborated with the Discrete Fracture Network (DFN) in order to model the three-dimensional structure of the discrete features.

Another computer programm, which is based on the DEM equations, is the UDEC (universal distinct element code), employed to study rock masses that contain numerous fractures (Fan et al., 2004; Zhao et al., 2008). The computational domain in UDEC is quantized into blocks using a finite number of intersecting discontinuities and each block is discretized with the use of a finite-difference scheme in order to calculate stresses, strains and deformation. The basic limitation of this technique was the fact that the failure mechanism in rocks was described either through plastic yielding or through deformation of pre-existing fractures. Therefore new fractures could not be modelled and hence fracturing of intact rocks was impossible. This limitation was addressed by Lorig and Cundall, (1989) who introduced a polygonal block pattern into the modelling and enhanced the UDEC/3DEC’s simulation capability. UDEC/3DEC is a relatively new approach to rock failure and thus verifications and improvements of the code are some of the required tasks of experts in the field. Applications of the code can be found on grain-based numerical modelling to conduct numerical triaxial simulations of lithophysal rock samples, in cases where the laboratory triaxial testing is considered almost impossible (Christianson et al., 2006). Extended results of this study on the same rock material, with the use of the UDEC/3DEC, are presented by Damjanac et al., (2007) who focused on the mechanical degradation of the behaviour of the material. An up-scaled version of the developed model was employed to investigate the stability of the drifts from the region (Yucca Mountain) considering the in-situ thermal and seismic loading as well as the time-dependent degradation. Some more examples of investigating the fracking mechanism with the use of this code include the simulations: (i) of the time-dependent degradation of rock bridges (intact segments of material along discontinuities) with further application on the time-dependent failure of the drifts at the project of storing the nuclear waste at Yucca Mountain (Kemeny, 2005), (ii) the development of an expanded distinct element code (EDEM), based on UDEC/3DEC, to model the initiation and propagation of the possible microcracks due to the stress regime (shear and tension failures) in the internal of the rock blocks with further applications on underground excavations (Jiang et al., 2009), and (iii) the calculation of rock strength and damage, implementing the concept of a collection of deformable particles with arbitrary size and cohesive boundaries into UDEC/3DEC, and further validation of the numerical results against compressive and tensile laboratory trials on sedimentary rock and crystallised igneous (Kazerani et al., 2012; 2013) .

Finally, the DDA (discontinuous deformation analysis) is a method also based on DEM, but with similarities with the finite element method (FEM). Its concept is based on the block theory (utilises FEM mesh for modelling blocks) and the minimum energy principle. DDA was originally introduced by Shi and Goodman, (1988) and was further developed and utilised for coupled stress-flow problems (Jing et al., 2001). DDA is employed to simulate the stress, strain, sliding and detachment/re-joining of systems containing rock blocks. Similarly to the FEM the basic structure of the method, in terms of formulations, contains linear equations which results from differentiating and minimizing each energy contribution to the system. Improvements of the method have been employed over the years with the latest work being performed by Tang and Hy, (2013). They combined the DDA method with the Rock Failure Process Analysis (RFPA) software, the latter based in continuum mechanics (Tang, 1997), to investigate large-scale deformations of discontinuous rock systems using the capability of RFPA to capture small deformation, crack initiation/propagation and coalescence in intact rocks. In the DDA method the fractures within the rock masses which affect their stability must be modelled using joint attitude, length, spacing and bridge. Some typical examples of applications of the DDA method include; (i) modelling of the damage along natural structural planes and the estimation of the relationship between the angle of friction and the space of joints of rock masses (Hatzor and Benary, 1998), (ii) the simulation of a tunnel stability (Jing, 1998), or (iii) the investigation of the effect of the mechanical layering on the deformation of rocky sedimentary blocks around underground openings and the improvement of stability analysis (Bakun-Mazor et al., 2009).

1.2.8 Combined FEM/DEM and other hybrid techniques

The FEM and its improved approaches are considered a standard technique that can be successfully applied to numerous problems, such as the modelling and evaluation of rock materials, or rock failure with internal discontinuities (Belytschko and Black, 1999; Moës et al., 1999; Hammah et al., 2007; Li et al., 2013; Giamundo et al., 2014). An example of a FEM is the two-dimensional finite difference programm FLAC (Itasca Consulting Group, 2005). This programm is employed to investigate the behaviour of materials such as soil and rocks and more specifically it simulates soil and rock structures that may undergo plastic deformation once their maximum yield limits have been reached. FLAC users create a grid, which consists of elements and zones, that fits the shape of the sample to be modelled. However, due to the geometric limitations of the FEMs, more discretization techniques have been developed to address these difficulties, such as the extended finite element method (XFEM) (Song et al., 2013a; 2013b) for computing the three-dimensional crack propagation (Areias and Belytschko, 2005; Duan et al., 2009), specifically focusing on the improvement of meshing sensitivity employed to compute the fragmentation problems (Cai et al., 2010). A number of hybrid techniques have been developed based on the FEM with DEM implementations (Li et al., 2014). This combination is called the hybrid finite dicrete element method or the FDEM (Lisjak et al., 2014) and includes models such as the ELFEN (Finite Element/Discrete Element System) (Rockfield Software Ltd, 2004), or the Y-Geo software (Munjiza et al., 1999; Munjiza, 2004) which are based on the finite element method to describe the solid part of interest but also adopt the theory of the discrete element method. The concept in FDEM is the transfer from continuum to discontinuum through fragmentation. Specifically, the sample’s matrix is modelled with the use of continuum mechanics and as the test progresses the equations of motion are integrated. Then the initiation of cracks/fragmentations is such that it satisfies suitable fracture criteria, which therefore leads to the formation of new individual discrete bodies. Comparing the FDEM with the FEM and the DEM, respectively, we can postulate that it is more capable of capturing the behaviour of post rock fragmentation and also it is more flexible in modelling the deformable and unique-shaped particles. Furthermore, between the two modelling techniques, the Y-Geo approach resembles more a discrete method. Specifically, the representation of a sample with the use of Y-Geo is closer to a particle-based model, where the particles and their bonds are replaced by deformable triangle elements and four-noded cohesive elements (Munjiza et al., 1999). Whereas in the ELFEN a transfer between a continuous elasto-plastic sample to a sample with discrete fractures is achieved by importing cracks into the sample (Owen and Feng, 2001).

1.2.9 Modelling of rock fragmentation and fluid flow

A wide range of engineering problems could utilise the DEM approach coupled with fluid models to analyse the fracking process within the rock specimen (Eshiet and Sheng, 2014b), or the influence of the significant parameters, such as the injection pressure, to a successful injection/storage application (Rutqvist et al., 2007). The coupling technique can also be used to simulate the behaviour of materials such as sandstone and limestone and the fluid-solid interactions among them (Walton, 1987; Potyondy and Cundall, 2004). Furthermore understanding the underlying mechanisms that compromise ongoing engineering operations, such as the investigation of groundwater flow under high water pressures and possible groundwater inrush incidents on hydropower stations (Wang et al., 2004) and in coal mining (Wu et al., 2011), is of high significance. The effect of high external water mechanical load and pore pressure is a key issue to the overall stability of the groundwater cavities and thus numerical analysis is essential in order to prevent possible leakage and help assist towards efficient design. The selection of an appropriate method to investigate groundwater flow and simulate pore pressure in fractured masses depend on several parameters, such as, the boundary conditions, the scale of the reservoir and the geological conditions of the region. However, the most popular methods for such analysis include the continuum medium approach (Zhu et al., 2014), the combination between the discrete fracture network (DFN) and DEM (Baghbanan and Jing, 2008; Harthong et al., 2012; Grenon et al., 2014), and methods coupling both continuum and discrete media (Wang et al., 2004; Huang et al., 2014). The continuum medium approach has proven to be inadequate in describing large scale regions since it has to oversimplify the fractured formation as a homogeneous zone (Neuman, 2005). Further, DFN approach cannot produce the detailed set of the geometrical parameters for individual fractures, which requires extensive computational time for large-scale simulations (Woodbury, 2001; Berkowitz, 2002). The third approach can be considered more efficient since it combines the advantages of both the continuum and discrete methods. Initially, the fluid-solid interactions were described by the Lattice-Boltzmann method, which computes the fluid flow and solves the discretised form of the Boltzmann equation, based on the Navier-Stokes equation (Chen and Doolen, 1998). Other methods for computing the fluid flow include Direct Numerical Simulation (DNS) (Moin and Mahesh, 1998; Dong, 2007), where the flow variables (e.g. pressure and velocity) exist as a function of space and time and can be obtained from the numerical solutions of the Navier-Stokes formulations, and Computational Fluid Dynamics (CFD). However, the need to provide linkages between the co-existing fluid and the solid phases, necessitates a coupling of these techniques with the modelling of the solid phase, such as the DEM. The Lattice-Boltzmann and the DEM coupling has been described in detail by Boutt et al., (2007), while approaches that incorporate CFD with the DEM have been presented by Tsuji et al., (1993) and Xu and Yu, (1997). In their work, the interaction between the solid and gas phases in a fluidized bed have been modelled by solving Newton’s second law of motion, with respect to the motion of the particles, and the Navier-Stokes equation with respect to the motion of the gas. Most of these coupling schemes are applied to granular or un-cohesive materials and in cases where the domain is dominated by fluid phases. Therefore, phenomena such as the deformation of the solid material and fracturing are not captured due to either the limitations in the coupling technique or the delineation of the study.

Understanding the behaviour of the underground rock formations is itself a complex subject and it has been investigated by several researchers in the past (Brace et al., 1966; Bieniawski, 1967; Cundall, 1971; Hanson et al., 1982; Ewy et al., 1988; Martin, 1997). The presence of heterogeneity in the form of discontinuities, combined with the complexity of the hydraulic fracturing technique, has resulted in more challenges in the topic of rock mechanics (Goodman, 1989). There has been extended ongoing research, both theoretical and experimental, in an attempt to understand the phenomena involved (Hanson et al., 1982; Blair et al., 1989; Matsunaga et al., 1993; Potyondy and Cundall, 2004; Boutt et al., 2007; Fang and Li, 2014; Zeidouni et al., 2014). More specifically, intact rocks are directly affected by the inhomogeneities resulting in the reduction of their strength and the induced overall non-linear behaviour in terms of stress versus strain. This is due to the kinematics restrictions on the rock formations, contributed by the presence of the discontinuities. The latter can cause the redistribution of stresses and displacements and therefore deviate from a typically linear elastic behaviour (Hoek, 1983; 2002; 2006). Several models have also been developed focusing on rock mechanics and the modelling of fractures (Rabczuk et al., 2014), such an example can be seen in Zhuang et al., (2012) and Zhuang et al., (2011), where 2D and 3D modelling of a fracture using a meshless method has been developed in order to provide stress analysis and describe the crack evolution or the study of cohesive crack models (Zi and Belytschko, 2003). The motivation behind the extended modelling researches is that they can be applied to solve some large scale engineering problems, such as the investigation of rock stability and rock failure (joints in rock masses) near hydropower stations (Zhu et al., 2011), or utilizing jointed hard rock for compressed air energy storage with the use of a coupled thermo-hydro-mechanical model (Zhuang et al., 2014). The fracturing behaviour of rock models, which contain a pre-existing single flaw, has been tackled by several researchers in the past using either the FEM approach (Bocca et al., 1990; Xu and Fowell, 1994), the Boundary Element Method (BEM) (Bobet and Einstein, 1998; Lu and Wu, 2006), or the hybridized displacement discontinuity method (DDM) (Chan et al., 1990). More specifically numerous studies, both numerical and experimental, have dealt with the investigation of pre-cracked natural rock and rock-like materials (limestone (Ingraffea and Heuze, 1980), granite (Martinez, 1999), molded gypsum (Wong and Einstein, 2007), sandstone-like material (Wong and Chau, 1998), concrete-like mix material (Mughieda and Alzo'ubi, 2004), etc.) under compression with the aim of providing further insight on the effect of the flow geometries to the fracturing mechanism and to characterize the coalescence patterns of the resulting new cracks (Lajtai, 1974; Ingraffea and Heuze, 1980; Petit and Barquins, 1988;

Jiefan et al., 1990; Chen et al., 1995; Li et al., 2005; Wong and Einstein, 2006; 2009a, b, c). The increasing energy demands in shale gas and oil, combined with the need for a more sustainable energy future has redirect research to focus on the fundamental cracking processes of hydraulically pressurized intact and pre-cracked rocks in the micro or meso-scale (Haimson, 2004; Nagel et al., 2011; Eshiet et al., 2013; Hamidi and Mortazavi, 2013; Sousani et al., 2015). An example of a hydraulically pressurized intact rock is the work performed by Sousani et al., (2014), who replicated a laboratory hydraulic fracturing, performed on a thick-walled hollow cylinder limestone rock sample. The work studied the micromechanical behaviour of the limestone sample under different fluid pressure and the comparison between the fracturing pattern of the virtual model and the laboratory rock sample. The modelling of the rock and the analysis of the fracturing mechanism was performed with the use of the DEM approach, while the simulation of the fluid flow was performed with the use of a fluid scheme (Itasca Consulting Group, 2008b). The numerical results were validated by Lame’s theory and were found to be in very good agreement with the experimental results (Sousani et al., 2014), while the numerical model captured the fracturing pattern induced by the hydraulic pressure. A similar study, on the particle scale, has been conducted by Al-Busaidi et al., (2005), who investigated the initiation and propagation of hydrofractures as well as the resulting seismic output and compared these results with experimental data produced from other scientists (Falls et al., 1992; Vinciguerra et al., 2004). Generally, their findings approached to replicate much of the laboratory behaviour observed in the hydrofracture experiments. More specifically, the numerical modelling was two-dimensional and part of the study used a number of homogeneous samples. The numerical results demonstrated some consistencies with the experimental results, showing a damage pattern along the potential macrocrack track. Another example is the work by Wang et al., (2014), who simulated a hydraulic fracturing process of a coal seam and analysed the relation between the macroscopic and the mesoscopic mechanical parameters of the material. The work has focused on the influence of the mechanical properties in the macroscale to the initiation and the size of cracks, the empirical calculation of the breakdown pressure and the analysis of the crack propagation due to the injection conditions and validated his results against the data obtained from field observations. Other studies have focused on the large scale numerical modelling and the observation of the behaviour of substantial formations. The work by Mas Ivars et al., (2011) is an example of a large scale 3D modelling approach (10 up to 100 m), obtaining a qualitative and quantitative understanding of the mechanical behaviour of the rock formation both pre-peak and post-peak failure. They used the synthetic rock mass (SRM) approach, which is based on the bonded particle model (BPM) for rocks and the smooth-joint contact model (SJIM) in order to replicate the intact rock and the in-situ join network, respectively. However, due to the nature of this study, factors that affect the behaviour of the formation in the particle scale, such as the grain size, the porosity, the pore structure, etc., were not considered. Moreover, the simulation of seismic events produced from fluid pressure distributions on large scale reservoirs (2×2 km), have been the focus from experts with the use of discrete particle joints models (Yoon et al., 2014). Many rock engineering projects, such as mining or exploitation of geothermal energy resources, are directly related to drilling and thus fracturing (Hoek et al., 2000). The rock formations in these problems show a highly pressure-dependent mechanical behaviour, which drives researchers towards the investigation of the wellbore instability for hard and low porosity sedimentary rocks (Jaeger et al., 2007). Fundamental and numerical analysis, such as the work performed by Zhang et al., (1999) and Sousani et al., (2014), were developed to deal with the effect of rock geometry and various pressure differentials on the wellbore instability. Comparisons of the numerical results towards analytical solutions and experimental data provide a better understanding of the behaviour of the material and the propagation of cracks in both mesoscopic and large scale rocks. Furthermore, factors such as measurements of the minimum in-situ stress and permeability are significant for the design of hydraulic fractures and therefore extended research has been conducted relating the changes in the rock permeability with in-situ stresses (Holt, 1990; Bryant et al., 1993; Bruno, 1994; Bouteca et al., 2000; Bachu and Bennion, 2008) as well as the influence of the in-situ stresses to the fracturing pattern (propagation and closure) on pressure sensitive materials (Papanastasiou, 2000). It is significant to observe how individual studies, such as the aforementioned or others related to the influence of stress and deformation on the propagation of hydraulic fractures (Bigoni and Radi, 1993; Desroches and Thiercelin, 1993; van Dam et al., 2000b), become part of the bigger picture of hydraulic fracturing and can be connected with more recent studies focusing on the use and stability of the proppants in the fractures (as previously discussed). Recently more engineering applications have emerged where the fracking procedure is the dominant part. Examples of such projects are the waste disposal by the injection of slurries, in depths between 600 and 830 m, into appropriate sandstone and shale formations (Warpinski et al., 1999) and the production of heat from the hot dry rocks within geothermal reservoirs (Green et al., 1988). Therefore understanding the mechanisms involved in fracking, in order to control and ameliorate the process and maximise its benefits, is essential.

1.2.10 Advantages of DEM over FEM

The advantages of the DEM methods over other traditional techniques, such as the FEM, are the simpler representation of the geometries of real rocks, which contain discontinuities, the easier simulation of complex engineering problems without the use of complicated constitutive equations and thus provide statistically more accurate results. Conversely, the increased simplification requires extensive experimental validation to verify the numerical results of the method and illustrates that the microscopic models can produce equivalent macroscopic behaviour of real rocks. Finally, the increased computational time due to the nature of the DEM approach (solving the governing equations for a large volume of particles) is another limitation that researchers have to tackle.

1.2.11 Existing studies on the modelling of fracking

The complexity of analysing the hydraulic fracturing is further increased due to a large number of variables in the process, such as varying material properties (compressive/tensile strength, elastic constants, properties of particles and bonds, etc.), stress boundary conditions, the viscosity of the fracturing fluid, the grain size and permeability of the rock and the pre-existing inhomogeneities within the rock’s matrix. The majority of the aforementioned variables are currently under investigation, such an example is the work by Martinez, (2012) who investigated the influence of varying material properties and boundary conditions in the micro-scale on the fracturing mechanism of poorly consolidated rock formation. Based on their overall results, it is suggested that conventional theory ignores the mechanisms, such as shear cracking, that control the propagation of fractures with respect to poorly consolidated rocks and that the assumption of a linear elastic behaviour of the material is not always dominant in DEM simulations. More examples of analysing essential parameters with respect to the fracking mechanism, are the work by Shimizu *et al.*, (2009, 2011; 2012) who dealt with the effect of the fluid viscosity and the grain size, on the behaviour of the hard rock and unconsolidated sands. It was observed that in the case of a homogeneous material and the use of a high viscous fluid, the breakdown pressure was much higher than in the case of a heterogeneous material. Their findings can be attributed to the defects between the grains, due to differences of grain size, which therefore trigger the initiation of fracking. His results were in agreement with laboratory results (Matsunaga et al., 1993; Ishida et al., 2000; Ishida, 2001) which show a decrease in the breakdown pressure with increasing grain size. Also it was concluded that when a low fluid viscosity was used, the fracture propagated along the direction of maximum compressive stress and the fluid penetrated directly into the fracture. The opposite occurred in the case of high viscosity, where the fluid cannot penetrate into the fracture unless the latter propagates first. The effect of the injection rate and fluid viscosity has also been investigated by other scientists using different techniques, such as the unconventional fracture model (UFM) and a new model called OpenT, which can mimic complex large-scale crossing fracture networks in a formation with pre-existing natural fractures and predict their propagation (Kresse et al., 2013). The latter has moved from previous modelling and its geometric limitations (built on the stress field at the imminent hydraulic fracture tip) to a mode advanced representation of the induced stress regime, the fracture network and crossing slippage zones along the natural fracture. Other researchers have produced similar studies, such as Ishida *et al.,* (2004; 2012) who performed a set of similar hydraulic experiments (same in-situ stress and flow rate) in the laboratory, using low and high viscous fluids (water/oil and supercritical/liquid CO_2, respectively). The aim of his study was to investigate the effect of fluid viscosity on the breakdown pressure and compare the results from both studies. According to their findings, he suggests that the supercritical CO_2 (sc-CO_2) tends to initiate cracks which extend more three-dimensionally compared to the liquid CO_2 (l-CO_2) which generates cracks that extend in a 2D flat plane. The comparison between the aforementioned results and the acoustic emissions from the use of water and oil were observed to be distributed in a narrower region. Furthermore, it was concluded that the breakdown pressures were lower for the sc-CO_2 than for the l-CO_2, while the breakdown pressures produced from water and oil were significantly higher in comparison. Furthermore, the work done by Bruno, (1994) investigated the damage and the stress-induced permeability anisotropy in weakly-cemented geological materials at the microscopic level. The results compare well with the acoustic emissions of experimental data, with the reduction scale of the stress-induced permeability being dependant on the relationship between the amount of intergranular bonds and the stress levels. Specifically, the fluid permeability is reduced for both low and near hydrostatic stress levels, whereas for high deviatoric stress levels the flow channels increase affecting the induced permeability reduction. An overall anisotropy of the permeability is observed in the macroscopic level.

1.3 Summary

This chapter provides a detailed background of the origin of the hydraulic fraturing mechanism, its applications and the potential risks derived from the fracking operations. It also discuss numerous experimental and modelling studies which have focused on the mechanical behaviour of rock formations and the simulation of applications which involve fracking. Finally, it presents the available computer softwares and/or techniques and categorizes them according to their mathematical principles. It can be concluded that even though the risks from the fracking operations exist, we now have a good knowledge of a safe hydraulic fracturing mechanism and we are able to predict the behaviour of formations. However, due to the fact that hydraulic fracturing operations are directly related with EOR/EGR operations and thus with highly heterogeneous and pre-fractured rock materials, there is apparent need for more research on the influence of the geometry of the formations, or the properties of fluids to the fracking mechanism. The mechanical behaviour of rocks in both the macro and particle scale has been widely investigated and many researchers have simulated fluid flow through porous media. However, to the author’s knowledge, none of the aforementioned studies have investigated the behaviour of pre-fractured rocks under a hydraulic fracturing mechanism,and only limited studies have used DEMs, such as PFC, to simulate fracking experiments. Finally, compared to the volume of the numerical studies, direct comparisons between experimental results and modelling techniques are still lacking.

This thesis deals with some of the variables that interact with the fracking mechanism, affecting the micro-mechanical behaviour of the material. Part of this thesis presents a three-dimensional modelling of strong rock with pre-existing fractures, targeting on the investigation of the influence of these micro-fractures, the in-situ pressure conditions and the fluid properties to the overall fracturing process.

1.4 Aims and objectives

The aim of the research was set to improve the understanding of the mechanical behaviour of porous rock formations under intense injection conditions and the influence of natural pre-existing rock damage to the hydraulic fracturing mechanism. Also, this study aims to provide a valuable outcome for EOR and/or EGR applications since it can contribute a further insight towards estimations of safe injection pressures in cases of reservoirs of known strength. The investigation of the fracturing process can also be useful not only to prevent failures that may lead to leakages but to control fractures towards safer reservoir productivity.The detailed objectives can be listed as follows:

i. to create a 3D rock specimen, with the use of the DEM and calibration procedures, replicating a real limestone sample. It aims to investigate the effectiveness of the DEM and verify its effectiveness as a tool.

ii. to reproduce a laboratory hydraulic fracturing test performed on a thick-walled hollow cylinder limestone sample. It aims to investigate the implications of the fluid flow on the behaviour of the micro structure of the rock sample and validate the experimental results via numerical modelling.

iii. to relate the Linear Fracture Mechanics (LEFM) laws that describe the mode I fracture toughness (K_I) of a material which contains a pre-existing fracture with the ones that are employed by DEM. Also it aims to suggest a methodology that directly relates the K_I of a real rock with the micro-properties of its equivalent discrete sample.

iv. to develop a DEM limestone sample with pre-existing fractures and perform a horizontal hydraulic injection replicating a real life scenario in the small scale. It aims to investigate the effects of the fluid injection and the various parameters on the mechanical behaviour of the limestone sample on the particle – scale.

1.5 Assumptions used in the numerical modelling

In this thesis the DEM approach was employed to replicate a real limestone rock. The same virtual sample, with changes on its internal structure, has been used to replicate two different real life applications in the particle-scale. During the thick-wall hollow cylinder test (first hydraulic fracturing application) a pressure difference, between the hollow core and the outer surface of the sample, was applied. The fluid penetrates the sample's matrix, thus initiating the fracturing process. The sample was surrounded by fixed solid walls, replicating the actual laboratory conditions, apart from the side of the fluid flow. The propagation of the micro-fractures was simulated until the total collapse of the sample.

For the horizontal injection (second hydraulic fracturing application) fluid was injected, from one end, under a high pressure gradient. The fluid penetrated the sample, thus forcing the bonds between the particles of the sample to break and the micro-cracks to initiate. The sample was surrounded by fixed solid walls in order to prevent sliding and replicate in situ conditions. The propagation of the micro-fractures was simulated until the overall fracture growth reached and exceeded the pre-existing inhomogeneities of the material and at the same time being away from the specimen limits to eliminate any boundary effects .

The limestone sample used for the simulations considered porous, homogeneous, isotropic and it was categorized as a strong rock, in terms of compressive strength. The virtual rock sample was modelled as an assembly of numerous particles attached by strong bonds, which obey a linear force-displacement law. The particles were considered independent of one another and they interact only at the contact between them. The generated particles were taken to be spheres and the bonds were modelled as linear elastic springs with constant normal and shear stiffness, uniformly distributed over a circular cross-section with its centre at the contact point between the particles. The interaction between the particles, as well as the interaction between particles and walls, create forces that are transmitted to the point of contact. In contrast, there is no interaction between the walls. Furthermore, the interaction between the particles is treated as a dynamic process in the DEM, and the system is considered to be in equilibrium when the internal forces balance. The dynamic behaviour of the system is numerically represented by an algorithm in which it is assumed that the velocities and accelerations are constant within each time-step.

The main principle is that the macroscopic behaviour of the material is derived from the collective behaviour of numerous microscopic particles, used to represent the rock sample and that the macroscopic dynamics of the system is not sensitive to the underlying microscopic mechanisms. For the simulated tests a built in programming language, named ‘’Fish’’ , was utilised under the

3D version of the PFC software by Itasca. The hydraulic fracturing simulations were performed using the fluid coupling algorithm embedded in the PFC3D. The fluid flow scheme solves the mass and momentum equations of a two-phase fluid flow (solid and fluid) based on the generalised Navier-Stokes formulation for incompressible flow. The fluid analysis is performed with the use of a fluid cell grid and the boundary conditions are applied at the edges of the grid. The corresponding files, which include the relevant codes for the execution of the simulations, are provided at Appendix I, II and III.

1.6 Outline of the thesis

This thesis includes seven chapters and they are described as follows:

Chapter 1 provides a detailed background of the technologies that the hydraulic fracturing is applicable and describes the fracking mechanism and its potential risks. It also provides a critical review of the existing literature, the recent developments of this technique, the available computer softwares and their limitations, as well as their applications in real life projects. The aims and objectives of this research, as well as the assumptions used for the numerical part of this study, have been presented herein.

Chapter 2 includes the ‘’Theoretical background of the analytical and numerical techniques in DEM’’ which provides a summary of the governing equations used for the fluid flow tests that follow in the future chapters and the theoretical background of the coupled DEM and fluid flow.

Chapter 3 includes the ‘’Calibration of microscopic parameters’’ which provides the procedure of creating a virtual model that represents a real rock. It provides a detailed description of a series of tests that calculate the relevant mechanical properties of the virtual model including the uniaxial compressive simulation (UCS), the Brazilian test and the single edge notch bending test (SENB). It also presents a methodology that directly relates the mode I fracture toughness of a real rock with the micro-properties of its equivalent discrete sample, eliminating additional factors.

Chapter 4 includes the ‘’The DEM analysis for hydraulic fracturing in a hollow hard rock cylinder’’ which discusses the mechanical behaviour of the DEM model during the calibration procedure, gives a detail description of the hydraulic fracturing simulated test and provides the results.

Chapter 5 includes the ‘’The DEM analysis for hydraulic fracturing in hard rocks under horizontal fluid injection’’. It describes the mechanical behaviour of the DEM model during the calibration procedure and provides a comprehensive description of the hydraulic fracturing simulated test. The effect of the relevant factors is presented and discussed.

Chapter 6 includes the ‘’Conclussions and future work’’ which summarizes the overall results and findings from this study and identifies the knowledge gaps for future work.

Chapter 2 Theoretical background of the analytical and numerical techniques in DEM

2.1 Introduction

The DEM approach was initially developed by Cundall, (1971) in order to model and analyse fundamental rock-mechanics problems and then applied to granular materials as a means to model the behaviour of solids (Bortolan Neto and Kotousov, (2012)). The concept of DEM is based on the translational and rotational movement of particles due to forces and moments which act at the contact point between the particles. Furthermore, a collaboration between DEM and a matching technique (Itasca Consulting Group, 2008a) in order to simulate the fluid flow is employed. This technique is a coarse-grid fluid flow scheme and is based on the generalised Navier-Stokes formulation for incompressible fluid flow in porous media. It is translated into a discretised version, in order to simulate discrete particles.

PFC3D software, by the Itasca Consulting Group, was used in this thesis for the numerical simulations. It provides an implementation of the DEM , and an embedded fluid coupling algorithm based on the aforementioned Navier-Stokes equation. The simulated tests are formed and executed with the use of test files (codes), written in Itasca’s programming language (Fish). The coding texts, which are developed by the software’s user, are provided in AppendixI, II, III.

2.2 PFC3D calculation cycle and stress distribution

As already mentioned, the DEM is based on the generation of a virtual assembly of particles interacting with each other and this is translated into a general contact law that is applied to the particles and their bonds. The two basic laws used repeatedly at every time-step of the DEM calculations is Newton's second law for particles and a force displacement law at the contacts. More specifically, Newton's second law is applied in order to calculate the motion of particles due to the contact and the resulting body forces (updated velocities and locations) and the force displacement law provides the updated contact forces and moments derived from the relative displacements of the particles at the contacts. Furthermore, Newton's second law is not used for the walls as their movement is directly specified by the user, thus only the force displacement law is applicable for walls in this code (Itasca Consulting Group, 2008e).

Newton's law of motion between particles involves displacement, velocity and acceleration, whereas the rotational motion of the particles is described in terms of the angular velocity and angular acceleration. Furthermore, in the PFC the DEM analysis is a fully dynamic method and thus local damping, which acts on each ball, is necessary to dissipate the kinetic energy. For any particle in translational motion, the equation of motion is given by:

$$F_i + F_i^d = \begin{cases} m_p \ddot{x}_i, & for\ i = 1, 2, 3 \\ I\dot{\omega}_{(i-3)} & , for\ i = 4, 5, 6 \end{cases} \qquad (2.1)$$

where F_i is the generalized force which includes the gravitational force, F_i^d is the damping force, m_p is the particle's mass, $\ddot{x}_i$ is the particle's translational acceleration, I is the moment of inertia, and $\dot{\omega}$ is the angular acceleration. The dots ''.'' on top of the variables denote derivatives with respect to time and the subscript '' i'' , is a free index that denotes the direction of the movement (i=1-,3 translational movements and 4-6 rotation).

Integrating the Eq.(2.1) yields the particle's generalized velocity U_i given by:

$$U_i = \begin{cases} \dot{x}_i & for\ i = 1,2,3 \\ \omega_{(i-3)} & for\ i = 4,5,6 \end{cases} \tag{2.2}$$

Where $\dot{x}_i$ and ω are the particle's translational and rotational velocities, respectively. The general equation describing the damping force is as follows:

$$F_i^d = -\alpha |F_i| sign(U_i) \tag{2.3}$$

where α is a non-dimensional frequency-independent damping constant with a default value of 0.7. From Eq.(2.3) it is clear that only accelerating movement is damped, ensuring that no damping occurs in steady-state motion.

A parallel bond replicates the presence of cementation deposited after the neighbouring particles are in contact (Fig. 2.1(**a**)). It can be translated as a set of elastic springs that are evenly distributed over a circular cross-section in the contact plane and their centres at the contact point. Furthermore, they have a similar behaviour to a beam of length L as shown in Fig.2.1(**c**). For the case of two particles in contact with a parallel bond, they are assumed to be spheres in PFC3D. As shown in Fig.2.1(**b**), the action of particle A on particle B due to the parallel bond is as follows:

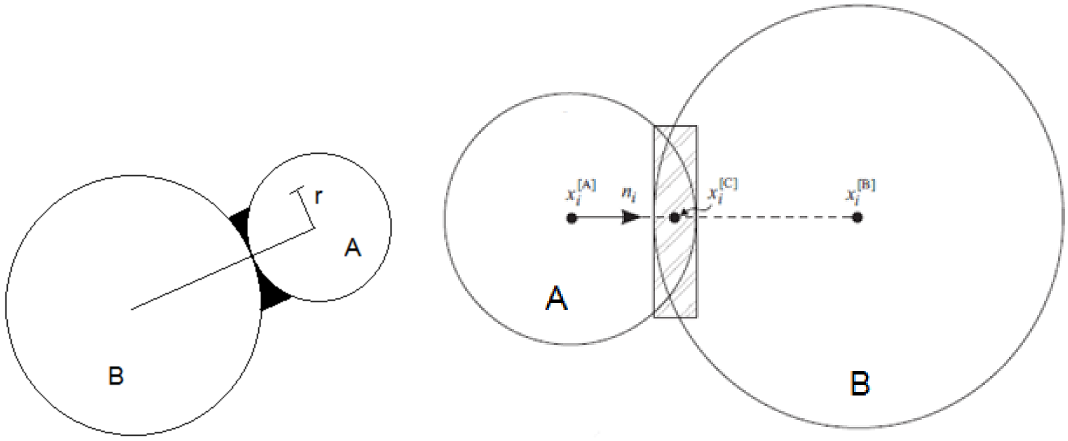

(a) (**b**)

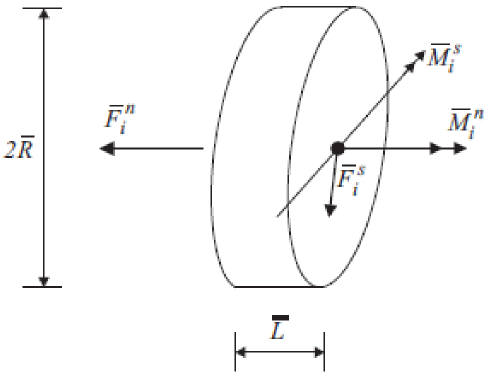

(**c**)

Figure 2.1 Schematic of the (**a**) parallel bond between two particles representing additional cementation, (**b**) force between two particle spheres due to the presence of the parallel bond, and (**c**) forces carried to a 3D parallel bond (Itasca Consulting Group, 2008e).

The Force-Displacement Law relates the forces applied on the system with the particles' mass and acceleration, an inertial damping coefficient necessary to dissipate kinetic energy, the resulting moment at each particle individually and at the system as a whole. Figure 2.2(**a**), (**b**) illustrates the schematics of the contact plane between two particles and between a particle and a wall.

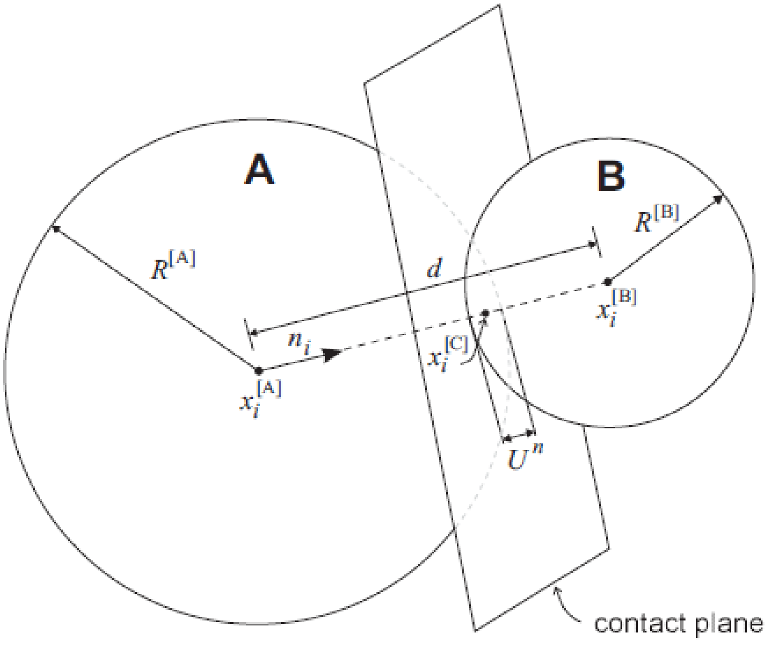

(**a**)

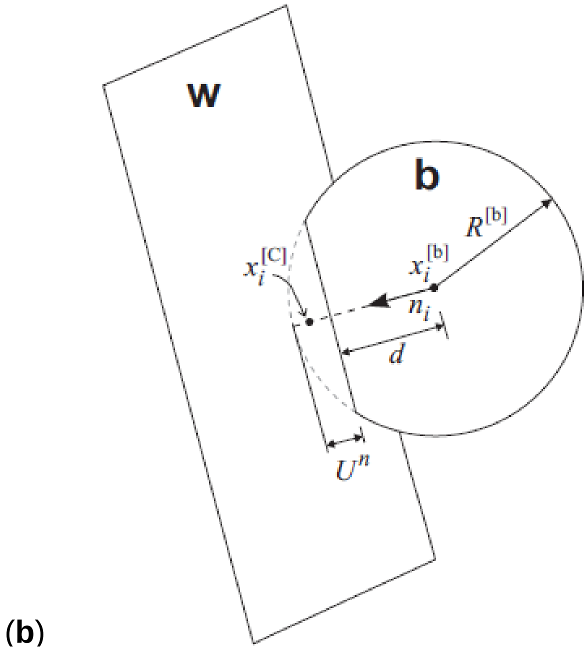

Figure 2.2 Schematics of the (**a**) ball-ball contact point and (**b**) ball-wall contact point (Itasca Consulting Group, 2008e).

The forces and moments acting on the system are given by:

$$F_i^T = F_i^n + F_i^s \tag{2.4}$$

$$M_i^T = M_i^n + M_i^s \tag{2.5}$$

where F_i^T, M_i^T, are the total force and moment vectors and F_i^n,F_i^s, M_i^n, M_i^s are the axial and shear components in respect to the contact plane, respectively.

At the beginning of bond creation, the initial F_i and M_i are set to zero but each relative displacement and rotation increment results in an increment in the values of elastic force and moment (Itasca Consulting Group, 2008f). These are added to the previous quantities, so that the total quantity at any time-step is given by

$$F_i^n = (F_i^n)_t + (\Delta F_i{}^n)_{t+1} \tag{2.6}$$

$$F_i^s = (F_i^s)_t + (\mathit{\Delta} F_i{}^s)_{t+1}$$

$$M_i^n = (M_i^n)_t + (\mathit{\Delta} M_i{}^n)_{t+1}$$

$$M_i^s = (M_i^s)_t + (\mathit{\Delta} M_i{}^s)_{t+1}$$

The increments of the elastic force, as well as the moment, are given as follows:

$$\mathit{\Delta} F_i^n = (-k^n A_b \mathit{\Delta} U^n) n_i$$

$$\mathit{\Delta} F_i^s = -k^s A_b \Delta U_i^s$$

$$\mathit{\Delta} M_i^n = (-k^n J \mathit{\Delta} \theta^n) n_i \qquad (2.7)$$

$$\mathit{\Delta} M_i^s = -k^s I \Delta \theta_i^s$$

with $\Delta U_I = V_i \Delta \mathrm{t}$ and $\mathit{\Delta} \theta_i = (\omega_i^B - \omega_i^A) t$

where k^n, k^s are the normal and shear stiffness of the bond, respectively, V_i is the relevant motion at the contact, $\mathit{\Delta} U^n, \Delta U_i^s$ are the normal and shear displacement overlap, respectively, and A_b, J, I are the area, polar moment of inertia and moment of inertia of the cross-section of the bond, respectively. These sub-quantities are given by

$$\mathrm{k^n} = {}^{\overline{\mathrm{E}}_\mathrm{C}}/_{\mathrm{L}}$$

$$\mathrm{k^s} = \frac{12\mathrm{I}\overline{\mathrm{E}}_\mathrm{C}}{\mathrm{A}_b \mathrm{L}^3} = \frac{3\pi \mathrm{R}^4 \overline{\mathrm{E}}_\mathrm{C}}{\pi \mathrm{R}^2 \mathrm{L}^3} \qquad (2.8)$$

$$\mathrm{n_i} = \frac{\mathrm{x_i^{[B]}} - \mathrm{x_i^{[A]}}}{\mathrm{d}} : \text{ ball} - \text{ball}$$

$$\mathrm{d} = \mathrm{R}^{(B)} - \mathrm{U^n} : \text{ ball} - \text{wall}$$

$$\mathrm{V_i} = (\dot{\mathrm{x}}_\mathrm{i})_\mathrm{B} - (\dot{\mathrm{x}}_\mathrm{i})_\mathrm{A}$$

$$\mathrm{A}_b = \pi\mathrm{R}^2$$

$$\mathrm{I} = {}^1\!/_4\,\pi\mathrm{R}^4$$

$$J = {}^1\!/_2\,\pi R^4$$

where $\overline{E}_C$ is the Young's modulus of the parallel bonds, d is the shortest ball-ball or ball-wall distance and $\mathrm{R}^{(B)}$ is the radius of the particle B.

The distribution of the stress due to the parallel bonds and the interaction between the particles is calculated at every time-step. The maximum values of the tensile (σ_{max})and shear (τ_{max}) stress on the parallel bond perimeter are calculated using the general equation of stress following the beam theory, namely

$$\sigma_{max} = -\frac{F_i^n}{A_b} + \frac{M_i^s}{I} R$$

$$\tau_{max} = \frac{\left|F_i^S\right|}{A_b} + \frac{\left|M_i^n\right|}{J} R \tag{2.9}$$

Furthermore, in reality stress is considered a continuum quantity and, hence, does not exist at every time-step in the PFC3D model because the model is discrete. The contact forces and displacements, attributed to the particle movement used for the investigation of the mechanical behaviour of the model in the micro-scale, cannot be converted directly to a continuum model. They must follow a process of averaging its quantities in order to make the transition from the micro-scale to continuum. With the assumption that the stress is continuous and in equilibrium for each particle, the average stress ($\bar{\sigma}_{ij}$) in a measurement region can be expressed as follows (Itasca Consulting Group, 2008g):

$$\bar{\sigma}_{ij} = \left(1 - n \Big/ \sum_{N_p} V^{(p)}\right) \left(\sum_{N_p} \sum_{N_c{}^{(p)}} (x_i{}^{(c)} - x_i{}^{(p)}) F_j{}^{(c,p)}\right) \qquad (2.10)$$

where $\bar{\sigma}_{ij}$ is the stress acting throughout the measurement region, n is the porosity and N_p is the number of particles in that region. $V^{(p)}$ is the volume of the particle (p), x_i is the location of a particle centroid and its contact, and F_j is the force acting on the particle p at contact c, respectively (Potyondy and Cundall, 2004). The latter includes the normal and shear forces from Eq.(2.4) but neglects the parallel-bond moment.

2.3 Crack growth theory

As already known (Potyondy and Cundall, 2004; Itasca Consulting Group, 2008h), a micro-crack in the PFC3D assembly is the subsequent bond breakage between two bonded particles. More specifically, each contact point develops a maximum tensile strength in the normal direction and maximum shear contact-force strength due to the parallel bond. Therefore, every time either the maximum tensile or shear force exceeds the tensile or shear strength ($\sigma_{max} \geq \bar{\sigma}$, $\tau_{max} \geq \bar{\tau}$) of the spring (bond) then the parallel bond breaks (Fig.2.3) (Itasca Consulting Group, 2008h). Thus the number and position of the possible micro-cracks are limited by the number and position of the parallel bonds in the virtual assembly. In this work, the material demonstrates brittle behaviour under continuously increased load which is directly related to the presence of numerous micro-cracks propagated throughout the sample. The shift of this behaviour in a larger scale and hence, the transition from micro-cracks to macro-cracks, with a continuously increased load, can describe the brittle behaviour of a real rock.

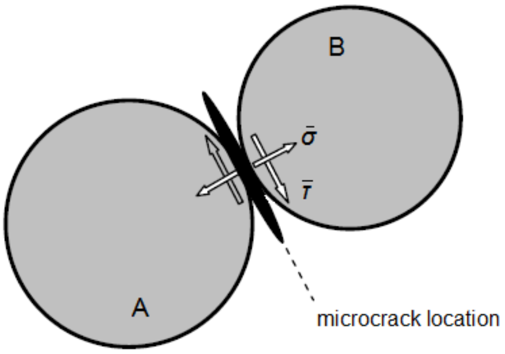

Figure 2.3 Microcrack location between particles A and B.

In PFC there are two computational methods for modelling this behaviour: the indirect method, where the damage is represented through its effects on the constitutive relations and the direct method, with the monitoring and tracking of the micro-cracks (Potyondy and Cundall, 2004). In most indirect approaches, the material is considered to be continuous, and thus the relevant quantities of the material degradation are averaged in order to be used in fundamental relations and characterize the microstructural damage (Krajcinovic, 2000). In contrast, most direct approaches consider the material as a collection of structural units, such as springs and beams, or discrete particles bonded together at their contacts. Furthermore, they use the breakage of each structural unit or bond to characterize the damage (Schlangen and Garboczi, 1997).

In the past it was difficult to characterize problems with specific boundary conditions, such as the solution of a solid-boundary problem involving complex deformation, using direct methods. Furthermore, these direct methods were used in order to study the general behaviour of the problem and develop complex relations that later the indirect methods will use to solve the problem. However, modern computers possess the required processing power to enable the simulation of the entire problem bypassing the development of complex relations. Modelling the damage of a rock sample in PFC is such an example and falls into the category of the direct method. The interpretation of its mechanical behaviour is a complex procedure, due to extensive micro-cracking, and it is difficult to be discussed accurately with the use of continuum mechanics (Itasca Consulting Group, 2008c).

2.4 Stress distribution on a hollow cylinder

Chapter 4 involves the simulation of a fluid flow on a thick-wall hollow cylinder and the equations that best describe it are discussed herein. The purpose of the test is to provide an indication of the stress field of the model and to validate the results based on theory, as well as to investigate its overall behaviour under high pressure differentials and compare the results with laboratory data. The equations that best describe such tests are known as Lame’s equations (Timoshenko, 1941; Finlayson, 1990) and they are used to determine the stresses in thick wall cylindrical pressure vessels (Fig.2.4).

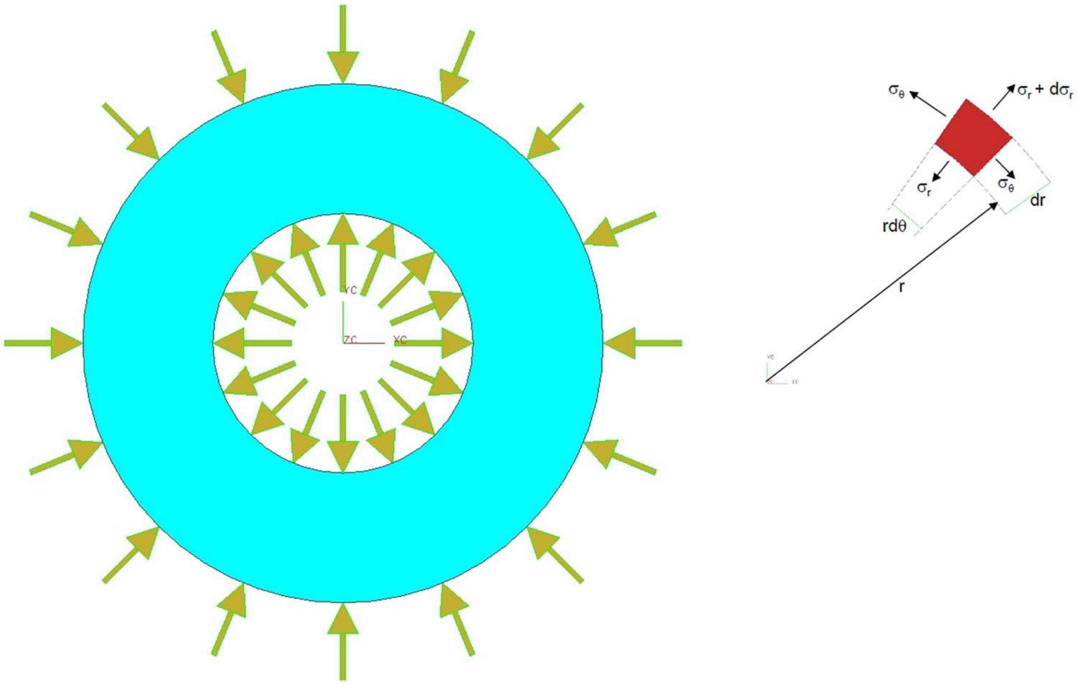

Figure 2.4 Two dimensional schematic of a hollow cylinder and an element at radius r from the centre of the cylinder (Timoshenko, 1941).

The stresses in thick-walled cylinders are given by the following equations:

$$\sigma_r = A - \frac{B}{r^2} \tag{2.11}$$

$$\sigma_\theta = A + \frac{B}{r^2} \tag{2.12}$$

Where σ_r and σ_θ are the radial and tangential stresses respectively, while A and B are constants given by:

$$A = \frac{P_i {r_i}^2 - P_0 {r_0}^2}{{r_0}^2 - {r_i}^2} \tag{2.13}$$

$$B = \frac{(P_i - P_0)_{{r_i}^2} {r_0}^2}{{r_0}^2 - {r_i}^2} \tag{2.14}$$

Substituting Eq.(2.13), (2.14) into (2.11) and (2.12) we conclude

$$\sigma_\theta = \frac{P_i r_i{}^2 - P_0 r_0{}^2}{r_0{}^2 - r_i{}^2} + \frac{(P_i - P_0) r_i{}^2 r_0{}^2}{(r_0{}^2 - r_i{}^2) r^2} \tag{2.15}$$

$$\sigma_\mathrm{r} = \frac{\mathrm{P_i r_i{}^2 - P_0 r_0{}^2}}{\mathrm{r_0{}^2 - r_i{}^2}} - \frac{\mathrm{(P_i - P_0) r_i{}^2 r_0{}^2}}{\mathrm{(r_0{}^2 - r_i{}^2) r^2}} \tag{2.16}$$

For the longitudinal stress acting on the cut of the cylinder, the force equilibrium law is used where a pressure P_i acts on an area $\pi r_i{}^2$ and a pressure P_0 acts on an area $\pi r_o{}^2$, thus the longitudinal stress acts on the area $\pi(r_0{}^2 - r_i{}^2)$ and is given by:

$$\sigma_L = \frac{P_i r_i{}^2 - P_0 r_0{}^2}{r_0{}^2 - r_i{}^2} \tag{2.17}$$

For the case of a closed ends cylinder with zero internal pressure P_i and r_i internal radius, P_0 external pressure and r_0 external radius, the stresses at a given radial distance r are given by:

$$\sigma_\theta = \frac{-P_0 r_0{}^2}{r_0{}^2 - r_i{}^2}\left[1 + \frac{r_i{}^2}{r^2}\right], \sigma_r = \frac{-P_0 r_0{}^2}{r_0{}^2 - r_i{}^2}\left[1 - \frac{r_i{}^2}{r^2}\right], \sigma_L = \frac{-P_0 r_0{}^2}{r_0{}^2 - r_i{}^2} \tag{2.18}$$

where σ_θ, σ_r and σ_L are the tangential, radial and longitudinal stress, respectively.

2.5 Simulated fluid flow test

The following Chapters (4 and 5) present simulated fluid flow tests and aim to investigate the micro-mechanical behaviour of a porous rock under single phase fluid flow. In this Chapter the theory and the fundamental equations for the setup of the aforementioned tests, as well as the interpretation of the results are discussed. The aim of the simulated fluid flow test is to provide a good indication of the material’s hydraulic conductivity and the behaviour of the sample under high pressure. The flow rate, in m^3/sec, for the liquid flow through the porous media is given by

$$Q = q\acute{A} \tag{2.19}$$

where $\acute{A}$ is the cross sectional area perpendicular to the direction of flow, and q is the velocity of the liquid given by Darcy’s Law (Dullien, 1979; Nield and Bejan, 2006):

$$q = -\frac{k}{\mu_D}(\nabla P_f - \rho g \nabla z) \tag{2.20}$$

where k is the absolute permeability of the sample, μ_D is the fluid’s dynamic viscosity, P_f is the fluid pressure, g is the magnitude of the gravitational acceleration, ρ is the density of the fluid, z is the elevation in the direction of the flow (which in this case is set to zero as the fluid moves horizontally). In steady-state, the velocity q in Eq.(2.19) becomes the interstitial velocity u_0 of the fluid. This can be derived from the combination of the well-known Navier-Stokes (Itasca Consulting Group, 2008d) and Erqun’s relations (Ergun., 1952; Jia et al., 2009), Eq.(2.21) and Eq.(2.22), respectively, for fluid flow through beds of granular solids, which for the case of a fixed homogeneous porous material takes the form:

$$\rho\frac{\partial\varepsilon\vec{u}}{\partial t} + \rho\overrightarrow{u_0}\cdot\nabla(\varepsilon\vec{u}) = -\epsilon\nabla p + \mu\nabla^2(\varepsilon\vec{u}) + f_{\vec{\beta}} \tag{2.21}$$

$$\frac{\Delta_p}{L} = \frac{150\mu(1-\varepsilon)^2 u_0}{\varepsilon^3\overline{d_p}^2} + \frac{1.75(1-\varepsilon)\rho {u_0}^2}{\varepsilon^3\overline{d_p}} \tag{2.22}$$

where, ε is the porosity of the granular solid, $f_{\vec{\beta}}$ is the body force per unit volume, the interstitial fluid velocity is denoted as u_0, L is the height of the granular solid bed, Δ_p is the pressure difference, $\overline{d_p}$ is the mean particle diameter, and 150 and 1.75 are constants obtained by experimentation.

During the typical generation process the sample is packed with particles of uniform size (described in detail in Chapter 3 in the uniaxial test procedure). At this stage the assembly is reaching equilibrium with the use of some stabilizing strategies (i.e., target isotropic stress) thus all body forces acting on the particles prior to fluid movement are being eliminated. In the fluid-scheme of the PFC3D, driving forces from the fluid flow are applied to the particles as body forces. The body force is the drag force applied by the particles to the fluid element and is given by:

$$f_{\vec{\beta}} = \beta(\vec{\bar{u}} - \overrightarrow{\overline{u_0}}) \tag{2.23}$$

where $\vec{\bar{u}}$ is the average velocity of all the particles in a fluid element and β is a coefficient, that for samples of low porosity, is given by:

$$\beta = \frac{\{150\mu(1-\varepsilon) + 1.75\overline{d_p}(\vec{\bar{u}} - \overrightarrow{\overline{u_0}})\rho\}(1-\varepsilon)}{\varepsilon^2 \overline{d_p}^2} \tag{2.24}$$

where ρ is the density of the fluid.

Next a drag force equal in magnitude and opposite in direction is applied to the particles in each given fluid element, given by (Itasca Consulting Group, 2008a):

$$\overrightarrow{f_{drag}} = \frac{4}{3}\pi r^3 \frac{f_{\vec{\beta}}}{1-\varepsilon} \tag{2.25}$$

The total force applied by the fluid to the particles is the sum of the drag force and the force due to buoyancy, given by:

$$\overrightarrow{f_{fluid}} = \overrightarrow{f_{drag}} + \frac{4}{3}\pi r^3 \rho \vec{g} \tag{2.26}$$

Furthermore, local non-viscous damping is provided by PFC3D meaning that body forces approach zero for steady motion. If we assume that the assembly of particles is similar to a packed bed, then when there is no flow through the packed bed the net gravitational force (including buoyancy) acts downward. When the flow starts moving, friction forces act upward and counterbalance the net gravitational force. For high enough fluid velocities, the friction force is large enough to lift the particles (Finlayson, 1990; Itasca Consulting Group, 2008d).

Generally, two different formulations can be encountered for the fluid velocity in porous flow: one is the aforementioned interstitial velocity u_0, and the other is the macroscopic or Darcy velocity $\varepsilon\vec{u}$. The interstitial velocity is the actual velocity of a fluid parcel flowing through the pore space. The macroscopic velocity is the volumetric flow rate per unit cross-sectional area. This is a non-physical quantity calculated on the basis that the flow occurs across the entire cross-sectional area, although in reality the flow only occurs in-between the pore space.

In the case of steady uniform flow, the macroscopic velocity is assumed to be constant and thus the terms on the left-hand side of Eq. (2.21) become zero. On the right-hand side, the term $-\epsilon\nabla p$ is the applied pressure gradient, $\mu\nabla^2(\varepsilon\vec{u})$ denotes the momentum loss due to viscosity, and $f_{\vec{\beta}}$ corresponds to the drag force exerted by the particles on the fluid. The viscous term $\mu\nabla^2(\varepsilon\vec{u})$

is negligible for large pressure gradients which in turn induce significant body forces, and therefore Eq.(2.21) can be reduced to:

$$\epsilon \nabla p = f_{\vec{\beta}} \tag{2.27}$$

Combining Eq.(2.21) and Eq.(2.22) the second order Eq.(2.28) gives the solution of

$$u_0 = \frac{\sqrt{(1-\varepsilon)4\overline{d_p}^3 \varepsilon^3 \Delta_p \rho 150 + (\varepsilon - 1)^4 \mu^2 150^2} - 150\mu(\varepsilon - 1)^2}{2\overline{d_p}(1-\varepsilon)\rho 1.75} \tag{2.28}$$

Eq.(2.29) was used during the simulations in order to provide the volumetric flow rate results of the discharging liquid through the virtual assembly.

$$q_{vol} = u_0 \times A \tag{2.29}$$

The macroscopic properties of a real rock cannot be directly described in a DEM model due to the fact that the particles size distribution of the virtual model does not have to copy the actual rock's grain size distribution (explained in detail in Chapter 3.6). This results in a mismatch between the hydraulics of the real rock and the virtual model in terms of pressure drop and fluid relative velocity. Furthermore, it is actually advantageous to decouple the micro-properties of the DEM specimen from those of the actual rock. This is because attempts to match the porosity of the actual rock would lead to a broader particle size distribution, which in turn lowers the time-step, in order to achieve better accuracy, resulting in impractical simulation time. For these reasons it was considered best to use calibration factors that will alter the fluid flow parameters of the virtual model. The simulated fluid flow tests are presented in Chapters 4 &5.

According to Ergun’s relation in Eq.(2.22)

$$\frac{\Delta_p}{L} = C_1 \mu u_0 + C_2 \rho {u_0}^2 \tag{2.30}$$

where

$$C_1 = \frac{150(1-\varepsilon)^2}{\varepsilon^3 \overline{d_p}^2}$$
$$C_2 = \frac{1.75(1-\varepsilon)}{\varepsilon^3 \overline{d_p}} \tag{2.31}$$

In order to match the pressure drop of the DEM specimen with that of an actual rock the terms of Eq.(2.30) on the right hand side should be scaled. The following process results in the scaling factors of viscosity and density used in the virtual model.

Combining C_1 from Eq.(2.31) with the Kozeny-Carman equation (Carman, 1997), then the permeability of a real rock is given by

$$k = \frac{1}{180} \frac{\varepsilon^3 D^2}{(1-\varepsilon)^2} \tag{2.32}$$

where D is the grain diameter of the real rock. It is concluded that C_1 corresponds to the inverse of the permeability for the DEM specimen and it is given by

$$C_1 = \frac{150(1-\varepsilon)^2}{\varepsilon^3 \overline{d_p}^2} = \frac{150}{180} \frac{1}{k} \tag{2.33}$$

It is clear that the permeability depends on the specimen’s microparameters thus a calibration factor a_μ was multiplied with the above equation in order to match the specimen’s parameters with that of the actual rock with the use of the following relation

$$[C_1]_{PFC} \times a_\mu = \left[\frac{150}{180}\frac{1}{k}\right]_R \tag{2.34}$$

where the terms PFC and R mean that the equations inside the brackets refer to the PFC model and the real rock respectively. According to the literature the permeability for a limestone rock lies within the range of 2×10^{-11}- 4.5×10^{-10}cm^2 (Nield and Bejan, 2006). Choosing a mean value for the permeability the calibration factor is calculated as follows and it refers to the viscosity term of Eq.(2.30)

$$a_\mu = \left[\frac{\varepsilon^3 \overline{d_p}^2}{150(1-\varepsilon)^2}\right]_{PFC} \frac{150}{180}\frac{1}{k} \tag{2.35}$$

The same process was followed regarding the calibration factor a_ρ referring to the density parameter of Eq.(2.30) with the use of the following relation

$$[C_2]_{PFC} \times a_\rho = \left[\frac{1.75(1-\varepsilon)}{\varepsilon^3 d}\right]_R \tag{2.36}$$

Using the Kozeny-Carman Eq.(2.32) to calculate the diameter d of the real rock and install it into Eq.(2.36), the calibration factor for the density is given by

$$a_\rho = \frac{\left[\varepsilon^3 \overline{d_p}^2\right]_{PFC}}{\left[\varepsilon^{3/2}\sqrt{180k}\right]_R} \tag{2.37}$$

In terms of the coding these factors are used by multiplying the viscosity term with a_μ and the density term with a_ρ.

In conclusion, in this Chapter the concept of the PFC calculation cycle, as well as the fundamental equations of Lame’s theory, the Navier-Stokes formulation, Ergun’s relation and the process of decoupling the fluid flow parameters of the virtual model, have been presented. In the next Chapter the theory and equations, which were previously discussed, have been employed in order to describe the fluid flow test performed on a thick-wall cylinder rock sample.

Chapter 3 Calibration of microscopic parameters

3.1 Introduction

The procedures presented in this Chapter aim to specify the mechanical properties of a DEM specimen (both the particles and their bonds), on the particle scale. This PFC model is named LIM_0, where the initials LIM stand for limestone. The aim of the test is to calibrate the PFC model by matching its maximum uniaxial compressive strength, tensile strength, fracture toughness and elastic properties (Young's modulus E and Poisson's ratio v) with those of a real limestone rock. The calibration process is built upon a series of tests, namely the uniaxial compressive simulation (UCS), the brazilian tensile test and the single edge notch bending test (SENB), using the 3D version of PFC. The real limestone rock sample was provided by the Laboratory of the University of Leeds. However, due to lack of appropriate documentation regarding the properties of the laboratory limestone sample, it was considered necessary to obtain the relevant properties from the literature (Knill et al., 1970; Hallsworth and Knox, 1999; Academia.edu, 2013) and the experimental work by Schmidt, (1976) and Assane Oumarou et al., (2009). The general geo-mechanical properties of a limestone rock provide a wide range of values (see Table 3-1) and the experimental work by Schmidt and Assane Oumarou deliver the linkage between the virtual model and the actual experimental data. More specifically, part of the Assane Oumarou's investigation was to calculate the compressive and tensile strength on a number of cored Indiana LS limestone samples. According to his findings, the average uniaxial compressive strength was 44 MPa and the average tensile strength corresponded to 1/9 of the average UCS strength (4.9 MPa). He also conducted a tensile strength sensitivity analysis, concluding that the material's tensile strength ranges between 3.1 and 6.2 MPa, validating his sample against the general geo-mechanical properties. Furthermore, part of the work performed by Schmidt on Indiana Limestone was to calculate the tensile strength and Young's modulus on a number of specimens. It was estimated that the material's tensile strength was in the range 4.67-5.51 MPa, while its Young's modulus was in the range 32.5-34.3 GPa. The results obtained showed that Indiana limestone, used by both researchers, lie well within the range provided in the literature (Knill et al., 1970; Hallsworth and Knox, 1999; Academia.edu, 2013) and therefore their findings can be used as part of the calibration procedure. Further, the uniaxlal compressive, tensile strength, mode I fracture toughness and the elastic constants of a real limestone sample obtained from the existing literature are summarised in Table 3-1. The laboratory limestone sample was a moderately weak sample, thus a maximum uniaxial compressive strength near the lower strength range reported in the literature was chosen for the simulation model.

A rectangular model is used to replicate and mimic the mechanical behaviour of the laboratory limestone rock by performing the aforementioned tests. The DEM used in this thesis to represent the solid body of the real rock and its short-term behaviour, was based on the characterization of the virtual specimen in terms of the parameters in the micro-scale (Itasca Consulting Group, 2008c).

Table 3-1 Typical geo-mechanical properties of limestone, according to the literature (Knill et al., 1970; Hallsworth and Knox, 1999; Academia.edu, 2013).

Limestone parameters	
UCS strength (MPa)	$\boldsymbol{q_{UCS}}$=30-250
Tensile strength (MPa)	σ_t^B=5-25
Mode I fracture toughness (MPa√m)	K_I=0.658-0.994
Young's modulus (GPa)	E=15-55
Poisson's ratio	v=0.18-0.33
Density (kg/cm^3)	2500-2700
Porosity	5-30%

More specifically the properties of the UCS/tensile strength, fracture toughness and elastic constants are the macroscopic properties and they cannot be directly described in a DEM model. Therefore a process has to be set that will determine the micro-properties of the assembly and these in turn will determine the overall macroscopic behaviour of the model. This involves the relationship between the deformability and the strength of the assembly (Young's modulus, angle of friction, Poisson's ratio and the strength of the particles and bonds) to their equivalent set of macro-responses.

3.2 Particle generation procedure

The following procedure involves the modelling of the DEM LIM_0 model as an assembly of particles, which fill a specific volume and are bonded together with cementation. The five step procedure starts with the generation of a rectangular vessel of dimensions 37.8×37.8×100 mm (Fig. 3.1) and 15% target porosity. The vessel consists of frictionless walls in the X, Y and Z directions forming an isotropic and well-connected virtual assembly.

The vessel is filled with randomly placed particles of uniform distribution with a minimum radius of 0.85 mm and a minimum to maximum particle radius ratio of 1 (determined by the user). The particles are initially generated at half their sizes in order not to overlap with one another. To ensure a reasonable tight initial packing the particle population is such that the initial porosity, n_0, within the vessel is about 35% (Itasca Consulting Group, 2008c). The number of generated particles, N, is given by:

$$N = \frac{3V(1 - n_o)}{4\pi\bar{R}^3} \qquad (3.1)$$

where V is the volume of the vessel and $\bar{\mathrm{R}}$ is the mean particle radius given by:

$$\bar{R} = \frac{R_{min} + R_{max}}{2} \qquad (3.2)$$

As the procedure progresses, each particle's radius is multiplied by a factor m in order to achieve the desired porosity, n (Itasca Consulting Group, 2008d):

$$m = \sqrt[3]{\frac{1 - n}{1 - n_0}} \qquad (3.3)$$

The second step of the generation process involves the static equilibrium of the assembly and the setup of an internal isotropic stress. More specifically, in order to reduce the possibility of unbalanced forces and locked-in stresses (both tensile and compressive) during the generation process, and thus provide better internal equilibrium to the assembly, an appropriate isotropic stress is set.

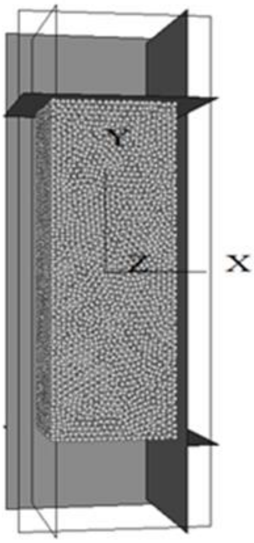

Figure 3.1 Schematic of the virtual limestone assembly during the standard genesis procedure. The size of the assembly is 37.8×37.8 mm in the horizontal X and Y axes, and 100 mm in the vertical Z axis, respectively.

This is achieved by reducing uniformly the radius of the particles until the target isotropic stress is obtained. Although there is no guideline concerning the required isotropic stress of the material and the literature does not shed any light regarding a typical value for limestone, the general rule of one-percent of the target uniaxial compressive strength of the material was employed (0.4 MPa) (Potyondy and Cundall, 2004). The required isotropic stress, σ_o, is the average of the direct stresses, $\bar{\sigma}_{kk}$, and is given by:

$$\sigma_o = \frac{\bar{\sigma}_{kk}}{\lambda}, \qquad \text{where } \lambda = 3 \tag{3.4}$$

The third step in the process involves the reduction of a number of particles, named floaters, that may have less contacts than those required, so that a denser network of bonds is achieved. Even though, for the purpose of this study, a densely packed and well-connected virtual sample is required, following the macroscopic behaviour of a real limestone rock, a number of particles are expected to be found that have no contacts. These particles are called ‘’floaters’’ meaning that they are detached from the assembly’s matrix and appear to be floating in the available space. From the modelling perspective, floaters are regarded as particles having less than three contacts with its neighbours (Itasca Consulting Group, 2008c), which corresponds to less than 50% of available contacts. Although floaters can be thought of as voids within the material's body, they do not correlate with any physical feature of the rock and therefore are meaningless to simulate. The effect of such anomalies, even though these may be small, can be eliminated in terms of the modelling by reducing the presence of floaters. Therefore, for this test the number of floating particles is set to zero. As a result, all floating particles that may have less than three contacts are removed from the vessel and the assembly is finally cycled in order to reach static equilibrium. Next the parallel bonds are installed between the particles of the virtual assembly, thus replicating the cementation between grains in real rocks. The complete set of their properties are presented in Table 3-2.

At the fifth and final step of the generation procedure, the specified internal friction coefficient is assigned (5.5 - a mean value suitable for most rocks) (Academia.edu, 2013), in order to provide a slip behaviour between particles. Specifically, in order for the particles to slip relative to one another, a friction coefficient is assigned which limits the shear force at contacts. In this case, where the particles of the virtual model are connected with parallel bonds, both the slip behaviour and the cementation can be combined and active throughout the procedure (Itasca Consulting Group, 2008f). Finally, the virtual assembly is removed from the vessel and cycled until static equilibrium is reached and the material is stress-free. A detailed description of the generation procedure and the governing equations has been presented by Poytondy and Cundall (2004).

3.3 Uniaxial compressive test

The purpose of the simulated UCS test is to calculate the maximum compressive strength and the elastic properties of the LIM_0 model and validate them against the literature (Table 3-1). During the simulated test, the top and bottom virtual walls are used as loading platens assigning a constant speed before initiating the test (Fig.3.2). In order to represent the real environment of an underground rock sample more realistically, the specimen is initially compressed before the test begins at P_c=0.1 MPa pressure, equivalent to the atmospheric confining pressure in laboratory uniaxial unconfined tests. The loading platens are considered frictionless and with a stiffness much higher than the particles' average one. Furthermore, the loading rate, produced by the movement of the loading platens, had to be slow enough so that the sample would remain in a pseudo-static state during the entire test. Thus, the velocity of the loading platens is applied gradually, reaching its final value in multiple steps so that the developing acceleration does not produce large inertial forces which in turn could cause dynamic damage to the core sample.

Initially both the Young's modulus of the particles and bonds are set to 40GPa, according to the conclusions of Akram and Sharrock (Akram and Sharrock, 2009).

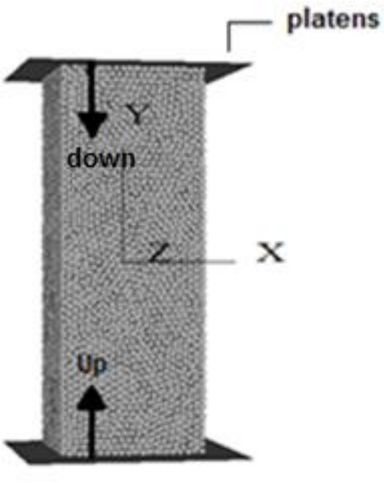

Figure 3.2 Schematic of the virtual limestone assembly during the simulated UCS. The sample is loaded by platens moving towards each other at a constant speed.

According to their findings, the Young's modulus of the particles is in good agreement with the Young's modulus of the bonds, as long as the stiffness ratio is about 1.0. Even though the referring sample was sandstone, it appears to be appropriate to use this finding in the case of limestone. This is because the two types of rocks are similar and the ratio of the normal and shear stiffness is also 1.0. A few trials indicated that the aforementioned micro-parameters should change and thus concluding to a final value of the Young's modulus of the particles E_C=30 GPa, whereas the Young's modulus of the parallel bonds is set to $\overline{E}_C$=20 GPa, lying within the broad range of 15-55 GPa (Table 3-1). Next, the Poisson ratio is set by defining the ratio of the shear to the normal contact stiffness for both the particles and bonds. A few iterations have been performed in order to match these micro-properties with the corresponding elastic constants of the material. Once the elastic constants have been matched, the maximum strength of the bonds is set near a low desired value within the range 30-250 MPa. Several trials (about 30) had to be executed in order to finally match and reproduce the relevant behaviour of a limestone rock. Table 3-2 demonstrates the complete set of input data used for the uniaxial simulation.

Table 3-2 The PFC micro-parameters employed for the Uniaxial simulated test on the LIM_0 limestone model.

Geometry	Sample height (mm)	100
	Sample diameter (mm)	37.8
	Sample porosity (%)	15
Micro-parameters that define the particles	Initial friction of balls	5.5
	Gravity (m/s^2)	9.81
	Ball radius (mm)	0.85
	Ball density (kg/m^3)	2600
	Young's modulus (GPa)	30
	Ball stiffness ratio	1.0
	Required isotropic stress (MPa)	0.4
Micro-parameters that define the parallel bonds	Radius multiplier	1.0
	Young's modulus (GPa)	20
	Normal/Shear stiffness ratio (Pa/m)	1.4
	Normal strength (MPa)	30
	Std. deviation of normal strength (Pa)	30×10^4
	Shear strength (MPa)	30
	Std. deviation of shear strength (Pa)	30×10^4

The test is performed with a velocity of $u_p = 0.005$ m/s and the axial stress (σ_a) is continuously monitored, rising to a maximum value and then decreasing as the sample fails. It is terminated when the recorded value of the axial stress is observed to be low enough in comparison to the peak axial stress. In this case the test is terminated when the current value of the sample's axial stress becomes less than 1% of the previously recorded maximum axial stress value ($|\sigma_a| < \alpha \times |\sigma_a|_{max}$). This is an arbitrary criterion nevertheless it captures the point of sample failure.

A number of uniaxial simulations for the limestone assembly were repeated in order to confirm that the PFC results from each test do not deviate and to evaluate the possible errors. Table 3-3 shows the results from the Uniaxial tests and their calculated error. The UCS results are considered accurate with an average relative error of 0.25% and standard deviation of 0.14 MPa for the measurement-based scheme, as well as 0.19% and 0.12 MPa for the wall-based scheme, respectively. The formula that calculates the error is given by:

$$relative\ error = \frac{|current\ value - mean\ value|}{mean\ value} \times 100\%$$

The results from the simulated tests were monitored and recorded by two different measurement schemes: wall-based (corrected) and measurement based (Itasca Consulting Group, 2008c). The difference between the two is that, in the wall-based scheme, the results are derived from measurements at each ball-wall contact point, where the effect of possible ball-wall overlap has been removed, whereas the measurement-based quantities are derived from three measurement spheres located in the upper, central and lower portions of the specimen.

In terms of calibration, even though the measurement-based scheme provides a more uniform averaged response over the entire specimen, it results in larger stresses and smaller strains compared to the wall-based scheme.

Table 3-3 Trial results and calculated error from Uniaxial simultions for the LIM_0 limestone assembly.

UCS strength (MPa)						
Trials	**Measurement -based**	**Standard deviation**	**Error (%)**	**Wall-based**	**Standard deviation**	**Error (%)**
1	50.7	0.14	0.00	45.2	0.12	0.44
2	50.9		0.39	45.0		0.00
3	50.5		0.39	44.8		0.44
4	50.8		0.19	45.1		0.22
5	50.6		0.19	45.0		0.00
6	50.9		0.39	44.9		0.22
7	50.8		0.19	45.0		0.00
Mean value	**50.7**		**0.25**	**45.0**		**0.19**

Thus it was considered best for this thesis to calibrate the virtual sample by matching the results from the wall-based scheme with the ones from the literature. The UCS results lie well within the wide range of limestone's elastic constants and strength (compressive and tensile) provided from the literature and agrees with the experimental results obtained by Schmidt and Assane Oumarou (Table3-4).

After the end of the test, the sample showed the expected behaviour in terms of stress versus strain. Fig.3.3 illustrates typical curves obtained from both schemes (wall-based and measurement-based) characterizing a rigid material that undergoes an abrupt failure. In the first region the strength increases linearly with increasing strain, thus showing that the material is in its elastic regime, until it reaches the point of its ultimate axial strength. Beyond that point, the material enters the plastic deformation regime, indicating irreversible damage. The maximum uniaxial compressive strength of the sample is 45 MPa based on the wall-based scheme.

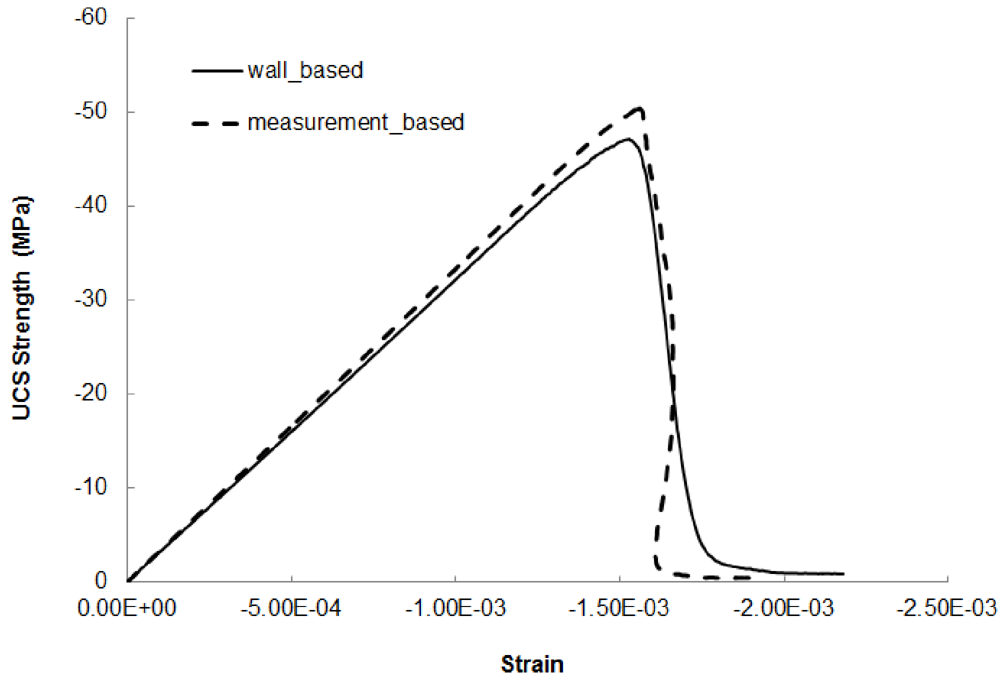

Figure 3.3 The PFC3D output of the stress versus strain for the LIM_0 limestone assembly used in the simulated Uniaxial test utilising both the wall-based and measurement-based schemes.

The comparison between the numerical mechanical results obtained from the simulated UCS and those provided from the literature are given by Table3-4.

Table 3-4 Typical geo-mechanical properties of limestone, according to the literature (Academia.edu, 2013) and the test results obtained from the UCS.

Properties	**Literature**	**Uniaxial test results**
UCS strength (MPa)	q_{UCS} = 30-250	q_{UCS}= 50.7measurement-based q_{UCS}= 45 wall-based
Young's modulus (GPa)	E = 15-55	E = 34
Poisson's ratio	v = 0.18-0.33	v = 0.21

3.4 Brazilian tensile test

Next the ultimate tensile strength of the material was calculated by employing the Brazilian test. In the simulated test, the virtual specimen is a cylindrical disc with the same micro-properties obtained from the aforementioned rectangular specimen used in the Uniaxial test (Table 3-2). A well-connected assembly of uniform size particles is created using the genesis procedure and the required stresses are applied so that the sample reaches the target isotropic stress. The specimen then is trimmed into a cylindrical disc of size 50mm diameter and 30mm thickness, and comprised of 12162 particles. The disc is in contact with the lateral walls in the X direction, whereas both the walls in the Y and Z directions are moved apart by a distance of 0.05×h, where h is the height of the initial rectangular assembly, and 0.05×d, where d is the diameter of the disc. This is an arbitrary value which agrees with the suggested values for a typical Brazilian test as described in the PFC3D manual (Itasca Consulting Group, 2008c). During the test, the Y and Z walls have zero velocity whereas the X-lateral walls are moving towards each other using the same platen-loading logic described previously in the uniaxial test (Fig.3.4). During the test the force, acting on the sample is initiated by the movement of the X-lateral walls, is calculated and the maximum value is recorded. The force is found to reach a maximum value and then decrease as the sample fails.

The same configuration for terminating the test, as in the Uniaxial test, is utilised. Therefore the test is completed when the current average force becomes less than 1% of the previously recorded maximum force ($F < \alpha \times F_{max}$), following the same termination criterion concept as in the UCS.

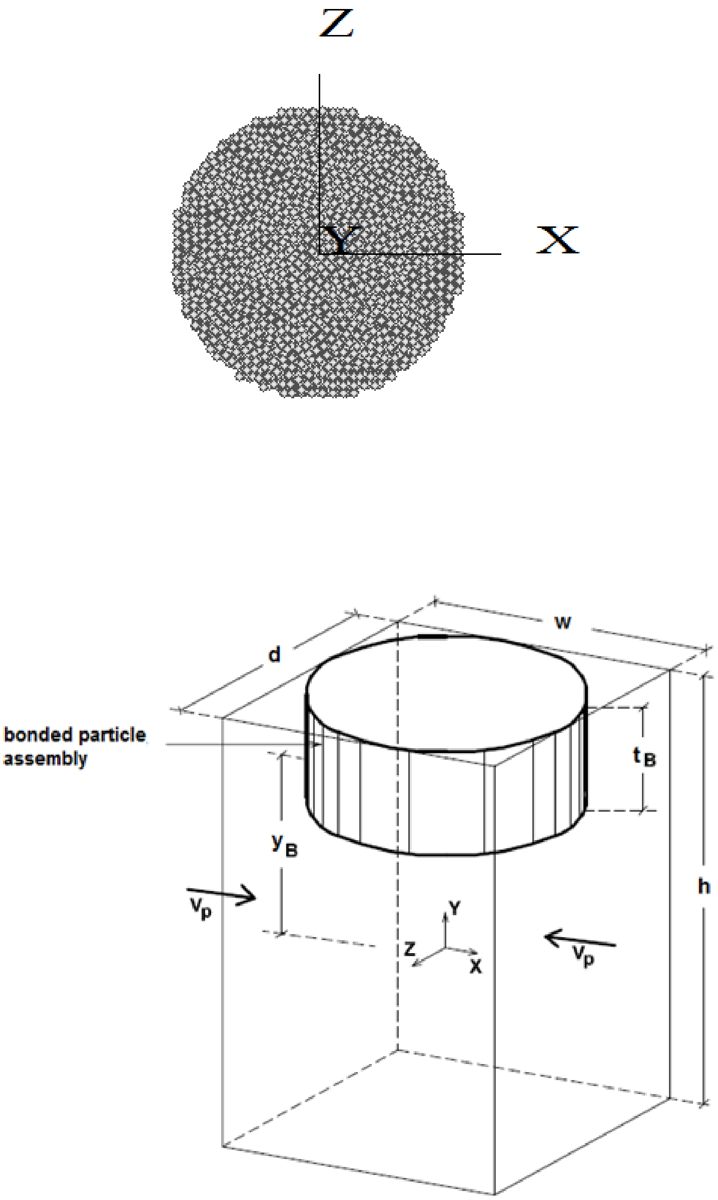

Figure 3.4 Schematic of the PFC Brazilian disc (Itasca Consulting Group, 2008c).

Fig.3.5 demonstrates the behaviour of the material until it reaches the ductile area and the point of its peak force 14 kN. When a cylindrical sample is subjected to a compressive loading perpendicular to its axis and in a diametrical plane, it fails under tension (Wright, 1955). The Brazilian tensile strength, σ_t^B, (6.0 MPa) is calculated by

$$\sigma_t^B = \frac{F_{max}}{\pi R t_B} \tag{3.5}$$

where F_{max} is the peak force acting on the platens and R and t_B are the radius and the thickness of the virtual disc, respectively.

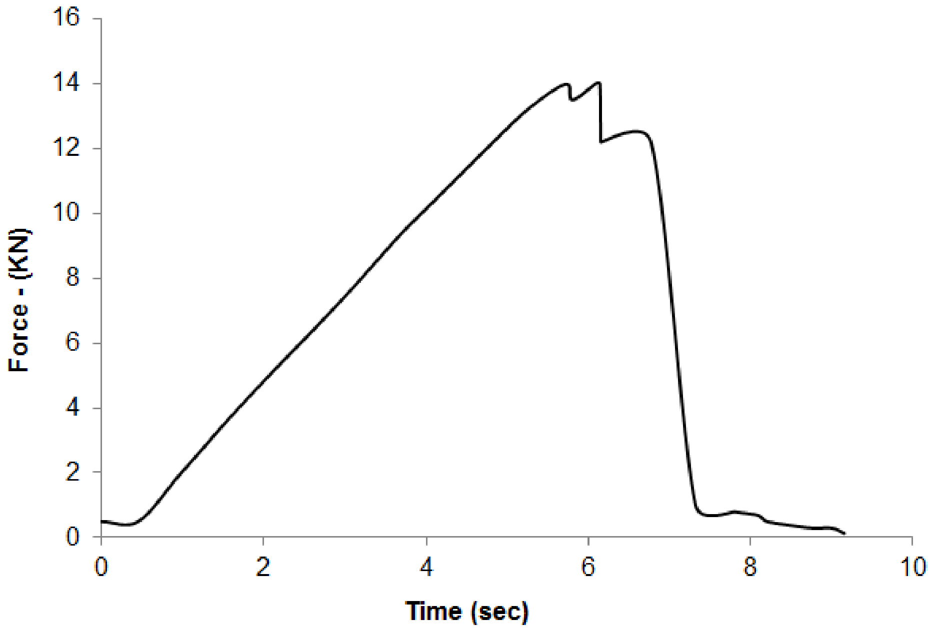

Figure 3.5 Force acting on the platens of the limestone virtual disc versus time. The sample fails under $\boldsymbol{F_{max}}$= 14 kN.

Fig.3.6 shows the corresponding behaviour in terms of the stress versus strain. It can be observed that there is an almost linear increase of the strength with the increasing strain, reaching a maximum value of about 6.0 MPa stress and then there is a sudden decrease which results in failure. This validates the strength values obtained from literature and the fact that rocks are extremely weak in tension putting their tensile strength in the range of the order of one sixth to one tenth of the UCS strength.

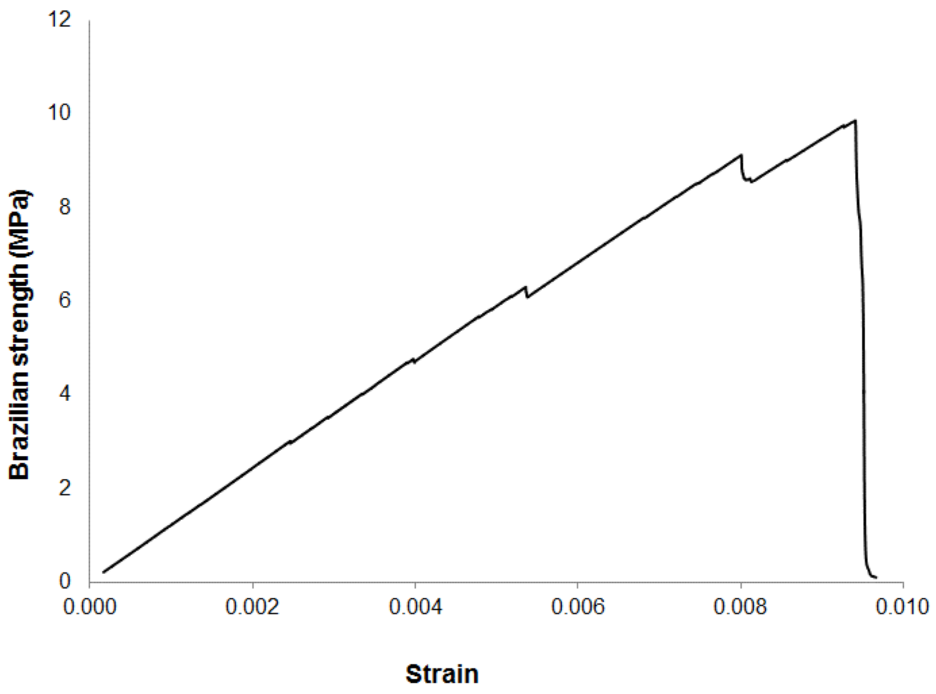

Figure 3.6 The PFC3D output of the stress versus strain for the limestone assembly used in the simulated Brazilian test. The material has a maximum tensile strength of 6.0 MPa.

3.5 Single edge notch bending test (SENB)

One of the most important mechanical parameters of a rock sample is the calculation of its stress intensity factor and therefore its fracture toughness, meaning the resistance of the material that contains a crack towards failure. In the simulated three point bending test, a rectangular limestone specimen of dimensions 115×25×12.5 mm (Fig.3.7) is generated by a standard sample genesis procedure including: (i) generation and compaction of the particles; (ii) setup of the isotropic stress to provide internal equilibrium; (iii) adjustment of particle sizes to reach at least three contacts with the neighbouring particles and elimination of those which do not follow the rule; and, (iv) finalization of the assembly. During this process, the virtual model consisting of particles and parallel bonds (cementation) is produced in the specified vessel. A notch has been created at the centre of the bottom part of the assembly by deleting the particles contained in the notched region. The size of both the virtual assembly and the notch are chosen according to Schmidt's work (Schmidt, 1976) and the American Society for Testing and Materials (ASTM) E1820-01 recommended specifications (ASTM, 2003). Specifically, according to Schmidt's findings, the linear fracture mechanics approach, which is extensively used in modelling the failure of metallic and other materials, can also be applied in rock samples. He concluded that the ASTM criterion (crack length and specimen width must be greater than 2.5) proves to be an appropriate check for a valid measure of the stress intensity factor for this rock material. Based on Schmidt's findings, the size that could provide more accurate results of the fracture toughness is shown to coincide with the ASTM for the measurement of fracture toughness for metal alloys.

The procedure is similar to the Uniaxial test, where frictionless walls in the X, Y and Z directions surround the vessel, forming an isotropic and well-connected virtual assembly. Next, all the walls are removed and the model is cycled in order to absorb any residual forces caused by the lateral walls. Two fixed circular walls of high stiffness are set on the bottom ends of the virtual assembly in order to provide the basic support (Fig.3.7). Their radius is 3.1 mm and the span between the supports is 100 mm, both following the ASTM E1820 guidelines (R_{min}=W/8 and S=4×W). The loading platen in this case is represented by 4 well-connected particles with strong contact bonds in order to act as a single unit. Their stiffness is much higher than the average particle's stiffness, considering their role as a loading platen, and they are set just above the top surface of the assembly moving towards the top surface.

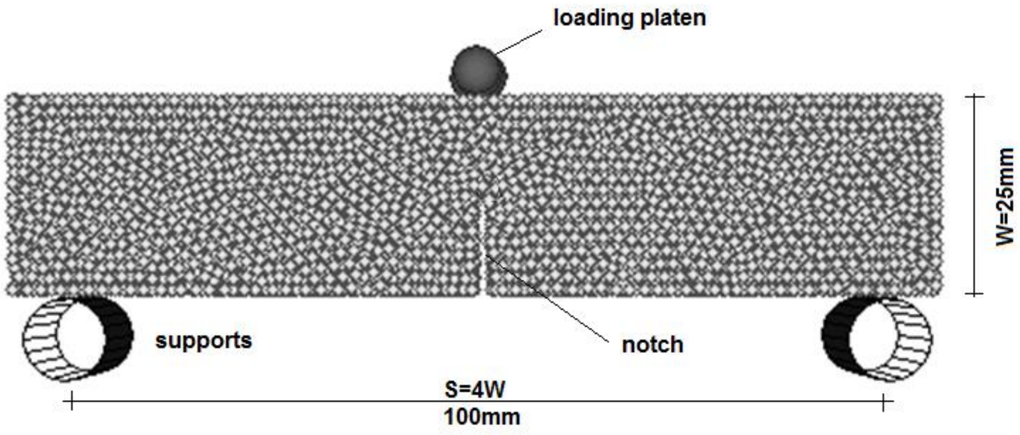

Figure 3.7 Dimensions of the virtual limestone assembly for the Single Edge Notch Bending (SENB) test.

The complete set of input data used for the SENB test is summarized in Table 3-5.

The test is performed with a vertical platen velocity of $u_p = 0.01$ m/sec and the mode I stress intensity factor is continuously monitored until the failure of the sample and the measurement of the fracture toughness, following the equation given by the ASTM Designation E1820-01:

$$K_I = \left[\frac{PS}{(BB_N)^{\frac{1}{2}}W^{\frac{3}{2}}}\right] f(a/W) \qquad (3.6)$$

where:

$$f({}^{a}/_{W}) = \frac{3(a/W)^{1/2}\left[1.99-(a/W)(1-a/W)\times(2.15-3.93\left(\frac{a}{W}\right)+2.7(a/W)^2\right]}{2(1+\frac{2a}{W})(1-a/W)^{3/2}} \qquad (3.7)$$

where K_I is the mode I stress intensity factor, P and S are the load to failure and the span, respectively. Finally, a, B_N, W and B are the length of the notch, the depth of the notch and the width and the depth of the sample respectively.

Table 3-5 Dimensions of the virtual limestone assembly and notched region for the Single Edge Notch Bending test.

Input data		
Sample dimensions	Length (mm)	115
	Width (mm)	25
	Depth (mm)	12.5
Notch dimensions	Length a (mm)	12.5
	Width W (mm)	1.7
	Depth (mm)	12.5
Supports	Diameter (mm)	5
	Stiffness (GPa/m)	50
Loading platen	Diameter (mm)	3.1
	Stiffness (GPa/m)	200
	Density (kg/cm^3)	7800
	Normal strength (GPa)	80
	Shear strength (GPa)	80

The loading process is terminated when the required termination criterion is reached. More specifically, the stress intensity factor $(\mathrm{K_I})$ is continuously monitored, increasing to a maximum value and then decreasing as the sample fails. Its maximum value $(\mathrm{K_{I_{max}}})$ is recorded and the test is terminated when the current value of the stress intensity factor becomes less than 0.3 times the previously recorded maximum value $(\mathrm{K_I} < \alpha \times \mathrm{K_{I_{max}}})$. Preliminary tests showed that this ratio may be considered to be sufficient for the sample to reach its maximum fracture toughness and a drop of more than 30% in the value of the stress intensity factor indicates a failure of the sample and thus this condition is used as a termination criterion. Fig.3.8 demonstrates the progress of the test at intervals, whereas Fig.3.9 shows the profile of the stress intensity factor versus the opening of the notch and the maximum fracture toughness of the material.

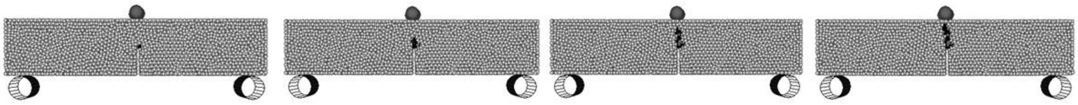

Figure 3.8 Progressive damage of the assembly resulting to micro-cracks at the tip of the notch and towards the top surface of the sample.

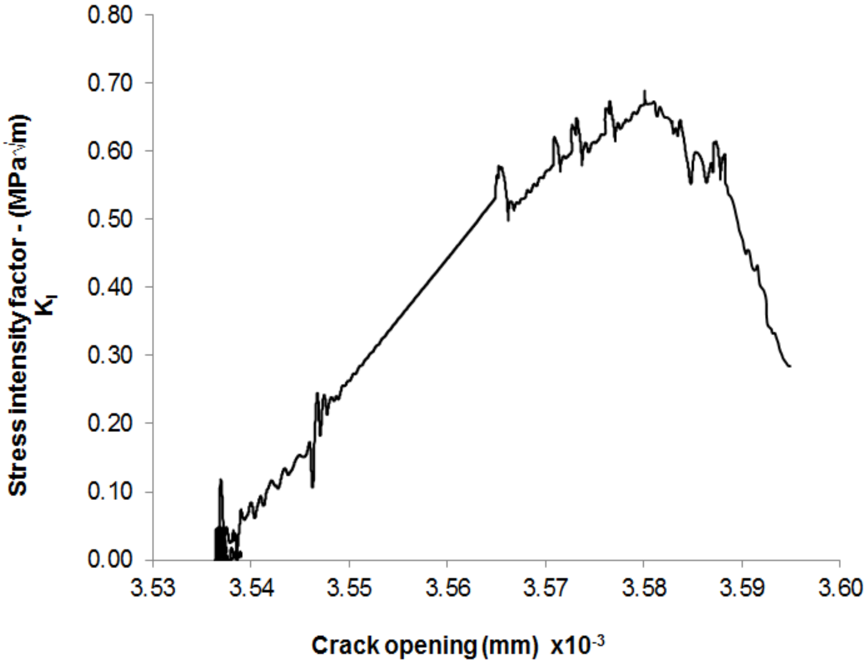

Figure 3.9 Plot of the stress intensity factor versus crack opening, maximum value of fracture toughness 0.66 MPa√m.

According to the plot the material's resistance towards fracture is gradually increasing, reaching the maximum value of fracture toughness at 0.660 MPa√m, followed by a sharp decrease. The relatively low value of the fracture toughness of the material and the layout of the stress intensity factor, as well as the very low deformation compared to the Uniaxial compressive stress and the complete failure of the sample (Fig.3-3), indicates that the material undergoes brittle failure (Hertzberq, 1996).

3.6 Fracture Mechanics in DEM

The presence of faults in rocks can contribute towards the escalation of any applied load as a result of the relationship between the surrounding loads, the geometry of the faults and the mechanical properties of the porous medium (Griffith, 1921). Relations that relate the above parameters are defined in terms of the stress intensity factors. In Linear Elastic Fracture Mechanics (LEFM), there are three different types of loading that a crack can experience due to external forces on the material as illustrated in Fig.3.10. The most common type of loading for rocks is the Mode I (Schmidt, 1976; 1977), where the principal load is applied in a normal direction with respect to the crack plane and tends to open the faces of the crack.

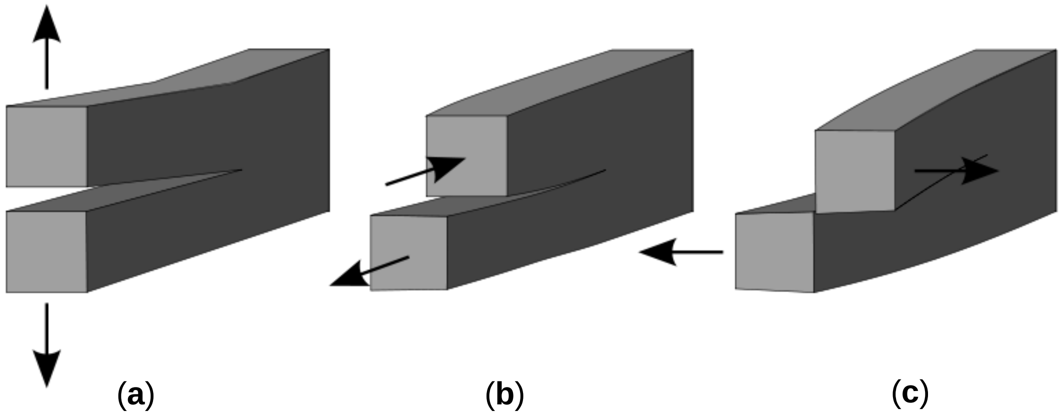

Figure 3.10 The three types of fracture toughness modes, (**a**) Mode I normal to the crack plane, (**b**) Mode II in-plane shear that tends to slide the faces of the crack, and (**c**) Mode III out-of-plane shear (Anderson, 1991).

UCSs are performed on five limestone samples of the same geometric size as LIM_0, named LIM1 to 5, in order to calculate their ultimate compressive strength. The micro-parameters of each of the samples are identical with the LIM_0 limestone sample discussed in the previous chapters, so that the elasticity of the samples remains constant, whereas the normal and shear strength of the parallel bonds has been altered. The SENB test is then performed on the LIM1 to 5 samples in order to estimate their fracture toughness. The ratio on the shear to normal strength is chosen to be 1.3 based on the experimental work of Assane Oumarou et al., (2009) for five different samples of Indiana limestone. According to their findings, the normalized stress ratio was mainly between 0.5 to 2.0 and therefore it was considered appropriate to take the average value of 1.3. The purpose of this test is to validate the simulated fracture toughness results with the ones obtained from the limited existing literature and relate the simulated SENB test with the LEFM. The test results show that the fracture toughness of the PFC limestone assemblies are in excellent agreement with the work of Schmidt, (1976), which gives results between 0.658 MPa.m$^{1/2}$ and 0.994 MPa.m$^{1/2}$ for 18 limestone samples, thus emulating the actual laboratory macro-scale measurement technique for fracture toughness. Table 3-6 shows the values of the normal and shear strength of the parallel bonds for each PFC sample, as well as the Uniaxial and the SENB test results.

Table 3-6 Input parameters of the normal and shear bond strengths for the conduction of the UCS and SENB simulations, and the results obtained by the UCS and SENB.

	LIM1	LIM2	LIM3	LIM4	LIM5
Parallel-bond normal strength (MPa)	30	35	40	45	50
Parallel-bond shear strength (MPa)	39	45.5	52	58.5	65
UCS results (MPa)	Wall-based: 51	59	68	77	86
SENB results (MPa.m$^{1/2}$)	0.670	0.790	0.910	0.990	1.030

It can be observed that the values from the SENB test are in excellent agreement with the experimental values provided by the work of Schmidt. It is important to point out that in DEM, a PFC particle must not be correlated with a real rock grain (Itasca Consulting Group, 2008d). This is due to the fact that the virtual assembly is a precise micro-structural sample and should not be confused with the microstructure of a rock. The particles in the PFC are used only as a means to discretise the rock’s matrix and provide a comprehensive description of the model’s mechanical behaviour in terms of the breakage of the bonds (Itasca Consulting Group, 2008b). For these reasons, and the fact that DEM analysis is based on the discontinuity of the model (due to fractures), the stress intensity factor obtained from the DEM approach cannot be directly compared with the one obtained from LEFM techniques. However, with the assumption that the individual micro-cracks in the DEM are connected as part of the propagation process of a macroscopic fracture, the simulation results can be interpreted by the LEFM. Several researchers have worked on this topic relating the measurements of fracture strength obtained from the DEM with those from the LEFM (Potyondy and Cundall, 2004; Moon et al., 2007; Huang et al., 2013). The work of Potyondy and Cundall, (2004) related the LEFM to the bonded-particle model for a synthetic rock. More specifically, they translated the mode I fracture toughness of an infinite plate with a horizontal crack subjected to a remote tensile stress (Fig.3.11(**a**)), to the following suggested formula for a parallel-bonded material:

$$K_I = \beta \sigma'_t \sqrt{\pi \alpha R} \tag{3.8}$$

where K_I is the mode I fracture toughness, α, β are non-dimensional constants with $\alpha \geq 1$ and $\beta < 1$, σ'_t is the normal strength of the parallel bond and R is the radius of the particles.

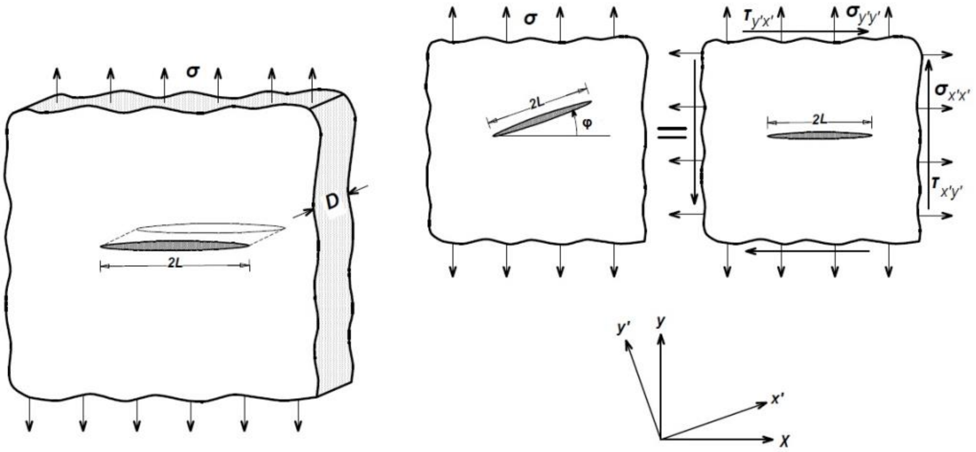

(**a**) (**b**)

Figure 3.11 (a) Infinite plate (width>>2L) with a horizontal crack subjected to a remote tensile stress - $\boldsymbol{K_I = \sigma\sqrt{\pi \mathrm{L}}}$, and (**b**) infinite plate with a inclined crack subjected to a tensile stress that is not perpendicular to the crack plane - $\boldsymbol{K_I = \sigma_{y'y'}\sqrt{\pi L} = \ \sigma cos^2(\varphi)\sqrt{\pi L}}$ (Anderson, 1991).

Furthermore, the LEFM calculates the mode I fracture toughness for the generalised case of an infinite plate with a inclined crack subjected to a remote tensile stress (see Fig.3.11(**b**)), given by:

$$K_I = \sigma_{y'y'}\sqrt{\pi L} = \ \sigma cos^2(\varphi)\sqrt{\pi L} \qquad (3.9)$$

Based on the work of Potyondy and Cundall, (2004) Eq.(3.8) can be converted into the following formula:

$$K_I = (\beta\sigma'_t\sqrt{\pi\alpha R})\cos^2(\varphi) \qquad (3.10)$$

In this thesis, the total effect of the parameters α, β were merged into a single correlation factor μ that bridges the domain between the Discrete Element Method and the Linear Fracture Mechanics, given by:

$$K_I = (\mu \sigma'_t \sqrt{\pi R}) cos^2(\varphi) \tag{3.11}$$

More specifically, the factor μ can be used to relate the fracture toughness derived from the LEFM (in this case obtained from the SENB tests) with the fracture toughness based on the DEM approach. Samples LIM1 to LIM5 correspond to the case where the angle φ is zero and therefore according to Eq.(3.11) values of the factor μ close to unity will ideally result in the elimination of the effect of the parameters α and β and hence the mode I fracture toughness of the assembly will be directly related with its microproperties. Furthermore, inserting the values of the fracture toughness obtained from the SENB test for the samples LIM1 to 5, as well as the values of the tensile strengths of the parallel bonds into Eq.(3.11), we can obtain through curve fitting a DEM relationship between μ, K_I and σ'_t:

$$\mu = 0.04055 + 0.09147K_I - 0.001893\sigma'_t - 0.04761{K_I}^2 + 0.000972K_I\sigma'_t \tag{3.12}$$

Eq.(3.12) is illustrated in Fig.3-12. According to the figure, the fracture toughness and the tensile strength of the bonds are denoted in the X and Y axes, respectively, while the factor μ is denoted in the Z axis. According to Eq.(3.12), the aforementioned set of values for K_I and σ'_t result to a range of values for factor μ between 0.045 and 0.040. Even though these values are not close to unity, the peak value of about 0.045 corresponds to a set of values for K_I and σ'_t, 0.910 MPa√m and 40 MPa, respectively, and yields to the most effective model.

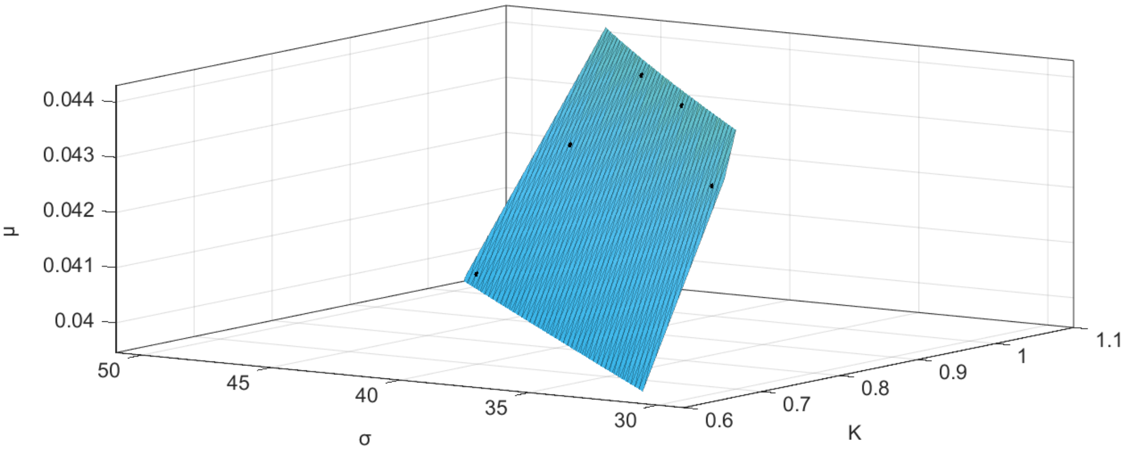

Figure 3.12 3D plot of calibration factor $\boldsymbol{\mu}$ versus the mode I fracture toughness $\boldsymbol{K_I}$ and the tensile strength of the parallel bonds $\boldsymbol{\sigma'_t}$.

Furthermore, Eq.(3.11) indicates that the fracture toughness is directly related to the geometry of the sample and more importantly to the tensile strengrh of the parallel bonds. Therefore an additional step is followed in order to eliminate the effect of the correlation factor μ and relate the fracture toughness of a material with its micro-properties, as mentioned above. Specifically, combining the values of the fractures toughness, obtained from the SENB simulations with the values of the tensile strength of the parallel bonds (Table 3-6), we obtain a relationship between K_I and σ'_t which gives an approximate solution:

$$K_I = -6 \times 10^{-10}{\sigma'_t}^2 + 0.0669\sigma'_t - 788857 \qquad (3.13)$$

According to Eq.(3.13) there is a second order relationship between the two parameters, however the second order factor is very small and thus it can be considered negligible. Fig.3-13 demonstrates the relationship between K_I and σ'_t. It can be observed that when the tensile strength of the parallel bonds is between 30 and 40 MPa the fracture toughness increases almost linearly and for larger values of σ'_t the curve of the graph is relatively shallow. This finding validates the DEM theory and comes in good agreement with Eq.(3.11), where the mode I fracture toughnes of a material with inclined fracture is linearly increased when the right hand-side of the equation is increased.

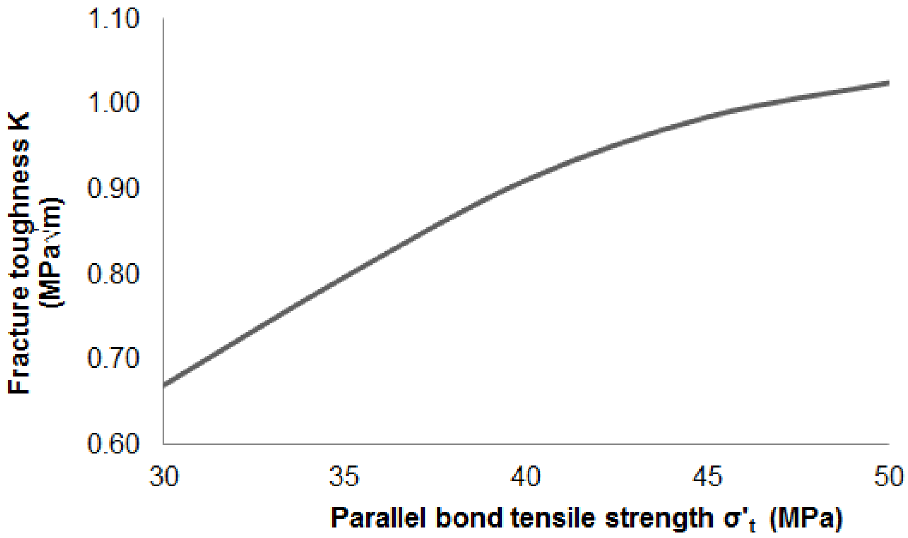

Figure 3.13 Fracture toughness of the samples LIM1 to LIM5 obtained from the SENB tests versus the tensile strength of their parallel bonds.

Additional research steps are needed, and these include the generation of many more samples in order to produce a more accurate version of both the Eq.(3.12) and Eq.(3.13) and describe the relationship between the fracture toughness of a limestone material with the DEM correlation factor and the microproperty that defines its bonds more efficiently.

In conclusion in the previous chapters the calibration procedure of a limestone virtual sample has been described. The mechanical properties (elastic parameters compressive and tensile strengths, as well as the fracture toughness) of the material have been calculated by performing Uniaxial

Compressive, Brazilian and Single Edge Notch Bending tests. These results have been validated against the values provided from the literature and the experimental work from researchers. Furthermore, a concept for relating the fracture toughness of the limestone material, obtained from the SENB test, with the fracture toughness based on the DEM approach, and the elimination of the correlation factors with the use of a simplified relationship between K_I and σ'_t, as well as the simplification of the calibration procedure, has been suggested and described. The calibration procedure has provided a fully validated limestone virtual specimen which will be further utilised to perform simulated fluid flow tests in Chapters 4 & 5.

The complete coding files that describe the calibration procedure (Uniaxial, Brazilian and SENB tests) have been included in Appendix I.

Chapter 4 The DEM analysis of hydraulic fracturing in a hollow hard rock cylinder

4.1 Introduction

Even though hollow cylinder tests are commonly used in studies pertaining to wellbore instability and sand production, nonetheless they are also used to investigate fracturing processes (Ewy et al., 1988; Enever and Bailin, 2001; Elkadi and van Mier, 2004; Ayob et al., 2009). As the mode of fluid application is a major determinant of the rock material behaviour, the simulated hollow cylinder test replicates the laboratory fracture test exploring the resulting stress regime and the micro-cracking. A hydraulic fracturing test, which was performed in the laboratory of the School of Earth and Environmnet, in the Univeristy of Leeds, on a cylindrical limestone sample with a hollow core has been simulated. A virtual DEM specimen has been utilised, that represents the real rock and the laboratory loading conditions have been duplicated.

4.2 Calibration results

The virtual model is a calibrated limestone rock sample and the mechanical parameters of the virtual sample (LIM_0) have been calculated and presented in Chapter 3. The calibration tests include the UCS, Brazilian tensile and SENB simulations, as previously discussed, validating the model against a real limestone rock. Table 4-1 illustrates the complete set of the mechanical parameters provided from the literature and those measured from the calibration tests.

Table 4-1 Mechanical parameters of a typical limestone rock provided by the literature (Schmidt, 1976; Academia.edu, 2013) and calibration test results.

Limestone parameters	**Literature**	**Calibration test results**
UCS strength (MPa)	q_{UCS}=30-250	q_{UCS}=45.0 wall-based
Tensile strength (MPa)	σ_t^B=5-25	σ_t^B=6.0
Fracture toughness (MPa√m)	K_I=0.658-0.994	K_I=0.670
Young's modulus (GPa)	E=15-55	E=34
Poisson's ratio	v=0.18-0.33	v=0.21

4.3 Laboratory experiment

Laboratory fracturing experiments are often used to monitor the deterioration and disintegration of rocks under prescribed and controlled simulated sub-surface reservoir conditions. As part of this numerical investigation, a number of experimental tests were conducted on a series of synthetic and natural rock samples subjected to differing operating and boundary conditions. Artificial samples were created to imitate soft permeable rocks that are low in strength (bonded glass bead materials), while the natural samples consisted of limestone. The early and non-progressive collapse, meaning the sudden disintegration of the synthetic samples during the initial stages of fluid flow, illustrates the combined effects of permeability and strength on the failure mode. This phenomenon is not observed in the limestone samples which are less permeable but have a higher strength. Observed occurrences of pressure build-up, deformation and fracturing during the tests show the role of an operating well and reservoir conditions as well as the physical and mechanical properties of materials on mechanisms that result in collapse failure and the mode of application of injected water inside the sample.

To determine the mechanical behaviour of natural rock under prescribed fluid flow conditions, a set of tests was conducted on a cylindrical limestone sample (37.8 mm diameter and 100 mm height) which was drilled along its axis to create a cylindrical cavity. The test was performed on a specimen with a cylindrical cavity of 21.5 mm sourced from Tadcaster, North Yorkshire, U.K. An initial pressure differential was established between the outside of the specimen and the hollow centre, which was kept at zero pressure. The outer boundary fluid pressure was then gradually increased until failure. The laboratory equipment for the fracturing test included a permeameter combined with a CT scanner and hydraulic hand pumps in order to drive and regulate the injection fluid at the prescribed pressure through the specimen cavity and around the circumference of the specimen. A set of computers to monitor and control test operations as well as to process the scan images were also included.

Fracture initiation was observed to occur after about 8000 sec and the eventual collapse of the cavity wall occurred at 5056 Psi (35 MPa) followed by a rapid drop in the circumferential pressure to 29 Psi (Fig. 4.1). The initial state of the specimen and the progressive fracturing and collapse is illustrated in Fig. 4.2.

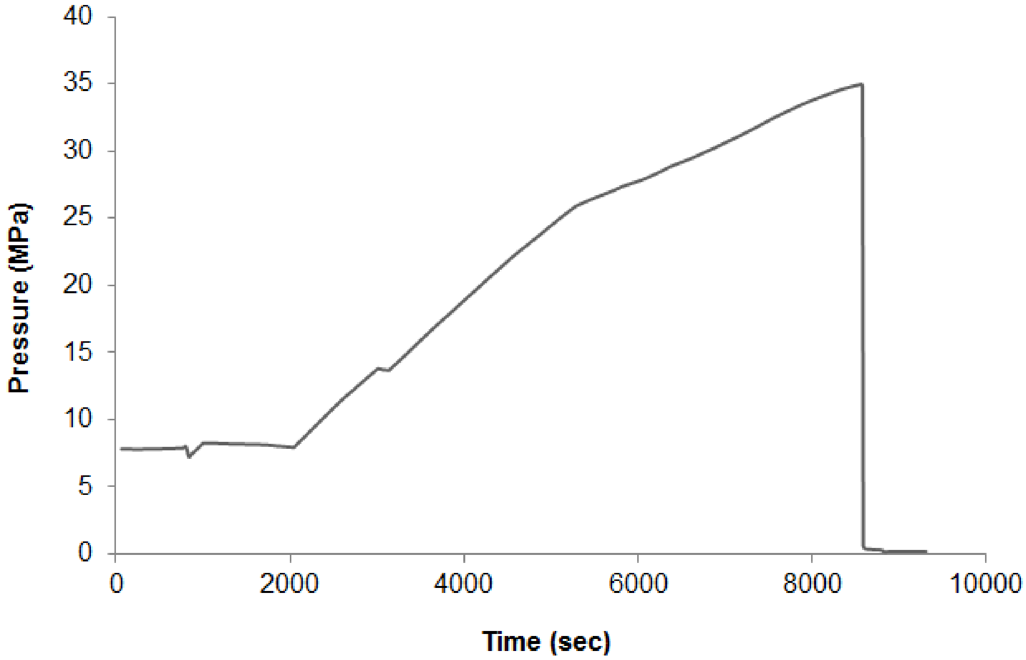

Figure 4.1 Laboratory fluid pressure differential between the hollow core and the outer surface of the sample, versus time. The maximum fluid pressure differential is 35 MPa.

The hydraulic fracturing experiments were performed on a variety of synthetic and natural rock samples and they illustrate a fracturing and failure behaviour that is predominantly influenced by the material mechanical and physical properties, boundary conditions, as well as the mode of application of the injection fluids. It was observed that for soft rocks, i.e. highly permeable, it is generally difficult to attain a significant pressure build-up and the inward collapse of the cavity, combined with a severe deformation of the material within the outer radius of the sample is imminent, occurring irrespective of the existence of a pressure gradient developed between the outer surface and the inner hollow core, where the minimum pressure occurs at the inner hollow core. When the material strength and stiffness is increased, the maximum allowable build-up fluid pressure also increases. In this case, which has been simulated in Chapter 4.4, the integrity of the outer surface of the sample is more likely to be maintained and the process of failure at the cavity is such that there is an initial expansion prior to the collapse of the cavity. More specifically, regarding the limestone sample, the size of the cavity plays a major role which means that larger size cavities appear to be considerably less stable than smaller ones. In any case, sample failure occurs at pressures close to the reported compressive strength of the material. Furthermore, in the cases where externally applied stresses are negligible, initiation and propagation of fractures will always occur perpendicular to the axis of the cavity.

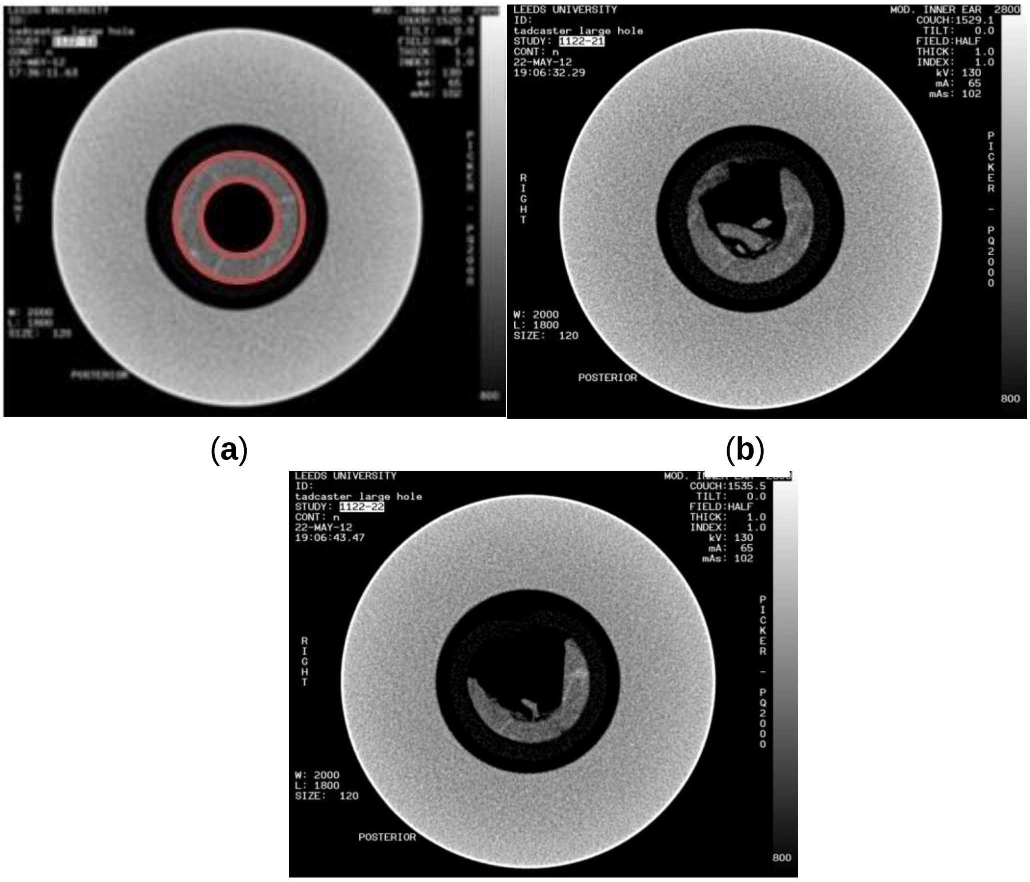

(**a**) (**b**)

(**c**)

Figure 4.2 Scan image of the large cavity limestone specimen inside the test-tube (**a**) in the initial state (red), and (**b**), (**c**) in various stages of the collapse of the cavity wall.

4.4 Rock specimen and simulation setup

The virtual model, for the following simulated fluid flow test, is cylindrical with dimensions of diameter 37.8 mm, length 50 mm and comprised 12840 particles of uniform size (Fig. 4.3). It is important to point out that although a PFC model in general demonstrates similar behaviour with that of a real rock, we do not correlate a PFC particle with a real rock grain. The virtual sample itself is a precise micro-structural assembly in its own right and should not be associated with the micro-structure of a rock (Itasca-Consulting-Group, 2008a). The model has a hollow central region (pipe-like) with a diameter of 21.3 mm, along the axis of the cylinder following the layout of the laboratory sample.

During the laboratory experiment, the rock sample is placed inside a tube through which water is injected. The movement of the fluid through the body of the sample is activated by setting a pressure difference between the outer perimeter of the sample and its internal hollow core. The purpose of the hollow core is to allow the fluid’s movement through the pipe to make the rock fully saturated and keeping its internal pressure close to zero, while the external pressure is gradually increased. This pressure difference forces the fluid to radially penetrate the rock’s body towards its core.

The fluid-particle scheme is used for this work as a function already developed by the Itasca Company (Itasca Consulting Group, 2008d). It can be considered as a two way coupling as the fluid injection has altered the structure of the rock (in terms of fractures) and the fracturing also altered the path of the fluid flow.

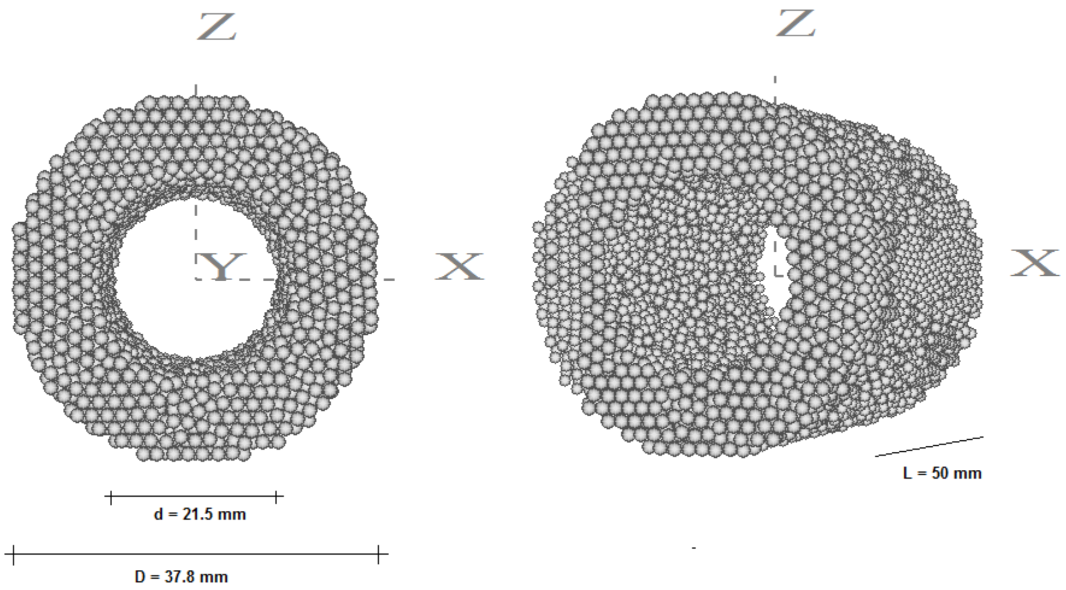

Figure 4.3 Schematic of the virtual limestone model with a hollow cylindrical core.

As the problem simulated in this thesis is not diluted particle flow in a fluid, but instead, it is a densely packed medium with flow passing through its pores, the particle fluid rate has no significant impact on the model.

Initially, a three-dimensional mesh (filter) which encapsulated the sample is created, thus allowing the discharge of water through it. The mesh that consists of 1-dimensional (line) walls specified at regular locations around the sample, has a minor effect in terms of the interaction with the particles. The purpose of the filter walls is mainly to provide the basic support to the movement of the particle. The spacing between the line walls is set to be equal to the minimum ball radius of the sample. It is important that the filter is sufficiently dense to merely support the sample during the fluid flow, but not so dense as to interfere with the model's overall behaviour. Next, the fluid pressure boundary conditions have to be set. Due to software restrictions in terms of boundary conditions, a simplified but equivalent representation of the laboratory conditions has to be developed. More specifically, there is no way of defining a pressure boundary condition upon the fluid cells that do not reside at the edges of the fluid cell mesh, that is also applied, and therefore another equivalent concept has to be devised. An alternative approach to overcome this limitation in the PFC software is to use a rectangular slice of the assembly, instead of the whole cylindrical sample, applying the filter walls and the fluid cell mesh. The spacing between the filter walls is set equal to the particle radius of 1.0mm in all directions (Fig.4.4).

Moreover a fluid cell grid is also applied to the rectangular slice of the assembly covering the outer perimeter and the inner hollow core of the model, as illustrated in Fig.4.5. The whole assembly may be considered to consist of eight (8) of these slices. Since the actual laboratory experiment had radial symmetry (water flowing from the outside towards the inside in all directions along the z-x plane), it is valid to state that the flow through each slice should correspond to approximately 1/8th of the total flow through the complete assembly.

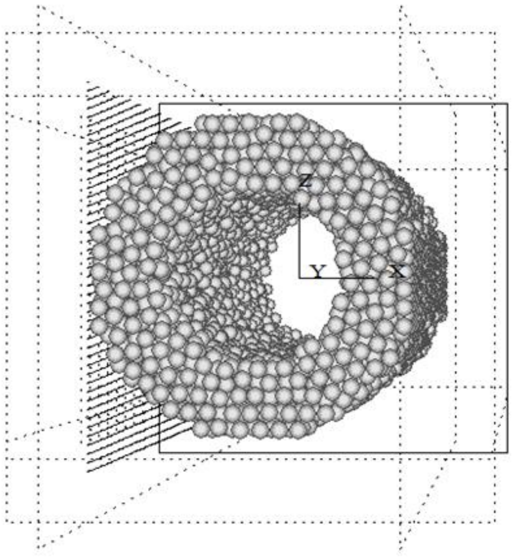

front view

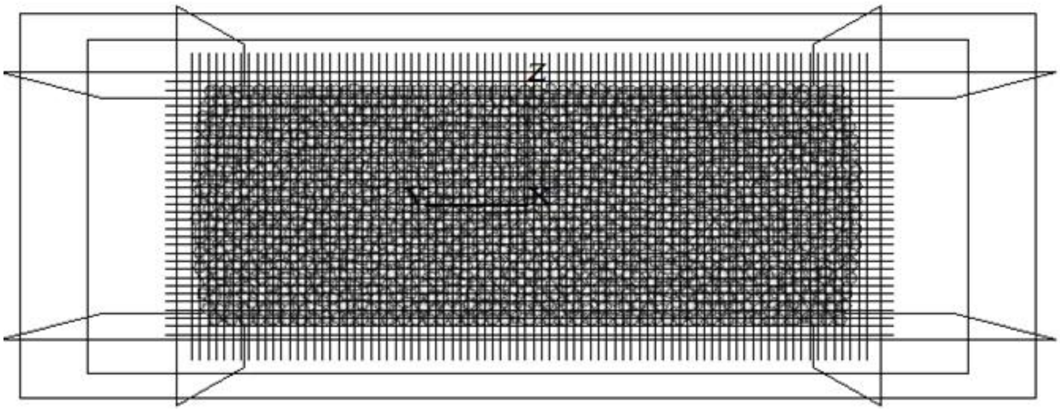

Side view

Figure 4.4 Schematic of the 3D mesh (filter) used to support the sample. Each side of the mesh consists of horizontal and vertical 1D walls.

The parameters defining the grid are its dimensions and the number of cells along each direction. There are no guidelines on the grid's parameters, other than in the case of a porous medium it was considered best that the cells should have a size comparable to that of a few particles. This is due to the fact that the porosity and permeability are calculated through each cell, thus the cell grid must be coarse. During this test, 240 fluid cells are created, each with a cell size of 2.6×8.3×1.26 mm. In the laboratory experiment, the sample was placed inside a tube where the fluid pressure was applied uniformly around the outer surface of the body of the rock. Therefore, the exerted forces at each point of the rock's outer surface was neutralised by an equal and opposite force on the other side of the sample which keeps the sample in a static equilibrium position during the experiment. To model this effect, solid boundary walls are placed around the sample, except for the one on the left hand-side where the fluid is injected. The fixed impenetrable walls prevent the movement of the sample and emulate the sample equilibrium maintained during the laboratory experiment.

The pressure differential applied during the laboratory experiment was gradually increased, starting from 8 MPa with a loading rate of 0.004 MPa/sec until the failure of the sample in a time frame of about 8400sec. In order to replicate the laboratory pressure inside the simulated test, the plot of the fluid pressure versus time is divided into two regions, covering the periods of time 0 to 2000 sec, and 2000 to 8400 sec, as shown in Fig. 4.6 (dashed). In the first region, the simulated fluid pressure is set to 8 MPa, which is the average of the plot points in that section (Fig. 4.6 solid black). In the second region of the plot, the pressure is gradually increased from 8MPa until failure.

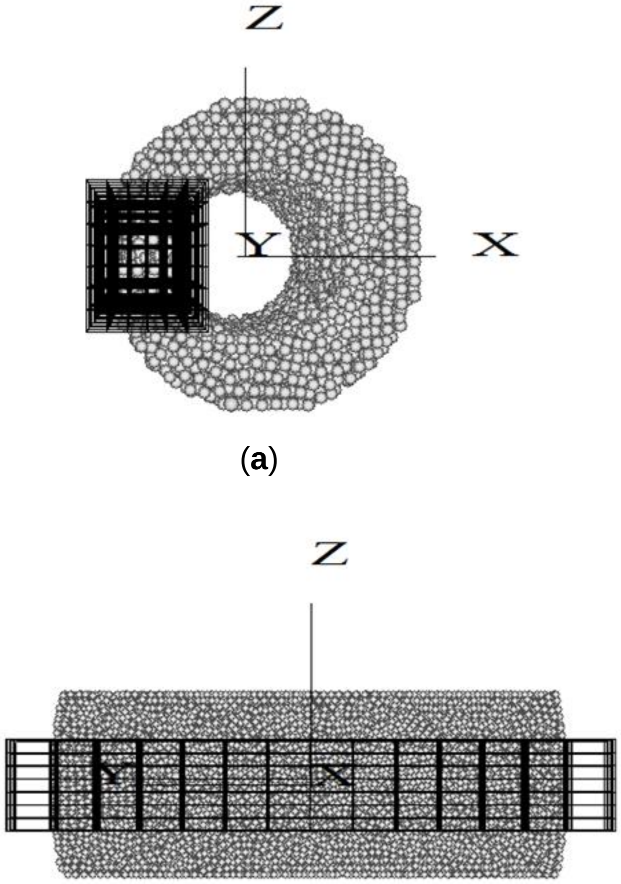

(**a**)

(**b**)

Figure 4.5 Application of the fluid cell grid around a slice of the sample, (**a**) front view, and (**b**) side view.

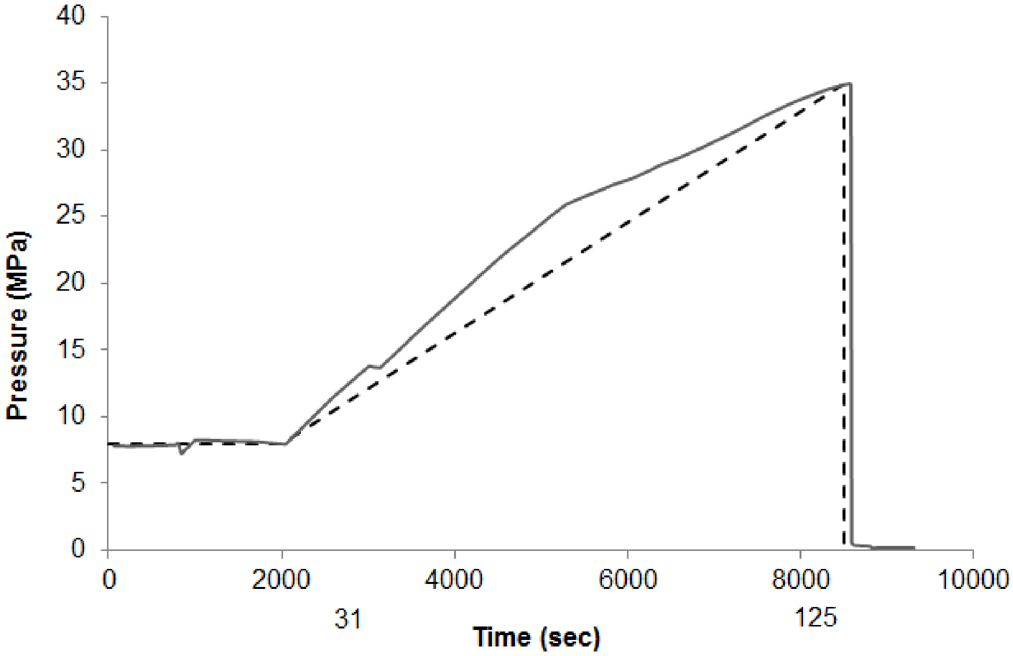

Figure 4.6 Laboratory (solid) and simulated (dashed) fluid pressure differential applied on the outer surface of the sample as a function of time.

The small timestep inherent in the PFC simulations, in order to ensure stability (typically of the order of tens of microseconds), results in impractical computational run-times when attempting to model the complete 8400 sec experiment. To alleviate this, the simulated time of the test had to be scaled down to a feasible value. The overall runtime of the shortened test is about 125 sec, with the stable pressure region spanning 31 sec (=1/4 of the total runtime) which corresponds to the 2000 sec (=1/4 of the total 8362 sec runtime) region of the physical laboratory experiment. Due to the fact that the overall time of the test has to be scaled down, the loading rate has to be scaled up in order for the physical and simulated tests to be equivalent. Thus the pressure gradient is set to 0.12 MPa/sec. Even though in reality the increase of the pressure gradient will have an effect on the overall strength of the rock, in the case of the PFC assembly the Navier-Stokes equation for incompressible fluid flow is pressure-free since there is no explicit mechanism for advancing the pressure in time. Furthermore the pressure gradient is not included in the formula, thus does not affect the behaviour of the virtual assembly. Numerical tests have been performed to confirm that this increase in the loading rate has very little influence on the material behaviour of the sample.

In order to maintain the equilibrium of the sample, the pressure increment is performed in distinct steps and this allows the sample to reach a steady state with the current pressure step before moving to the next pressure step. In order to estimate an appropriate duration for each pressure step, the model is simulated several times under different pressures (13 and 30 MPa, respectively) within the range of 8 to 33 MPa until it reaches equilibrium in terms of the flow rate. Fig.4.7 (**a**) illustrates the flow rate for constant pressure differentials of 13 MPa and 30 MPa. It can be observed that the water discharge is stable within approximately 10 seconds. Thus, 10 seconds is deemed to be a suitable time period for the sample to adjust to the applied pressure step and ensure that although there is an overall pressure built-up during the experiment, the sample retains its equilibrium satisfying the criteria for steady and uniform flow. Fig.4.7(**b**) illustrates the applied fluid pressure for the simulated test, which remains stable for the first 25 seconds and then the applied pressure is increased by 1.2 MPa every 10 seconds.

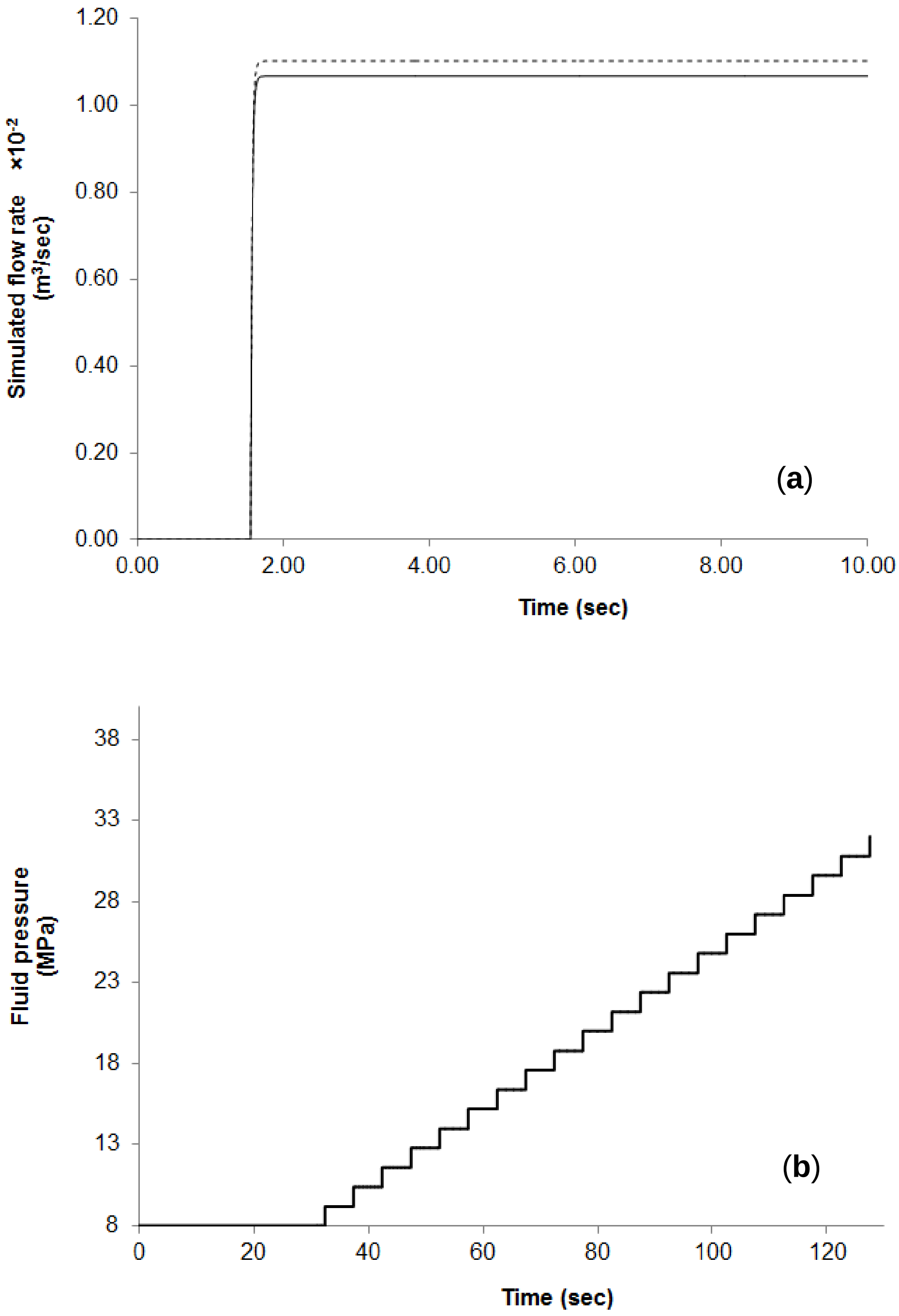

Figure 4.7 (**a**) Simulated flow rate versus time for 13 MPa (solid black) and 30 MPa (dashed) constant pressure differential between the outer and inner perimeters of the limestone assembly, and (**b**) applied fluid pressure versus time during the simulation of the single phase flow through the limestone sample. The pressure is kept at 8MPa for 25 seconds before starting to rise in steps of 1.2 MPa every 10 seconds. Sample failure occurs at 32.3 MPa.

The simulated fluid is water with a density and viscosity of 1000 kg/m^3 and 10^{-3} Pa.s, respectively. The described pressure gradient is applied to the outer side of the fluid cell grid (leftmost side as seen in Fig.4.8) whereas the pressure on the inner side of the grid (rightmost side as seen in Fig.4.8) is set to 0. Finally in order to replicate the actual laboratory experiment in PFC, the applied fluid pressure is considered uniform and thus the assumption that the fluid travels along the X axis has to be made.

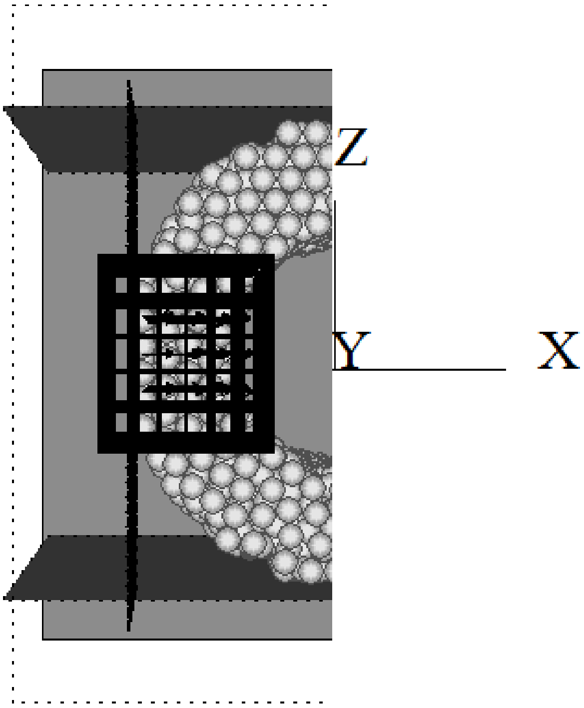

Figure 4.8 Fluid pressure boundary conditions for the PFC model under the assumption that the movement of the fluid is horizontal. The pressure on the outer perimeter of the model in constantly increased, whereas the pressure inside the cavity is zero.

4.5 Results and discussion

Fig.4.9 illustrates the results of the stress distribution in the centre of the virtual limestone slice under the applied fluid pressure differential, whereas Fig.4.10

demonstrates the stress distribution based on the analytical solution (Lame's equations). Both the tangential and radial stresses change linearly with the applied fluid pressure bringing the analytical and numerical results in good qualitative agreement. This also validates the fact that the bonded-assembly (DEM) approach, followed by the PFC software, is specifically designed to reproduce stresses-strains in microscopic media and that Lame's theory can be adequately applied. Quantitatively, the difference in the magnitude of stresses can be attributed to the fact that Lame's equations assume a continuous medium whereas the virtual model is non-continuous.

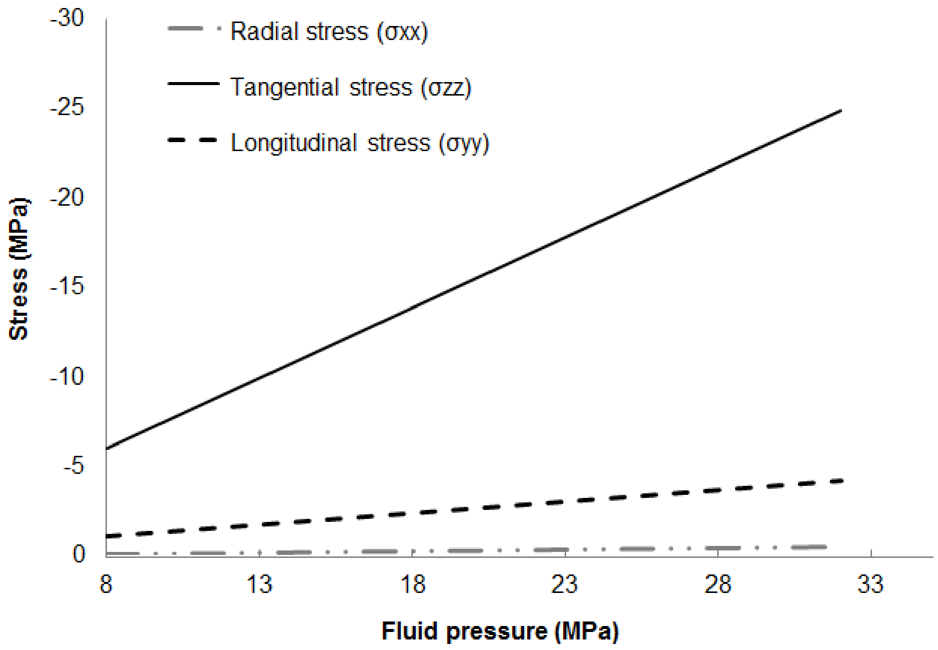

Figure 4.9 Simulated stress field at the middle of the slice (radial (σ_{xx}) dashed grey, longitudinal (σ_{yy}) dashed black, tangential (σ_{zz}) solid black) versus fluid pressure differential.

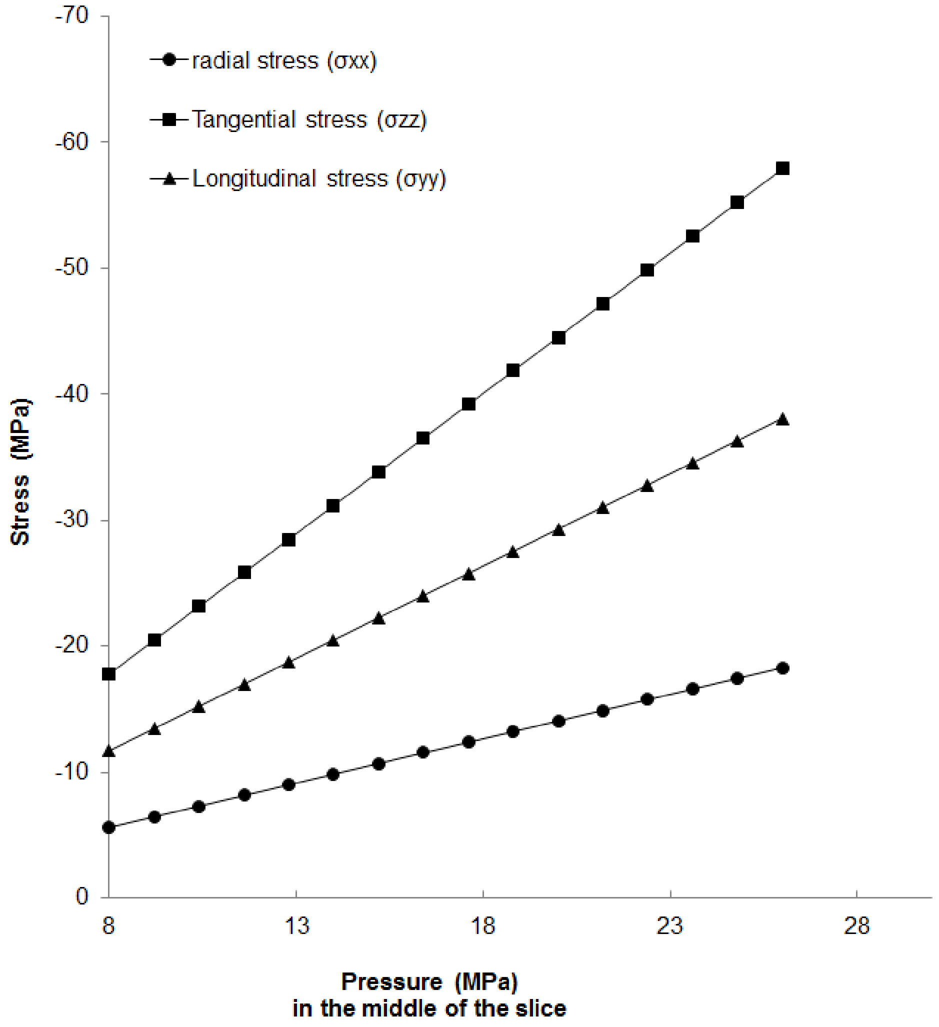

Figure 4.10 Stress field versus fluid pressure differential at the middle of the slice according to Lame's equations (radial (σ_{xx}) circle, longitudinal (σ_{yy}) triangle, tangential (σ_{zz}) square).

A micro-crack in the PFC3D sample is the subsequent bond breakage between two bonded particles. Thus the number and position of the possible micro-cracks are limited by the number and position of the parallel bonds in the virtual sample. The shape of each micro-crack is cylindrical, whose axis is located alongside the line connecting the two neighbourhood particles. The parameters that define each micro-crack are its thickness (t_c), radius (R_c) and centroid location. The thickness is the distance between the two neighbourhood particles, the radius is the intersection between the cylinder's bisection plane and a stretched membrane among two neighbourhood particles and the centroid is the centre of the bond and is located in the middle of the line formed by the centres of the two neighbourhood particles (Fig. 4.11). Figures 4.12 and 4.13 demonstrate the fracturing process of the virtual assembly at different stages under the gradual increase of the fluid pressure differential resulting to its total collapse, and the development of the micro-cracks versus the applied fluid pressure.

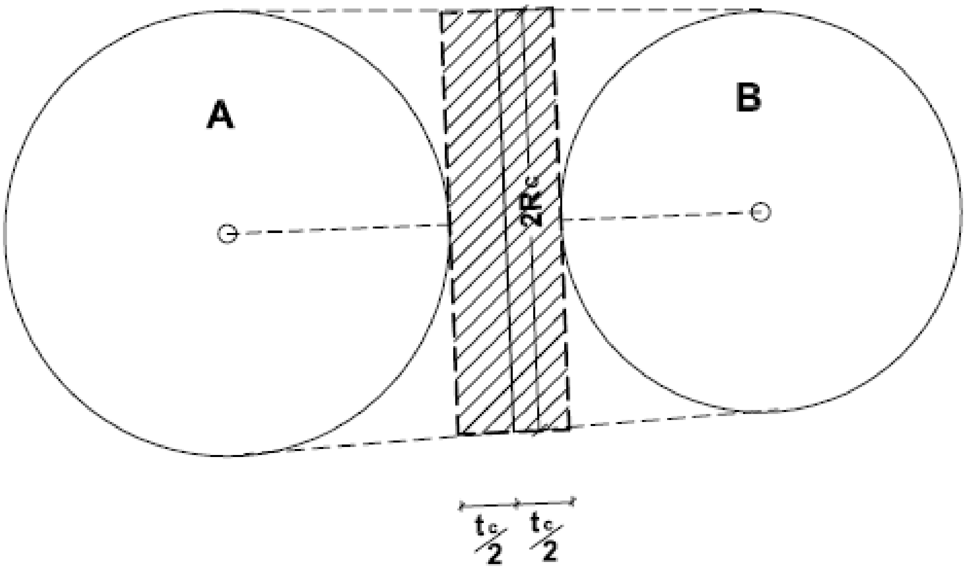

Figure 4.11 Schematic of the geometry and location of each micro-crack (Itasca-Consulting-Group, 2008b).

A micro-crack can occur either in the perpendicular (normal) or shear direction with respect to the bond plane. It was found that there were 5000 micro-cracks formed inside the rectangular slice with 3512 of them in the normal direction and 1493 in the shear direction.

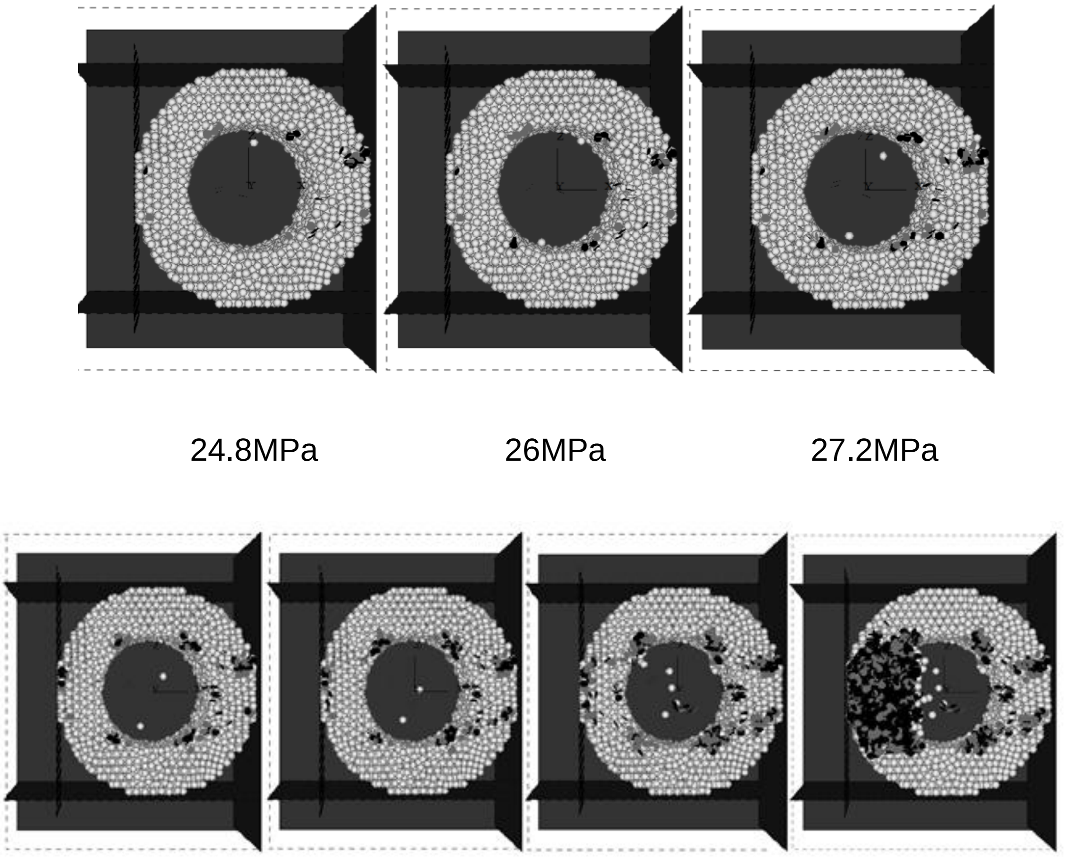

24.8MPa 26MPa 27.2MPa

28.4MPa 29.6MPa 30.8MPa 32.3MPa

Figure 4.12 Initiation and propagation of micro-cracks of the virtual assembly at different stages.

It can be observed that even though failure forms early at the outside perimeter of the sample, it propagates in a lower rate compared to the crack propagation of the inner surface. The latter begins from the vicinity of the inner surface at approximate 26 MPa pressure differential and expands outwards as a result of the stress distribution, leading to sample failure at 32.3 MPa where the particles are detached and are forced towards the inside of the cavity.

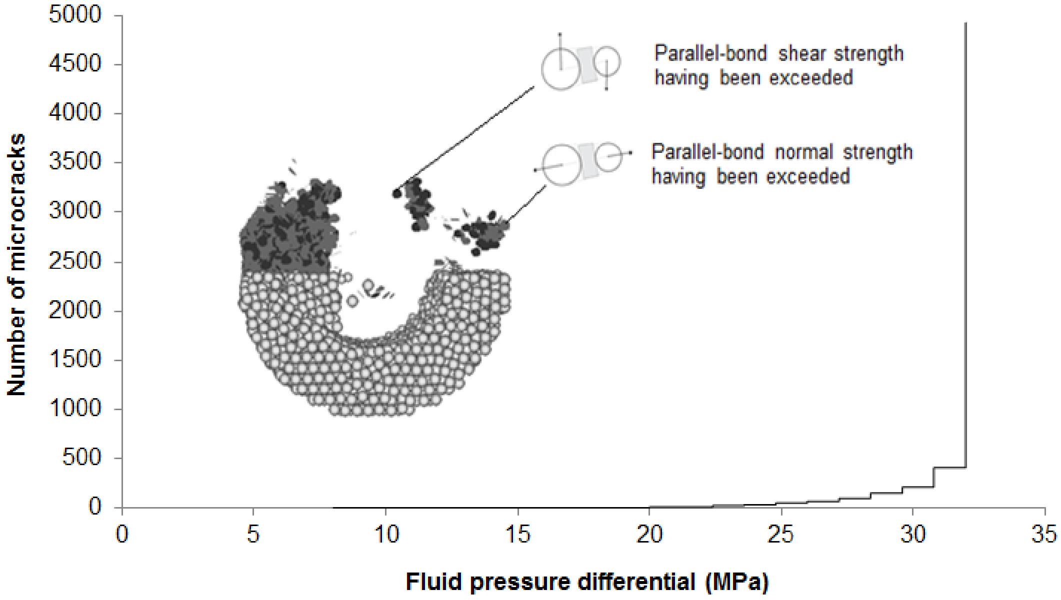

Figure 4.13 Total number of micro-cracks versus the applied fluid pressure differential (the black dots indicate the parallel-bond breakage in the shear direction, whereas the grey dots indicate the parallel-bond breakage in the normal direction).

This is in very good agreement with the failure point of about 35MPa measured during the laboratory experiment and close to the material's UCS strength (wall-based measurement – 45 MPa) measured by the Uniaxial test. The fracturing pattern is dominated by the shear and compressive stresses forming a total of 5000 micro-cracks at the failure point.

The failure mode is also in agreement with Lame's theory, indicating that all the principal stresses are compressive and even though the highest radial compressive stress occurs at the outer surface, which is the same as the applied fluid pressure mode, the maximum compressive stresses are tangential, and act in the vicinity of the inner diameter (Eq.(2.15)). Thus, relatively, compressive stresses are high towards the inner surface. The longitudinal stress remains almost constant acting in the axial direction and the shear stress is maximum at the inner surface. The theoretical explanation of this is illustrated in Fig.4.14

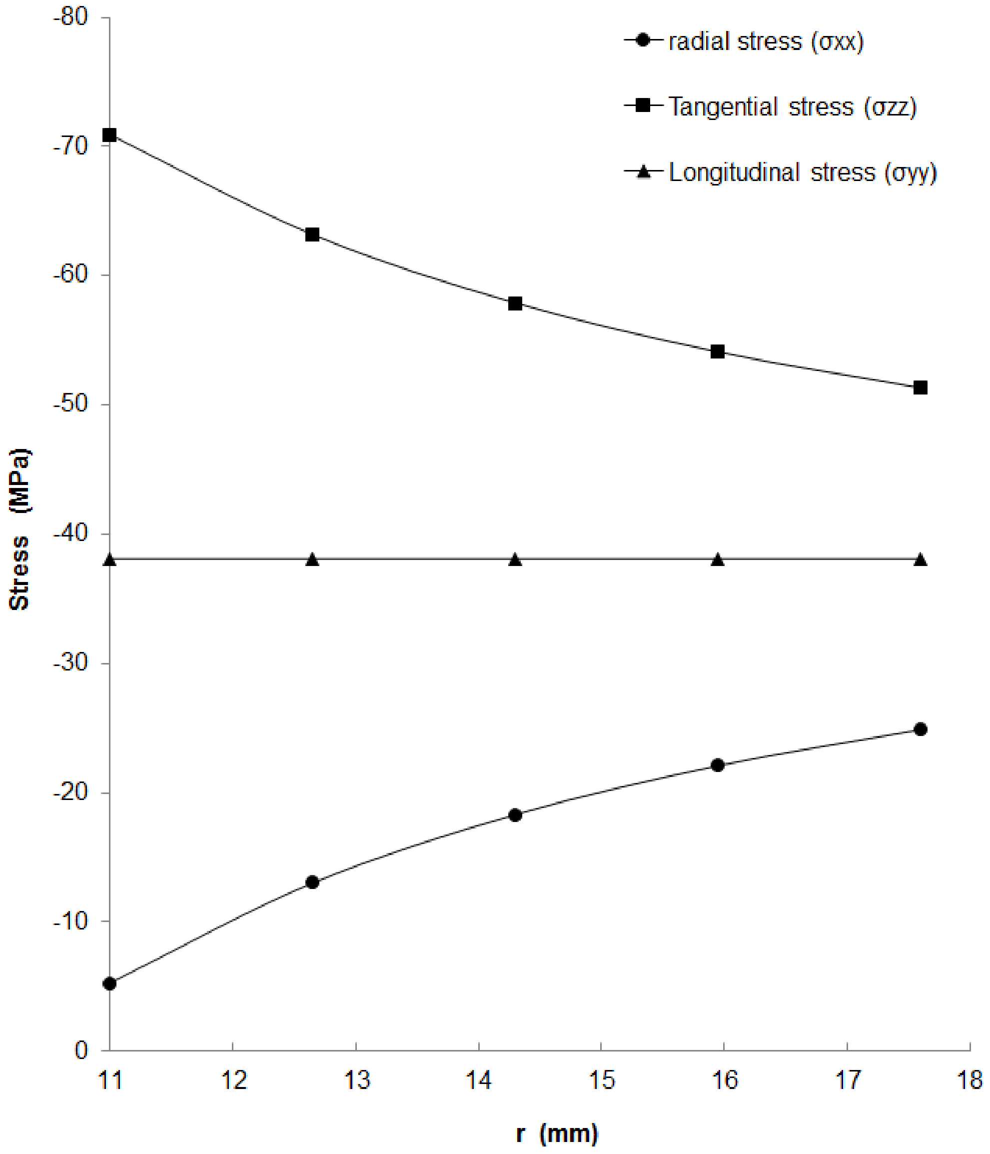

Figure 4.14 Variation of the stress field along the wall thickness according to Lame’s equations (radial (σ_{xx}) circle, longitudinal (σ_{yy}) triangle, tangential (σ_{zz}) square).

Figure 4.15 demonstrates the resulting flow rates of the water, from all the calculations methods, through the virtual rectangular slice of the assembly during the simulated test. According to the Figure, as soon as the fluid starts to penetrate the sample then a small flow rate is recorded which remains stable during the steady pressure regime (0-25 sec). As the pressure gradient is varied (25-125 sec), the simulated flow rate increases gradually, reaching 0.035 m^3/s after 125 sec. It can be observed that for the steady pressure regime both the simulated flow rate and the analytical flow rates (Darcy and Steady state solution) are in very good agreement.

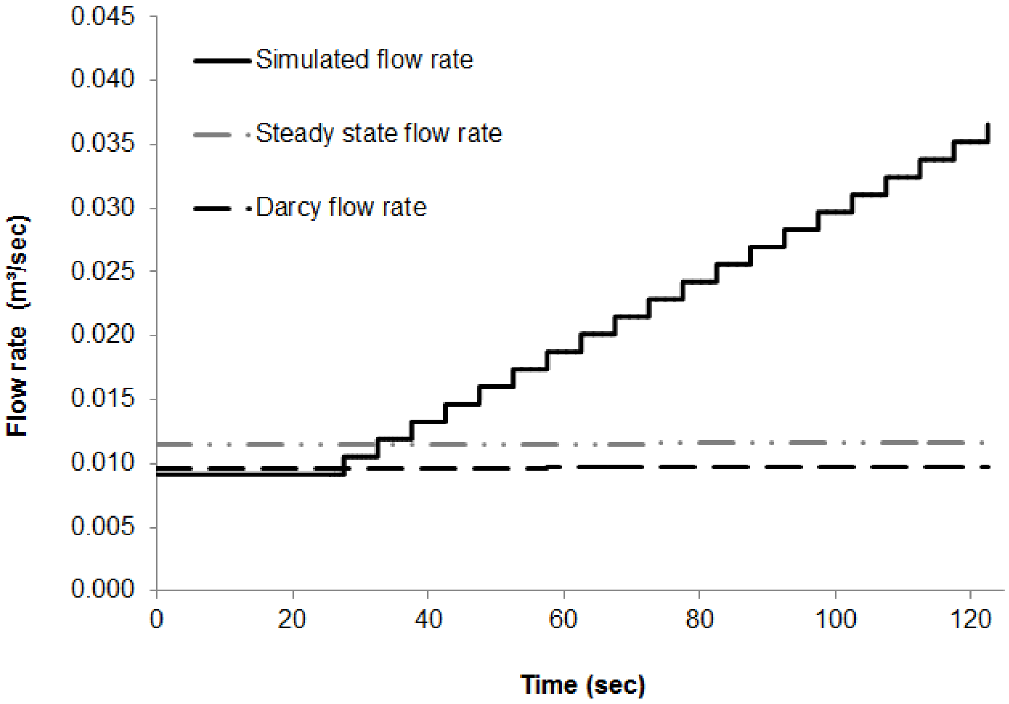

Figure 4.15 Simulated flow rate of the water through the virtual rectangular slice of the assembly versus time.

Table 4-1 summarizes the results obtained from the fluid flow fracturing test during the steady pressure regime on the rectangular limestone slice. It is clear that all three different flow rates are in very good agreement in the steady pressure regime. According to the results, the simulated flow rate is closer to Darcy's flow rate than to the steady-state flow. This can be attributed to the fact that the steady-state solution is referred to as an idealised flow assuming that the pressure gradient and particle drag forces due to fluid flow are much greater than the viscous losses. This is due to the assumptions made that relate the viscous losses to the macroscopic fluid velocity. The steady-state solution assumes uniformity in the velocity gradient and this results in an underestimation of the losses due to the viscous stresses. However, the values of the steady-state flow rate and the simulated flow rate indicate that the disparity between them is negligible.

Table 4-2 Summary of the hydraulic fracturing simulation.

Fluid flow results for the first 25sec	
Number of cracks	5000 (3512 normal, 1493 shear)
Permeability (m^2)	6.68×10^{-9}
Darcy flow rate (m^3/s)	0.096×10^{-2}
Steady-state flow rate (m^3/s)	0.0115×10^{-2}
Simulated flow rate (m^3/s)	0.091×10^{-2}

In conclusion Chapter 4 has presented the DEM computational modelling of the hydraulic fracturing test for a limestone sample with a hollow core. The mechanical response of the rock specimen to the fluid injection is analysed by evaluating the volumetric flow rate at which the fluid is discharged, the initiation and propagation of cracks through the simulated model and the relation between its UCS strength and the failure pressure. In the PFC, a generalised form of the Navier-Stokes equation (Eq.(2.21)) that accounts for fluid-solid interactions is solved using a grid fluid flow scheme. These formulations have been adapted herein by firstly, incorporating this technique into the DEM simulation of a bonded particle assembly representing an intact material. Secondly, an extension of its applicability is demonstrated via the modelling of hollow-cylinder laboratory test. Applications of this type, where direct numerical and experimental comparisons were performed, are still lacking.

Both the simulated model and the physical limestone have been illustrated to behave in a similar manner. The fluid flow results were found to be in very good agreement with the laboratory observations, in terms of the fracture pattern and the geo-mechanical behaviour, thus showing that the sample fails under 32.3 MPa pressure differential, and this is very close to the failure point measured during the laboratory test (35 MPa) and close to the UCS strength of the sample (45 MPa).

The simulated hollow-cylinder fluid flow test, along with the simplified version of a horizontal fluid flow injection test, is presented in the following Chapters, comprise two of the most representative examples of engineering applications in industry.

The complete coding file that describes the hydraulic fracturing simulation of the hollow cylinder can be found in Appendix II.

Chapter 5 The DEM analysis of hydraulic fracturing in hard rocks under horizontal fluid injection

5.1 Introduction

This Chapter presents a series of solid - fluid coupled simulations of a natural fractured limestone sample. The fluid is injected into one end of the PFC sample, thus simulating a simplified version of an on-site horizontal injection operation, and the flow rate is gradually increased. The aim of this work is to investigate the influence of the fluid injection on its mechanical behaviour at the particle – scale and the effect of various parameters, such as pre-existing fractures, external stress regime and fluids with different viscosity, to the overall behaviour of the PFC model. A detailed study of the influence of the fluid flow on the micro structure of the virtual model, including its internal stress state, the fracture initialisation and propagation, and also the interactions between the existing fracturing networks and the new hydraulically induced fractures, has been performed.

5.2 Rock specimens with pre-existing fractures and simulation conditions

The PFC limestone model, utilised for the following series of tests, is the LIM1 sample and the complete set of its micro-properties has been illustrated in Table 5-1. The discontinuity caused by the pre-existing internal fractures may result in imbalance within the sample as the test progresses. Therefore, preliminary tests were required in order to diagnose the state of the model at the end of each rate change.

Table 5-1 The PFC micro-parameters employed for the hydraulic fracturing simulated tests on the LIM1 model.

Micro-parameters that define the sample	Sample width (mm)	40
	Sample length (mm)	60
	Sample depth (mm)	40
	Sample porosity (%)	15
	Initial friction of balls	5.5°
	Gravity (m/s^2)	9.81
Micro-parameters that define the particles	Ball radius (mm)	0.85
	Ball density (kg/m^3)	2600
	Young’s modulus (GPa)	30
	Ball stiffness ratio	1.0
	Required isotropic stress (MPa)	0.4
Micro-parameters that define the parallel bonds	Radius multiplier	1.0
	Young’s modulus (GPa)	20
	Normal/Shear stiffness ratio (Pa/m)	1.4
	Normal strength (MPa)	30
	Std. deviation of normal strength	30×10^4
	Shear strength (MPa)	39
	Std. deviation of shear strength	30×10^4

It was concluded that 3000 mechanical cycles were sufficient for the pressure disturbance to be transmitted throughout the sample in all test conditions. During these tests the algebraic sum of the forces acting between the particles and walls is almost zero, meaning that the forces acting on each particle are almost in balance. Fig.5.1 illustrates the mean unbalanced force versus the injection rate for all cases of pre-cracked samples (described in chapter 5.2.1), where abrupt jumps are recorded due to the rate gradient and then reaching zero every 3000cycles.

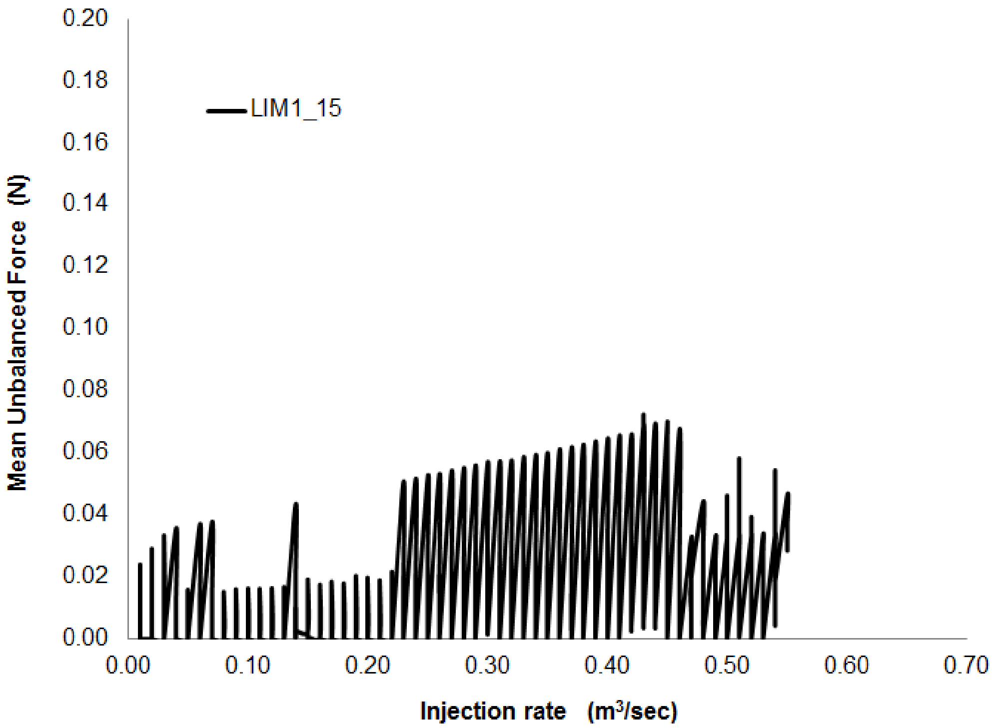
LIM1_15
Mean Unbalanced Force (N)
0.20
0.18
0.16
0.14
0.12
0.10
0.08
0.06
0.04
0.02
0.00
0.00
0.10
0.20
0.30
0.40
0.50
0.60
0.70
Injection rate (m³/sec)

(a)

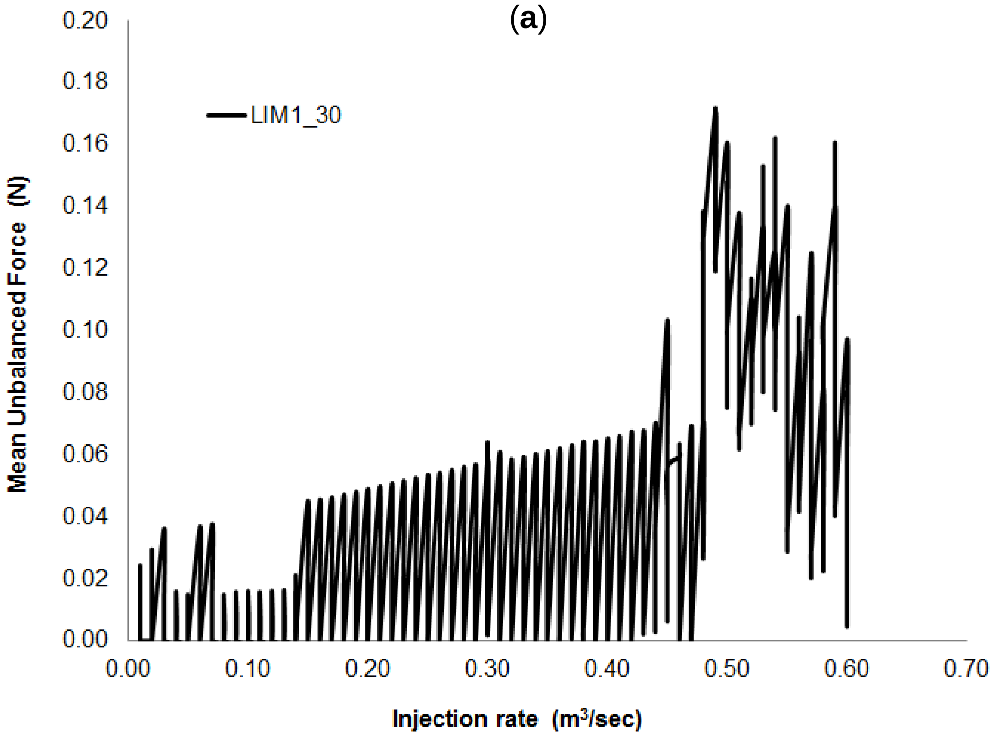
LIM1_30
Mean Unbalanced Force (N)
0.20
0.18
0.16
0.14
0.12
0.10
0.08
0.06
0.04
0.02
0.00
0.00
0.10
0.20
0.30
0.40
0.50
0.60
0.70
Injection rate (m³/sec)

(b)

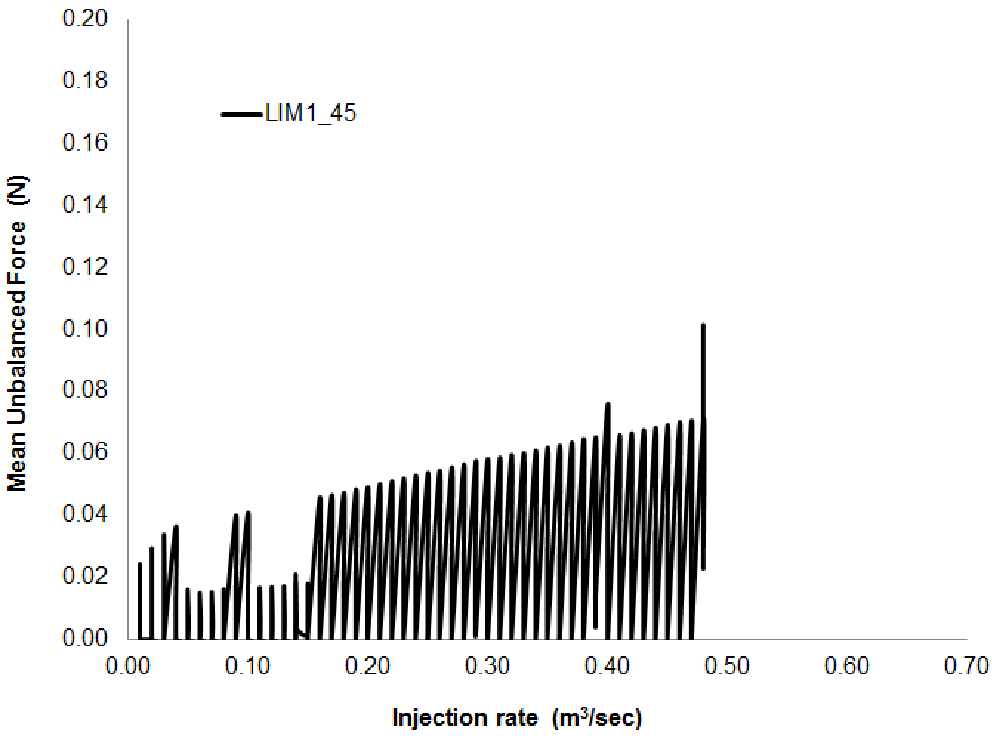
0.20
0.18
0.16
0.14
0.12
0.10
0.08
0.06
0.04
0.02
0.00
LIM1_45
Mean Unbalanced Force (N)
0.00
0.10
0.20
0.30
0.40
0.50
0.60
0.70
Injection rate (m³/sec)

(c)

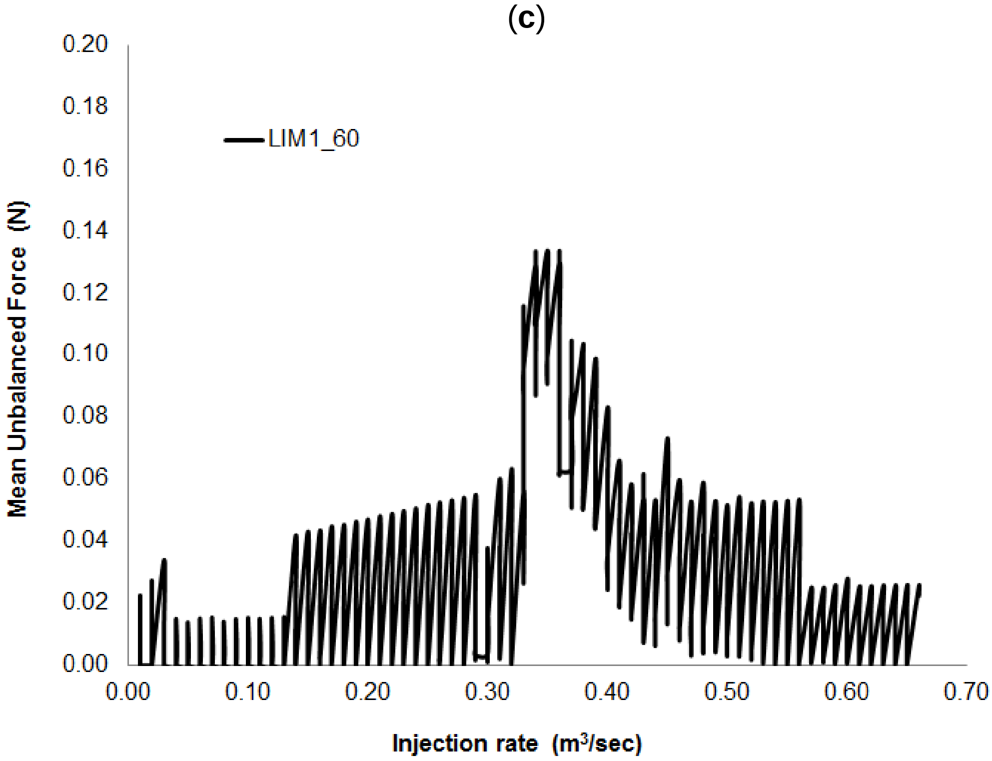
0.20
0.18
0.16
0.14
0.12
0.10
0.08
0.06
0.04
0.02
0.00
LIM1_60
Mean Unbalanced Force (N)
0.00
0.10
0.20
0.30
0.40
0.50
0.60
0.70
Injection rate (m³/sec)

(d)

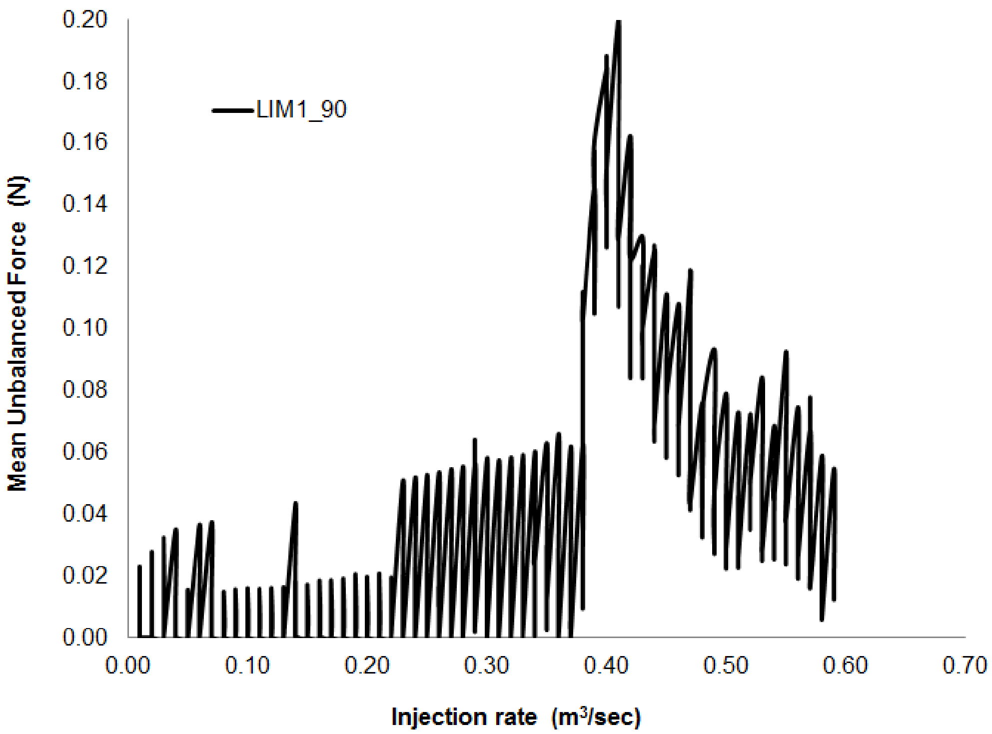

(**e**)

Figure 5.1 Progress of the mean unbalanced force versus injection rate for the (**a**)-(**e**) LIM1_15º to LIM1_90º, respectively. The force reaches a peak value and then drops to zero reaching equilibrium.

It can be observed that the mean unbalanced force (MUF) exhibits a pattern of peaks at the points where the injection rate increases, followed by a drop close to zero indicating that the sample has reached equilibrium after each injection-rate step has been applied. This is especially evident in samples LIM1_15º and LIM1_45º (their names indicate the angle of the induced fracture within the model) where the cracking behaviour is observed to be similar (Fig.5.2(**a**)). More specifically, they are observed to crack gradually, whereas for the LIM1_30º, LIM1_60º and LIM1_90º samples, there is a critical injection rate (0.49 m^3/s, 0.33 m^3/s and 0.39 m^3/s, respectively) followed by sudden and large increases in microcracking (Fig.5.2(**b**)). In these regions equilibrium is not always achieved between injection-rate steps and therefore the respective graphs of MUF demonstrate imbalance. This behaviour can be expected due to the sudden release of energy within the sample during cracking and does not pose a mechanical stability problem for the simulation.

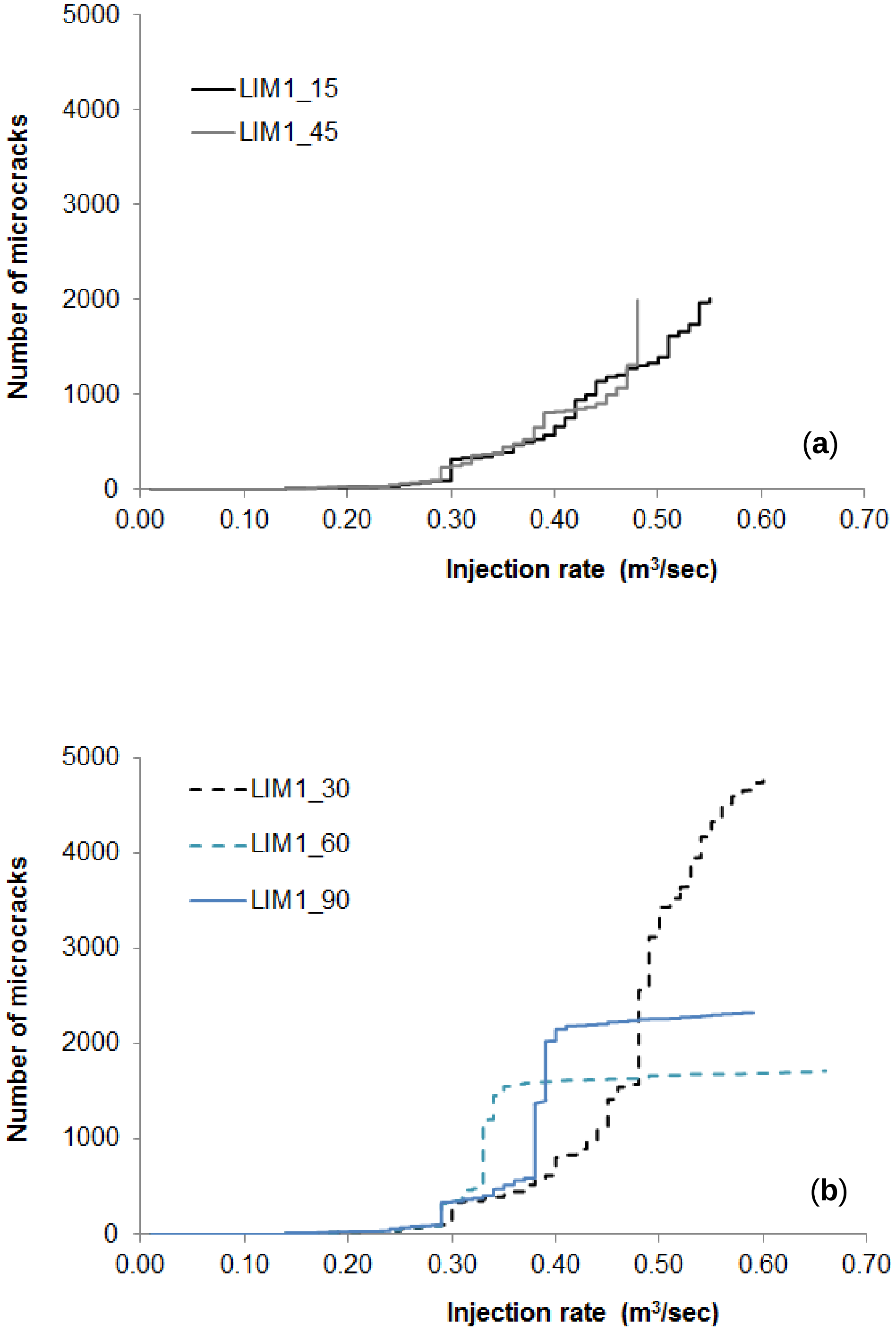

Figure 5.2 Total number of microcracks versus the injection rate for the LIM1_15°, LIM1_45° (**a**) and LIM1_30°, LIM1_60°, LIM1_90° (**b**) samples.

5.2.1 Orientation of individual pre-existing fractures & external stress regime

The virtual assembly has dimensions 60mm length, 40mm width and 40mm depth. Although there are no guidelines, the dimensions are carefully chosen so that the sample is large enough to enhance the fracking process while also being efficient in terms of simulation. It comprises of 31540 particles of uniform size and a pre-existing inclined fracture that is 15mm long at an angle increments of 15^{o} up to 90^{o} with respect to the horizontal (Fig.5.3(**a**),(**b**)). The fractures are created by deleting the particles and their bonds that are included in the inclined region of the fracture. The combination between the overall dimensions and the particle size determines the design of the model. More specifically, the angle 15^{0} is the smallest distinguishable angle for the particular particle size of the model. The test is repeated five times for each different inclined fracture. For brevity, the samples for the simulated fluid test are named LIM1_15^{o} to LIM1_90^{o} and the fluid injection well is replicated at the centre of the right hand side of the model. Finally, when the micro-cracks reach the hollow core of the inclined fracture, the test is terminated. Preliminary tests showed that the 2000 micro-cracks were considered sufficient in terms of propagation in order to be sufficiently far from the injection point and reach the inclined fracture.

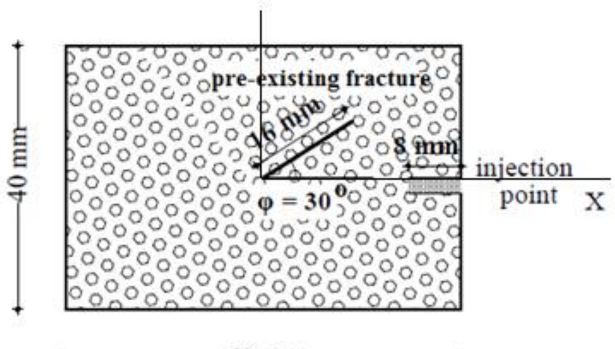

(**a**)

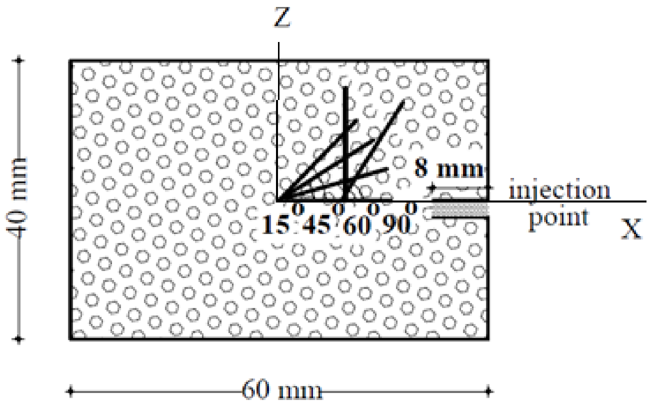

(**b**)

Figure 5.3 Schematics of (**a**) the geometry of the pre-existing fracture of the LIM1 assembly under the angle of 30°, and (**b**) the geometry of all the induced cracks under the angle of 15°, 45°, 60°and 90°. The coordinates of the fractures of 60° and 90° were chosen closer to the injection point to aid simulation time.

A fluid coupling algorithm, based on the Navier-Stokes equations for porous media (see Chapter 2), has been employed for this investigation as a function that has already been developed by the Itasca Consulting Group, (2008d). The fluid-flow logic can be considered as a two way coupling as the fluid injection has altered the structure of the rock (in terms of particle movement and fractures at the micro-level) and the fracturing has also altered the path of the fluid flow.

The aim of the test is to investigate the injection of a fluid flow into one end of a virtual rock sample, thus simulating an on-site horizontal injection well, and the creation of a pressure built-up until the internal stress state of the assembly is tense enough to initiate micro-cracks which will interact with the existing fractures. The progress of the fracture propagation is monitored in terms of broken parallel-bonds under the influence of the fluid. The breakage of the bonds is recorded as either tensile or shear cracks with respect to the bond plane. The virtual sample is enclosed within solid boundary walls in order to replicate the actual conditions, where underground rocks are naturally pressurized from the surroundings for reasons such as the depth of overburden, the interactions between tectonic plates or the topography in general. The walls are continuously moving in order to apply a constant confinement that simulates an example of an actual stress regime (Fig.5.4). The first simulation used the following pattern: the stress in the Z direction (vertical) is the principal stress (σ_{zz}=1.5 MPa) followed by the stress in the X direction (σ_{xx}=1 MPa) (same as the direction of the fluid flow) and the stress in the Y direction (σ_{yy}=0.5 MPa).

Two more simulations were performed with different confinements in order to investigate the effect of the external stress to the fracking mechanism. The values of the stresses for each simulation are as follows:

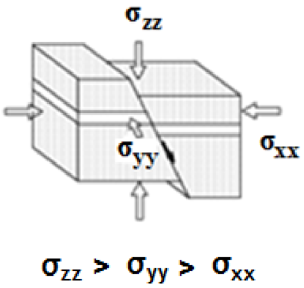

Figure 5.4 Example of an actual stress regime utilised for the first simulation.

(i) σ_{zz}=1.5 MPa, σ_{yy}=1 MPa, σ_{xx}=0.5 MPa for the first stress regime

(ii) σ_{xx}=1.5 MPa, σ_{yy}=1 MPa, σ_{zz}=0.5 MPa for the second stress regime

(iii) σ_{yy}=1.5 MPa, σ_{zz}=1 MPa, σ_{xx}=0.5 MPa for the third stress regime

For brevity, the models for this set of simulations are named LIM1_stress$_1$, LIM1_stress$_2$ and LIM1_stress$_3$ corresponding to each stress regime, respectively. The tests are terminated after a significant expansion of the damage (around 3500 micro-cracks) is achieved. Fig.5.5 demonstrates the aforementioned types of stress regimes.

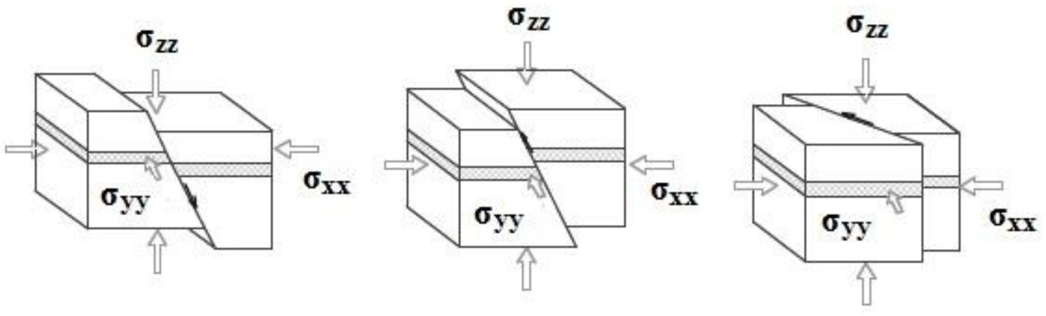

(**regime**$_1$) (**regime**$_2$) (**regime**$_3$)

Figure 5.5 The three types of external stress regimes used for the tests.

Next a fluid cell grid is applied to perform the fluid analysis (Fig.5.6). Only a part of the sample is surrounded by the fluid cells (45×40×40 mm), leaving enough space for the fluid to exit and still be within the rock. The purpose of the *partial* fluid grid is to replicate and comply with reality as close as possible, where the output of the fluid will still be inside the formation. The parameters and the dimensions which define the grid has been discussed in Chapter 4.3. The size of the cells is considered based on the allowable volume of particles so that the results will not be sensitive to the size. A sensitivity analysis showed that for the specific particle size (0.85 mm), a grid between 800 and 1200 cells provide similar results and therefore 1000 cells are created, each with a cell size of 5.625×5.0×5.0 mm. The simulated fluid for these tests is water with a density and viscosity of 1000kg/m^3 and 10^{-3}Pa.s, respectively.

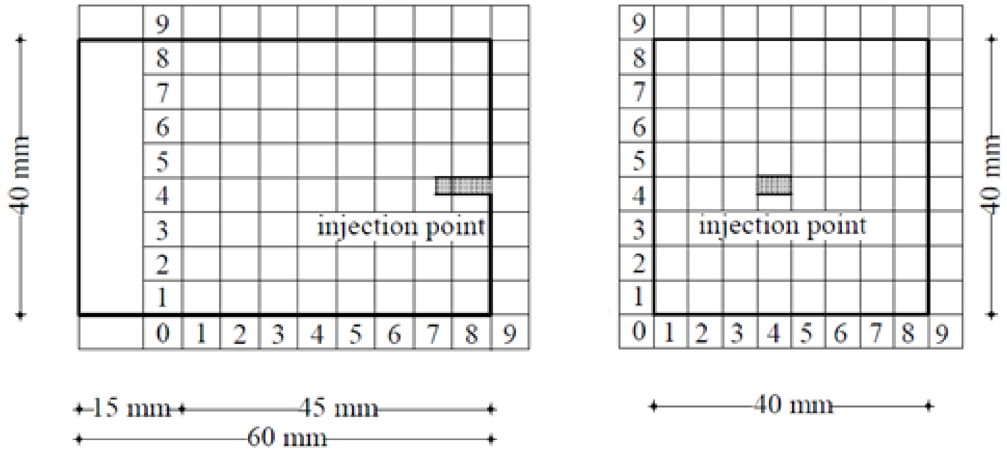

Figure 5.6 Fluid cell grid used in the PFC 3D in the xz and xy planes, respectively, for the fluid analysis.

The injection is invoked through a single cell (centre right hand-side of the fluid cell grid) with an initial rate of 9×10^{-6} m^3/sec and it is gradually increased with a gradient of 1×10^{-2} m^3/sec. This type of simulations is time consuming and the purpose of using a pressure gradient is to keep the simulations within an efficient timeframe by accelerating the fracking process. Given the available resources and the sample dimensions, injection pressure gradients were selected appropriately so as to lead to a feasible model in terms of simulation time. A preliminary study showed that in order for the test to be performed within a reasonable timeframe, a gradient within the range of 10^{-2}-10^{-3} had to be applied with no significant difference between the boundary values. Furthermore, convergence tests showed that even though a relatively high gradient has been used, the overall mechanical response on the virtual assembly is not significantly affected in order to compromise the results. The injection rate at the end of the test is measured to be between 0.50-0.79 m^3/sec for all pre-cracked samples.

5.2.2 Pre-existing fracture network

Another set of simulations is performed in order to investigate the effect of a network of pre-existing fractures, within the rock model, to the new hydraulically induced fractures and the overall behaviour of the material itself. For this set of tests, the aforementioned PFC sample(LIM1) is employed, containing a single inclined fracture of 20^o for the first simulation (Fig.5.7(**a**)) and a network of four inclined fractures of 20^o, for the second simulation (Fig.5.7(**b**)).

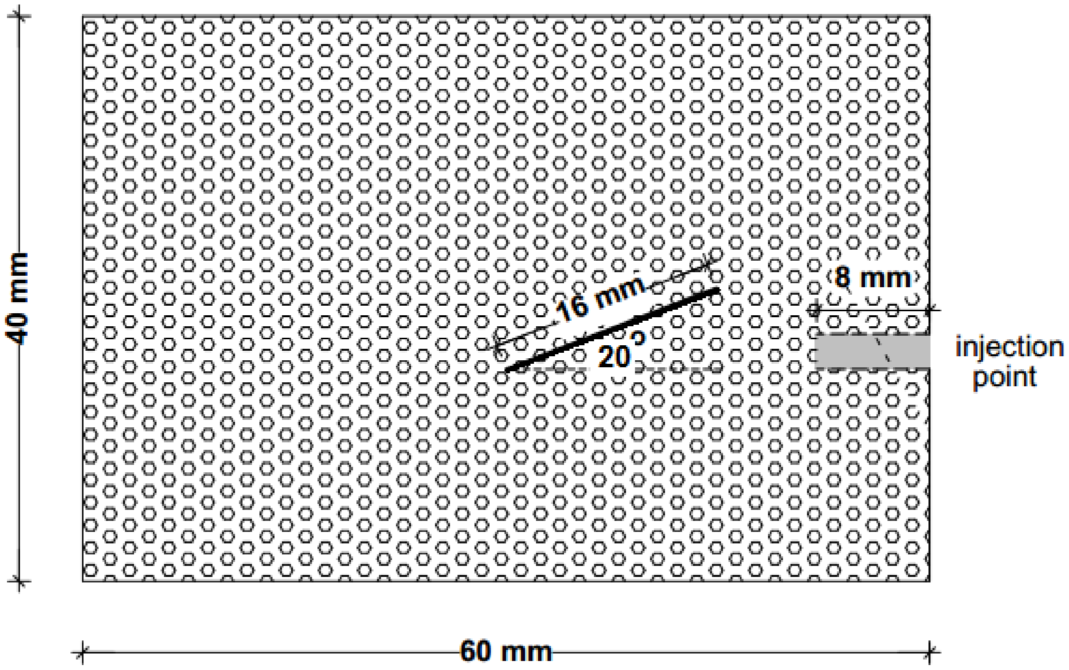

(**a**)

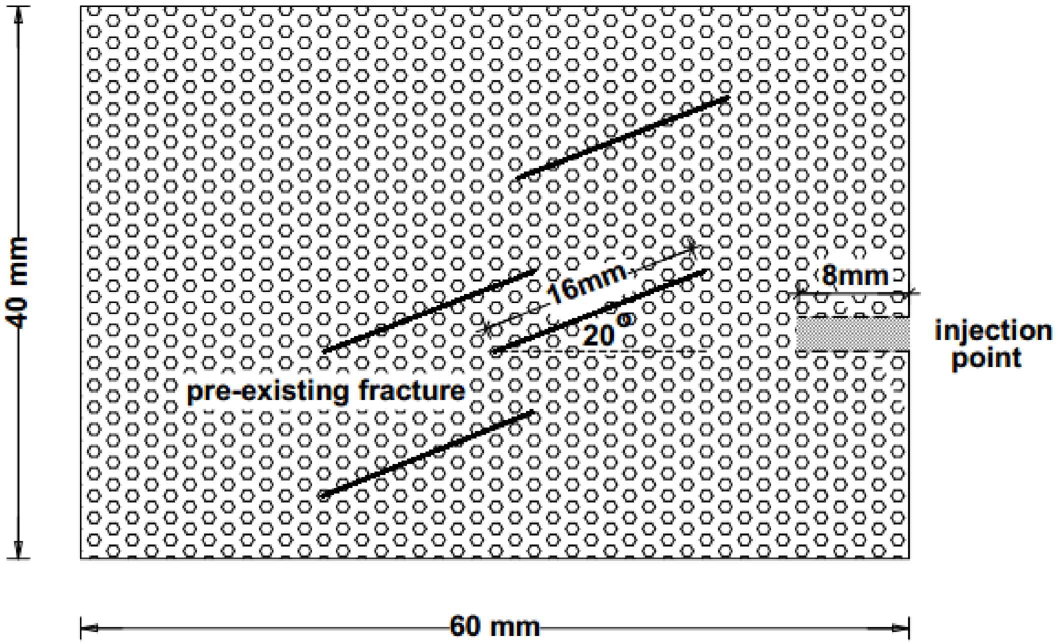

(**b**)

Figure 5.7 Schematics of (**a**) the geometry of the single natural fracture of the LIM1_ $frac_1$ model with a 20° angle and (**b**) the geometry of the multiple natural fractures of the LIM1_$frac_2$ model with 20° angles.

For brevity the samples are named LIM1_$frac_1$ and LIM1_$frac_2$, corresponding to the models with the single 20° and multiple 20° fractures, respectively. The size of the fractures is chosen according to the overall size of the model and their location is random, mimicking a real rock. The virtual model is a simplified version of a real rock that contains fractures with random orientation and size. Due to the fact that this is the first attempt to model and numerically analyse in three dimensions a pre-cracked hard rock with multiple discontinuities, it was considered prudent to begin with a less complex design. The test is terminated after a significant microcracking is reached (7000 micro-cracks) in order to be able to interact with the pre-existing fractures.

5.2.3 Injection of fluids

Another set of simulated tests is performed, changing the fluid that is used for the fracturing process in order to investigate the influence of the fluid viscosity. The aforementioned PFC model with a single 15° fracture (Fig.5.8) is employed for two fluid flow tests injecting water for the first simulation and the use of a more viscous fluid for the second simulation.

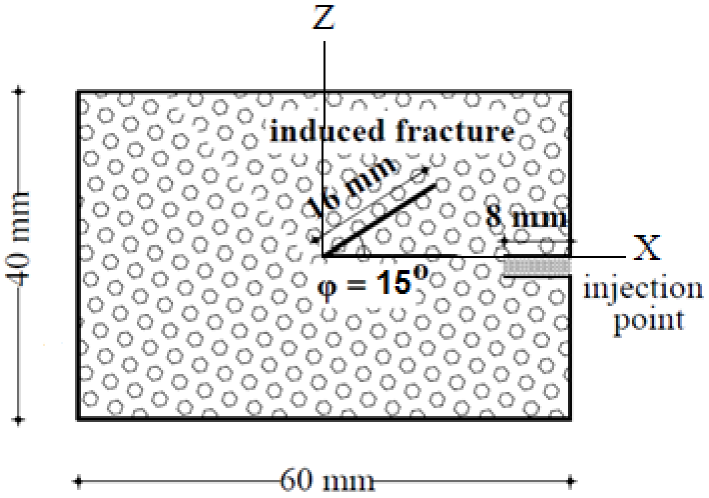

Figure 5.8 Geometry of the PFC assembly used for the simulations, including the low & high viscosity fluid (2 tests).

The horizontal injection is invoked with an initial rate of 9×10^{-6} m^3/sec and it is gradually increased with a gradient of 1×10^{-2} m^3/sec. The selection of the specific values follow the concept of an efficient simulation timeframe as previously discussed (Chapter 5.2.1). The viscosity of water is 10^{-3} Pa.s and thus it is considered a low viscosity fluid, whereas the viscosity of the latter is 0.1Pa.s and therefore considered high viscosity fluid. In the latter case, the use of the same rate gradient (1×10^{-2} m^3/sec), as the one used for water, causes the complete failure of the sample from the start of the simulation. Fig.5.9 clearly illustrates the abrupt development of microcracks as the viscous fluid penetrates the sample, indicating its total damage. In order to produce a meaningful simulation, the injection rate was reduced to 1×10^{-4} m^3/sec. For this set of tests, the termination required a significant expansion of the damage and the development of about 3000 micro-cracks. For brevity, the samples are named LIM1_fluid$_1$ and LIM1_fluid$_2$, corresponding to the low and high viscosity fluids, respectively.

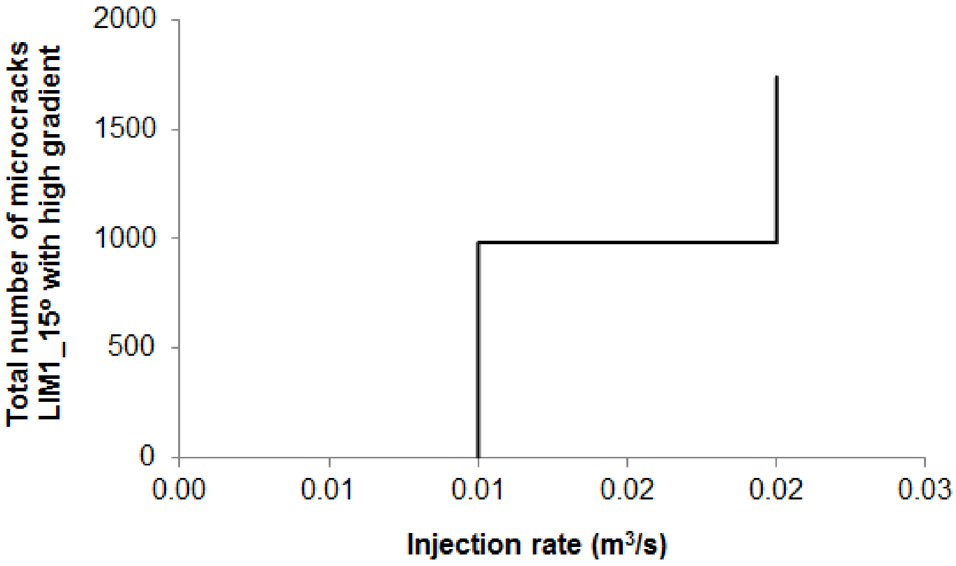

Figure 5.9 Microcracking versus injection rate for the LIM1_15° sample with the use of the more viscous fluid and high injection rate: 1×10^{-2} m^3/sec.

5.3 Results and discussion

5.3.1 Effect of the orientation of individual pre-existing fractures

Fig.5.10(**a,b**) illustrates the resulting injection pressure versus the injection rate for the LIM1_15°, LIM1_30°, LIM1_45° , LIM1_60° and LIM1_90° samples, respectively, as well as the total number of micro-cracks until the termination of the test. It can be observed that the cracks start to generate at around 3×10^{16}Pa pressure for all cases, a reasonable outcome since the reference point is almost the same for all samples (right-hand side of inclined fracture see Fig.5.3(**b**)). However it is interesting to note that the pressure that corresponds to the 2000 micro-cracks, and the end of the first set of tests (namely P_f), is being reduced for fractures below 45^o taking a maximum value of about 3.27×10^{18} Pa (when the angle is 15^o). The reversed behaviour has been observed for angles 45^o and upwards, marking the 45^o as a critical one. The additional injection required for shallow angles, can be attributed to the fact that the low angle is close to zero and thus can be considered horizontal, opposing to the horizontal fluid movement.

The observed high injection pressures during the investigation, act only as a medium to facilitate fracturing in a hydraulic manner, develop a simulation-time efficient model and are not strictly applicable in real applications, although it is not uncommon for similar studies (Martinez, 2012). Moreover, the aim of this work is to study the generation and microcracking patterns of a rock assembly and not to draw conclusions based on the injection pressure values for real-world applications. Furthermore, it can be observed that there are regions, within the sample’s matrix, with sudden increase of cracks (R1-R6) indicating brittle material behaviour in terms of crack generation/ propagation. More specifically for angles above the 45^o, the material demonstrates more aggressive behaviour in terms of fracking (Fig.5.10(**b**)) as soon as the fluid reaches the hollow zone within the fracture. This boosts the fluid velocity resulting in cumulating fracking.

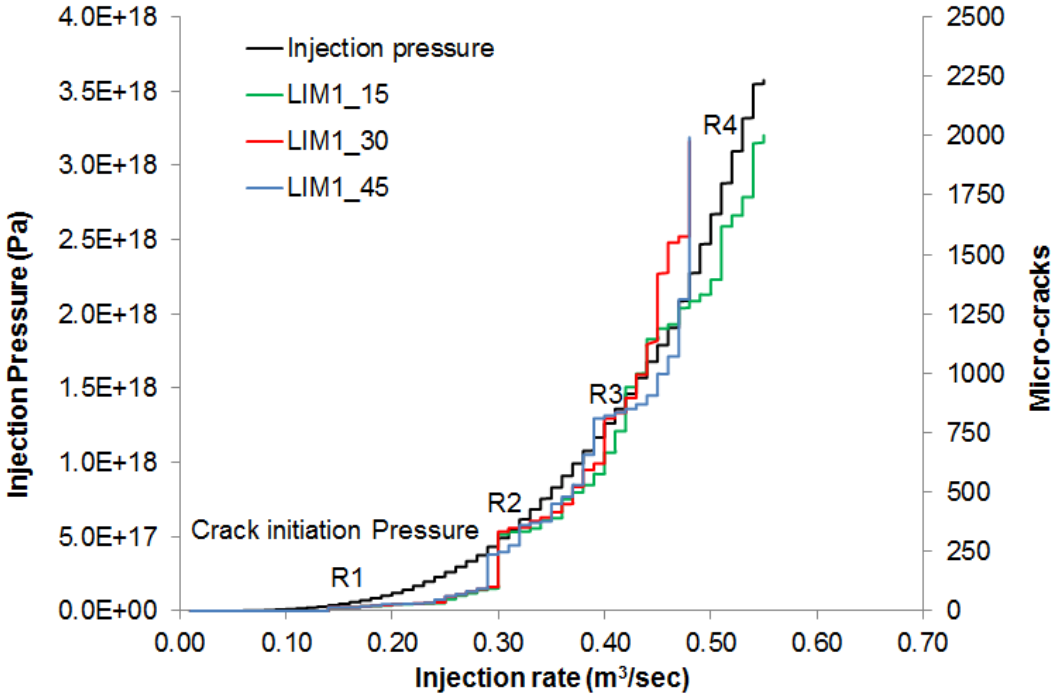

(**a**)

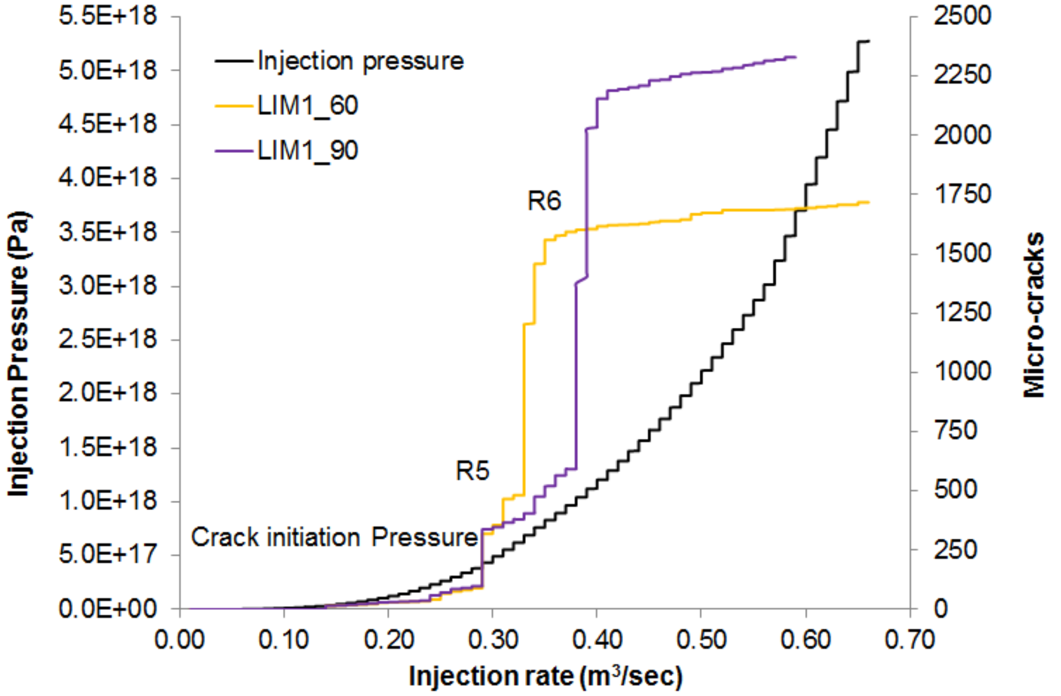

(**b**)

Figure 5.10 Injection pressure and total number of micro-cracks versus the flow rate for (**a**) the LIM1_15^o, LIM1_30^o and LIM1_45^o, and (**b**) the LIM1_60^o and LIM1_90^o samples.

Fig.5.11 and Fig.5.12 demonstrate the coordinates of the microcracks in the horizontal X and vertical Z directions, respectively, during the simulation for the LIM1_15° to LIM1_90° samples. It can be observed that for the LIM1_15°, 30° and 45° samples the cracks initiate near the injection point (x= 28 mm, marked with red) following horizontal (towards the diagonal fracture) and a slight downwards expansion, after the second half of the simulated time (after 0.006 sec). The movement towards the negative part of the Z axis can be attributed to the influence of gravity which even though it may be considered a minor effect on the macro scale, it affects the behaviour of the virtual assembly in the particle scale. The preferred direction of the cracks' propagation for the LIM1_60° and the LIM1_90° is dissimilar. More specifically, it requires less injection for the samples to reach the diagonal fracture (0.46 m^3/s for the LIM1_45° compared to 0.31 m^3/s for the LIM1_60° and 0.39 m^3/s for the LIM1_90°, respectively) and the horizontal cracks propagated further, reaching about x=10,3 mm for the LIM1_60° sample, and x=7.7 mm for the LIM1_90° sample (compared to 13.8 mm for the LIM1_45°) while the downwards expansion has been slowed down. More cracks tend to develop towards the positive part of the Z axis (upwards) in the second half of the simulated test. Considering the abrupt increase of microcracking in Fig.5.10(**b**), which occurs in the second part of the simulated test, it appears to enhance the fluid movement of the fractures above 45°, and therefore the propagation of cracks towards their relevant plane.

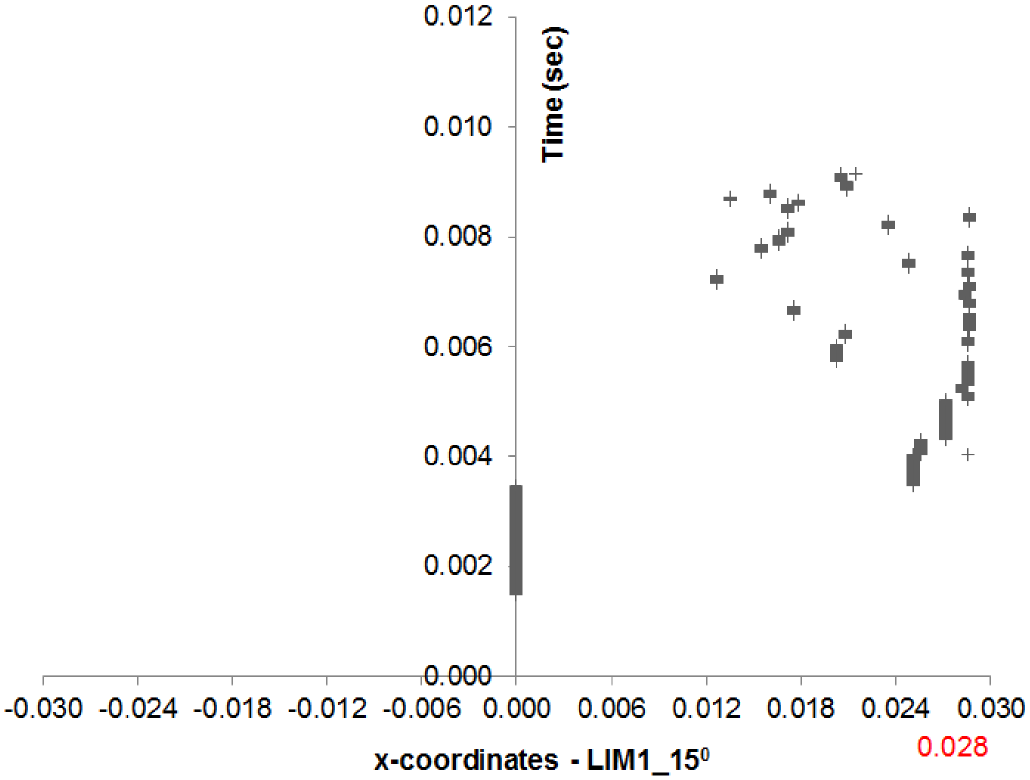
0.012
0.010
0.008
0.006
0.004
0.002
0.000
Time (sec)
-0.030
-0.024
-0.018
-0.012
-0.006
0.000
0.006
0.012
0.018
0.024
0.030
0.028
x-coordinates - LIM1_15⁰

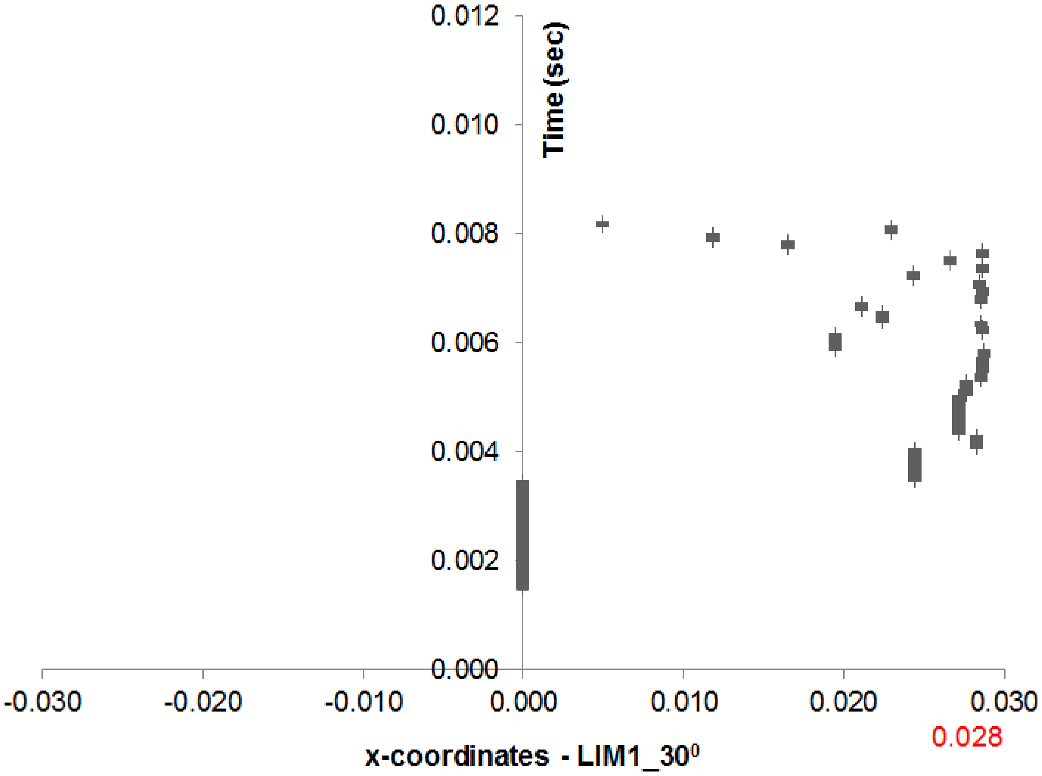
0.012
0.010
0.008
0.006
0.004
0.002
0.000
Time (sec)
-0.030
-0.020
-0.010
0.000
0.010
0.020
0.030
0.028
x-coordinates - LIM1_30⁰

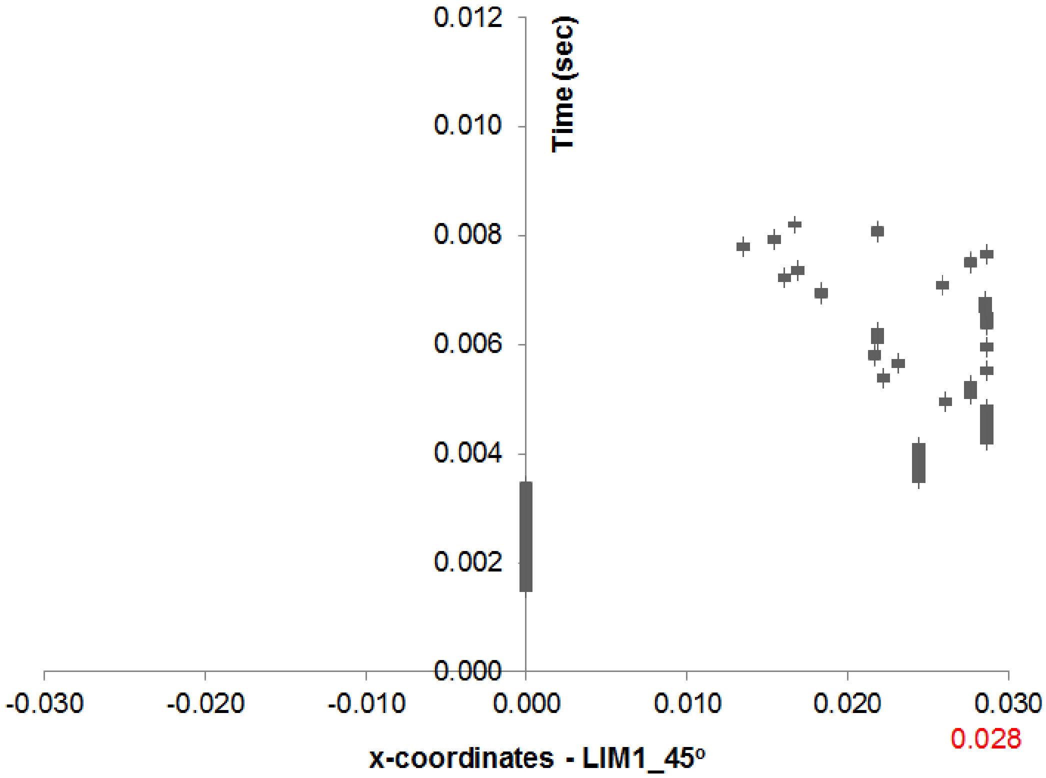
0.012
0.010
0.008
0.006
0.004
0.002
0.000
Time (sec)
-0.030
-0.020
-0.010
0.000
0.010
0.020
0.030
0.028
x-coordinates - LIM1_45°

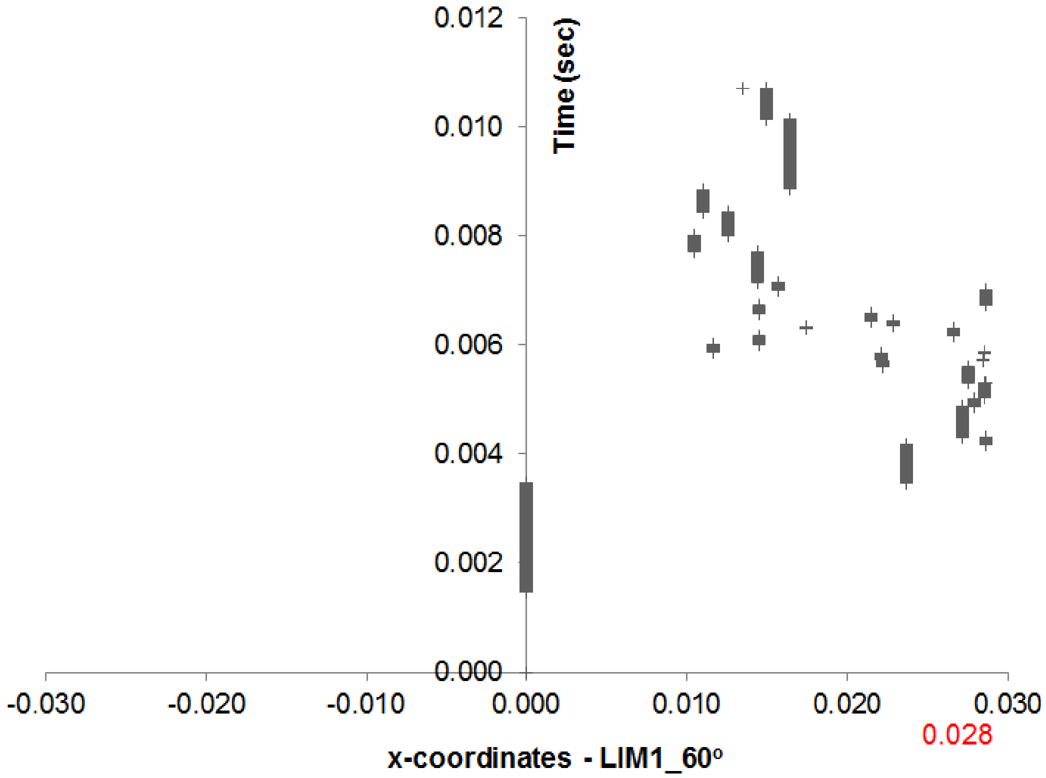
0.012
0.010
0.008
0.006
0.004
0.002
0.000
Time (sec)
-0.030
-0.020
-0.010
0.000
0.010
0.020
0.030
0.028
x-coordinates - LIM1_60°

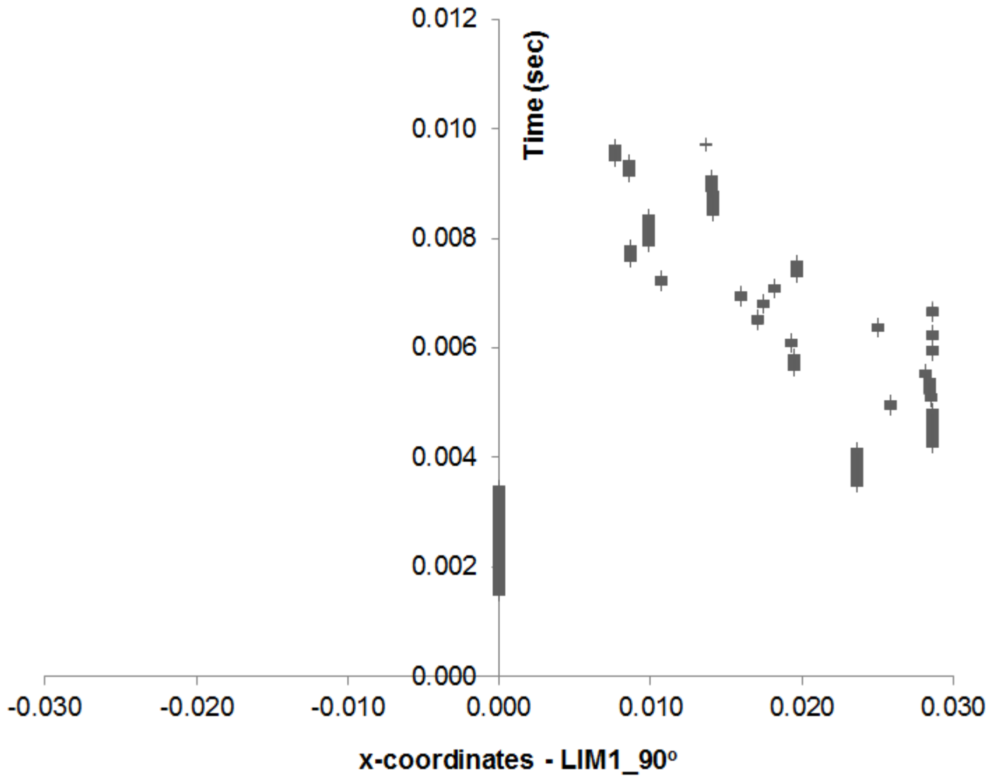

Figure 5.11 Coordinates of micro-cracks versus time in the X direction for the LIM1_15º to LIM1_90º samples, respectively.

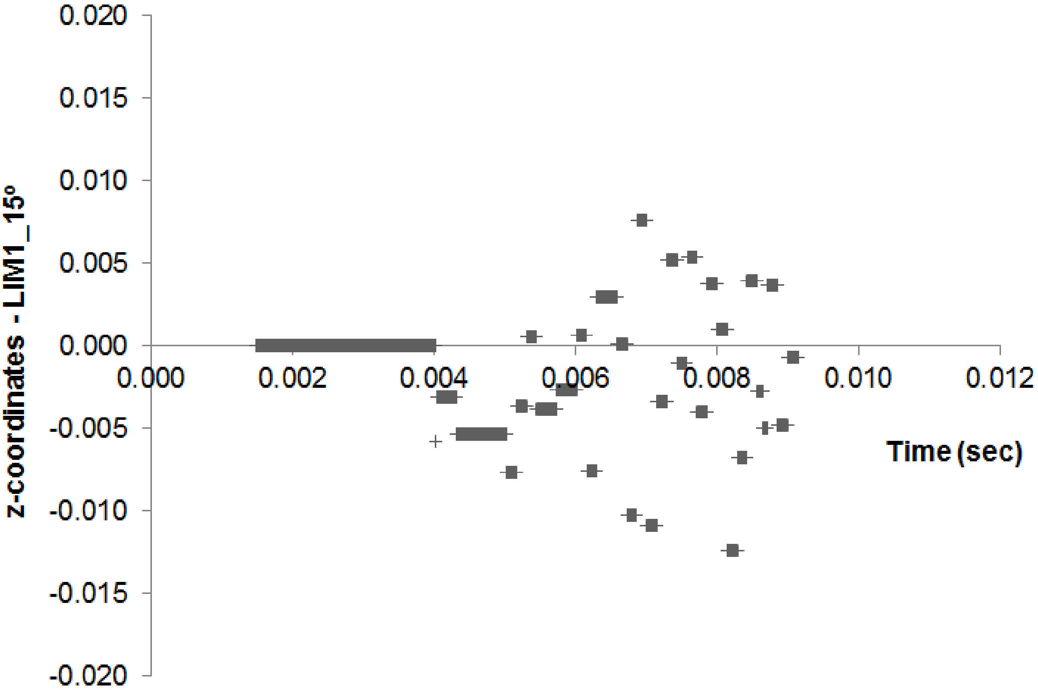
0.020
0.015
0.010
0.005
0.000
-0.005
-0.010
-0.015
-0.020
0.000
0.002
0.004
0.006
0.008
0.010
0.012
z-coordinates - LIM1_15º
Time (sec)

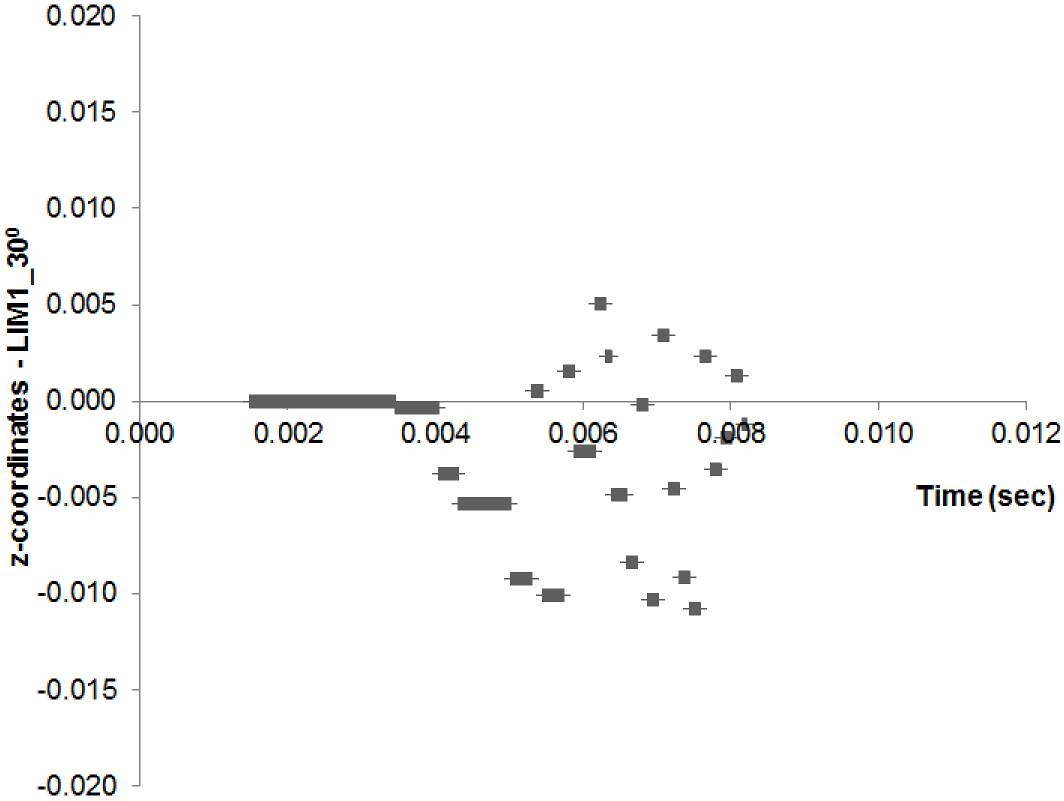
0.020
0.015
0.010
0.005
0.000
-0.005
-0.010
-0.015
-0.020
0.000
0.002
0.004
0.006
0.008
0.010
0.012
z-coordinates - LIM1_30º
Time (sec)

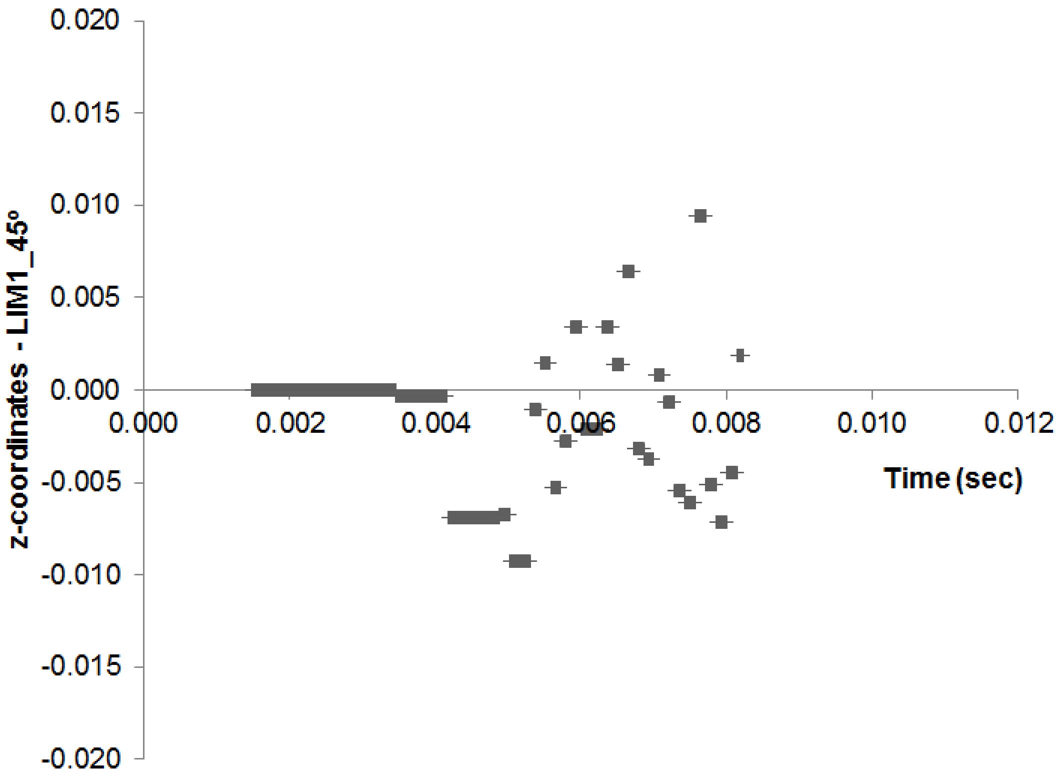
z-coordinates - LIM1_45°
0.020
0.015
0.010
0.005
0.000
-0.005
-0.010
-0.015
-0.020
0.000
0.002
0.004
0.006
0.008
0.010
0.012
Time (sec)

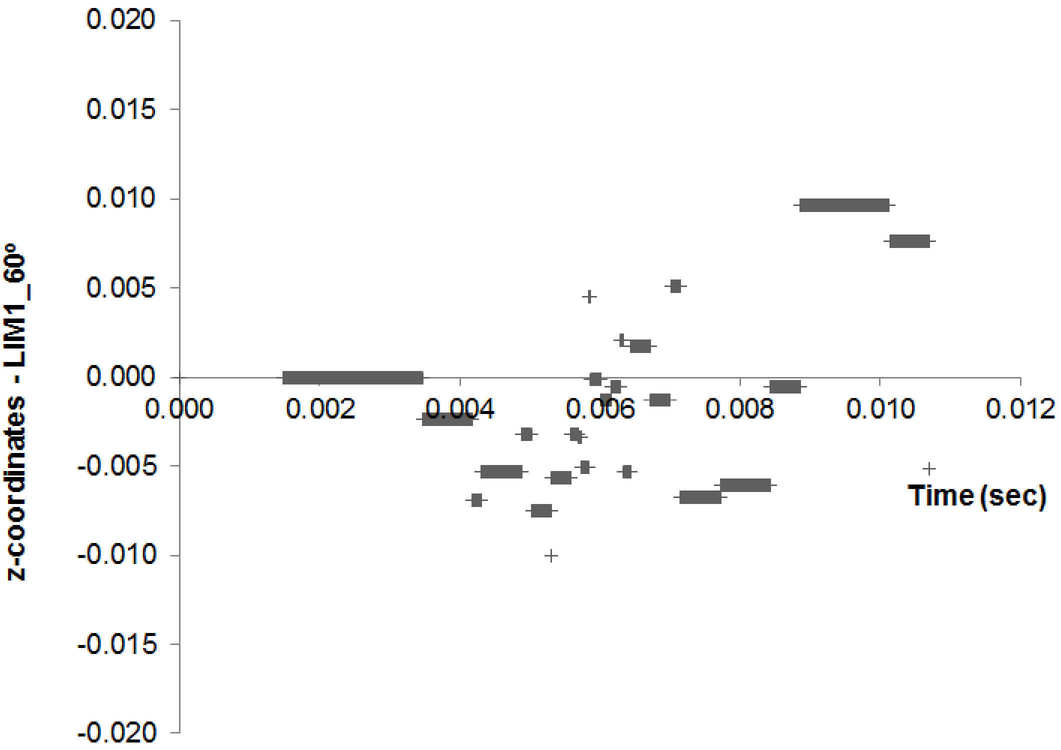
z-coordinates - LIM1_60°
0.020
0.015
0.010
0.005
0.000
-0.005
-0.010
-0.015
-0.020
0.000
0.002
0.004
0.006
0.008
0.010
0.012
Time (sec)

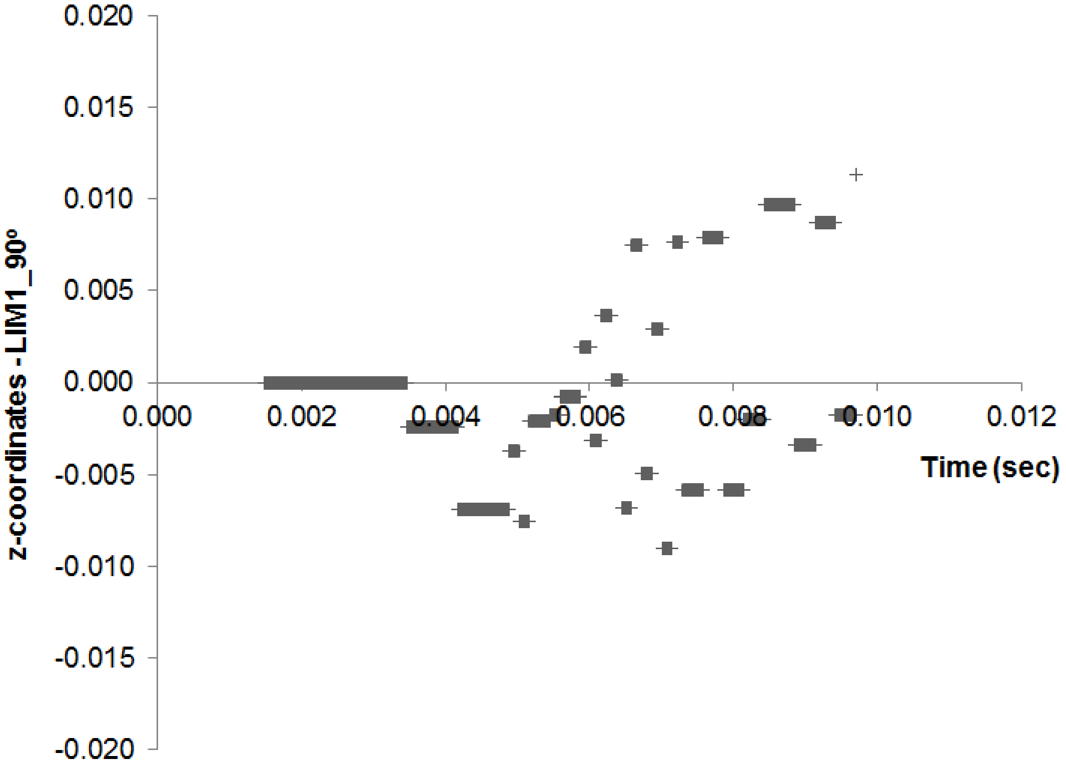

Figure 5.12 Coordinates of micro-cracks versus time in the Z direction for the LIM1_15° to LIM1_90° samples, respectively.

The aforementioned postulate can also be observed from the fluid vectors shown in Fig.5.13 which compares the samples LIM1_30° and LIM1_60°, respectively. All the samples containing a diagonal fracture below 45° have similar behaviour in terms of fluid velocity vectors and they can be described by Fig.5.13 (**top**). The velocity vectors between the upper and lower parts of the Z axis appear to have small differences near the inlet but they are observed to be larger at the lower part further ahead, thus verifying the symmetrical and slightly downward propagation of cracks for the LIM1_30°. Moreover, the velocity vectors for the LIM1_60° sample are sufficiently larger in the upper part of the assembly, thus indicating that the fluid tends to travel further in the upper part rather than the lower part.

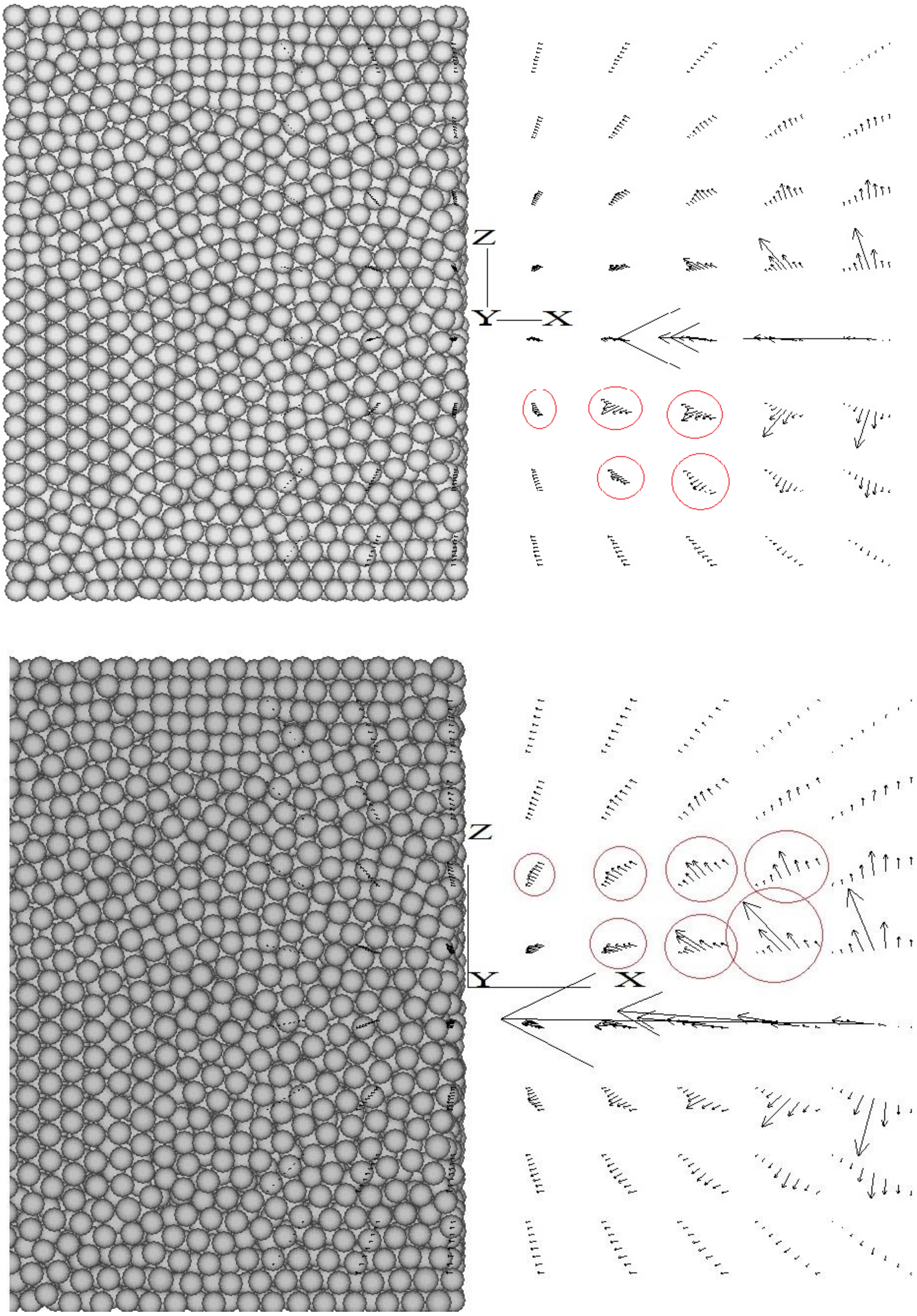

Figure 5.13 Side view of one half of the virtual assembly. The fluid velocity vectors in the upper part of the assembly for the LIM1_30^o (**top**) and the LIM1_60^o (**bottom**) samples, respectively. Each group of vectors refers to individual fluid cells and denote the distribution of magnitude and orientation of fluid velocity for each cell.

The boundary conditions for this test are based on the assumption that the external stress regime is normal and thus the vertical stress (σ_{zz}) is considered as the principal compressive stress. However, the mechanical load alters the stress pattern, due to the high amount of injection pressure, making the horizontal stress (σ_{xx}) the maximum compressive stress throughout the model. Moreover, the propagation of the micro-cracks, has been extended considerably in the horizontal and vertical directions, looking from the microscopic point of view, with the horizontal expansion gaining ground for the samples with fracrure angles below 45^o. Fig.5.14(**a**),(**b**) is a representative example, where the overall growth in the horizontal direction for the LIM1_30^o sample is larger than the one in the vertical direction. Even though, the difference between the horizontal and vertical overall expansion is not always noticeable (Fig.5.14(**c**),(**d**)), from a macroscopic point of view we can claim that the overall fracture growth in terms of a large rock which contains pre-existing inclined fractures below 45^o, extends along the principal compressive stress, agreeing with conventional theory (Valko and Economides, 1995). The differences between the conventional theory and the microscopic observations of the hydraulic fracture growth, can be attributed to the inhomogeneities of the PFC sample due to fractures and discontinuities.

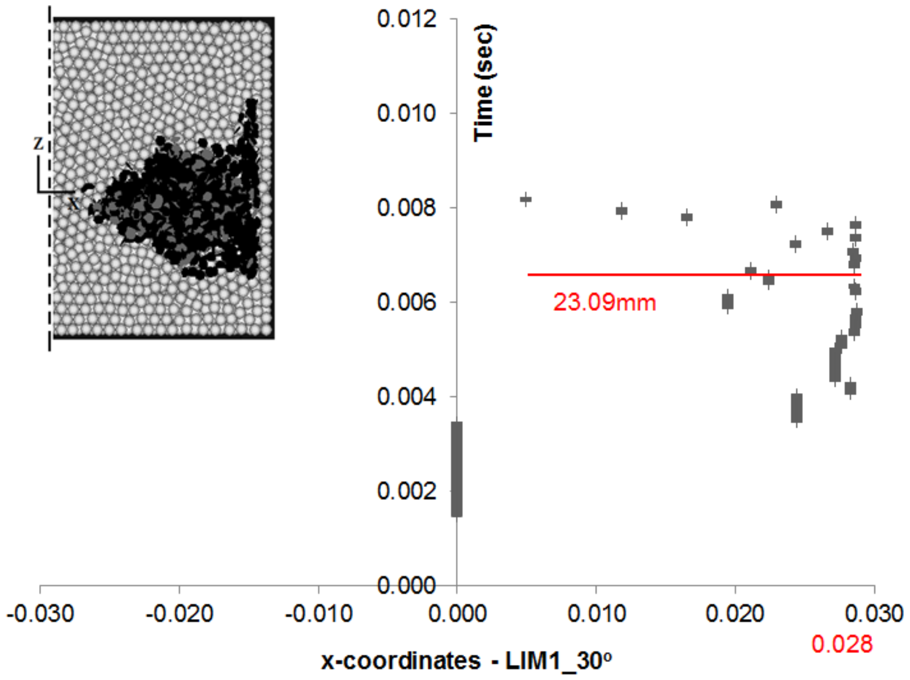
z
x
0.012
0.010
0.008
0.006
0.004
0.002
0.000
Time (sec)
23.09mm
-0.030
-0.020
-0.010
0.000
0.010
0.020
0.030
0.028
x-coordinates - LIM1_30°

(**a**)

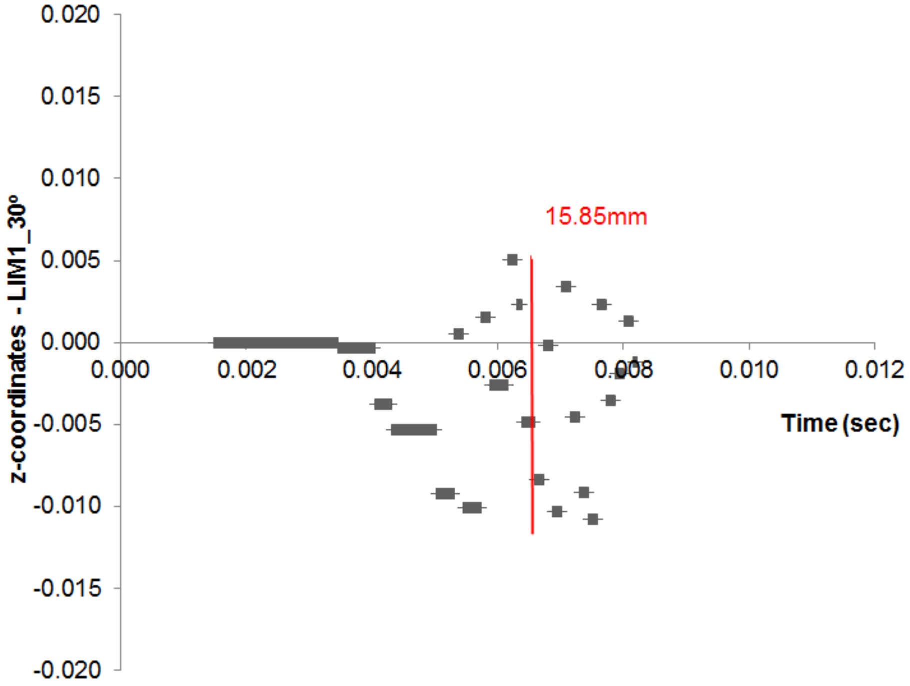
0.020
0.015
0.010
0.005
0.000
-0.005
-0.010
-0.015
-0.020
z-coordinates - LIM1_30°
15.85mm
0.000
0.002
0.004
0.006
0.008
0.010
0.012
Time (sec)

(**b**)

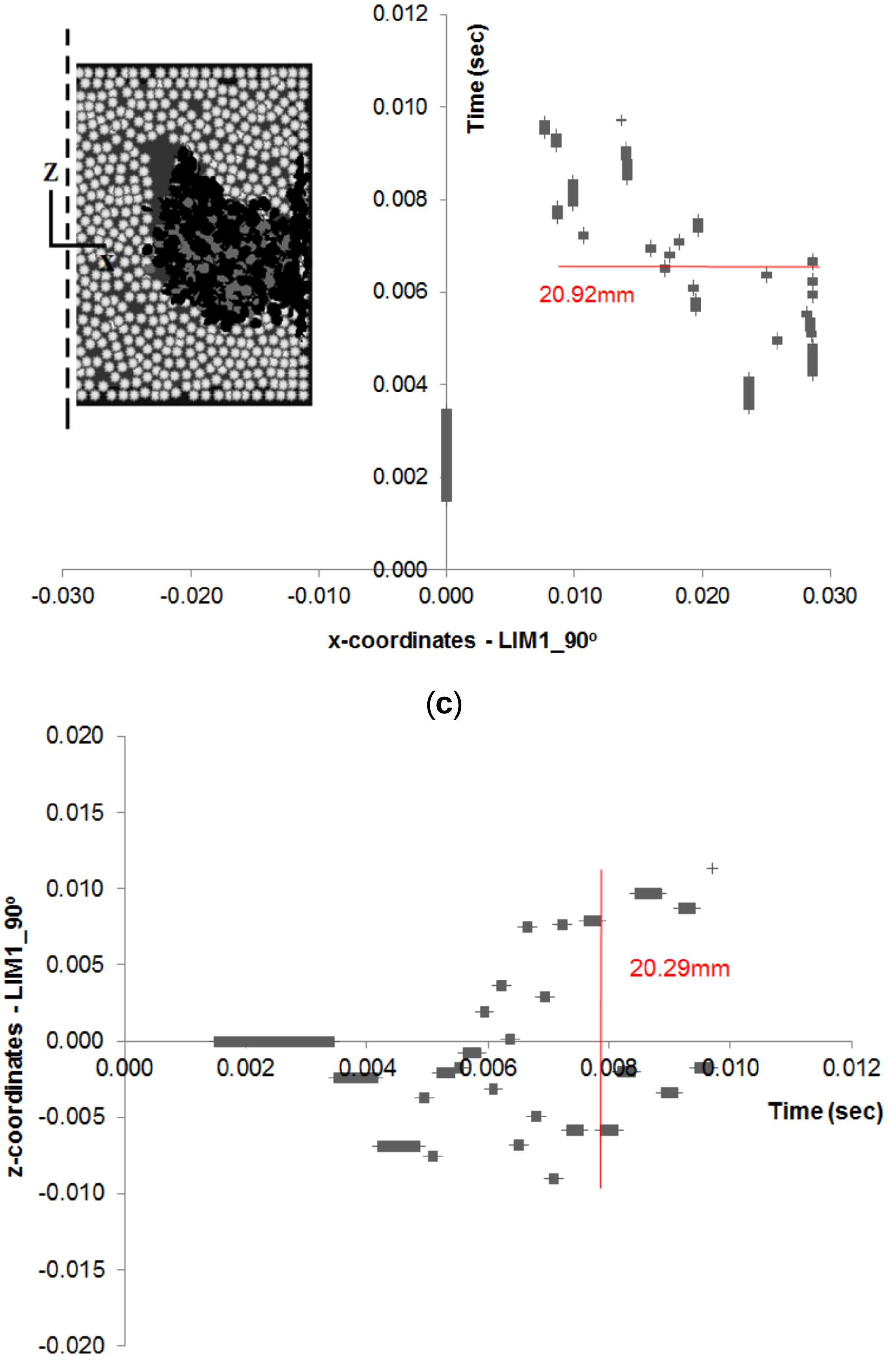

(**c**)

(**d**)

Figure 5.14 Coordinates of micro-cracks and the overall length of the microcracking in the x directions for (**a**) the LIM1_30° and (**b**) the LIM1_90° samples and in the z directions for (**c**) the LIM1_30° and (**d**) the LIM1_90° samples versus time.

Furthermore, as shown in Fig.5.15 (**bottom**), regions of groups of micro-cracks appear to stray from the main volume of the cracks and form individual strands that can enhance the hydraulic conductivity. It can be observed that more cracks tend to separate from the main volume, propagating further ahead and upwards when the fracture is at 60°, whereas for lower angles the cracks tend to develop in the lower part of the assembly and propagate as a cluster. The micro-cracks in the normal direction (black dots) are dominant, with a percentage of around 83%, whereas only 17% are formed in the shear direction (grey dots). This is an expected outcome since the ratio between the bonds' strength in the normal to shear direction is less than 1.

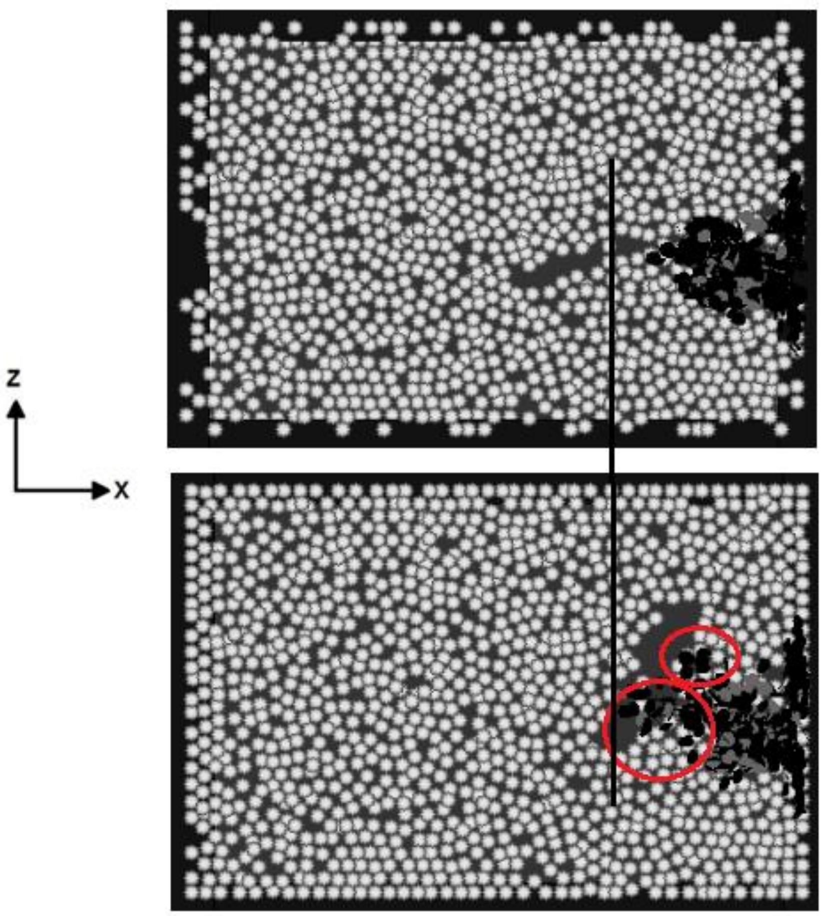

Figure 5.15 Schematic of the cross section for the LIM1_15° (**top**) and the LIM1_60° (**bottom**) samples, respectively, illustrating the location of the micro-cracks and the groups of cracks (read circles) that stray from the main volume.

Measurements of the stresses in the horizontal (σ_x) and vertical (σ_z) directions for all samples provide a further understanding of the fracturing process and the influence of the fracture angle of the virtual assembly. Critical regions, within each sample's matrix, are monitored providing measurements of the internal stress state and the progress of internal energy. Fig.5.16 illustrates the spherical monitoring regions near the fractures for each of the samples. The first part of their name indicate their number, compared to the total number of spherical regions, and the second part indicate the fracture angle. Moreover, as shown in Fig.5.17, the stresses in the area below the inclined fracture (Fig.5.17(**a**), (**b**)), for the samples with fractures between 15°-90°, are higher than those in the upper part of the fracture (Fig.5.17(**c**),(**d**)) and thus confirms the preferred propagation of cracks towards the negative part of the Z axis.

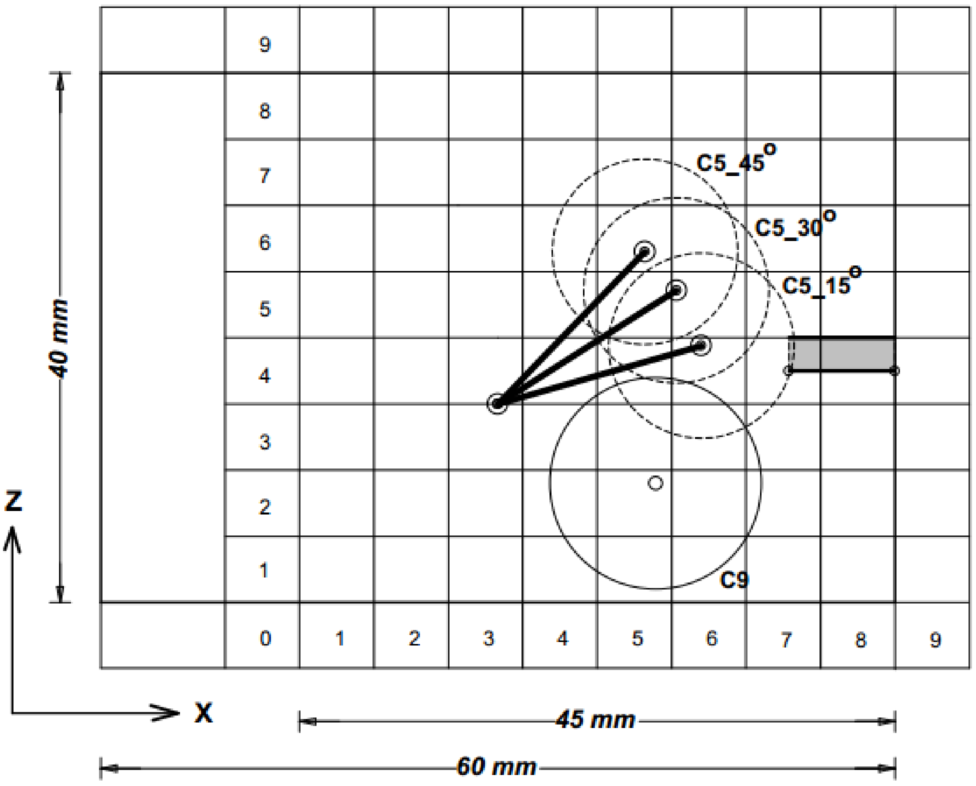

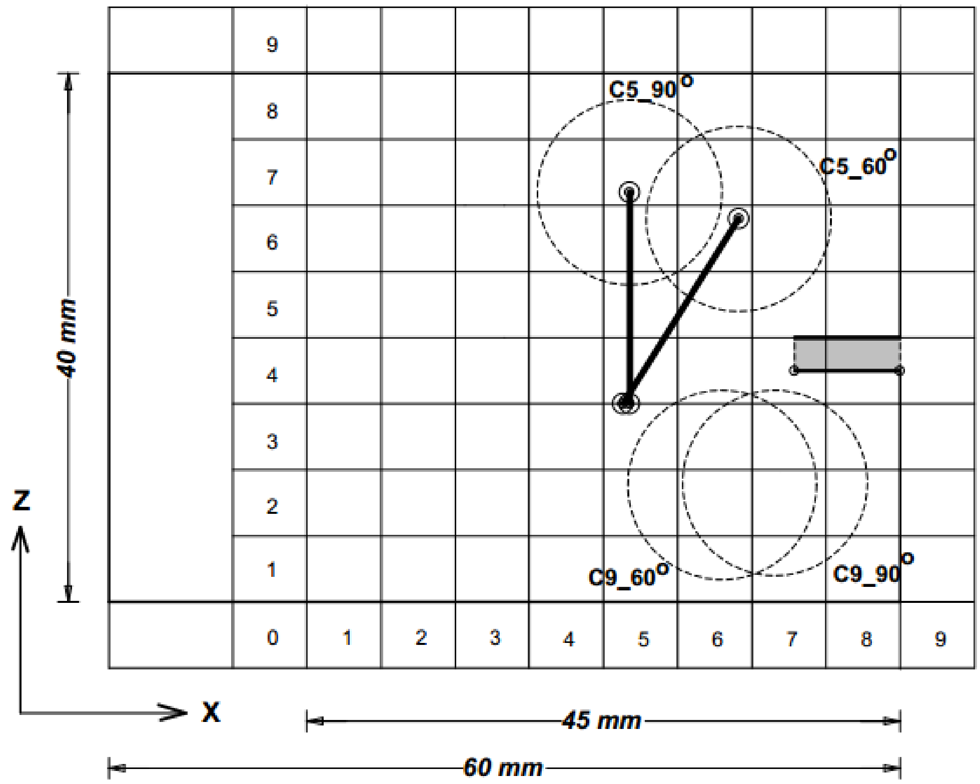

Figure 5.16 5th and 9th spherical regions in order to monitor the internal mechanical state of the samples. The coordinates of the measurement spheres C9_60° and C9_90° were chosen so that they do not overlap with the injection poit which may lead to compromised results.

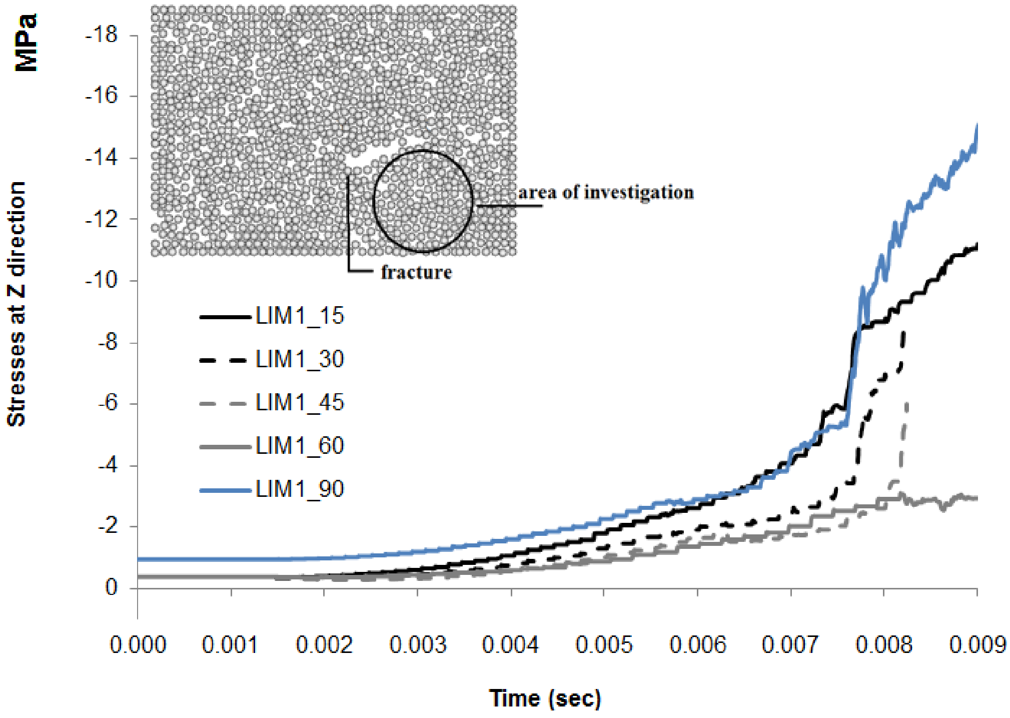

(a)

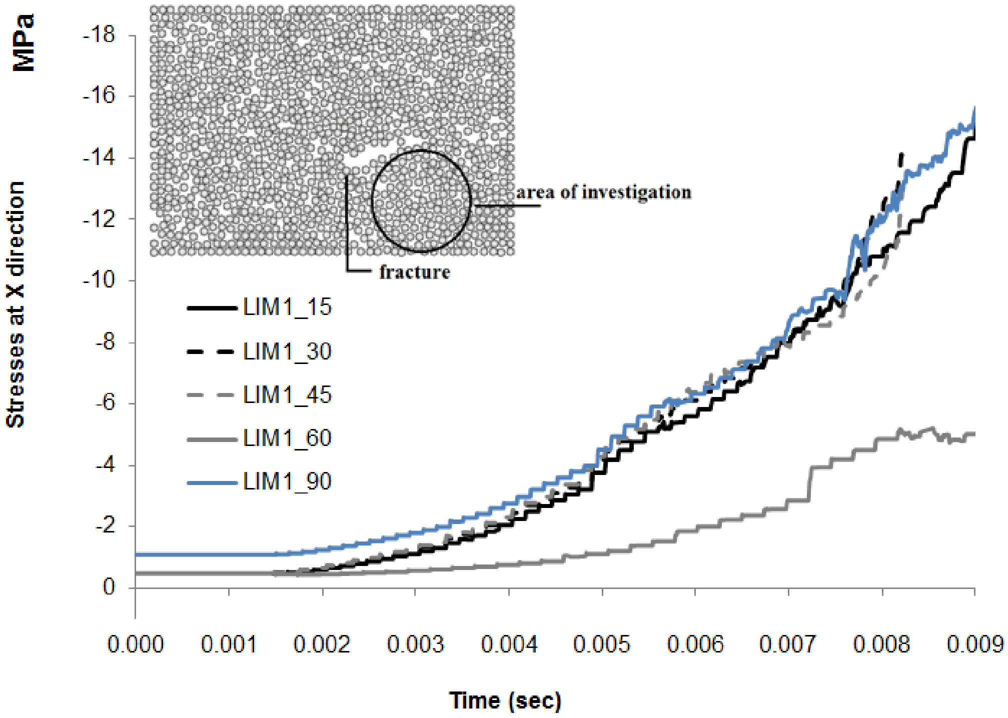
MPa
Stresses at X direction
-18
-16
-14
-12
-10
-8
-6
-4
-2
0
0.000
0.001
0.002
0.003
0.004
0.005
0.006
0.007
0.008
0.009
Time (sec)
area of investigation
fracture
LIM1_15
LIM1_30
LIM1_45
LIM1_60
LIM1_90

(b)

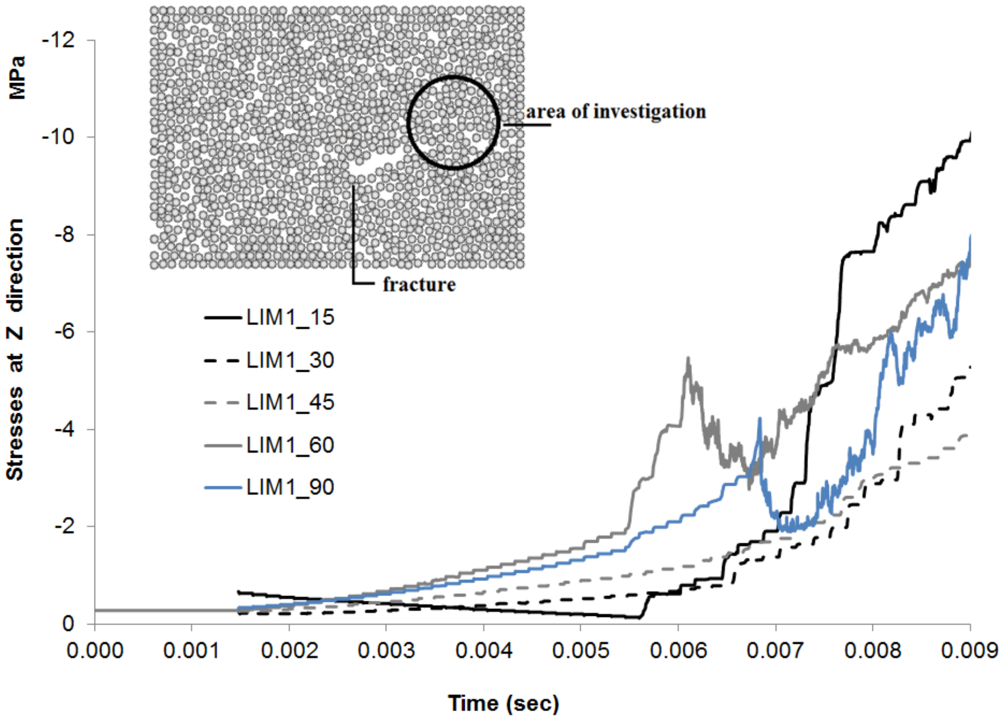
MPa
Stresses at Z direction
-12
-10
-8
-6
-4
-2
0
0.000
0.001
0.002
0.003
0.004
0.005
0.006
0.007
0.008
0.009
Time (sec)
area of investigation
fracture
LIM1_15
LIM1_30
LIM1_45
LIM1_60
LIM1_90

(c)

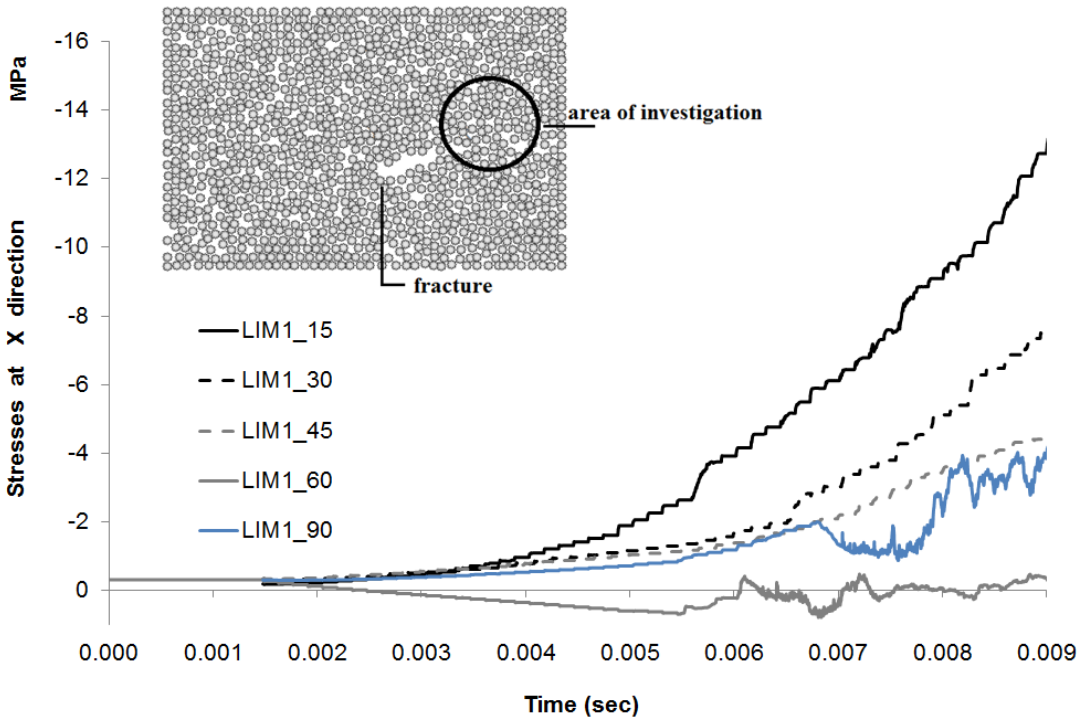

(**d**)

Figure 5.17 Stresses in the and Z and X direction versus time for the LIM1_15^o, 30^o, 45^o ,60^o, 90^o samples, respectively, in (**a**), (**b**) the lower part of the inclined fracture, and (**c**), (**d**) the upper part of the inclined fracture.

The description of the previous conclusion can be observed in Fig.5.18, where each micro-cracking corresponds to 0.32, 0.37 and 0.43 m3/sec injection rate, respectively. The red line demonstrates the height of the injection point, while the hollow region is the fracture at 60o. It can be observed that cracks propagate more towards the upper part of the assembly and that the breakage of the bonds, which connect the particles next to the facture, results in an abrupt increase in the number of cracks.This explains the boost in fluid velocity and this agrees with the results presented in Fig.5.10(**b**).

Previous research has established that the amounts of elastic energy which is stored within the virtual assembly in the form of bond, friction, kinetic, strain and body energy, is released every time a bond breaks.

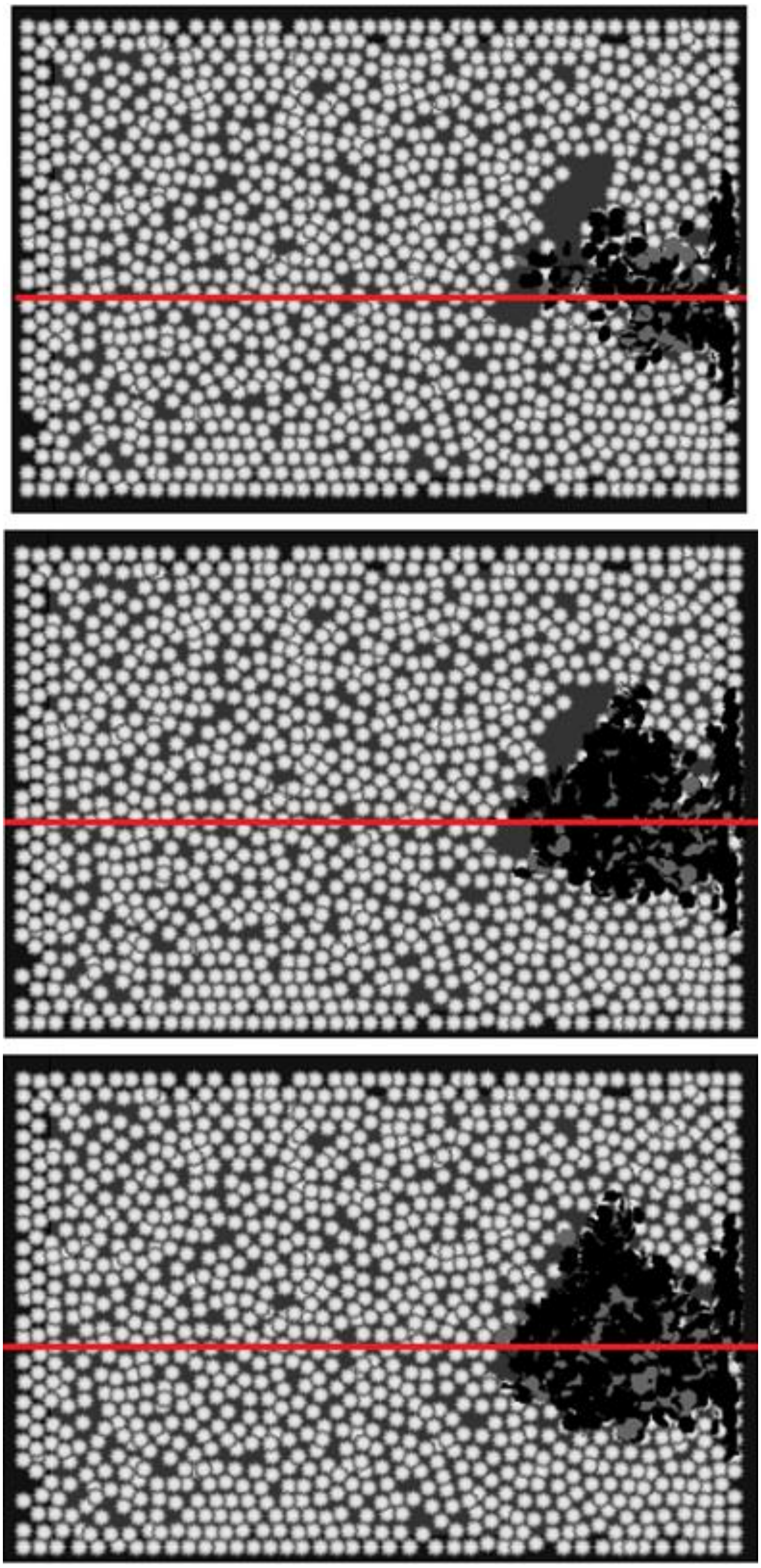

Figure 5.18 Propagation of the cracks for the LIM1_60^o sample after the second half of the simulated test. The red line indicates the height of the injection point.

The extra pressure at each time-step, and hence the higher stresses, causes a greater energy release during the rupture of the bonds, especially near the fracture tip and thus forcing the cracks to propagate to the next neighbouring location. This can be observed in Fig.5.19, which illustrates the stresses in all directions for the regions near the right hand-side of the diagonal fracture tip and at another point away from the fracture (top and left-end of the assembly – Fig.5.19(**b**)). It can be observed that the stresses near the tip are much higher (Fig.5.19(**a**)) than those in the remote locations (Fig.5.19(**b**)).

Moreover, Fig.5.20(**a**, **b**) illustrates the changes in the stored energy, indicating that in the critical regions R1-R6 abrupt micro-cracks increases are followed by sudden and large increases in the kinetic energy within the assembly.

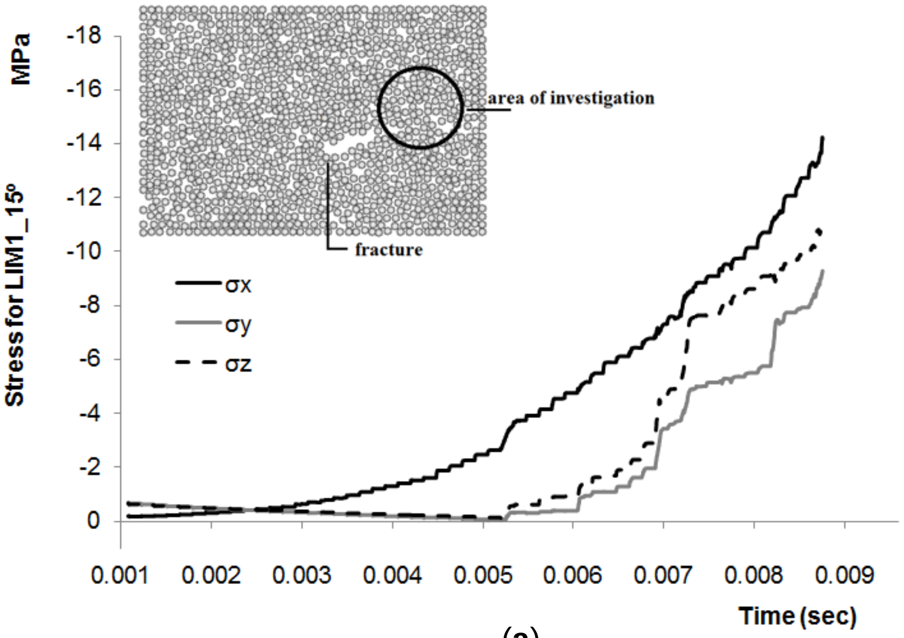

(**a**)

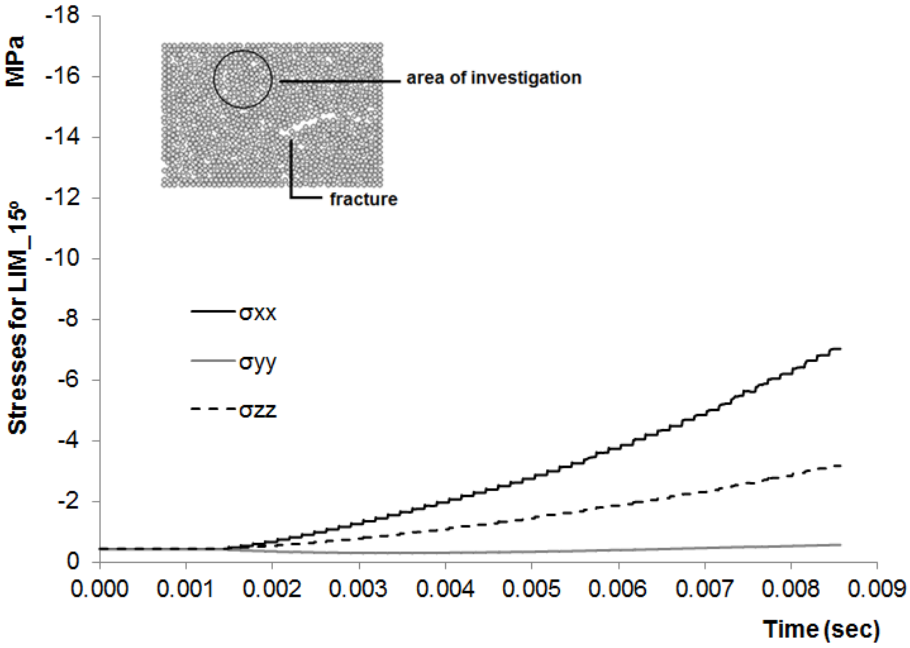

(**b**)

Figure 5.19 Stresses versus time for the LIM1_15º sample (**a**) in front of the fracture tip, and (**b**) at a remote location away of the fracture.

The LIM1_15º, 30º, and 45º samples demonstrate a similar behaviour, whereas for the LIM1_60º and 90º samples the kinetic energy shows concentrated high values in a time period near the second part of the simulated test. This is due to the enhanced fluid movement as it reaches the hollow region within the fracture as previously discussed. Furthermore, the visualization of the damage regions R1-R6 for all samples (cross section and front view), starting from LIM1_15º on top until LIM1_90º on the bottom, can be seen in Fig.5.20. It can be observed first the progressive and finally the sudden increase of the micro-cracks due to high hydraulic pressure, and their propagation towards the hollow region of the fracture. More specifically, Fig.5.20(**a**),(**b**) correspond to the R1, R2 and R4 damage regions of the LIM1_15º and LIM1_30º samples at injection rates of 0.15, 0.30 and 0.45 m^3/s, respectively, while Fig.5.20(**c**) corresponds to the R1, R2, R3 damage regions of the LIM1_45º sample at injection rates of 0.15, 0.30 and 0.40m^3/s.

Fig.5.20(**d**) corresponds to the progressive damage of the LIM1_60° sample at injection rates of 0.30, 0.35 (R5 damage region) and 0.45m^3/s, whereas Fig.5.20(**e**) illustrates the progressive damage of the LIM1_90° sample at injection rates of 0.15, 0.30 and 0.41 m^3/s (R6 damage region).

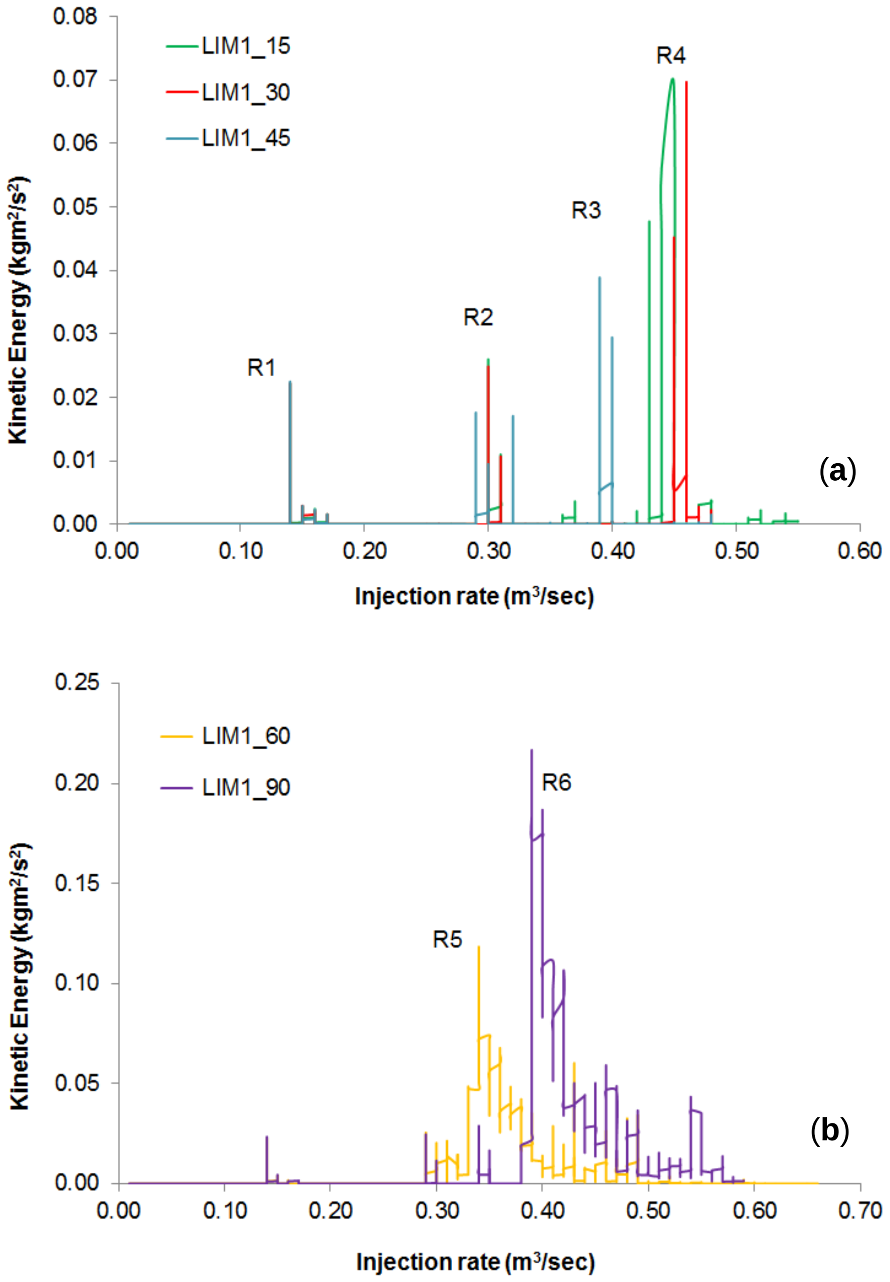

Figure 5.20 Critical regions of energy release versus the injection rate for (**a**) the LIM1_15°, LIM1_30°, LIM1_45° and (**b**) the LIM1_60°, LIM1_90° samples, respectively.

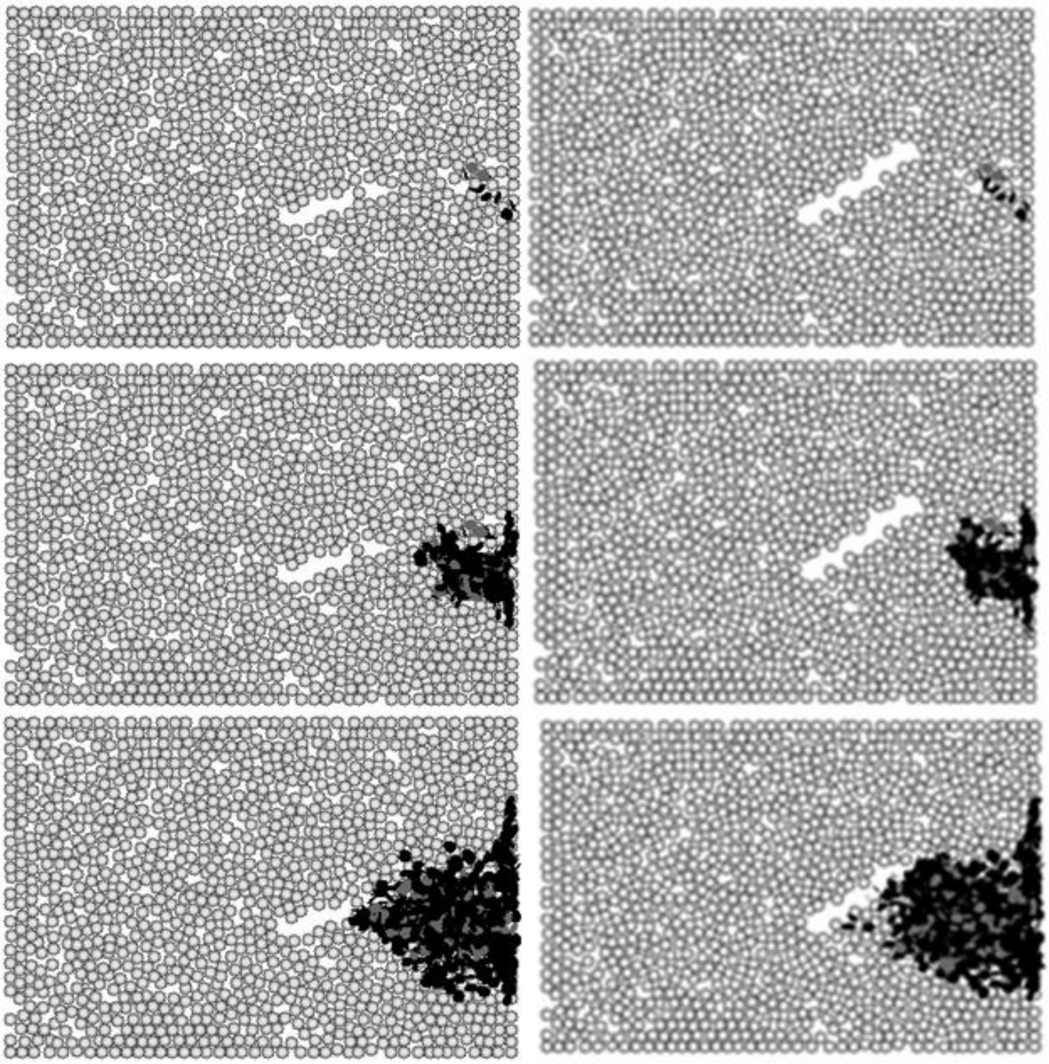

(**a**) (**b**)

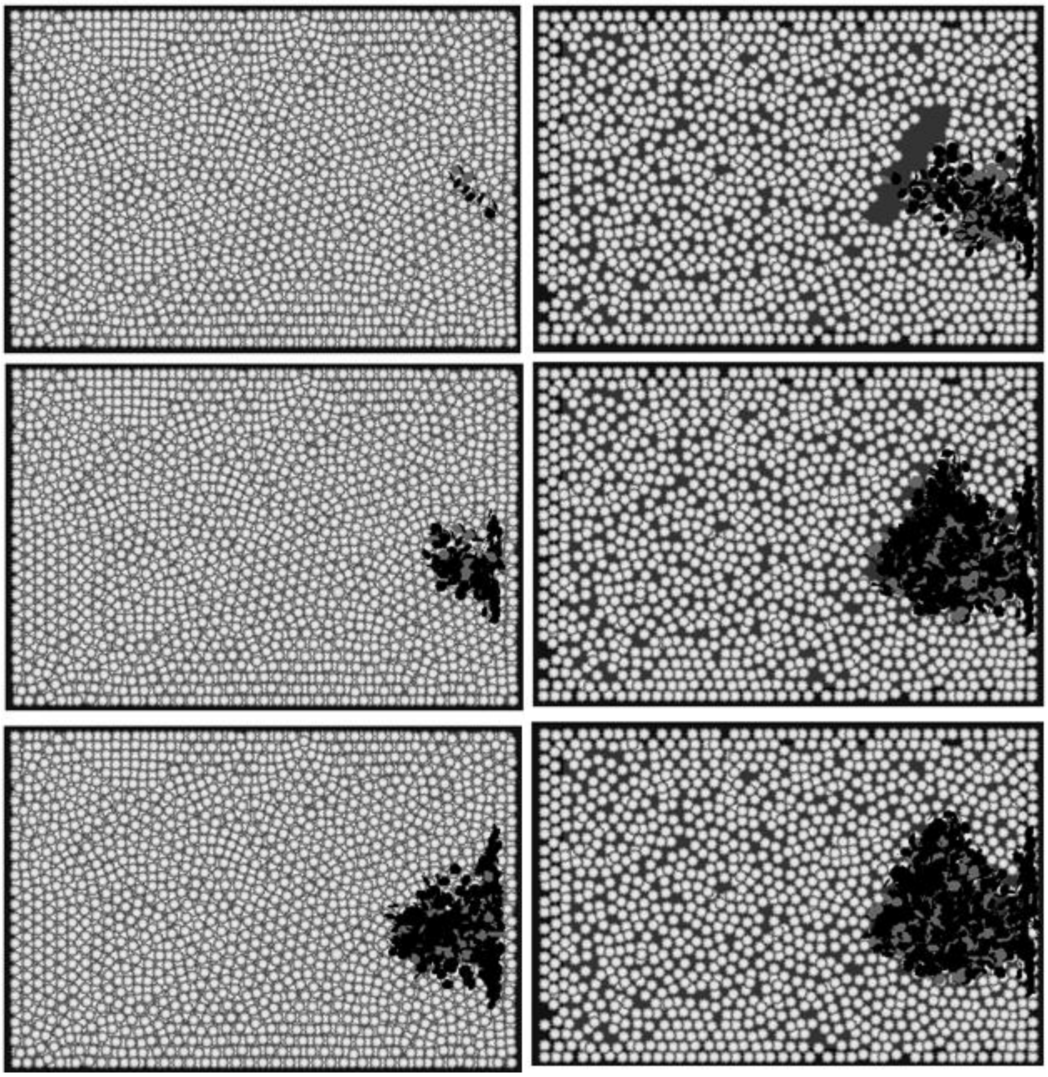

(**c**) (**d)**

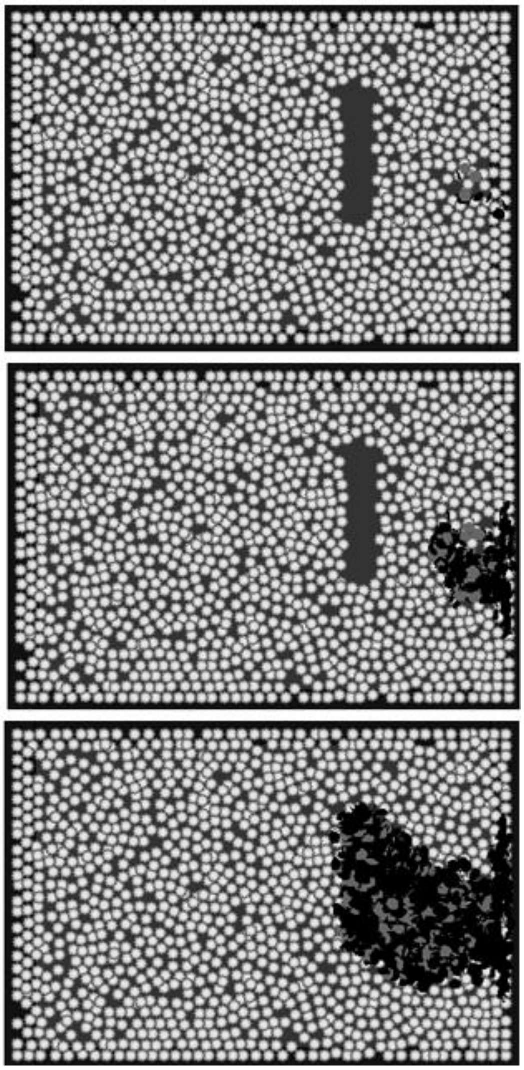

(**e**)

Figure 5.21 Cross sections of the regions R1- R6 of the (**a**) LIM1_15^o, (**b**) 30^o, (**c**) 45^o (side view of the sample, where the inclined fracture is within the body), (**d**) 60^o and (**e**) 90^o samples, respectively, showing the corresponding damage of the samples, relating the results with Fig.5.20.

5.3.2 Effect of the external stress regime on the hydraulic fracturing behaviour

From the cracking profile of the PFC model, illustrated in Fig.5.22, it can be observed that regardless of the different external stress regime, the model indicates almost identical behaviour. The fact that the effect of the external stresses appears less critical can be attributed to the combination of the high values of the injection pressure and the dimensions of the model. This can be minimized with the use of large reservoirs rather than individual rocks. Furthermore, it can be observed that there is a gradual increase in the micro-cracks, with regions followed by sudden and large increases of cracks. The most prominent region is marked as D1, followed by other regions with less aggressive generation of micro-cracks.

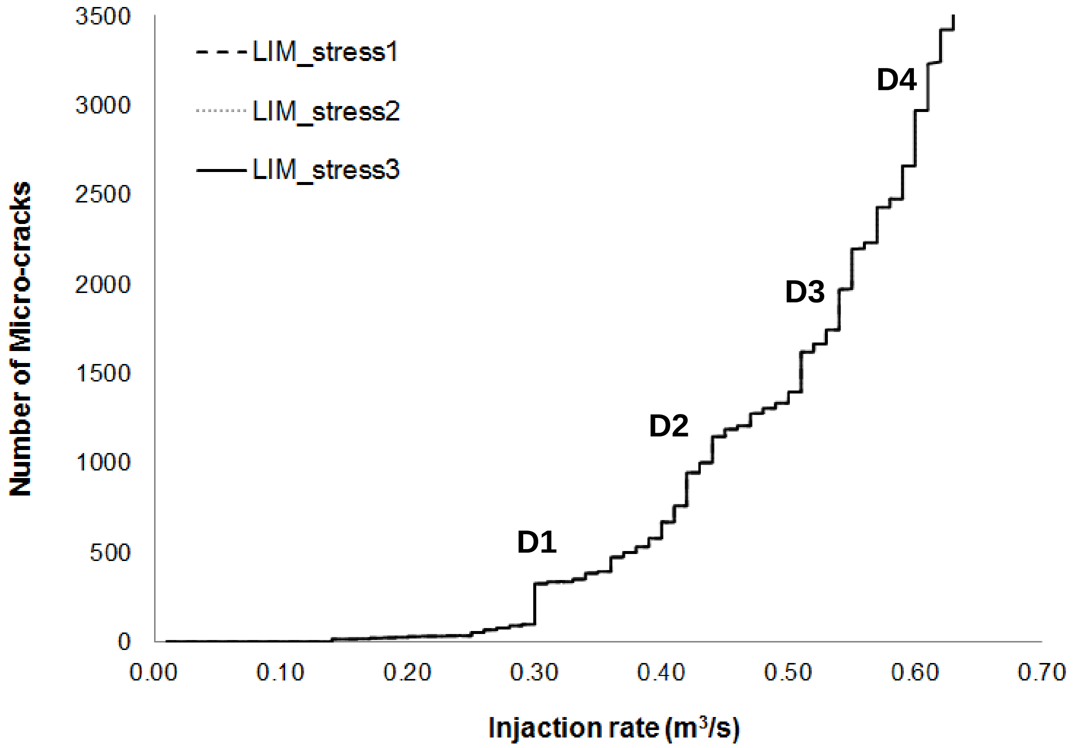

Figure 5.22 Number of micro-cracks versus the injection rate for the LIM1_stress$_1$, LIM1_stress$_2$ and LIM1_stress$_3$ models.

The visualisation of the state of the model in terms of damage can be observed in Fig.5.23. Each block of illustrations depicts the LIM1_stress$_1$, LIM1_stress$_2$ and LIM1_stress$_3$ PFC models, respectively, with pre-existing single fractures and corresponds to the damage regions illustrated in Fig.5.22.

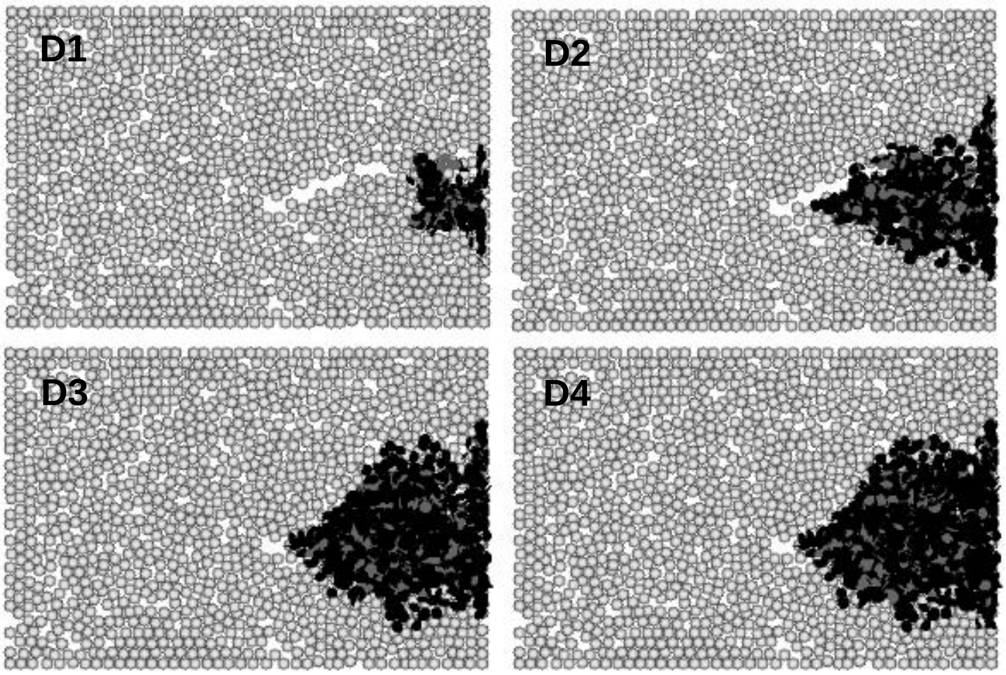
D1
D2
D3
D4

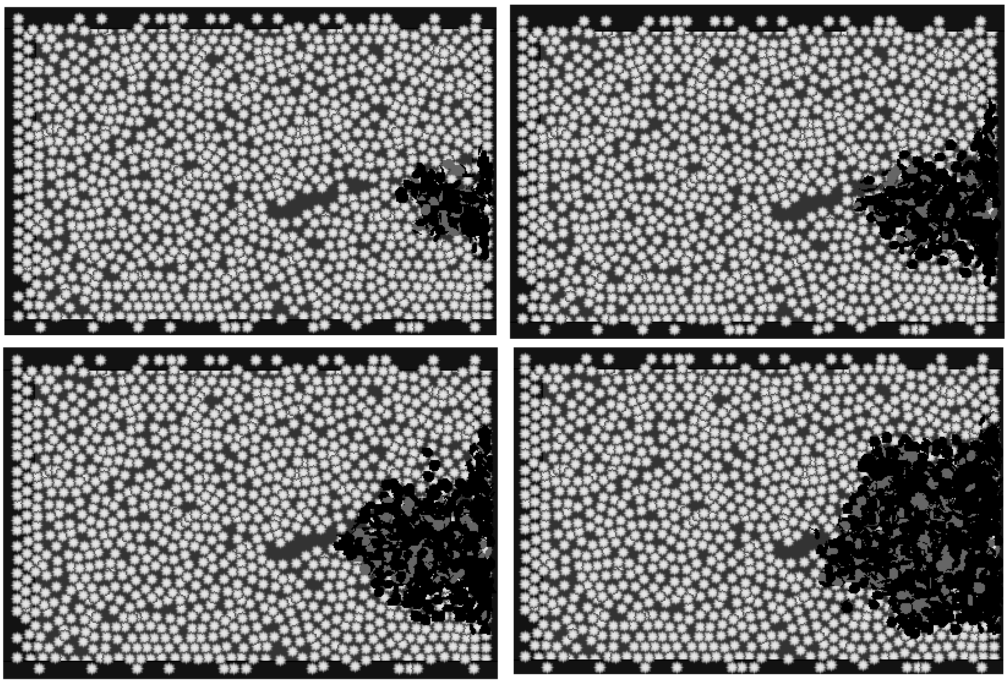

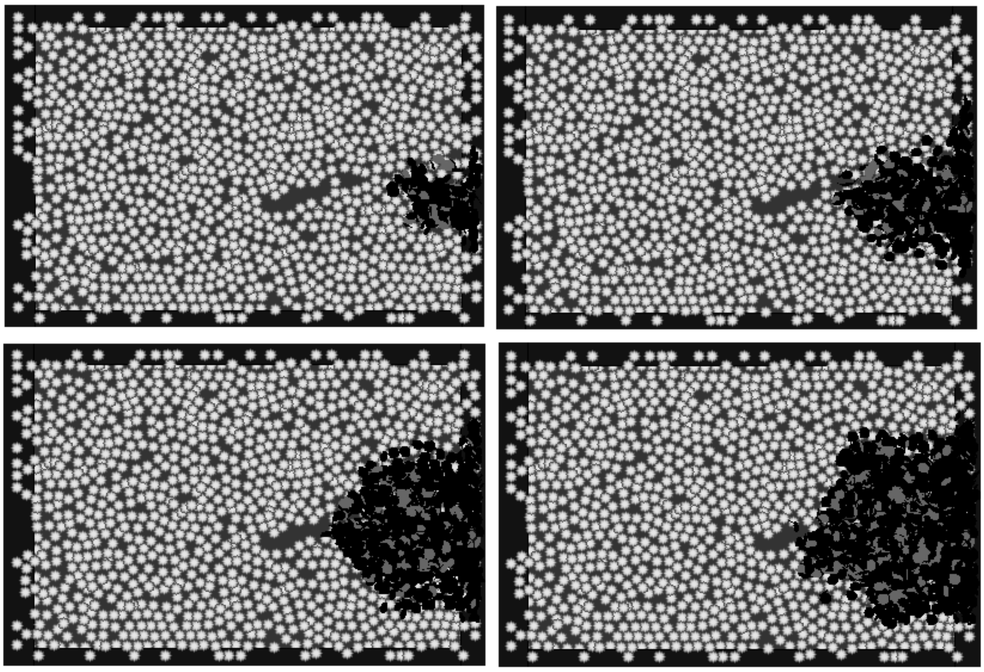

Figure 5.23 Progressive damage and abrupt increases of the micro-cracks of the LIM1_stress$_1$, LIM1_stress$_2$ and LIM1_stress$_3$ models at the critical regions D1 to D4.

Furthermore, the exact location of the micro-cracks in the X, Y and Z directions for all three cases revealed that the vertical propagation (Z) is gaining ground and that the largest crack expansion can be observed during the third stress regime (Fig.5.24). More specifically, both the horizontal and vertical expansions for the LIM1_stress$_3$ were found to be larger (21.48mm and 30.30mm, respectively) than all the other cases, while the horizontal expansion, in the Y direction, did not show significant changes under the influence of different stress regimes. However, it is important to note that even though the maximum compressive stress is in the horizontal X direction, due to the external mechanical load, the overall fracture growth is observed to extend along the vertical Z direction. This means that the effect of the confining stress in combination with the heterogeneity of the material, due to fracture, alters the orientation of the hydraulic fracture.

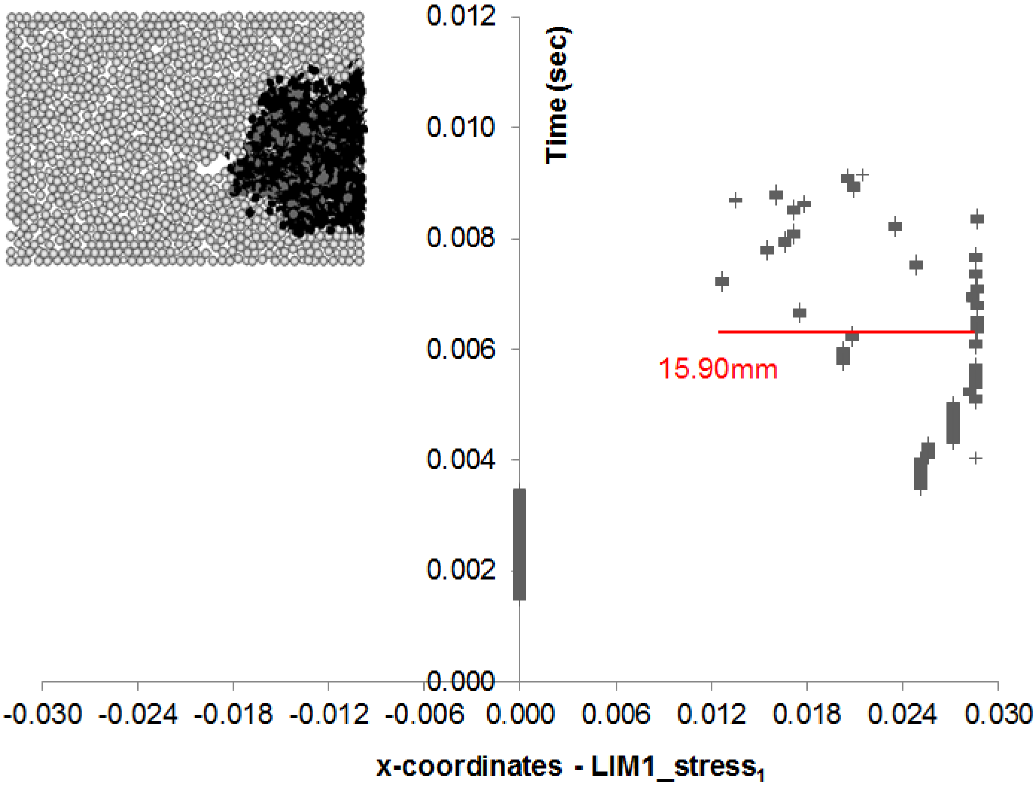
0.012
0.010
0.008
0.006
0.004
0.002
0.000
Time (sec)
15.90mm
-0.030 -0.024 -0.018 -0.012 -0.006 0.000 0.006 0.012 0.018 0.024 0.030
x-coordinates - LIM1_stress$_1$

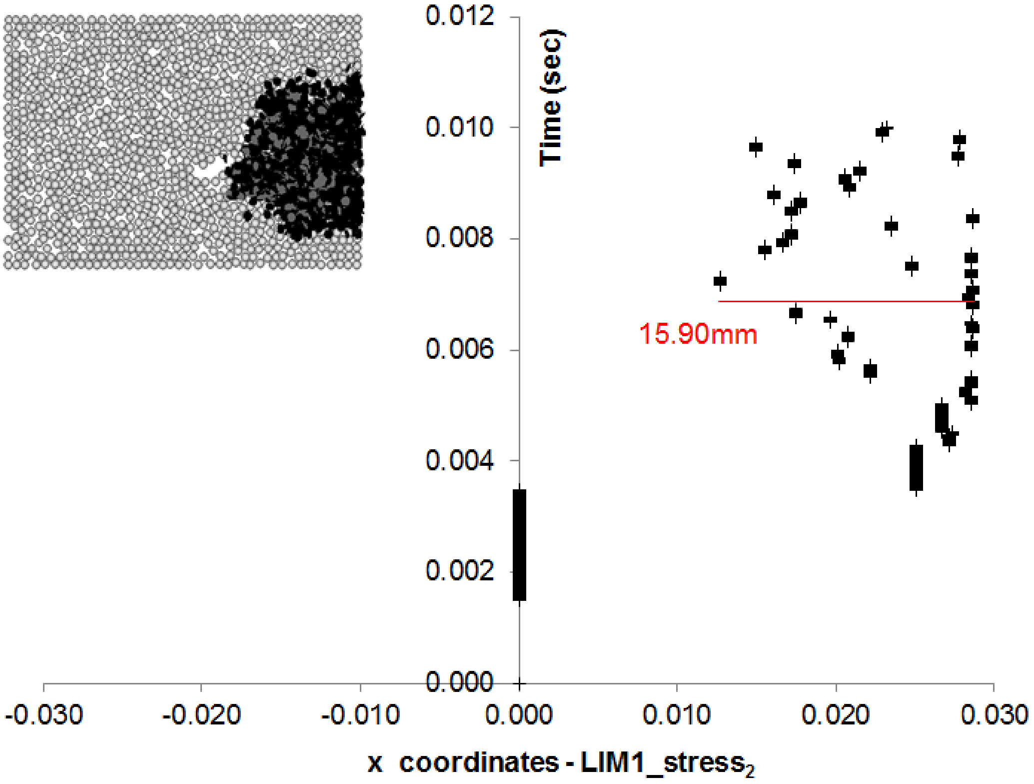
0.012
0.010
0.008
0.006
0.004
0.002
0.000
Time (sec)
15.90mm
-0.030 -0.020 -0.010 0.000 0.010 0.020 0.030
x coordinates - LIM1_stress$_2$

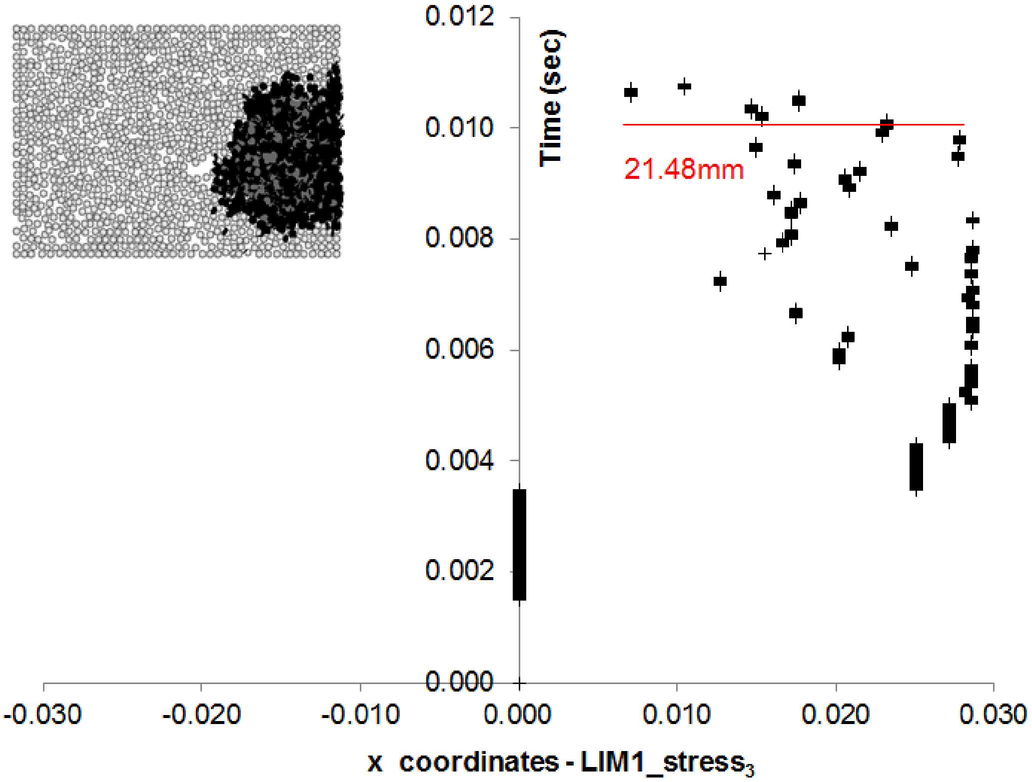
0.012
0.010
0.008
0.006
0.004
0.002
0.000
Time (sec)
21.48mm
-0.030
-0.020
-0.010
0.000
0.010
0.020
0.030
x coordinates - LIM1_stress3

(**a**)

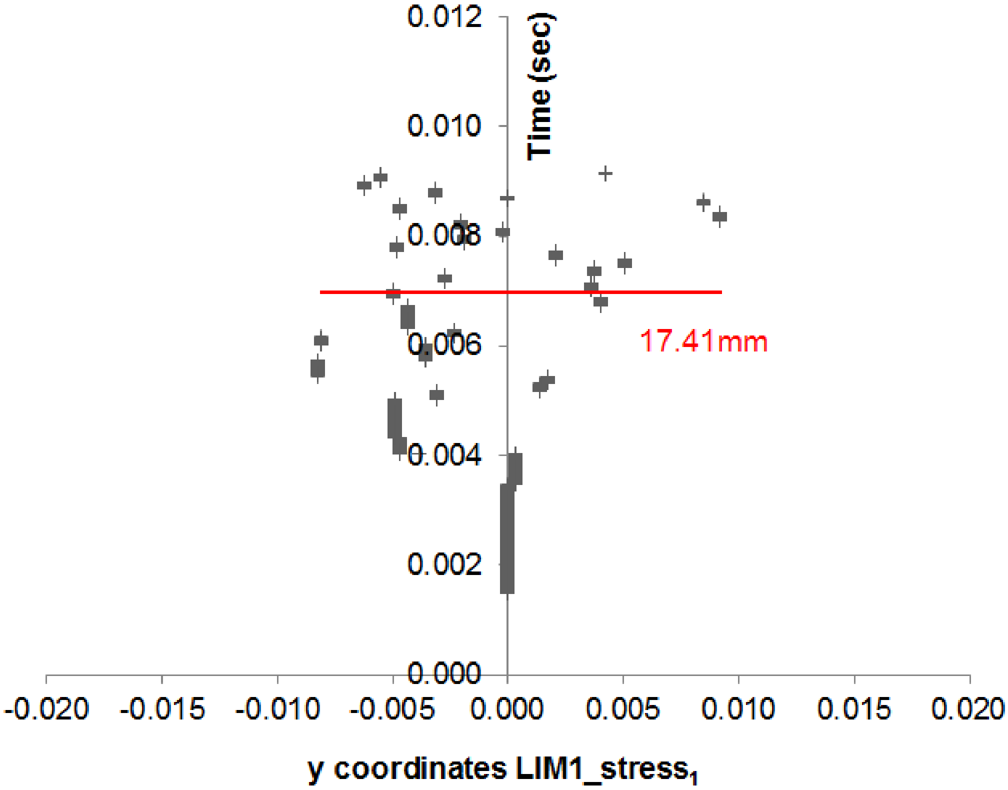
0.012
0.010
0.008
0.006
0.004
0.002
0.000
Time (sec)
17.41mm
-0.020
-0.015
-0.010
-0.005
0.000
0.005
0.010
0.015
0.020
y coordinates LIM1_stress1

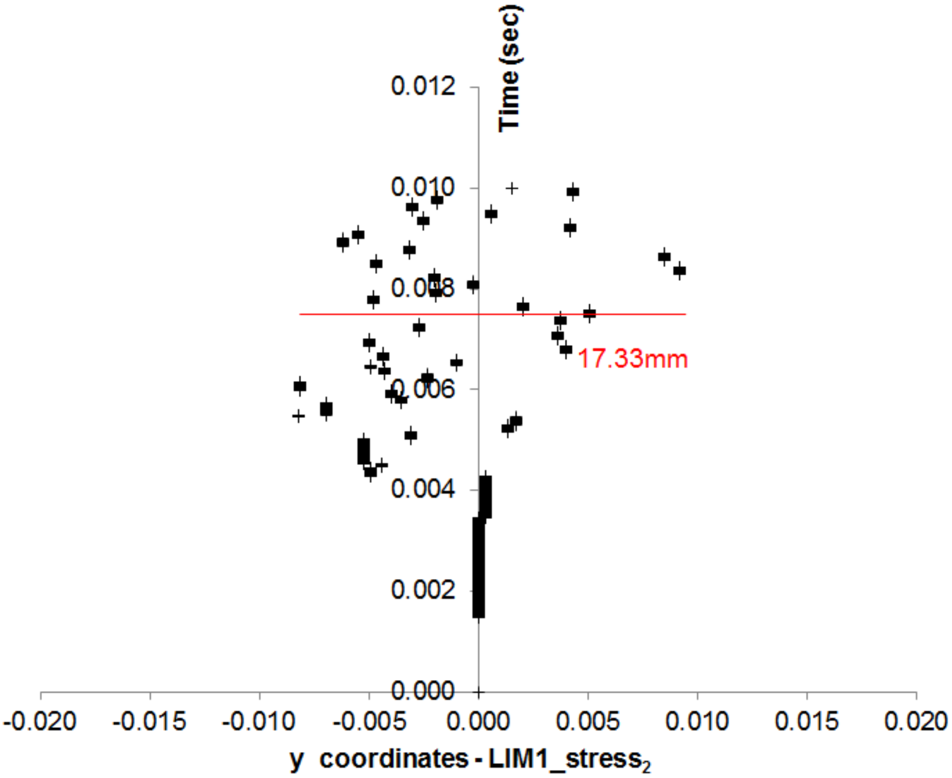
0.012
0.010
0.008
0.006
0.004
0.002
0.000
Time (sec)
17.33mm
-0.020
-0.015
-0.010
-0.005
0.000
0.005
0.010
0.015
0.020
y coordinates - LIM1_stress2

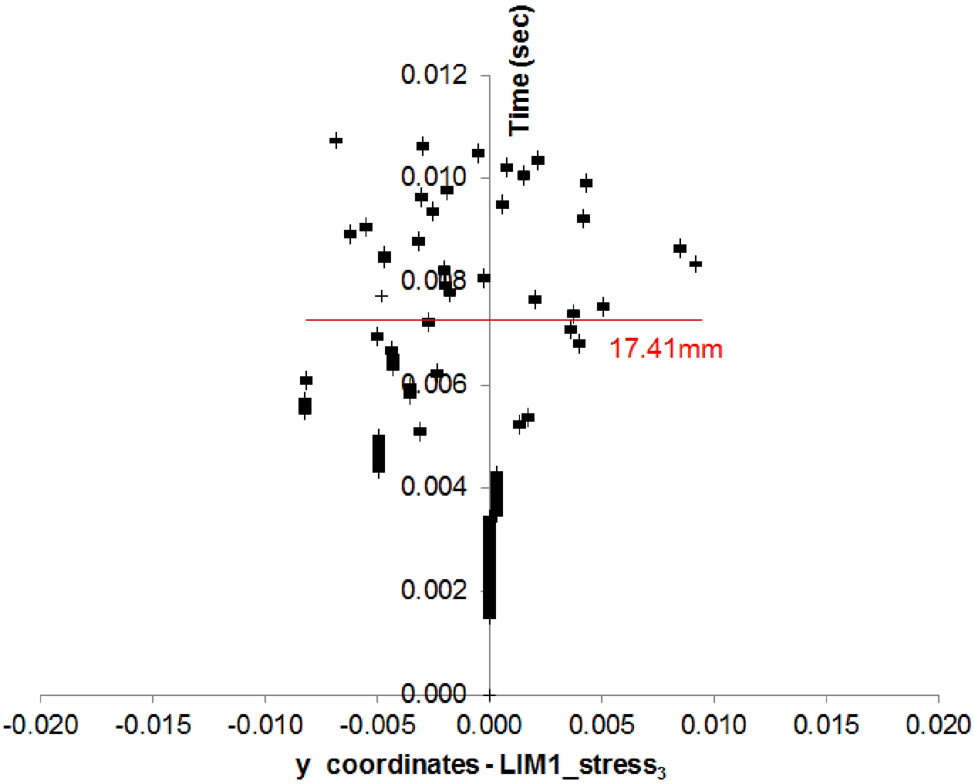
Time (sec)
0.012
0.010
0.008
0.006
0.004
0.002
0.000
17.41mm
-0.020
-0.015
-0.010
-0.005
0.000
0.005
0.010
0.015
0.020
y coordinates - LIM1_stress$_3$

(**b**)

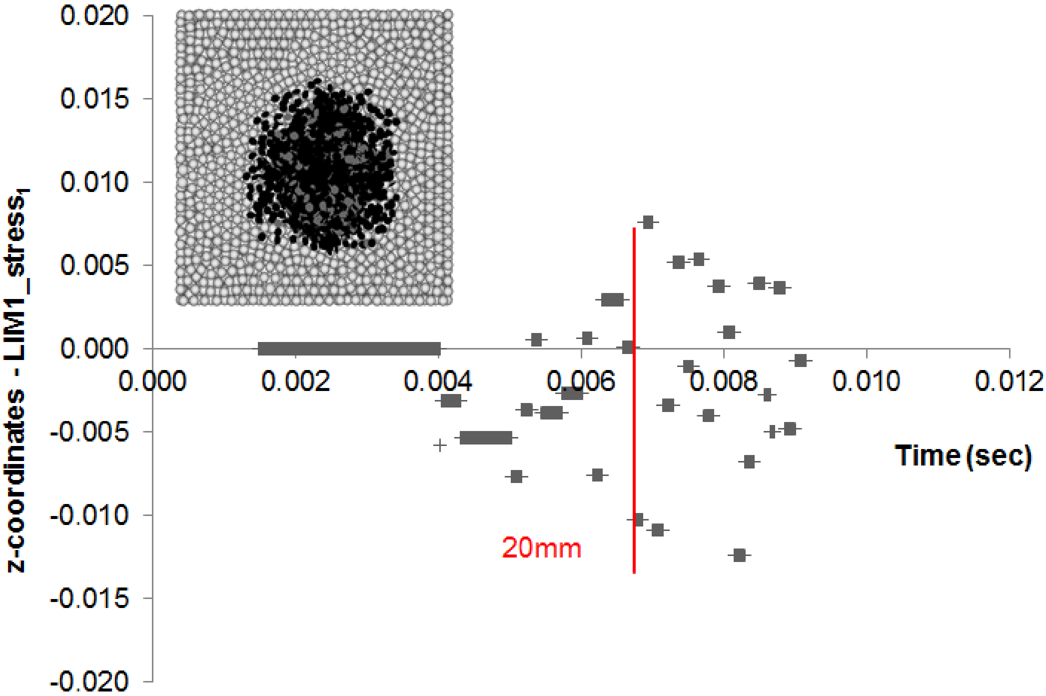
z-coordinates - LIM1_stress$_1$
0.020
0.015
0.010
0.005
0.000
-0.005
-0.010
-0.015
-0.020
0.000
0.002
0.004
0.006
0.008
0.010
0.012
Time (sec)
20mm

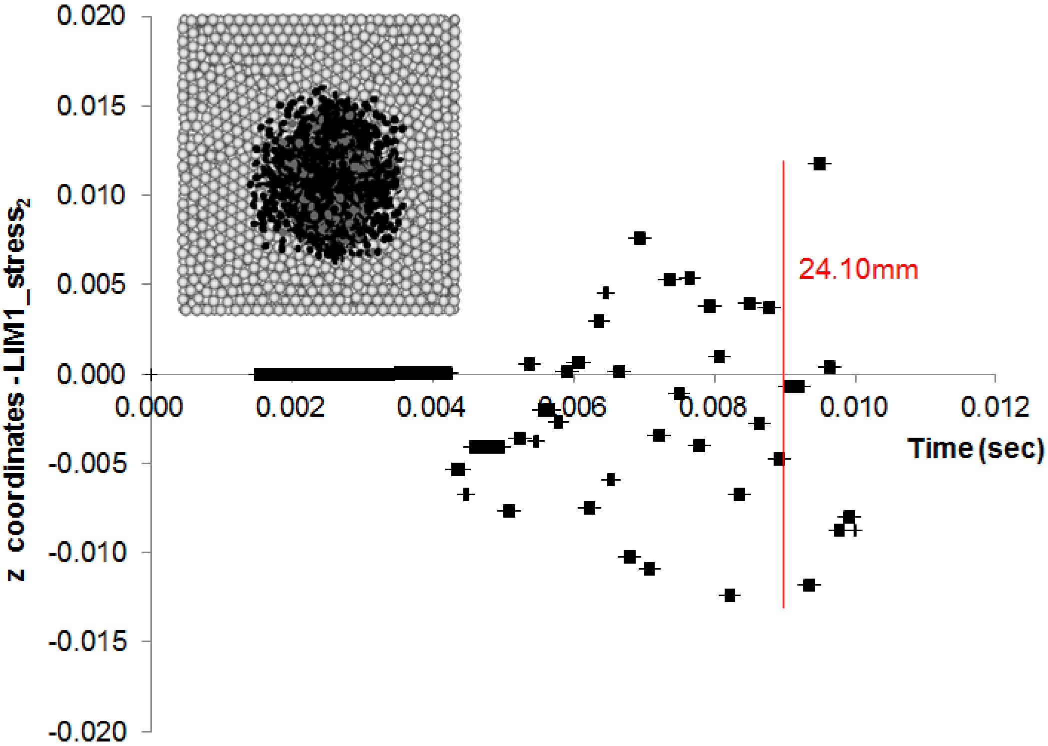
z coordinates -LIM1_stress$_2$
0.020
0.015
0.010
0.005
0.000
-0.005
-0.010
-0.015
-0.020
0.000
0.002
0.004
0.006
0.008
0.010
0.012
Time (sec)
24.10mm

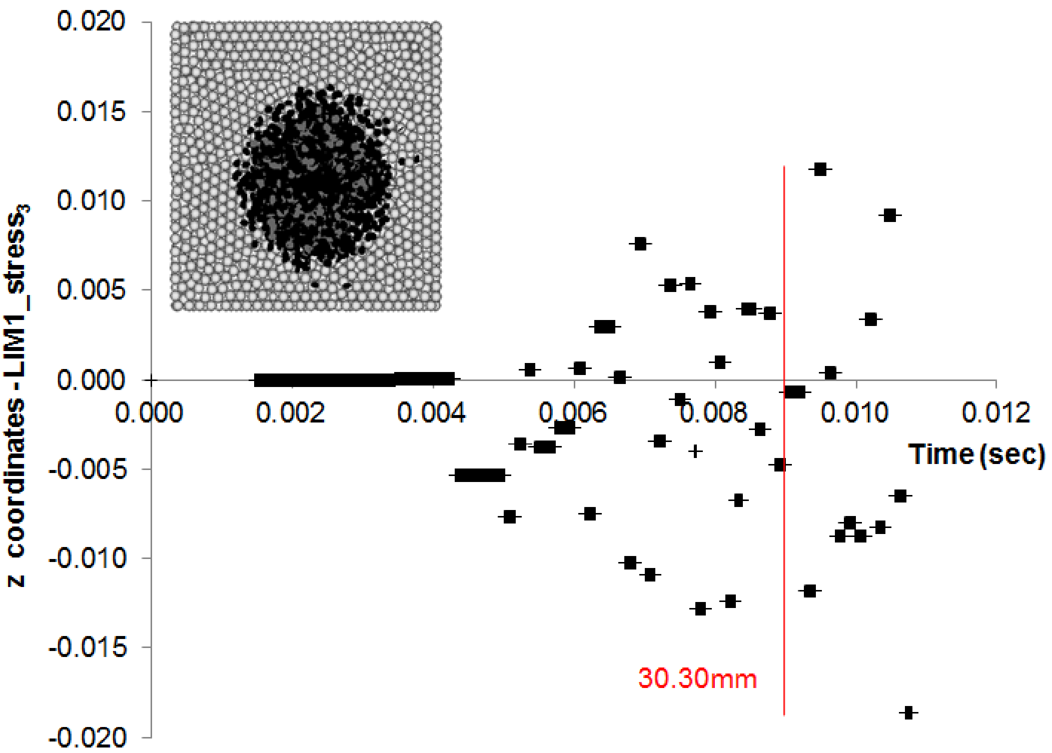

(**c**)

Figure 5.24 Location of micro-cracks and the total fracture expansion for the LIM1_stress$_1$, LIM1_stress$_2$, and the LIM1_stress$_3$ in (**a**) the X direction, (**b**) the Y direction and (**c**) the Z direction.

5.3.3 Effect of multiple pre-existing fractures

The next set of tests showed that the model which contains multiple fractures enhances breakage, as expected, and that the propagation of the micro-cracks extends further in all directions compared to the model with the single fracture. More specifically, comparing the location of the micro-cracks from Fig.5.25, at the end of the test (at a time of 0.012 sec) we observe that the model with the single fracture (LIM1_frac$_1$) has a lower total fracture growth in all directions (16.90 mm horizontally in the X direction, 21.20 mm vertically in the Z direction and 20.57 mm horizontally in the Y direction) compared with the fracture growth of the LIM1_frac$_2$ model (20.18 mm horizontally in the X direction, 25.09 mm vertically in the Z direction and 22.60 mm horizontally in the Y direction) and that the latter claims a wider area of expansion. Even though the propagation of the micro-cracks reveal small differences in the X, Y, Z directions for both samples, we can claim that macroscopically speaking, the overall fracture growth for the LIM1_frac$_1$ (single fracture) extends more along the vertical Z direction,while in the case of the LIM1_frac$_2$ (multiple fractures) the overall fracture growth is also extended more vertically. The disagreement between the conventional theory (Valko and Economides, 1995), and the overall damage of both models can be attributed to the volume of discontinuities due to the network of fractures within each model’s matrix.

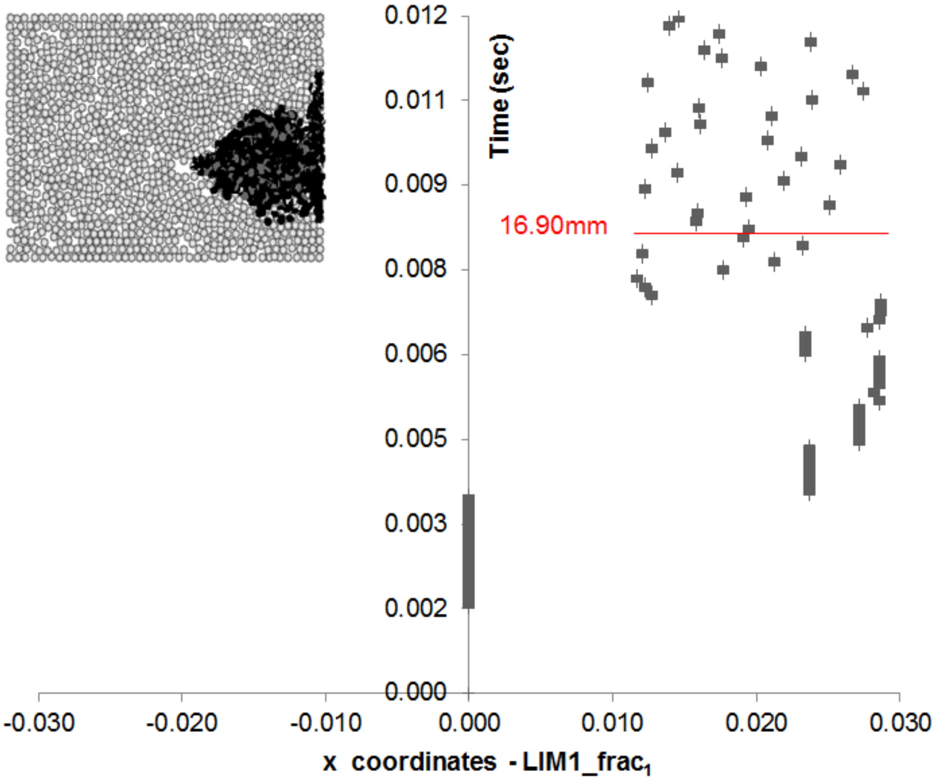

(a)

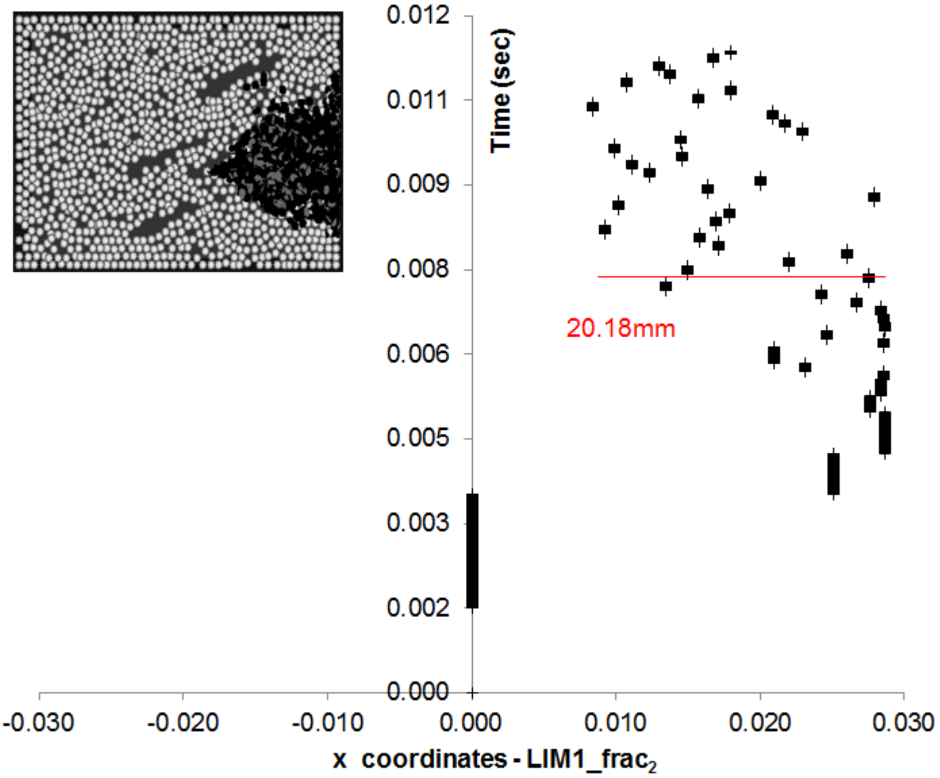
0.012
0.011
0.009
0.008
0.006
0.005
0.003
0.002
0.000
Time (sec)
20.18mm
-0.030
-0.020
-0.010
0.000
0.010
0.020
0.030
x coordinates - LIM1_frac$_2$

(**b**)

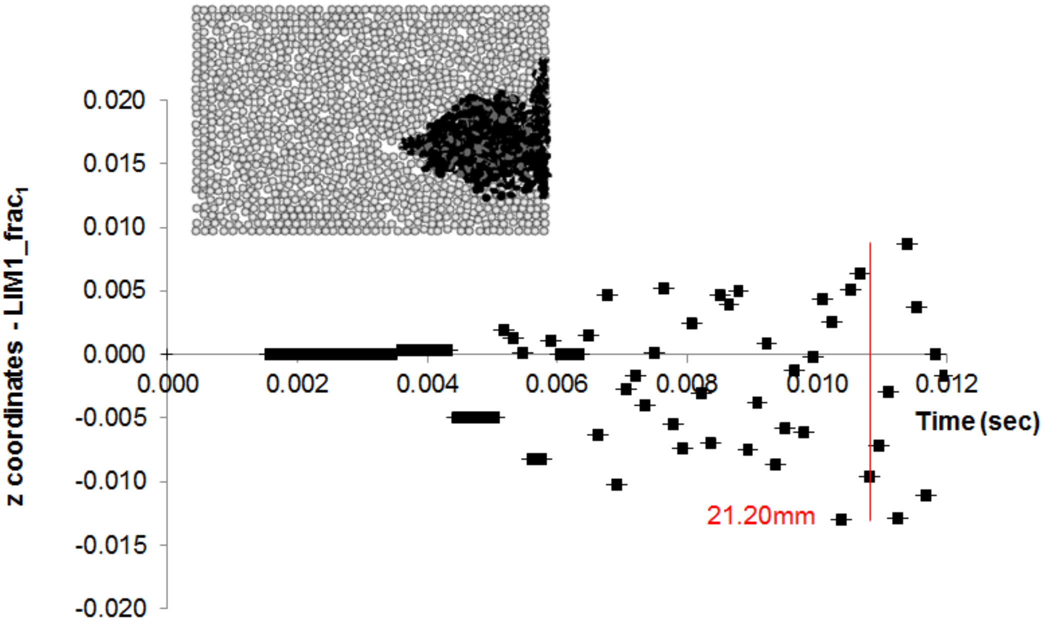
0.020
0.015
0.010
0.005
0.000
-0.005
-0.010
-0.015
-0.020
z coordinates - LIM1_frac$_1$
0.000
0.002
0.004
0.006
0.008
0.010
0.012
Time (sec)
21.20mm

(**c**)

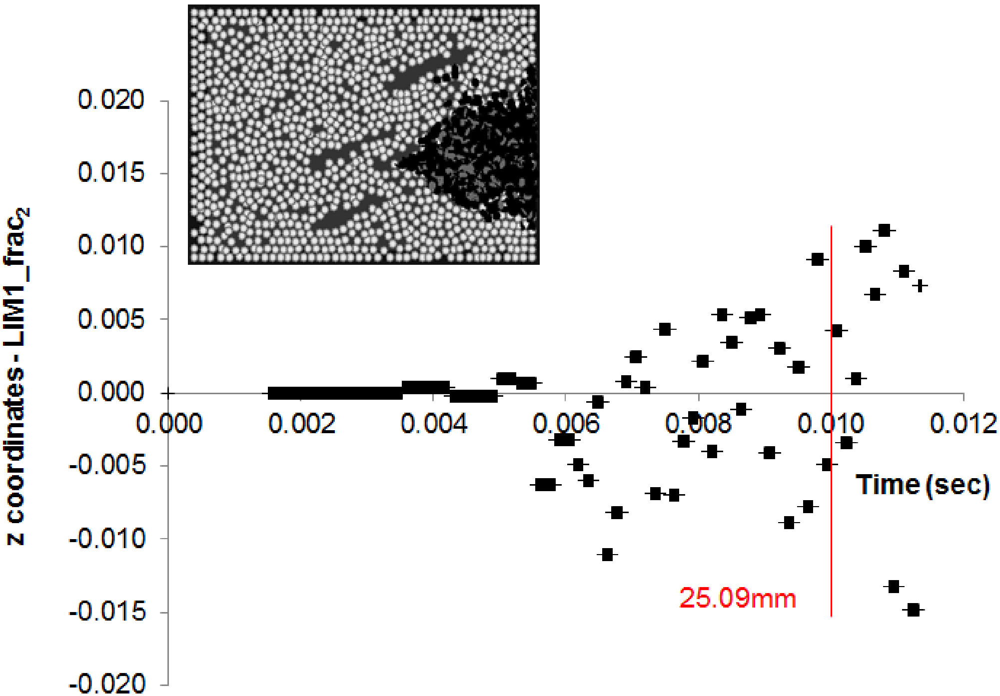
0.020
0.015
0.010
0.005
0.000
-0.005
-0.010
-0.015
-0.020
z coordinates - LIM1_frac$_2$
0.000
0.002
0.004
0.006
0.008
0.010
0.012
Time (sec)
25.09mm

(**d**)

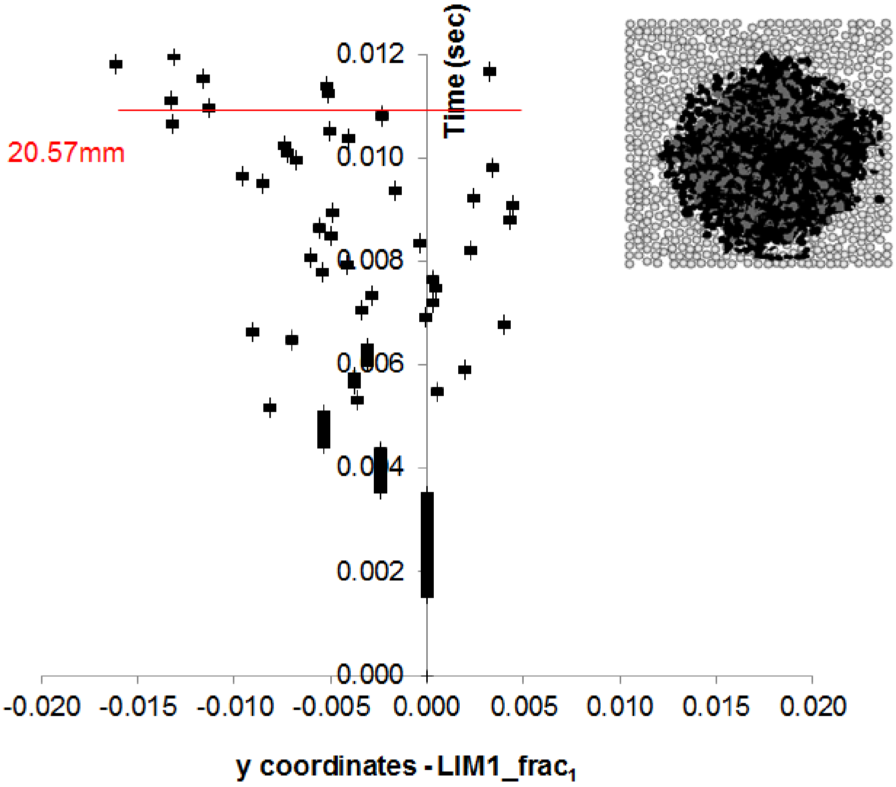
0.012
0.010
0.008
0.006
0.004
0.002
0.000
Time (sec)
20.57mm
-0.020
-0.015
-0.010
-0.005
0.000
0.005
0.010
0.015
0.020
y coordinates - LIM1_frac$_1$

(**e**)

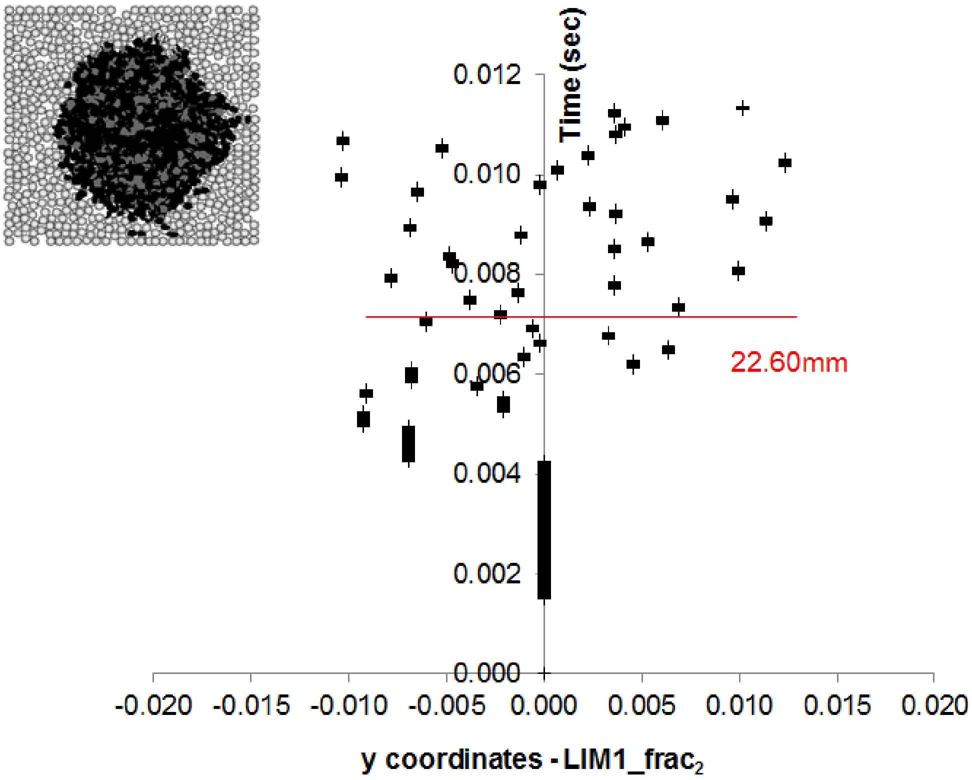

(**f**)

Figure 5.25 Coordinates of the micro-cracks for the LIM1_frac$_1$ and LIM1_frac$_2$ models in (**a**), (**b**) the X direction, (**c**), (**d**) the Z direction, and (**e**), (**f**) the Y direction.

Further insights on the effect of the existing fracture network to the fracturing process is also illustrated in Fig.5.26, which describes the stress profile of the LIM_frac$_1$ and the LIM_frac$_2$ models, respectively, in the X, Y, Z directions. The measurements have been taken from different regions within the model, as indicated by the circles on the pictures. It can be observed that in the case of the LIM_frac$_1$, the dominant stress is in the X direction (σ_{xx}) followed by the vertical stress (σ_{zz}) (Fig.5.26(**a**)-(**d**)), which can be attributed to the high external mechanical load following the direction of the cracking profile from Fig.5.25. In contrast the stress profile of the LIM1_frac$_2$ model does not follow the principal rules of conventional theory and, as the location of its micro-cracks from Fig.5.25 indicate that the principal stress is in the vertical (σ_{zz})

direction for the regions near the fractures (Fig.5.26 (**e**,**f**)). However, the opposite can be observed at the remote locations away from the fractures (Fig.5.26(**g**,**h**)), indicating the effect of pre-existing fractures on the rock's strength. It is observed that the highest stresses are located in the upper part of the assembly, near the fracture tip, for both models and the measurements taken from regions away from the fracture tip provide lower stresses.

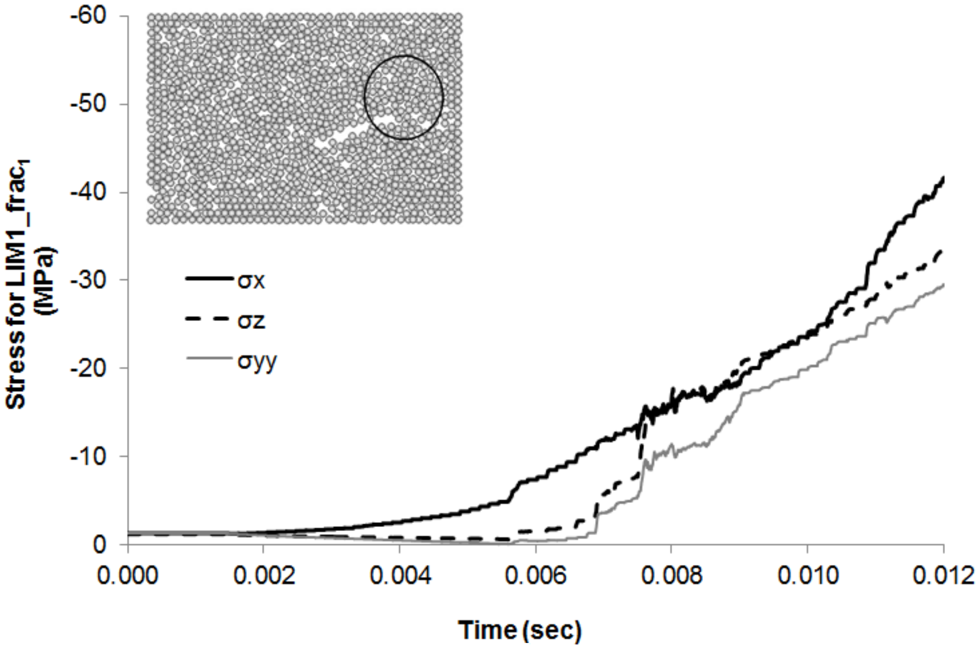

(**a**)

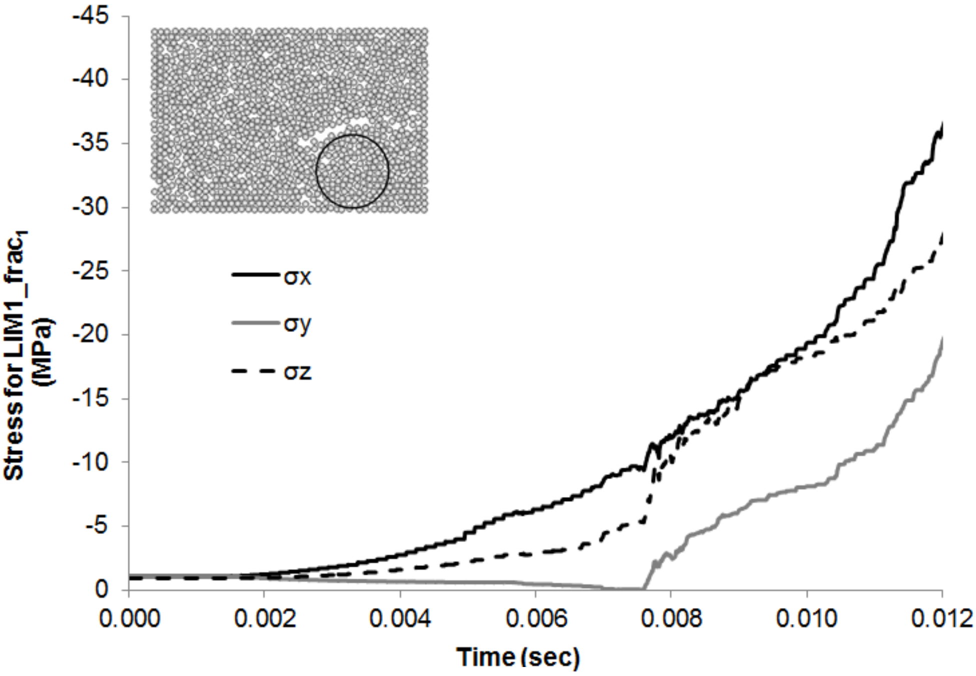

(**b**)

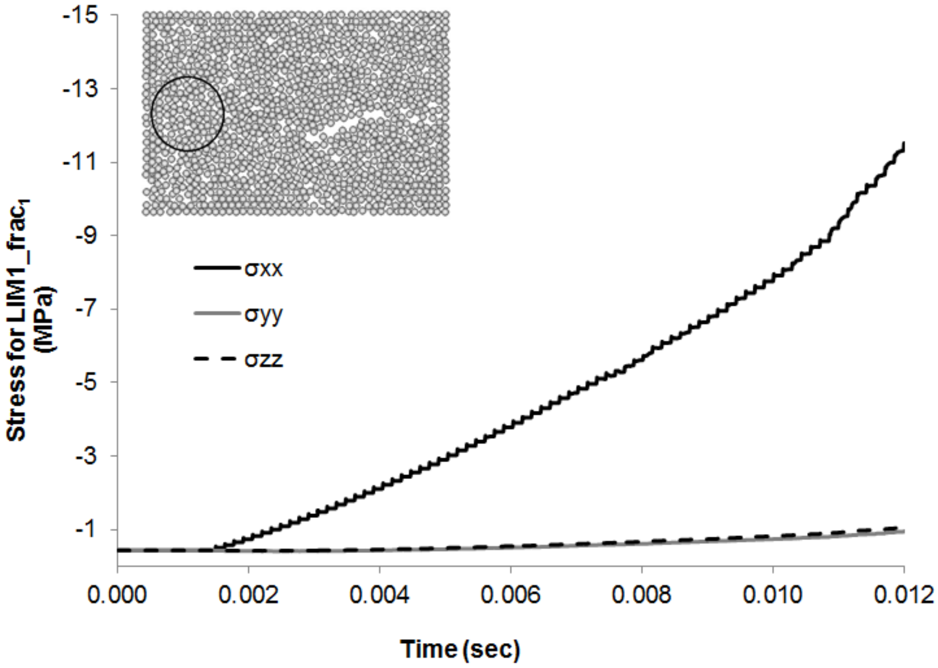
-15
-13
-11
-9
-7
-5
-3
-1
Stress for LIM1_frac$_1$ (MPa)
σxx
σyy
σzz
0.000
0.002
0.004
0.006
0.008
0.010
0.012
Time (sec)

(**c**)

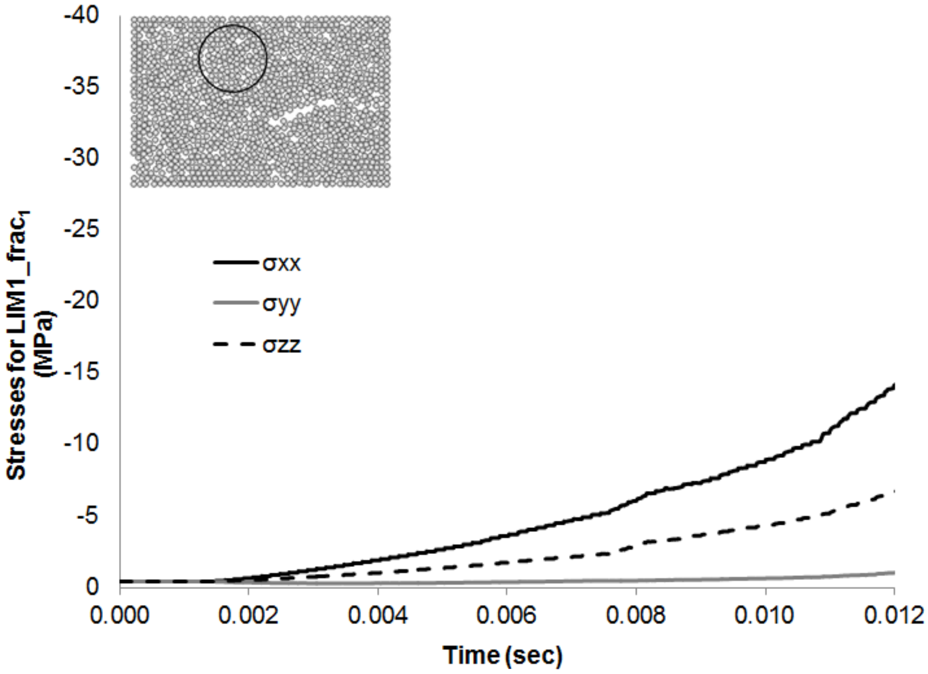
-40
-35
-30
-25
-20
-15
-10
-5
0
Stresses for LIM1_frac$_1$ (MPa)
σxx
σyy
σzz
0.000
0.002
0.004
0.006
0.008
0.010
0.012
Time (sec)

(**d**)

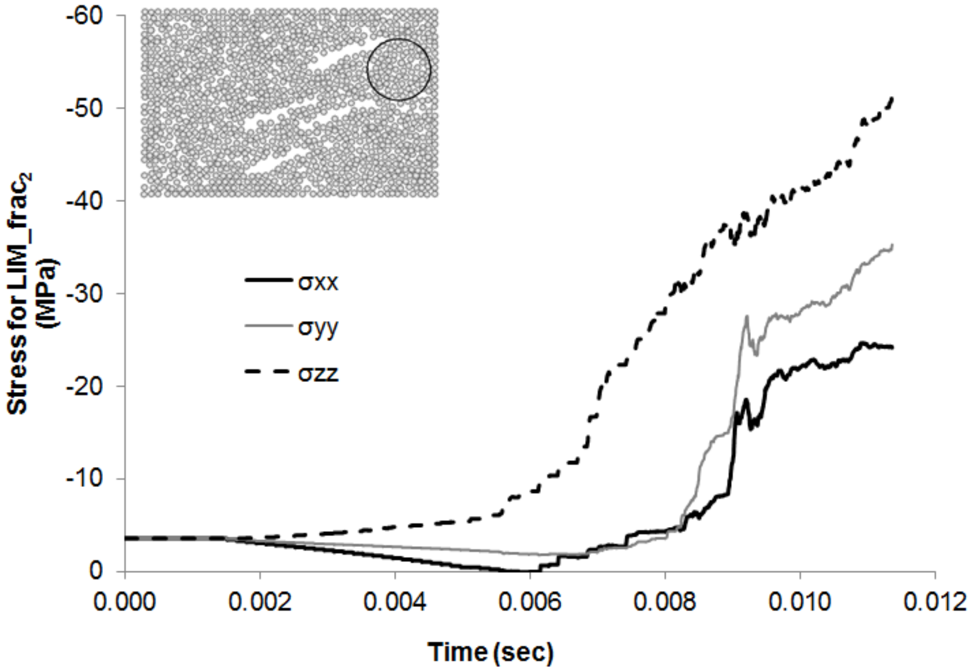
-60
-50
-40
-30
-20
-10
0
Stress for LIM_frac$_2$ (MPa)
σxx
σyy
σzz
0.000
0.002
0.004
0.006
0.008
0.010
0.012
Time (sec)

(**e**)

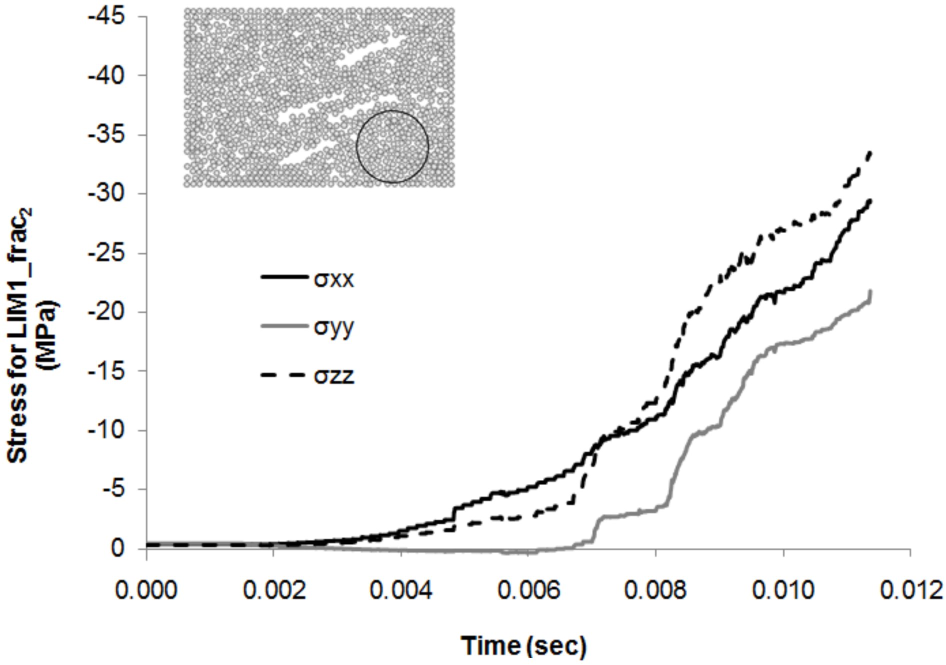
-45
-40
-35
-30
-25
-20
-15
-10
-5
0
Stress for LIM1_frac$_2$ (MPa)
σxx
σyy
σzz
0.000
0.002
0.004
0.006
0.008
0.010
0.012
Time (sec)

(**f**)

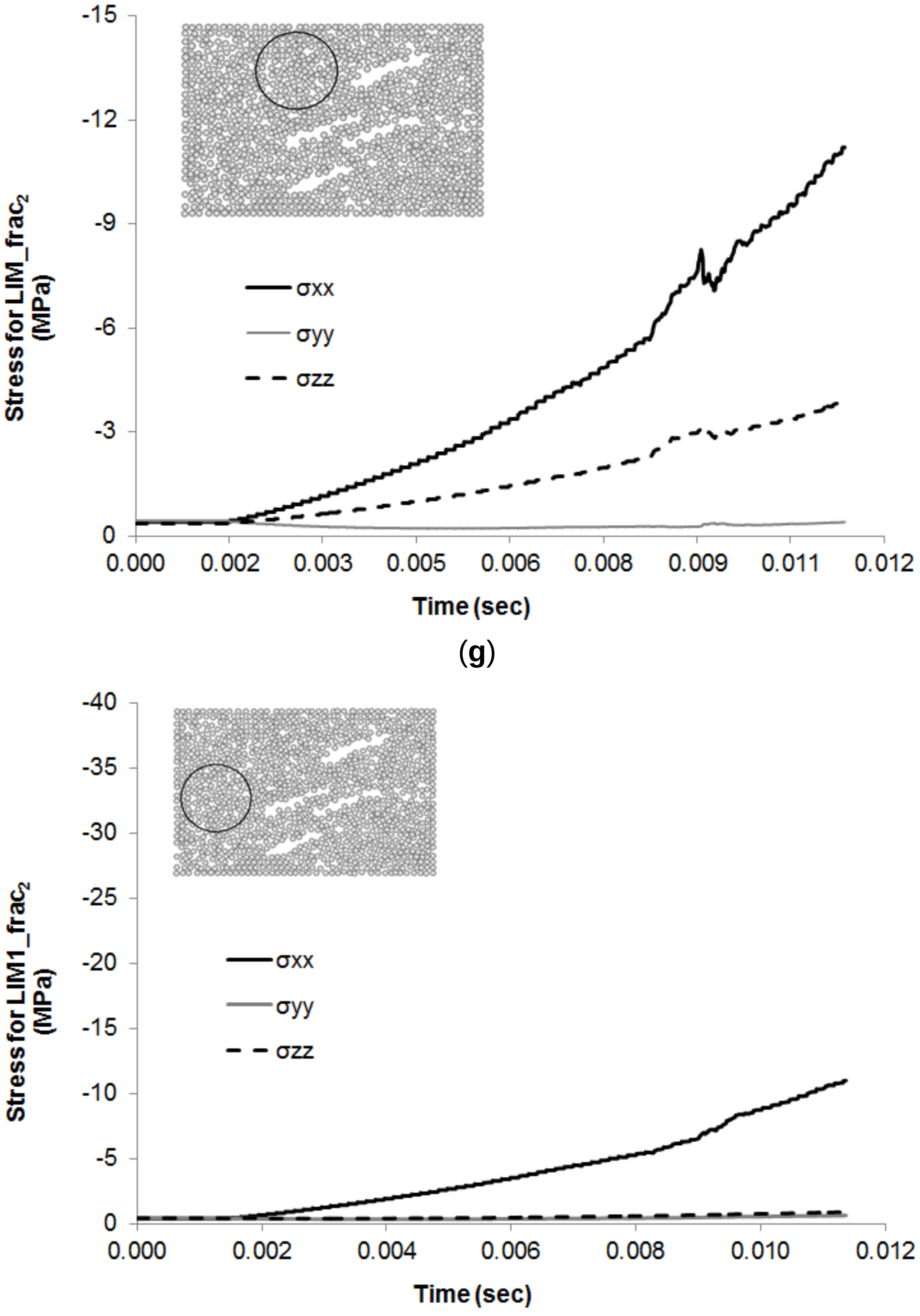

(**g**)

(**h**)

Figure 5.26 Stresses in the X , Y, Z directions versus time in different regions within (**a**),(**b**), (**c**), (**d**) the LIM1_frac$_1$ and (**e**), (**f**), (**g**), (**h**) the LIM1_frac$_2$ model.

Furthermore, Fig.5.27 illustrates the progressive expansion of the micro-cracks at critical injection rate intervals (Fig.5.28) for both the LIM1_frac$_1$ (bottom row) and the LIM1_frac$_2$ (top row) models, and describes the effect of the pre-existing fractures to the fracturing process. It can be observed that at the first interval of 0.30m^3/s, more cracks have been created in the LIM1_frac$_2$ model (around 337 micro-cracks) compared to the LIM1_frac$_1$ model (around 327 micro-cracks). Furthermore, as the test progresses reaching an injection rate of 0.45 m^3/s, the LIM1_frac$_2$ model continues to develop a greater number of cracks than the LIM1_frac$_1$, but a different mode of cracking is observed. Specifically, the LIM1_frac$_2$ forms individual groups of cracks away from the main volume thus enhancing hydraulic conductivity whereas in LIM1_frac$_1$ the cracks initiate and expand as a single large group. The same behaviour, both in terms of volume of micro-cracks as well as fracturing mode, is observed at the 0.53 and 0.60m^3/s intervals and throughout the test in general.

In addition, the information provided by Fig.5.25 suggests that the cracks are propagating faster in the LIM1_frac$_2$ model compared to the LIM1_frac$_1$. This may be attributed to the non-uniform distribution of the stresses, due to the fracturing network, resulting in locally bond breakage. The latter can cause extra non-uniformity within the model, the stresses are centralized elsewhere and this may results in new bond breakage and so on.

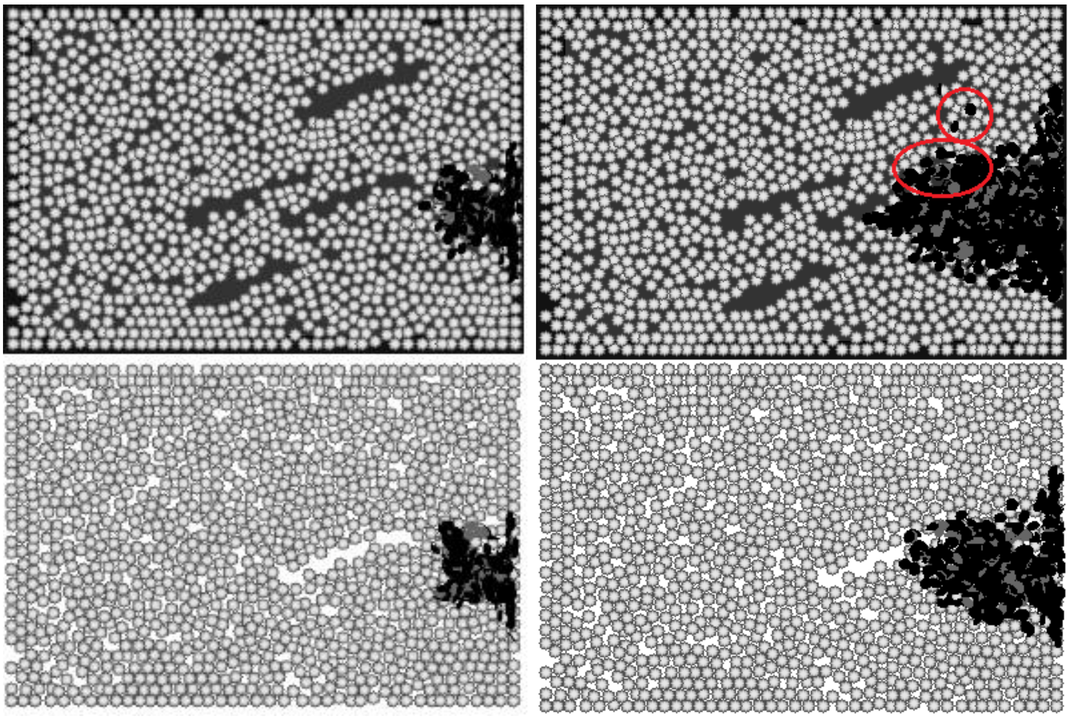

(**0.30m^3/s**) (**0.40m^3/s**)

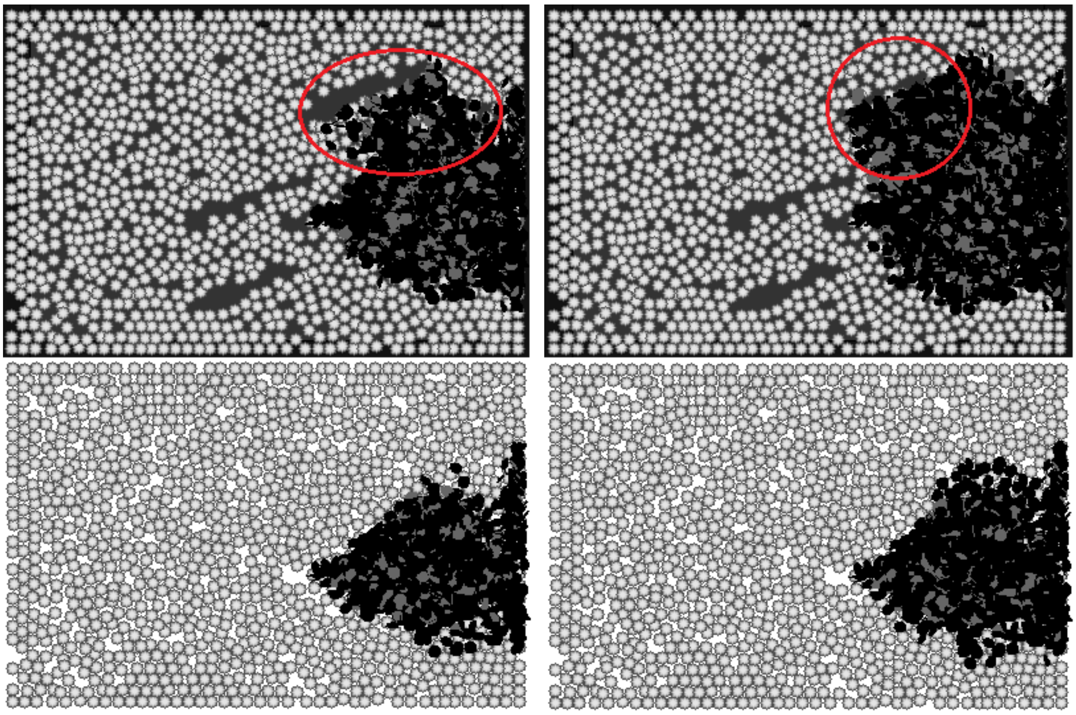

(**0.50m^3/s**) (**0.55m^3/s**)

Figure 5.27 Schematic of the cross section for the LIM1_frac$_2$ (**top row**) and the LIM1_frac$_1$ (**bottom row**) at intervals of the injection rate.

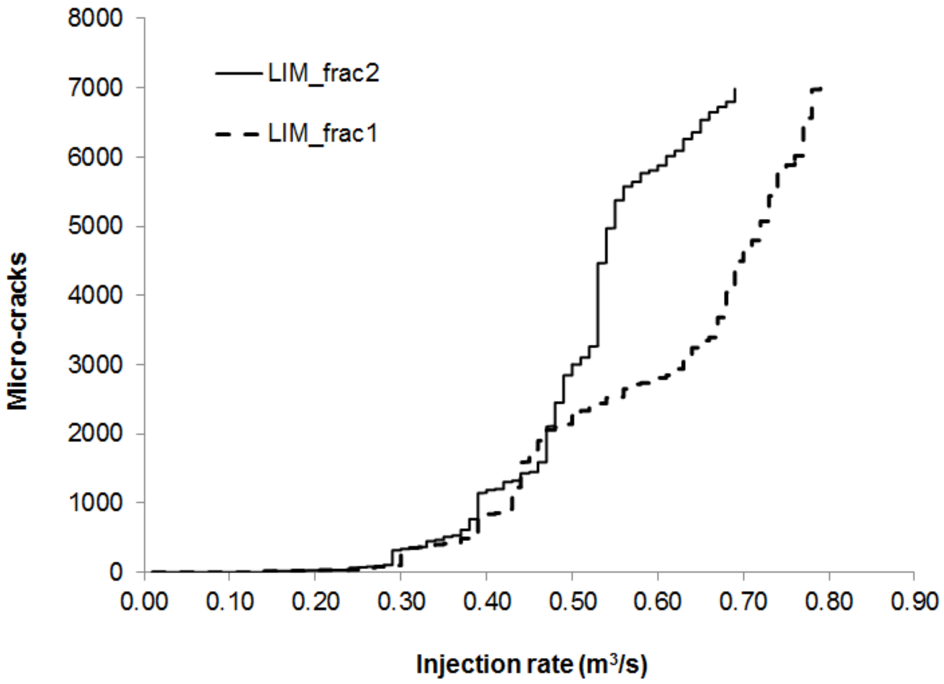

Figure 5.28 Total number of microcracks versus injection rate for the LIM1_frac$_1$ model and the LIM1_frac$_2$ models, respectively.

5.3.4 Fluid viscosity

As expected, when the high viscosity fluid is injected into the model, the crack initiation pressure becomes lower compared to the low viscosity fluid. More specifically, the particles start to separate at an earlier stage (9.2×10^{15} Pa) due to the bond breakage. This means that the inter-particle forces become larger than the maximum bond strength resulting in bond breakage. Moreover, the fluid pressure which leads to failure (about 3000 micro-cracks) is measured to be about 2.59×10^{17} Pa, which is lower compared with the low viscous fluid (about 3.5×10^{17} Pa). The fact that the crack initiation pressure, as well as the pressure that leads to failure is lower for the high viscous fluid, is opposite compared with the observed behaviour in samples from other reserachers (Shimizu et al., 2011; Ishida et al., 2012), indicates the influence of the pre-existing fractures to the cracking mechanism. More specifically, in intact rocks the breakdown pressures tend to be lower for low viscous fluids, compared with high viscous ones. Therefore, the presence of pre-existing fractures within the sample, allows more space for the fluid to travel, combined with the fact that the low viscous fluid can travel easier through the fractures, thus require additional pressure build up in order to reach the same amount of damage. Moreover, in both cases of the low and high viscosity fluids, tensile cracks (normal, with respect to the bond plane) are dominant, over the shear cracks, with their percentage being about 81% for the LIM1_fluid$_1$ and about 89% for the LIM1_fluid$_2$ sample, as shown in Fig.5.29.

Table 5-1 includes the measured values for the crack initiation and the failure pressure, as well as the total number of micro-cracks in the tensile and shear directions for both cases of the low and the high viscosity fluids, respectively.

Furthermore, it is observed that the cracking behaviour of the model is more aggressive; cracks propagate further under the influence of the high viscosity fluid and that the overall damage expands in several areas (Fig.5.30 (A), (B), (C)), creating secondary branches, rather than that of a propagation as a main volume. Fig. 5.30 illustrates the state of the damage of the model when it reaches about 3000 micro-cracks.

It can be observed that in the case of water (top picture) the cracks appear to expand as a unity, whereas in the case of the high viscosity fluid (bottom picture) the cracks appear to abandon the central volume of cracks and are reconfigured in individual groups that propagate further, thus covering the distance from the injection point up to the base of the fracture in the xz plane (red circles).

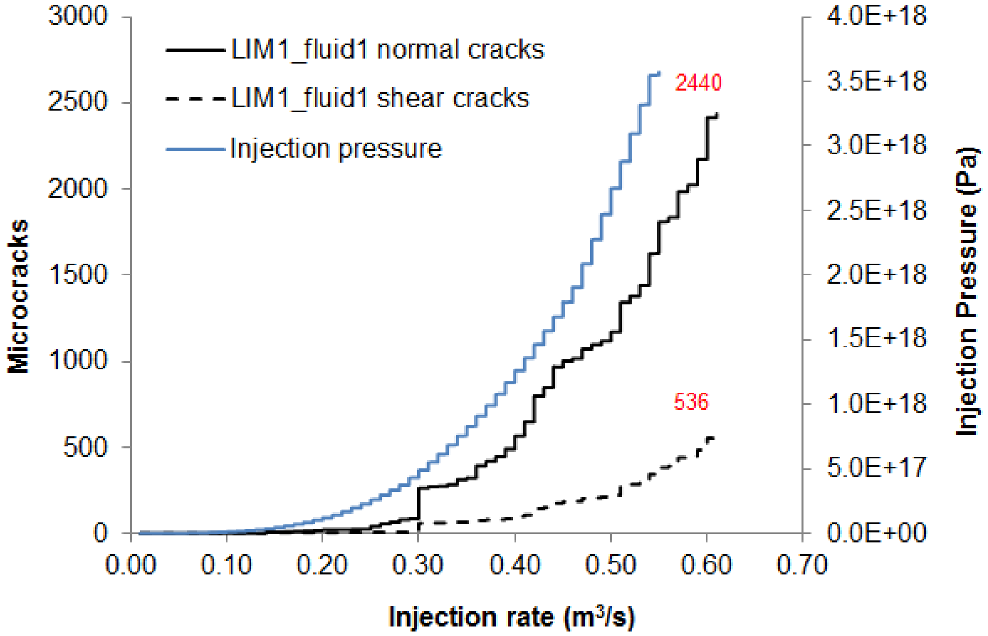

(**a**)

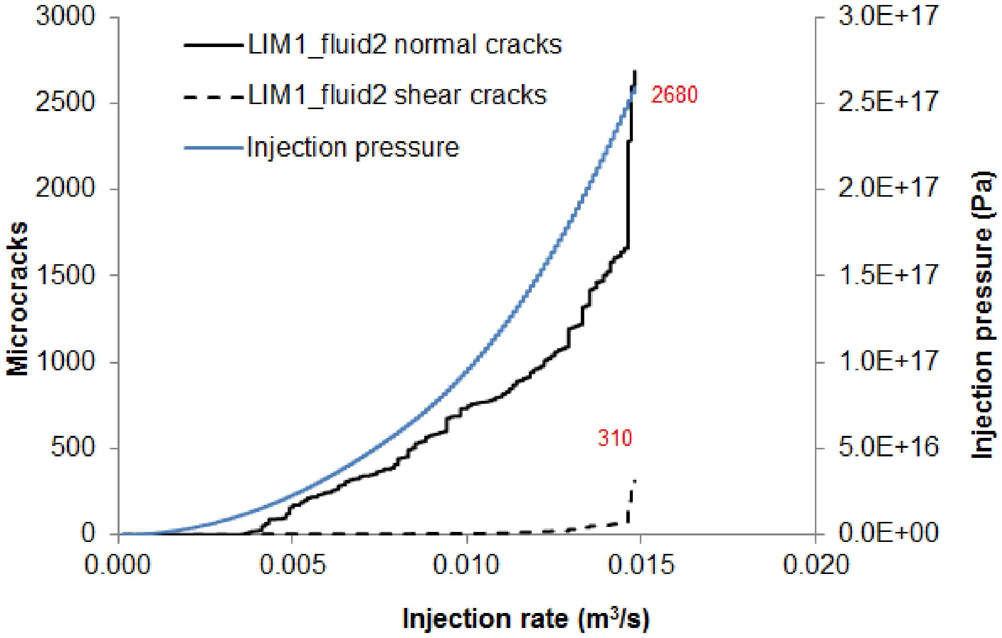

(**b**)

Figure 5.29 Microcracks in the normal and shear direction versus the injection rate for the (**a**) LIM1_fluid$_1$ and (**b**) LIM1_fluid$_2$ samples, respectively.

Table 5-2 Crack initiation and failure pressure and the total number of micro-cracks in the normal and shear directions for the low and high viscosity models.

	Fluid pressure		Micro-cracks	
	Crack initiation Pressure P_i (Pa)	Failure pressure P_f (Pa)	Normal direction	Shear direction
LIM1_fluid$_1$(low)	3.0×10^{16}	3.27×10^{18}	2440	536
LIM1_fluid$_2$(high)	9.2×10^{15}	2.59×10^{17}	2680	310

The objectives of Chapter 5 are the computational modelling of a hydraulic fracturing test for a naturally fractured limestone sample, the analysis of its mechanical behaviour and the interaction between the natural fractures and the new hydraulic fractures. A parametric study of (i) the angles of invidual induced fractures, as well as induced fracture network, (ii) the external stress regime, and (iii) the fluid viscosity, attempts to shed more light on how a fractured rock and the aforementioned parameters can influence and possible enhance the fracking process.

It analyses the mechanical response of the rock model due to fluid flow by using the fluid-couple DEM code in a number of hydraulic fracturing simulations. It involves detailed monitoring of the initiation/propagation of micro-cracks, analysis of the stresses in different regions within the rock's matrix and evaluation of the relation between the energy release and the development of cracks. Observations of the simulated fracking tests show that the angle of the fracture directly relates with the stress pattern within the model, thus affecting the direction and propagation of cracks.

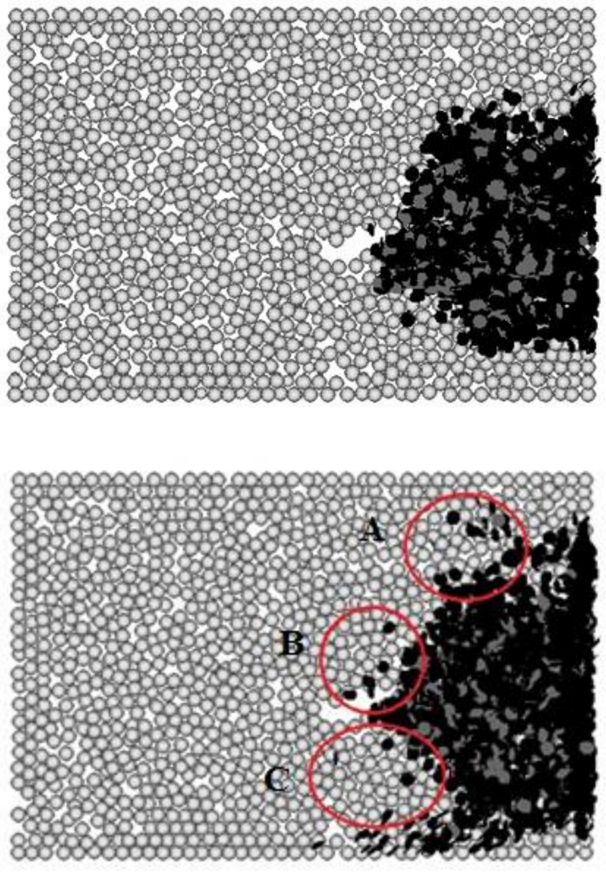

Figure 5.30 Expansion of micro-cracks before the termination of the test for the low viscosity LIM1_frac$_1$ (**top**) and the high viscosity LIM1_frac$_2$ (**bottom**) models.

It can be concluded that the cracking behaviour for angles below 45^o is followed by high stresses and expands mainly downwards as a group of cracks, whereas for angles above 45^o the microcracking forms clusters that stray from the main volume of cracks. In the single pre-cracked samples, the fracture is mainly observed towards the horizontal X axis, namely along the direction of the maximum compressive principal stress, and this is in agreement with the conventional theory, whereas in the case of the pre-carcked sample with multiple fractures the overall fracture is extended perpendicular to the maximum compressive stress. In addition, a relation between the important cracking events (large increases of micro-cracks) in each model with the energy release within the models, has been observed. Finally, highest stresses have been observed in the upper part of the assembly, near the fracture tip, whereas the measurements taken from regions away from the fracture tip provide lower stresses.

Modelling of this nature, where natural fractured rocks are submitted into hydraulic fracturing and studied in the particle-scale, are in an early stage and therefore this study attempts to provide further insights.

The complete code that describes one of the simulations of the horizontal fluid injection to the pre-cracked limestone sample (LIM1_15^{o}) has been included in Appendix III. Furthermore, the codes that describe the rest of the simulations of Chapter 5 are similar with the aforementioned code and include fractures and measurement spheres at different locations.

Chapter 6 Conclusions and Future Work

6.1 Summary

This thesis presents a computational modelling of hydraulic fracturing tests on hard rocks (limestone) based on the DEM approach. It includes a detailed description of the calibration procedure in order to validate the developed DEM model and its mechanical parameters against the mechanical parameters of a real rock. During the calibration procedure, which includes a series of UCS, Brazilian and SENB simulations, 13 simulated calibration tests in total were performed and all the results obtained were found to be in very good agreement with the data provided from the literature and/or from previously reported experimental work. The aim of this thesis is to simulate different types of fracturing experiments, based on the DEM approach, and to observe the mechanical behaviour of the material at the particle-scale. Also a parametric study on parameters, such as the volume and the orientation of fractures, the external stress regime and the fluid viscosity, that either affect or enhance the fracturing process of hard rocks has been included herein. The aforementioned fracking tests include the simulation of a hydraulic pressurisation of a hollow cylinder, with model configurations almost identical to the conditions of the laboratory test, and also a simplified version of a horizontal fluid injection. The latter has not been validated against a laboratory experiment, nevertheless it is considered a simplified version of a real case scenario.

Moreover, the mechanical response of the rock specimen to the fluid injection is analysed by evaluating the volumetric flow rate at which the fluid is discharged, the initiation and propagation of the cracks through the simulated model, the relation between its UCS strength and the failure pressure and the influence of the aforementioned parameters to the fracking process. Next, a concept for relating the fracture toughness of the PFC sample, obtained from SENB laboratory tests, with the fracture toughness based on the DEM approach, has been suggested and described. Additional research steps are required, which include the generation of more samples in order to produce a more accurate version of the equation that describes more efficiently the relationship between the fracture toughness of a material and the DEM correlation factor.

In the PFC, a generalised form of the Navier-Stokes equation that accounts for fluid-solid interactions is solved using a grid fluid flow scheme and these formulations have been adopted herein firstly by, incorporating this technique into the DEM simulation of a bonded particle assembly representing an intact material. Secondly, an extension of its applicability is demonstrated via the modelling of the hollow-cylinder laboratory test, where applications involving direct numerical and experimental comparisons are still lacking, and the horizontal fluid injection into the pre-cracked discrete element model.

6.2 Conclusions

A summary of the key outcomes is as follows:

(a) **Chapter 3**: The estimation of the mode I fracture toughness of a rock is one of the most important mechanical parameters that determines its resistance towards failure. However, limited simulated SENB tests have been performed in hard rocks due to the difficulty of relating the real value of the fracture toughness with the one obtained from the simulated tests. This is due to the fact that there is no clear relationship which can correlate the formulations used in LEFM, to calculate the mode I fracture toughness of a material, with the equations employed by DEM methodologies. Therefore, Chapter 3 suggests and describes a concept for relating the general case of the mode I fracture toughness of a limestone material, which contains an inclined fracture, derived from the LEFM, with the equivalent fracture toughness based on the DEM approach. Also a simplified relationship that directly relates the real value of the mode I fracture toughness of the limestone rock with the micro-properties of its corresponding virtual assembly has been proposed. Nevertheless, additional research steps are required, which include the generation of many samples in order to produce a more accurate version of the approximate solution that describes the relation between a correlation factor (μ), relating the real fracture toughness of the material measured in the laboratory and the fracture toughness (K_I) obtained from DEM simulated tests, as well as the relationship between the real fracture toughness and the tensile strength of the parallel bonds of its corresponding model.

(b) **Chapter 4**: From the hydraulically pressurised simulated test, which has been described in Chapter 4, the following observations have been made:

(i) For the PFC hollow cylinder sample, both the tangential and radial stresses change almost linearly with the applied fluid pressure, bringing the numerical results in good qualitative agreement with the analytical results obtained from Lame’s theory. Quantitatively, a difference in the magnitude of the stresses has been observed, and this can be attributed to the fact that the Lame’s equations assume a continuous medium whereas the virtual PFC model is non-continuous. The agreement between the numerical and analytical results can also validate the fact that the bonded-assembly (DEM) approach, followed by the PFC software, is specifically designed to reproduce stresses-strains in microscopic media and that Lame's theory can be adequately applied.

(ii) The overall behaviour of the virtual model was found to be in very good agreement with the behaviour of the rock material in the laboratory experiment. More specifically, the failure at the outside perimeter of the hollow cylindrical sample is observed to propagate at a lower rate, compared to the microcracking of the inner surface. Also, the damage at the hollow cavity begins from the vicinity of the inner surface and expands outwards as a result of the stress distribution, leading to total collapse of the sample. In addition, the fluid pressure that leads the PFC model to fail is found to be close to the material's UCS strength measured by the uniaxial simulation (45 MPa). Finally, the fracturing pattern is dominated by the shear and compressive stresses.

(iii) The failure pattern is in agreement with Lame's theory that indicates all the principal stresses are compressive and even though the highest radial compressive stress occurs at the outer surface, the maximum compressive stresses are tangential and act in the vicinity of the inner diameter of the hollow cylinder. This results in relatively compressive stresses towards the inner surface. The longitudinal stress remains constant and acts in the axial direction, whereas the shear stress is maximum at the inner surface of the hollow cylinder.

(iv) The simulated flow rate is observed to agree better with the Darcy's flow rate than to the steady-state flow rate. A possible explanation is that the steady-state solution refers to an idealised flow, with the pressure gradient and particle drag forces being much greater than the viscous losses. This is due to the assumptions made that relate the viscous losses to the macroscopic fluid velocity. Further, the steady-state solution assumes uniformity in the velocity gradient and this results in an underestimation of the losses due to the viscous stresses.

(c) **Chapter 5**: From the horizontal fluid injection simulated test, which has been presented in Chapter 5, the following observations are made:

(i) The pressure (P_f) that corresponds to the damage limit of the material (2000 micro-cracks), and hence the end of the first set of tests, is observed to reduce for fractures below 45°. The opposite behaviour has been observed for fractures 45° and upwards, marking the 45° fracture a critical value. In addition, the shallow angles require additional injection which may be attributed to the fact that the low angle is close to zero and thus can be considered horizontal, and therefore not favouring the horizontal fluid movement.

(ii) The microcracking has been extended considerably in the horizontal X and vertical Z directions, looking from the microscopic point of view, with the horizontal expansion gaining ground in cases where the angle of the pre-existing fracture is below 45°. However, the combination of the external stress regime and the angles of the inclined fractures have altered the propagation of cracks, where the overall fracture growth is observed to extend along the vertical Z direction. This means that even though the maximum compressive stress is horizontal, the effect of the confining stress combined with the heterogeneity of the material, due to fracture, affects the orientation of the hydraulic fracture. This effect is restricted in magnitude by the sample dimensions and the need for computational time efficiency.

(iii) The angle of the propagation, with respect to the XZ plane, is directly related with the stress pattern within the model, thus affecting the direction and propagation of the cracks. It can be concluded that for angles below 45^o the internal stress regime below the fracture is always higher than the one in the upper part of the model and thus the cracks tend to propagate downwards and travelling mostly as a group of cracks. In contrast, for angles above 45^o there is the opposite stress regime and the cracks form clusters that stray from the main region of the cracks. In addition, it has been observed that the highest stresses are located in the upper part of the assembly, near the fracture tip, compared with the measurements taken from regions away from the fracture tip provide lower stresses.

(iv) It has been observed that there is a clear relation between the important cracking events (large increases in the micro-cracks) in each model with the energy release within the models. This validates the claim that bond breakage causes further movement of particles and therefore increases the internal kinetic energy of the material.

(v) The presence of multiple pre-existing fractures within the rock’s body is observed to enhance breakage, with the microcracking extending further and faster in all directions compared with a single pre-cracked sample.

Also it has been observed that the overall fracture growth is extended perpendicular to the maximum compressive stress.

(vi) Finally, injections with high viscosity fluids force the sample to earlier bond breakage than in the case of the low viscosity fluid, and to a more aggressive cracking behaviour. The latter includes overall damage which expands in several regions, thus creating secondary branches, rather than that of a propagation as a main volume of cracks. Further, tensile cracks are observed to be dominant in both cases (of low and high viscosity fluids).

6.3 Original contributions

Overall, this thesis presents the simulations of the hydraulic fracturing experiments using three-dimesional modelling and captures the mechanical phenomena within the sample in the particle-scale. A significantly original observation is the fact that the modelling results confirmed the importance of compressive and shear cracking in the hydraulic fracturing process, whereas conventional theory relates hydraulic fracturing with tensile cracking.

In addition, modelling of this nature where rocks are subjected to hydraulic fracturing is currently at an early stage, therefore, models developed in this thesis will provide a better understanding of the hydraulic fracturing process by performing 3D simulation of horizontal fluid injection in pre-cracked hard rocks at the meso-scale.

From the simulations results it can be concluded that the presence, both in volume and in orientation, of pre-existing fractures within the sample affect the mechanical behaviour of the rock samples during the hydraulic fracturing process in terms of different initiation and propagation of the damage and microcracking.

The effect of the external stress regime was not dominant in this study due to the combination between the scale of the sample and the large injection rate, however this is not expected to be the case in macro-scale conditions of a real reservoir.

Finally it was observed that the more viscous fluid lead to a more aggressive cracking profile with secondary regions of cracking away from the main volume.

The 3D DEM models, employed in this thesis, interpret complex macroscopic behaviours and provide more realistic representation of the fracturing behaviour without using complex constitutive equations.

6.4 Future work

Modelling the failure mechanism of hard rocks is a challenging task and the presence of pre-existing discontinuities (fractures, faults) makes the problem even more complex. Engineering problems, which have been performed in the laboratory, such as hydraulic pressurisation on hollow cylinder rocks, or simplified versions of industrial applications, such as horizontal fluid injection, can be adequately explained from the results obtained from the DEM simulations. In order to fully understand the fracking mechanism for the successful design of relevant EOR/EGR applications a more detailed 3D simulations and analysis is required. Future work may include topics such as:

- The micro-scale 3D modelling of pre-cracked rocks using a larger variety of fracture angles ranging from 0^o to 180^o with fine granularity so as to explore with more detail the effect of the fracture orientation on the cracking profile. As a further step, multiple fractures could be combined to form an extensive fracture network. Finally, parameters such as the width and length of each fracture of the network could be randomized to represent a more realistic scenario.

- The exploration of various injection and fluid conditions with respect to injection rate, fluid viscosity and density, as well as studying the effect of radial injection. Moreover, multi-phase fluid injection could also be explored, along with its associated parameters. This could be a particularly interesting topic since it is directly related with practical engineering problems encountered in the petroleum industry.
- The transition to 3D DEM modelling of a pre-cracked macro-scale structure, such as a reservoir, in order to improve the accuracy of modelling the field scale hydraulic fracturing process with the considerations and benefits of the microscopic mechanisms. However, this would mean overcoming the requirements for extensive simulation time and increased processing power.
- The validation of an extended 3D model, similar to the ones described above, against field data obtained from the experimental and laboratory study of an actual reservoir or rock sample.
- The study, in the micro-scale, of fluid flow in porous rocks using advanced imaging techniques such as SEM, X-Ray CT and MRI scans, etc. Such an investigation could yield important information with respect to permeability, pore network conductivity and its influence on trapping and transport of immiscible fluid phases. Also flow patterns, porosity profile and could be explored. This obtained experimental data could then be

used to validate a DEM model and also be part of further parametric study during simulation.

- The 3D modelling of fluid flow in inhomogeneous formations containing more than one material, such as unconsolidated rocks. Other inhomogeneities, such as hydrates, can appear either as solid particles within the pore space blocking the fluid flow, or as structures enveloping the grains of the formation. Of particular interest would be to study the interface between the fluid and the solid, both in single-phase and multi-phase cases.

Appendix I: Calibration Procedure

```
;######################
; Uniaxial Test
;######################
set random              ;Each time the test runs, the generated assembly is unchanged
call %fist%\2d_3d\fishcall.fis
call %fist%\2d_3d\md_setup.fis
call %fist%\2d_3d\md.fis
call %fist%\2d_3d\flt.fis
call %fist%\3d\et3.fis

SET md_run_name = 'Uniaxial_test'
title Test sample Genesis procedure
; ======================
; Define sample parameters
; ======================
def mg_set
mg_quiet=1
mv_shape = 0
mv_Wx = 37.8e-3
mv_Wz = 37.8e-3
mv_Hp = 100e-3
mt_eq_lim=0.01
mg_ttol=0.5
target_poros = 0.15
mg_wfac=1.1
mg_Nf=3
; ===============
; Define ball properties
```

```
; ===============
mg_Rrat=1.0
mg_Rmin=1.0e-3
ball_dens = 2600
ba_bulk(1) = 1
ba_Ec(1) = 30e9
ba_krat(1) = 1.0
ba_fric(1) = 0.6
command
	SET gravity=0 -9.81 0
end_command
; ===================================
; Define parallel bond parameters
; ===================================
 pb_add=1
 pb_Rmult(1)=1.0
 pb_krat(1)=1.4
 pb_Ec(1)=20e9
 pb_sn_mean(1)=30e6
 pb_sn_sdev(1)=30e4
 pb_ss_mean(1)=39e6
 pb_ss_sdev(1)=30e4
 command
	SET gen_error
end_command
mg_ts0 = -0.4e6
mg_nfrat=0.0
mt_UCS = 1
mt_ttol=0.5
```

```
mt_eq_lim=0.0001
mt_eq_Ns=10000
mt_pwfac=1.0
mt_cwfac=0.01
mt_tas=-0.1e6
mt_tcs=-0.1e6
mt_psr = 0.001
mt_pm = 0
mt_pn=400
mt_ps=10
mt_code=0
mt_alpha=0.01
pk_ci_fac=0.01
end

mg_matgen              ; Invoke the specimen-genesis procedures
cycle 3000             ; cycles to reach equilibrium

; ===================================
; Execute Uniaxial test at Pc=0.1MPa
; ===================================
set safe_conversion on
SET md_run_name='Uniaxial_test'
title 'Uniaxial_test'
set dt = 4e-5
call %fist%\3d\_ttw.DVR
set log off
```

```
;######################
```

```
; Brazilian Test
;######################
set random              ; Each time the test runs, the generated assembly is unchanged
call %fist%\2d_3d\fishcall.fis
call %fist%\2d_3d\md_setup.fis
call %fist%\2d_3d\md.fis
call %fist%\2d_3d\flt.fis
call %fist%\3d\et3.fis

SET md_run_name = 'Brazilian_Genesis_procedure'
title Test sample Genesis procedure
; ====================================
; Define sample parameters
; ====================================
def mg_set
mg_quiet=1
mv_shape = 0                                                          ;
mv_Wx = 50e-3
mv_Wz = 50e-3
mv_Hp = 100e-3
mt_bt = 30e-3              ; ASTM standards 0.2 < t/d < 0.75, t = d*0.6=50*0.6=30mm
mt_by = 25e-3
mg_ttol=0.5
target_poros = 0.15
mg_wfac=1.1 mg_Nf=3
; ====================================
; Define ball properties
; ====================================
mg_Rrat=1.0
```

```
mg_Rmin=0.95e-3
ball_dens = 2600
ba_bulk(1) = 1
ba_Ec(1) = 30e9
ba_krat(1) = 1.0
ba_fric(1) = 0.6
command
        SET gravity=0 -9.81 0
end_command
; ====================================
; Define the parallel bond parameters
; ====================================
pb_add=1
pb_Rmult(1)=1.0
pb_krat(1)=1.4
pb_Ec(1)=20e9
pb_sn_mean(1)=30e6
pb_sn_sdev(1)=30e4
pb_ss_mean(1)=39e6
pb_ss_sdev(1)=30e4
command
        SET gen_error
end_command
mg_ts0 = -0.4e6
mg_nfrat=0.0
mt_ttol=0.5
mt_eq_lim=0.0001
mt_eq_Ns=10000
mt_pwfac=1.0
```

```
mt_cwfac=0.01
mt_tas=-0.1e6          ; 0.1 MPa target axial stress
mt_tcs=-0.1e6          ; 0.1MPa target confinement
mt_psr = 0.001
p_close = 1
p_islat = 1
mt_pn=400
mt_ps=10
mt_code=1
mt_alpha=0.01
pk_ci_fac=0.01
end
mg_matgen              ; Invoke the specimen-genesis procedures
cycle 3000             ; cycles to reach equilibrium
; ===================================
;Execute Brazilian test at Pc=0.1MPa
; ===================================
set safe_conversion on
SET md_run_name='Brazilian_test'
title 'Brazilian_test'
set dt = 8e-6
call %fist%\3d\_braz.dvr
set log off
```

```
;######################
; SENB Test
;######################
set random             ; Each time the test runs, the generated assembly is unchanged
call %fist%\2d_3d\fishcall.fis
```

```
call %fist%\2d_3d\md_setup.fis
call %fist%\2d_3d\md.fis
call %fist%\2d_3d\flt.fis
call %fist%\2d_3d\crk.fis
call %fist%\3d\et3.fis

; =================
; Create notch
; =================
def make_notch
notch_z = 0
notch_y = -mv_Hp/2
notch_width = 2*mg_Rmin
notch_height = ((0.55 + 0.45)*mv_Hp)/2  ; mean value 0.45<a/h<0.55 ASTM stds
bp = ball_head
loop while bp # null
bnext = b_next(bp)
if b_y(bp) > notch_y then
  if b_y(bp) < (notch_y+notch_height) then
    if b_z(bp) < (notch_z + notch_width) then
      if b_z(bp) > notch_z then
      ii=b_delete(bp)
      end_if
    end_if
  end_if
end_if
bp = bnext
end_loop
end
```

```
SET md_run_name = 'Fracture_Toughness_test_Genesis'
title Test sample Genesis procedure
; ====================================
; Define sample parameters
; ====================================
 def mg_set
 mg_quiet=1
 mv_shape = 0          ; ASTM sds: Span=4*width, 0.45 ≤ a/width ≤ 0.70, depth = 0.5*W
mv_Wx = 12.5e-3
mv_Wz = 115e-3
mv_Hp = 25e-3
mt_eq_lim=0.01
mg_ttol=0.5
target_poros = 0.15
mg_wfac=1.1
mg_Nf=3
==================
; Define ball properties
==================
mg_Rrat=1.0
mg_Rmin=0.95e-3
ball_dens = 2600
ba_bulk(1) = 1
ba_Ec(1) = 30e9
ba_krat(1) = 1.0
ba_fric(1) = 0.6
command
        SET gravity=0 -9.81 0
```

```
end_command
pb_add=1
pb_Rmult(1)=1.0
pb_krat(1)=1.4
pb_Ec(1)=20e9
pb_sn_mean(1)=30e6
pb_sn_sdev(1)=30e4
pb_ss_mean(1)=39e6
pb_ss_sdev(1)=30e4
command
        SET gen_error
end_command
mg_ts0 = -0.4e6
mg_nfrat=0.0
end
mg_matgen               ; Invoke the specimen-genesis procedures
make_notch
cycle 3000              ; cycles to reach equilibrium
set log off
; ========================================
; Plot microcracks versus time
; ========================================
def crk_vs_time         ; Generates the cracks-versus-time plot
command
        title 'Limestone Fluid Scheme : PFC3D'
        plot creation of the crk vs time
        plot set title text 'crk_num vs time'
        plot set caption size 30
        plot add his 1
```

```
end_command
end
; ====================================
; Plot the assembly
; ====================================
def show_assembly       ; Generates the assembly plot
command
        plot creation of the assembly
        plot set caption size 30
        plot add axes black
        plot add ball yellow
end_command
end
; ====================================
; Plot platen vertical position
; ====================================
def ypos_platen
command
        plot creation of the ypos platen
        plot set caption size 30
        plot add his 13
end_command
end
; ===========================
; Plot force exerted by platen
; ===========================
def ball_off_bal_force
command
plot creation of the off bal force
```

```
plot set caption size 30
plot add his 15
end_command
end
; ==============================
; Fixed balls at supports
; ==============================
def make_fixed_balls
bp = ball_head
loop while bp # null
bnext = b_next(bp)
if b_y(bp) > mv_Hp/2 then
  b_xfix(bp) = 1
  b_zfix(bp) = 1
end_if
bp = bnext
end_loop
end
; =================================
; Create fixed supports
; =================================
def make_supports
kn_w=50e9
ks_w=50e9
cyl_rad = 5e-3
w1_end1_x = -mv_Wx/2 - 5e-3
w1_end1_y = -mv_Hp/2 - cyl_rad
w1_end1_z = -mv_Wz/2 + 7.5e-3
w1_end2_x =  mv_Wx/2 + 5e-3
```

```
w1_end2_y = -mv_Hp/2 - cyl_rad
w1_end2_z = -mv_Wz/2 + 7.5e-3
w2_end1_x = -mv_Wx/2 - 5e-3
w2_end1_y = -mv_Hp/2 - cyl_rad
w2_end1_z =  mv_Wz/2 - 7.5e-3
w2_end2_x =  mv_Wx/2 + 5e-3
w2_end2_y = -mv_Hp/2 - cyl_rad
w2_end2_z =  mv_Wz/2 - 7.5e-3
command
        wall id=6000 type cylinder kn=kn_w ks=ks_w end1 w1_end1_x
w1_end1_y w1_end1_z end2 w1_end2_x w1_end2_y w1_end2_z
        rad cyl_rad cyl_rad
        wall id=6001 type cylinder kn=kn_w ks=ks_w end1 w2_end1_x
w2_end1_y w2_end1_z end2 w2_end2_x w2_end2_y w2_end2_z
        rad cyl_rad cyl_rad
end_command
end
; ==============================
; Locate the central ball
; ==============================
def find_center_ball
bp = ball_head
loop while bp # null
bnext = b_next(bp)
if abs(b_y(bp)) < 2*mg_Rmin then
  if abs(b_x(bp)) < 2*mg_Rmin then
    if abs(b_z(bp)) < 2*mg_Rmin then
    center_id = b_id(bp)
    start_ypos = b_y(bp)
    b_pointer  = bp
```

```
    end_if
  end_if
end_if
bp = bnext
end_loop
ii=out('#### The center ball ID is:')
command
          print center_id
end_command
ii=out('#### The start ypos of center ball is:')
command
          print start_ypos        ; provides the Y position of the central ball
end_command
end
; ==================================================
; Measure the vertical displacement of the central ball
; ==================================================
def report_ypos
ii=out('#### The end ypos center ball is:')
end_ypos = b_y(b_pointer)
command
          print end_ypos              ; prints the final Y position of the central ball
end_command
ii=out('#### The vertical displacement of center ball is:')
vert_disp = abs(end_ypos - start_ypos)
command
          print vert_disp              ; prints the Y vertical displacement of the central ball
end_command
end
```

```
; ================================
; Calculate the notch opening
; ================================
def crack_opening
legA = ball_head
legA = find_ball(8119)                ; bottom leftmost ball at notch
legA_zpos = b_z(legA)
legB = ball_head
legB = find_ball(5835)                ; bottom rightmost ball at notch
legB_zpos = b_z(legB)
crack_opening = abs(legA_zpos-legB_zpos)
end

; ==================================
; Calculate the Fracture Intensity factor
; ==================================
def factor_KIc
_a = notch_height
_W = mv_Hp
nom = 3*((_a/_W)^0.5)*(1.99 - (_a/_W)*(1-(_a/_W))*(2.15 -
3.93*(_a/_W)+2.7*(_a/_W)^2))
denom = 2*(1+2*(_a/_W))*((1-(_a/_W))^1.5)
_f = nom/denom
notch_depth = mv_Wx
factor_KIc
=((ball_off_balance_force*4*mv_Hp)/(((mv_Wx*notch_depth)^0.5)*(_W^1.5))
)*_f
end
; ================================
; Export bitmap image
```

```
; ==============================
def make_bitmap_plot
command
        plot creation of the BitmapOutput
        plot add ball yellow
        plot add wall
        plot add fish crk_item
        plot set color off
        plot set window position 0 0
        plot set window size 1 1
        plot set mode model rotation 90 90 0
end_command
end
; =================================
; Run the SENB simulation
; =================================
def run_test
command
        set echo on
end_command
cnt = 0
file_cnt = 0
command
        prop yvel -0.008 range id 90001
        fix y range id 90001
        prop yvel -0.008 range id 90002
        fix y range id 90002
end_command
loop qq (1 , total_steps)
```

```
          command
                    cycle50
                    print crk_num
          end_command
if crk_num > termination_crk_num then
exit
end_if
cnt = cnt + 1
if cnt = 200 then
cnt = 0
file_cnt = file_cnt + 1
myfilename = 'bitmap_bend'+ string(file_cnt) + '.bmp'
command
          set output myfilename
          plot hardcopy 8
end_command
end_if
end_loop
end
; =================================
; Simulation inputs
; =================================
set total_steps = 1e9
set termination_crk_num = 3000
; =================================
; Main routine - START
; =================================
make_notch
make_fixed_balls
```

```
ball rad 3.0e-3 id=90001 x=3.0e-3 z=0e-3 y=16.0e-3
property density 7800 kn=200e9 ks=200e9 c_index 1 range id=90001
ini xv 0 yv 0 zv 0 range id=90001
ball rad 3.0e-3 id=90002 x=-3.0e-3 z=0e-3 y=16.0e-3
property density 7800 kn=200e9 ks=200e9 c_index 1 range id=90002
ini xv 0 yv 0 zv 0 range id=90002
group ball_platen range id 90001 90002
property s_bond=80e9 n_bond=80e9 range group ball_platen
delete wall 1
delete wall 2
delete wall 3
delete wall 4
delete wall 5
delete wall 6
wall property kn kn_w ks ks_w
make_supports
cycle 3000
crk_init
history id=1 crk_num                ; Provide histories of relevant quantities
history id=2 crk_num_cnf
history id=3 crk_num_csf
history id=4 crk_num_pnf
history id=5 crk_num_psf
history id=6 report_ypos
history id=7 end_ypos
history id=8 vert_disp
history id=9 ball ypos id 1462
history id=10 crack_opening
history id=11 legA_zpos
```

```
history id=12 legB_zpos
history id=13 ball ypos id 90001
history id=15 ball_off_balance_force
history id=16 ball_applied_force
history id=17 factor_KIc
show_assembly
ypos_platen
ball_off_bal_force
factor_KIc
crk_vs_time
find_center_ball
set plot bmp size 1024 780
make_bitmap_plot
run_test
report_ypos
set log off
```

Appendix II: Simulation of hydraulic fracturing on a hollow cylinder

```
;############################
; Fluid flow through hollow cylinder
;############################
set random              ;Each time the test runs, the generated assembly is unchanged
call %fist%\fishcall.fis
call %fist%\md_setup.fis
call %fist%\md.fis
call %fist%\et3.fis
call %fist%\flt.fis
call %fist%\crk.fis
; ==========================
; Plot the assembly
; ==========================
def plot_assembly_view
command
        title 'Limestone Fluid Scheme : PFC3D'
        plot creation of the making Assembly
        plot set title text 'making Assembly'
        plot set caption size 30
        plot set background white
        plot add ax brown
        plot add wall blue
        plot add cforce black
        plot add ball yellow red
end_command
end
```

```
; =================================
; Create plot of flow rate
; =================================
def plot_vol_frate
command
          title 'Limestone Fluid Scheme : PFC3D'
          plot creation of the vol_flowrate
          plot set caption size 30
          plot add his 6 vs 7
          plot show
end_command
end
; =================================
; Create the filter walls
; =================================
def make_filter
ext = mv_Wx/10.0
wid = 10.0
space = mg_Rmin * 1
wmin = -(mv_Wz/2+ext)
wmax = mv_Wz/2 + ext
x0 = -mv_Wx/2
y0 = -mv_Hp/2
loop while y0 <= mv_Hp/2
          command
          wall type line3d id wid end1 x0 y0 wmin end2 x0 y0 wmax
          end_command
wid = wid + 1
y0 = y0 + space
```

```
end_loop
wmin = -(mv_Hp/2+ext)
wmax = mv_Hp/2 + ext
z0 = -mv_Wz/2
loop while z0 <= mv_Wz/2
        command
                wall type line3d id wid end1 x0 wmin z0 end2 x0 wmax z0
        end_command
wid = wid + 1
z0 = z0 + space
end_loop
end
; =================================
; Create hollow cylinder
; =================================
def make_hollow_cylinder
command
        delete ball range cylinder end1=(0.0,@_yl,0.0) &
                                   end2=(0.0,@_yu,0.0) &
                                   rad=@mv_Rc
end_command
        delete ball range cylinder end1=(0.0,@_yl,0.0) &
                                   end2=(0.0,@_yu,0.0) &
                                   rad=@ff_r
end_command
end
; =================================
; Install measurement spheres
; =================================
```

```
def install_lame_meas_circle
md_radii
meas_rad =((mv_Wx/2)-ff_r)/2.0
;Install sphere #6 (middle) in slice
meas_x = ((-mv_Wx/2)-(-ff_r))/2 - ff_r
meas_y = 0.0
meas_z = 0.0
command
measure x=@meas_x y=@meas_y z=@meas_z rad=@meas_rad id=6
end_command
; Install circle #4 (front) in slice
meas_x = ((-mv_Wx/2)-(-ff_r))/2 - ff_r
meas_y = -20.87e-3                          ;((-mv_Hp/2)-meas_x)
meas_z = 0.0
command
measure x=@meas_x y=@meas_y z=@meas_z rad=@meas_rad id=4
end_command
; Install circle #5 (back) in slice
meas_x = ((-mv_Wx/2)-(-ff_r))/2 - ff_r
meas_y = 20.87e-3                           ;((mv_Hp/2)-meas_x)
meas_z = 0.0
command
measure x=@meas_x y=@meas_y z=@meas_z rad=@meas_rad id=5
end_command
mp6 = find_meas(4)
mp5 = find_meas(5)
mp4 = find_meas(6)
end
; ==================================================
```

```
; Calculate strains from measurement spheres
; ================================================
def lame_strains
oo = measure(mp6, 2)
oo = measure(mp5, 2)
oo = measure(mp4, 2)
lame_mexx_sphere6 = lame_mexx_sphere6 + m_ed11(mp6) * tdel
lame_meyy_sphere6 = lame_meyy_sphere6 + m_ed22(mp6) * tdel
lame_mezz_sphere6 = lame_mezz_sphere6 + m_ed33(mp6) * tdel
lame_mexx_sphere5 = lame_mexx_sphere5 + m_ed11(mp5) * tdel
lame_meyy_sphere5 = lame_meyy_sphere5 + m_ed22(mp5) * tdel
lame_mezz_sphere5 = lame_mezz_sphere5 + m_ed33(mp5) * tdel
lame_mexx_sphere4 = lame_mexx_sphere4 + m_ed11(mp4) * tdel
lame_meyy_sphere4 = lame_meyy_sphere4 + m_ed22(mp4) * tdel
lame_mezz_sphere4 = lame_mezz_sphere4 + m_ed33(mp4) * tdel
_avg = (m_ed11(mp4) + m_ed11(mp5) + m_ed11(mp6)) / 3.0
lame_mexx = lame_mexx + _avg * tdel
_avg = (m_ed22(mp4) + m_ed22(mp5) + m_ed22(mp6)) / 3.0
lame_meyy = lame_meyy + _avg * tdel
_avg = (m_ed33(mp4) + m_ed33(mp5) + m_ed33(mp6)) / 3.0
lame_mezz = lame_mezz + _avg * tdel
lame_mevol = lame_mexx + lame_meyy + lame_mezz
end
; ================================================
; Calculate stresses from measurement spheres
; ================================================
def lame_stresses
oo = measure(mp6, 1)
oo = measure(mp4, 1)
```

```
oo = measure(mp5, 1)
lame_msxx_sphere6 = m_s11(mp6)
lame_msxx_sphere5 = m_s11(mp5)
lame_msxx_sphere4 = m_s11(mp4)
lame_msyy_sphere6 = m_s22(mp6)
lame_msyy_sphere5 = m_s22(mp5)
lame_msyy_sphere4 = m_s22(mp4)
lame_mszz_sphere6 = m_s33(mp6)
lame_mszz_sphere5 = m_s33(mp5)
lame_mszz_sphere4 = m_s33(mp4)
lame_msxx = (m_s11(mp4) + m_s11(mp5) + m_s11(mp6)) / 3.0
lame_msyy = (m_s22(mp4) + m_s22(mp5) + m_s22(mp6)) / 3.0
lame_mszz = (m_s33(mp4) + m_s33(mp5) + m_s33(mp6)) / 3.0
lame_msm = (lame_msxx + lame_msyy + lame_mszz) / 3.0
lame_msd = lame_msyy - 0.5*(lame_msxx + lame_mszz)
end
; ========================
; Run the fluid flow simulation
; ========================
def run_time
loop zz (1,(stable_time/my_timestep))
        command
                cycle 1
        end_command
end_loop
loop qq (1,total_steps)
        myfilename = 'bitmap'+ string(p_set) + '.bmp'
                command
                        set output myfilename
```

```
                    plot hardcopy
                end_command
                p_set=p_set+p_set_gradient
                command
                    fluid boundary pres p_set xl
               end_command
loop ll (1,(each_sec/my_timestep))   ; repeat for every 10 sec
          command
               cycle 1
          end_command
if crk_num > termination_crk_num then
exit
end_if
end_loop
end_loop
end
; =========================================================
; Define start point of the measurement of the fluid pressure gradient
; =========================================================
def pres_grad
pres_grad = abs(fc_pre(0,1,1))        ; start from the pressure at 0,1,1 cell
time_grad=time-ftime0
end
; ==================
; Set fluid parameters
; ==================
def set_fluid
dens_f = 1000.0
visc_f = 1e-3
```

```
Rock_perm = 2e-10
Rock_poros = 0.15
spec_poros = et3_poros
diam = 2*mg_Rmin
alpha_dens = (spec_poros^3 * diam)/(Rock_poros^1.5 * (180 *
Rock_poros)^(0.5))
alpha_visc = (spec_poros^3 * diam^2)/(180 * (1 - spec_poros)^2 *
Rock_perm)
scale_dens = dens_f * alpha_dens
scale_visc = visc_f * alpha_visc
p_set = p_set_init
xsize = 4
ysize = 12
zsize = 5
x1=-(mv_Wx/2)
x2=-0.9*ff_r
z1=-(mv_Wz/6)
z2=(mv_Wz/6)
y1=-(mv_Hp/2)
y2=(mv_Hp/2)
command
        set gw_cellmap off ; etsi to eixame ston 2d code
        fluid model x1 x2 y1 y2 z1 z2 size xsize ysize zsize
        fluid prop dens scale_dens visc scale_visc
        fluid set tdel auto
        fluid set it 10000
        fluid set por_re 0.0
        fluid set crit 1e-6
        fluid set buo off
        fluid set gr on
```

```
    fluid boundary slip zu
    fluid boundary slip zl
    fluid boundary pres 0 xu
    fluid boundary pres p_set xl
    fluid boundary slip yu
    fluid boundary slip yl
    fluid set visterm on
end_command
end

def set_ftime0
ftime0 = time
end
; ================================
; Calculate the volumetric flow rate
; ================================
def ftime_volumetric
volumetric_rate = 0.0
area_per_cell = (2*z2*mv_Hp)/(ysize*zsize)
loop j (1,ysize)
    loop k (1,zsize)
        volumetric_rate = volumetric_rate + fc_xvel(xsize, j,
        k)*area_per_cell*fc_por(xsize, j, k)
    end_loop
end_loop
ftime_volumetric = time - ftime0
end
; ================================
; Calculate Darcy flow rate
```

```
; ===============================
def cal_tfrate
fpor = 0.0
loop i(1,xsize)
        loop j(1,ysize)
                loop k(1,size)
                        fpor = fpor + fc_por(I,j,k)
                end_loop
        end_loop
end_loop
fpor = fpor/(xsize*ysize*zsize)
tot_vol = 0.0
bp = ball_head
loop while bp # null
        tot_vol = tot_vol + (4.0/3.0)*pi*b_rad(bp)^3
        bp = b_next(bp)
end_loop
cyl_vol = pi*((mv_Wx/2)^2)*mv_Hp - pi*((ff_r)^2)*mv_Hp
permeability = (1/180.)* diam^2 * fpor^3 /(1.0-fpor)^2
gradp = p_set_init / (abs(x1-x2))
cross_section = mv_Hp * (2*z2)
darcy = (permeability / scale_visc) * (gradp) * cross_section
oo=out('average porosity: ' + String(fpor) +' [ ]')
oo=out('theoretical permeability: ' + String(permeability) + ' [m^2]')
oo=out('theoretical flowrate (darcy): ' + String(darcy) + ' [m^3/s]')
oo=out('calculated flowrate (volumetric): ' + String(volumetric_rate)+ '
[m^3/s]')
c1 = 150.0
c2 = 1.75
```

```
steady_solution = (sqrt((1-fpor)*4*diam^3*fpor^3*abs(gradp)*
scale_dens*c2+(fpor-1)^4*scale_visc^2*c1^2)-c1*scale_visc*(fpor-1)^2)
/(2*diam*(1-fpor)*scale_dens*c2)

steady_rate = steady_solution*cross_section

oo=out('steady solution: ' + String(steady_rate)+ ' [m^3/s]')

end

; ================================

; Define sample parameters

; ================================

def mg_set

ff_x=0

ff_z=0

ff_r=10.65e-3

mv_shape = 0

mv_Wx = 37.8e-3

mv_Wz = 37.8e-3

mv_Hp = 50e-3

mv_Rc = mv_Wx/2

mg_iso_steps = 100000

mg_ttol=0.5

target_poros = 0.15

mg_wfac=1.1

mg_Nf=3

mg_Rrat=1.0

mg_Rmin=0.85e-3

ball_dens = 2600

ba_bulk(1) = 1

ba_Ec(1) = 30e9

ba_krat(1) = 1.0

ba_fric(1) = 0.6
```

```
; ================================
; Define parallel bond parameters
; ================================
pb_add=1
pb_Rmult(1)=1.0
pb_krat(1)=1.4
pb_Ec(1)=20e9
pb_sn_mean(1)=30e6
pb_sn_sdev(1)=30e4
pb_ss_mean(1)=30e6
pb_ss_sdev(1)=30e4
command
        SET gen_error off
end_command
mg_ts0 = -0.4e6
mg_nfrat=0.0
end
; ================================
; Setup fluid pressure gradient
; ================================
def fluid_pres_grad
command
        SET total_steps = 25
        SET termination_crk_num = 5000
        SET stable_time = 31
        SET each_sec = 10
        SET p_set_init = 8e6
        SET p_set_gradient = 1.2e6
end_command
```

```
end
; ===============================
; Export bitmap image
; ===============================
def make_bitmap_plot
command
          plot creation of the BitmapOutput
          plot add ball yellow
          plot add wall
          plot add axes black
          plot add fish crk_item
          plot set color off
          plot set window position 0 0
          plot set window size 1 1
          plot set mag 2.2
 end_command
end
; ================================
; Main routine - START
; ================================
SET gravity=0 -9.81 0
mg_matgen
make_hollow_cylinder
cycle 5000
fluid_pres_grad
crk_init
history id=1 crk_num
history id=2 crk_num_cnf
history id=3 crk_num_csf
```

```
history id=4 crk_num_pnf
history id=5 crk_num_psf
plot_assembly_view
solve ratio 5                          ; Reduce the internal unbalanced forces save
hollow_cylinder_ASSEMBLY.sav
init xv 0.0 yv 0.0 zv 0.0 xs 0.0 ys 0.0 zs 0.0      ; wall velocities and spins =0
make_filter
delete wall wall prop fric 0.1
install_lame_meas_circle
save hollow_cylinder_FLOWREADY.sav
set plot bmp size 1024 780
make_bitmap_plot
set_fluid
set_ftime0
history id=6 p_set
history id=7 measure s11 id = 6
history id=8 measure s22 id = 6
history id=9 measure s33 id = 6
history id=10 measure s11 id = 4
history id=11 measure s22 id = 4
history id=12 measure s33 id = 4
history id=13 measure s11 id = 5
history id=14 measure s22 id = 5
history id=15 measure s33 id = 5
history id=16 lame_strains
history id=17 lame_mexx_sphere6
history id=18 lame_meyy_sphere6
history id=19 lame_mezz_sphere6
history id=20 lame_mexx_sphere4
```

```
history id=21 lame_meyy_sphere4
history id=22 lame_mezz_sphere4
history id=23 lame_mexx_sphere5
history id=24 lame_meyy_sphere5
history id=25 lame_mezz_sphere5
history id=26 lame_mevol
history id=27 lame_msm
history id=28 lame_msd
history id=29 steady_rate
history id=30 volumetric_rate
history id=31 ftime_volumetric
history id=32 cal_tfrate
history id=33 steady_rate
history id=34 darcy
SET my_timestep = 2e-5
SET dt=2e-6
run_time
ftime_volumetric
cal_tfrate
crk_fil_all
crk_makeview
save hollow_cylinder_FLOWDONE.sav
oo = out('======================')
oo = out('The fluid flow configuration for this test was as follows:')
oo = out('Initial pressure                  (Pa)       = '+string(p_set_init))
oo = out('Pressure gradient                 (Pa/sec) = '+string(p_set_gradient))
oo = out('Duration of stable pressure   (sec)      = '+string(stable_pres_time))
oo = out('Duration of fluid experiment  (sec) = '+string(final_time_secs))
oo = out('Results:')
```

```
oo = out('Total number of cracks = '+string(crk_num))
oo = out('======================================')
oo = out('* Copyright (c) - 2013, PhD Marina Sousani *')
oo = out('* Have a nice day! *')
; ================================
; Main routine - END
; ================================
```

Appendix III: Simulation of horizontal fluid injection (pre-cracked sample with single 15º fracture)

```
; ================================

; Initial environment setup

; ================================

set_env

set random

set hist_rep=10

call %fist%\2d_3d\md_setup.fis

call %fist%\2d_3d\md.fis

call %fist%\3d\et3.fis

call %fist%\2d_3d\flt.fis

call %fist%\2d_3d\crk.fis

call %fist%\2d_3d\fishcall.fis

; ================================

; Custom functions - START
; ================================
; ================================

; Plot the  assembly

; ================================

def plot_assembly_view                    ; Generates the Assembly view

command

        title 'Limestone Fluid Scheme : PFC3D'

        plot create making Assembly

        plot set title text 'making Assembly'

        plot set caption size 30

        plot set background white

        plot add ax brown

        plot add wall blue

        plot add cforce black
```

```
        plot add ball yellow red
end_command
end

; Install measurement sphere 4
def install_meas_circle4
md_radii
meas_rad = 7e-3
meas_x = 0
meas_y = 0.0
meas_z = -5e-3
command
        measure x=@meas_x y=@meas_y z=@meas_z rad=@meas_rad id=4
end_command
mp4 = find_meas(4)
end

; Installation of measurement sphere 5
def install_meas_circle5
md_radii
meas_rad = 7e-3
meas_x = 15.376e-3
meas_y = 0.0
meas_z = -0.592e-3
command
        measure x=@meas_x y=@meas_y z=@meas_z rad=@meas_rad id=5
end_command
mp5 = find_meas(5)
```

```
end

; Install measurement sphere 6
def install_meas_circle6
md_radii
meas_rad = 5e-3
meas_x = 22e-3
meas_y = -2.5e-3
meas_z = -2.5e-3
command
        measure x=@meas_x y=@meas_y z=@meas_z rad=@meas_rad
id=6
end_command
mp6 = find_meas(6)
end

; Install measurement sphere 7
def install_meas_circle7
md_radii
meas_rad = 7.1e-3
meas_x = -23e-3
meas_y = 0e-3
meas_z = 0e-3
command
        measure x=@meas_x y=@meas_y z=@meas_z rad=@meas_rad
id=7
end_command
mp7 = find_meas(7)
end
```

```
; Install measurement sphere 8
def install_meas_circle8
md_radii
meas_rad = 8e-3
meas_x = -3e-3
meas_y = 0e-3
meas_z = 10e-3
command
        measure x=@meas_x y=@meas_y z=@meas_z rad=@meas_rad id=8
end_command
mp8 = find_meas(8)
end

; Install measurement sphere 9
def install_meas_circle9
md_radii
meas_rad = 8e-3
meas_x = 11.93e-3
 meas_y = 0e-3
meas_z = -11e-3
command
        measure x=@meas_x y=@meas_y z=@meas_z rad=@meas_rad id=9
end_command
mp9 = find_meas(9)
end

; Install measurement sphere 10
def install_meas_circle10
```

```
md_radii
meas_rad = 13e-3
meas_x = -15e-3
meas_y = 0e-3
meas_z = -6e-3
command
        measure x=@meas_x y=@meas_y z=@meas_z rad=@meas_rad id=10
end_command
mp10 = find_meas(10)
end

; Calculate strains from sphere 4
def strains4
oo = measure(mp4, 2)
mexx_sphere4 = mexx_sphere4 + m_ed11(mp4) * tdel
meyy_sphere4 = meyy_sphere4 + m_ed22(mp4) * tdel
mezz_sphere4 = mezz_sphere4 + m_ed33(mp4) * tdel
mevol4 = mexx + meyy + mezz
end

; Calculate strains from sphere 5
def strains5
oo = measure(mp5, 2)
mexx_sphere5 = mexx_sphere5 + m_ed11(mp5) * tdel
meyy_sphere5 = meyy_sphere5 + m_ed22(mp5) * tdel
mezz_sphere5 = mezz_sphere5 + m_ed33(mp5) * tdel
mevol5 = mexx + meyy + mezz
end
```

```
; Calculate strains from sphere 6
def strains6
oo = measure(mp6, 2)
mexx_sphere6 = mexx_sphere6 + m_ed11(mp6) * tdel
meyy_sphere6 = meyy_sphere6 + m_ed22(mp6) * tdel
mezz_sphere6 = mezz_sphere6 + m_ed33(mp6) * tdel
mevol6 = mexx + meyy + mezz
end

; Calculate strains from sphere 7
def strains7
oo = measure(mp7, 2)
mexx_sphere7 = mexx_sphere7 + m_ed11(mp7) * tdel
meyy_sphere7 = meyy_sphere7 + m_ed22(mp7) * tdel
mezz_sphere7 = mezz_sphere7 + m_ed33(mp7) * tdel
mevol7 = mexx + meyy + mezz
end

; Calculate strains from sphere 8
def strains8
oo = measure(mp8, 2)
mexx_sphere8 = mexx_sphere8 + m_ed11(mp8) * tdel
meyy_sphere8 = meyy_sphere8 + m_ed22(mp8) * tdel
mezz_sphere8 = mezz_sphere8 + m_ed33(mp8) * tdel
mevol8 = mexx + meyy + mezz
end

; Calculate strains from sphere 9
def strains9
```

```
oo = measure(mp9, 2)
mexx_sphere9 = mexx_sphere9 + m_ed11(mp9) * tdel
meyy_sphere9 = meyy_sphere9 + m_ed22(mp9) * tdel
mezz_sphere9 = mezz_sphere9 + m_ed33(mp9) * tdel
mevol9 = mexx + meyy + mezz
end

; Calculate strains from sphere 10
def strains10
oo = measure(mp10, 2)
mexx_sphere10 = mexx_sphere10 + m_ed11(mp10) * tdel
meyy_sphere10 = meyy_sphere10 + m_ed22(mp10) * tdel
mezz_sphere10 = mezz_sphere10 + m_ed33(mp10) * tdel
mevol10 = mexx + meyy + mezz
end

; Calculate stresses from sphere 4
def stresses4
oo = measure(mp4, 1)
msxx_sphere4 = m_s11(mp4)
msyy_sphere4 = m_s22(mp4)
mszz_sphere4 = m_s33(mp4)
msm4 = (msxx + msyy + mszz) / 3.0
msd4 = msyy - 0.5*(msxx + mszz)
end

; Calculate stresses from sphere 5
def stresses5
oo = measure(mp5, 1)
```

```
msxx_sphere5 = m_s11(mp5)
msyy_sphere5 = m_s22(mp5)
mszz_sphere5 = m_s33(mp5)
msm5 = (msxx + msyy + mszz) / 3.0
msd5 = msyy - 0.5*(msxx + mszz)
end

; Calculate stresses from sphere 6
def stresses6
oo = measure(mp6, 1)
msxx_sphere6 = m_s11(mp6)
msyy_sphere6 = m_s22(mp6)
mszz_sphere6 = m_s33(mp6)
msm6 = (msxx + msyy + mszz) / 3.0
msd6 = msyy - 0.5*(msxx + mszz)
end

; Calculate stresses from sphere 7
def stresses7
oo = measure(mp7, 1)
msxx_sphere7 = m_s11(mp7)
msyy_sphere7 = m_s22(mp7)
mszz_sphere7 = m_s33(mp7)
msm7 = (msxx + msyy + mszz) / 3.0
msd7 = msyy - 0.5*(msxx + mszz)
end

; Calculate stresses from sphere 8
def stresses8
```

```
oo = measure(mp8, 1)
msxx_sphere8 = m_s11(mp8)
msyy_sphere8 = m_s22(mp8)
mszz_sphere8 = m_s33(mp8)
msm8 = (msxx + msyy + mszz) / 3.0
msd8 = msyy - 0.5*(msxx + mszz)
end

; Calculate stresses from sphere 9
def stresses9
oo = measure(mp9, 1)
msxx_sphere9 = m_s11(mp9)
msyy_sphere9 = m_s22(mp9)
mszz_sphere9 = m_s33(mp9)
msm9 = (msxx + msyy + mszz) / 3.0
msd9 = msyy - 0.5*(msxx + mszz)
end

; Calculate stresses from sphere 10
def stresses10
oo = measure(mp10, 1)
msxx_sphere10 = m_s11(mp10)
msyy_sphere10 = m_s22(mp10)
mszz_sphere10 = m_s33(mp10)
msm10 = (msxx + msyy + mszz) / 3.0
msd10 = msyy - 0.5*(msxx + mszz)
end

; ================================
```

```
; Define sample parameters
; ================================
def mg_set
mv_shape = 0
mv_Wx = 60e-3
mv_Wz = 40e-3
mv_Hp = 40e-3
mv_Rc = mv_Wx/2
mg_iso_steps = 100000
mg_ttol=0.5
target_poros = 0.15
mg_wfac=1.1
mg_Nf=3
;===================
 ; Define ball properties
; ===================
mg_Rrat=1.0
mg_Rmin=0.85e-3
ball_dens = 2600
ba_bulk(1) = 1
ba_Ec(1) = 30e9
ba_krat(1) = 1.0
ba_fric(1) = 0.6
;=========================
 ; Define parallel bond properties
; =========================
pb_add=1
pb_Rmult(1)=1.0
pb_krat(1)=1.4
```

```
pb_Ec(1)=20e9
pb_sn_mean(1)=30e6
pb_sn_sdev(1)=30e4
pb_ss_mean(1)=39e6
pb_ss_sdev(1)=30e4
command
    SET gen_error
end_command
mg_ts0 = -0.40e6
mg_nfrat=0.0
end
; =====================
; Create crack at xz plane
; =====================
def make_crack_xz
crack_angle=crack_angle*(pi/180)
bp = ball_head
loop while bp # null
    bnext = b_next(bp)
    if crack_angle=(pi/2) then
      if b_x(bp) > crack_x then
        if b_x(bp) < (crack_x+crack_width) then
          if b_y(bp) > crack_y then
            if b_y(bp) < (crack_y+crack_depth) then
              if b_z(bp) < (crack_z + crack_length) then
                if b_z(bp) > crack_z then
                  ii=b_delete(bp)
                end_if
              end_if
```

```
                    end_if
                  end_if
                end_if
              end_if
            else                    ; when the fracture angle is less than 90 degrees
if b_x(bp) > crack_x then
if b_x(bp) < (crack_x+crack_width+crack_length*cos(crack_angle)) then
if b_z(bp) > crack_z then
if b_z(bp) < (crack_z+crack_length*sin(crack_angle)) then
if b_y(bp) > crack_y then
if b_y(bp) < (crack_y+crack_depth) then
if b_z(bp)<(tan(crack_angle)*(b_x(bp)-crack_x)+crack_z) then
if b_z(bp)>(tan(crack_angle)*(b_x(bp)-crack_x-crack_width)+crack_z) then
ii=b_delete(bp)
end_if
end_if
end_if
end_if
end_if
end_if
end_if
end_if
end_if
bp = bnext
end_loop
end
; ==========================
; Create 1st continuous crack at xz plane
; ==========================
```

```
def make_multi_crack1_xz
crack_x = 0
crack_z = -5e-3
crack_y = -6e-3
crack_angle = 15
crack_length = 4e-3
crack_width = 4e-3
crack_depth = 13e-3
make_crack_xz
        crack_x = crack_x+(crack_length*cos(crack_angle))
        crack_z = crack_z+ (crack_length*sin(crack_angle))
        crack_y = -6e-3
        crack_angle = 17
        crack_length = 4e-3
        crack_width = 4e-3
        crack_depth = 13e-3
make_crack_xz
        crack_x = crack_x+(crack_length*cos(crack_angle))
        crack_z = crack_z+ (crack_length*sin(crack_angle))
        crack_y = -6e-3
        crack_angle = 15
        crack_length = 4e-3
        crack_width = 4e-3
        crack_depth = 13e-3
make_crack_xz
        crack_x = crack_x+(crack_length*cos(crack_angle))
        crack_z = crack_z+ (crack_length*sin(crack_angle))
        crack_y = -6e-3
        crack_angle = 17
```

```
        crack_length = 4e-3
        crack_width = 4e-3
        crack_depth = 13e-3
make_crack_xz
end
; ===========================
; Create 2nd continues crack at xz plane
; ===========================
def make_multi_crack2_xz
crack_x = 22e-3
crack_z = -2.5e-3
crack_y = -5e-3
crack_angle = 90
crack_length = 2.5e-3
crack_width = 8e-3
crack_depth = 5e-3
make_crack_xz
end
; ===========================
; Custom functions -END
; ===========================
; ===========================
; Main routine - START
; ===========================
SET gravity=0 -9.81 0
mg_quiet=1
mg_matgen
make_multi_crack1_xz
make_multi_crack2_xz
```

```
install_meas_circle4
install_meas_circle5
install_meas_circle6
install_meas_circle7
install_meas_circle8
install_meas_circle9
install_meas_circle10
cycle 5000                                    ; cycles to reach equilibrium
plot_assembly_view
solve ratio 5
save Genesis_angle15_ASSEMBLY.sav
; =========================
; Main routine - END
; =========================



; ====================================
; Create fixed balls (boundary conditions)
; ====================================
def make_fixed_balls
bp = ball_head
loop while bp # null
        bnext = b_next(bp)
        if b_z(bp) > ((mv_Wz/2)- 2*mg_Rmin)  then
          b_xfix(bp) = 1
          b_yfix(bp) = 1
          b_zfix(bp) = 1
        end_if
        if b_y(bp) > ((mv_Hp/2) - 2*mg_Rmin)  then
```

```
          b_xfix(bp) = 1
          b_yfix(bp) = 1
          b_zfix(bp) = 1
        end_if
         if b_x(bp) > ((mv_Wx/2) - 2*mg_Rmin)  then
          b_xfix(bp) = 1
          b_yfix(bp) = 1
          b_zfix(bp) = 1
         end_if
         if b_z(bp) < -((mv_Wz/2) - 2*mg_Rmin) then
          b_xfix(bp) = 1
          b_yfix(bp) = 1
          b_zfix(bp) = 1
        end_if
        if b_y(bp) < -((mv_Hp/2) - 2*mg_Rmin)  then
          b_xfix(bp) = 1
          b_yfix(bp) = 1
          b_zfix(bp) = 1
        end_if
        if b_x(bp) < -((mv_Wx/2 - 2*mg_Rmin)) then
          b_xfix(bp) = 1
          b_yfix(bp) = 1
          b_zfix(bp) = 1
        end_if
        bp = bnext
end_loop
end
; ======================
; Make confinement
```

```
; ======================
def make_confinement
et3_knxfac = 0.01
et3_knyfac = 0.01
et3_knzfac = 0.01
et3_wsxx_req = -1.0e6
et3_wsyy_req = -0.5e6
et3_wszz_req = -1.5e6
et3_wstol = 0.01
et3_ws_tol=0.5
mt_eq_lim=0.0001
mt_eq_Ns=10000
p_vel = 0.2
pk_ci_fac = 0.02
et3_wallstiff
et3_seattriax
et3_sample_dimensions
crk_init
et3_servo_xon = 1
et3_servo_yon = 1
et3_servo_zon = 1
et3_viewstriax
command
        prop xdisp=0.0 ydisp=0.0 zdisp=0.0
end_command
end
; ================================
; Calculate the forces upon the particles
; ================================
```

```
def measure_forces
tot_comp_force = 0
tot_tens_force = 0
tot_shear_xforce = 0
tot_shear_yforce = 0
tot_shear_zforce = 0
avg_comp_force = 0
avg_tens_force = 0
cp_cnt        = 0
cp = contact_head   ; get mean contact force
loop while cp # null
        norm_force = c_nforce(cp)
        if norm_force > 0 then
        tot_comp_force = tot_comp_force + norm_force
else
        tot_tens_force = tot_tens_force + norm_force
        tot_shear_xforce = tot_shear_xforce +c_xsforce(cp)
        tot_shear_yforce = tot_shear_yforce +c_ysforce(cp)
        tot_shear_zforce = tot_shear_zforce +c_zsforce(cp)
        end_if
cp_cnt = cp_cnt + 1
cp = c_next(cp)
end_loop
avg_comp_force = float(tot_comp_force / cp_cnt)
avg_tens_force = float(tot_tens_force / cp_cnt)
end
; ================================================
; ; Define start point of the measurement of the fluid pressure gradient
; ================================================
```

```
def pres_grad
pres_grad = abs(fc_pre(0,1,1))
time_grad=time-ftime0
end
; ================
; Setup flow rate
; ================
def fluid_rate_grad
command
        SET total_steps = 1000
        SET termination_crk_num = 3000
        SET inj_rate_init = 9e-6                    ; initial flow rate
        SET inj_rate_gradient = 1e-2                ; flow rate gradient
end_command
end

; ================
; Export bitmap image
; ================
def make_bitmap_plot
command
        plot create BitmapOutput
        plot add ball yellow
        plot add wall
        plot add fish crk_item
        plot set color off
        plot set window position 0 0
        plot set window size 1 1
        plot set mag 1.2
```

```
 end_command
end
; =================
; Setup of the fluid
; =================
def set_fluid
dens_f = 1000.0
visc_f = 1e-3
Rock_perm = 2e-10
Rock_poros = 0.15
spec_poros = et3_poros
diam = 2*mg_Rmin
alpha_dens = (spec_poros^3 * diam)/(Rock_poros^1.5 * (180 * Rock_poros)^(0.5))
alpha_visc = (spec_poros^3 * diam^2)/(180 * (1 - spec_poros)^2 * Rock_perm)
scale_dens = dens_f * alpha_dens
scale_visc = visc_f * alpha_visc
xsize = 8
ysize = 8
zsize = 8
x1=-(mv_Wx/4)
x2= (mv_Wx/2)
z1=-(mv_Wz/2)
z2=(mv_Wz/2)
y1=-(mv_Hp/2)
y2=(mv_Hp/2)
inj_rate = inj_rate_init
inj_areaZ = mv_Wz/zsize
inj_areaY = mv_Hp/ysize
```

```
inj_area = inj_areaZ*inj_areaY
inj_vel = -1*(inj_rate / inj_area)
command
        set gw_cellmap off ; etsi to eixame ston 2d code
        fluid model x1 x2 y1 y2 z1 z2 size xsize ysize zsize
        fluid prop dens scale_dens visc scale_visc
        fluid set it 10000
        fluid set por_re 0.0
        fluid set crit 1e-6
        fluid set buo off
        fluid set gr on
        fluid boundary nonslip zu
        fluid boundary nonslip zl
        fluid boundary nonslip xl
        fluid boundary nonslip yu
        fluid boundary nonslip yl
        fluid boundary vel 0 0 0 zu
        fluid boundary vel 0 0 0 zl
        fluid boundary vel 0 0 0 xl
        fluid boundary vel 0 0 0 xu
        ry vel 0 0 0 yu
        fluid boundary vel 0 0 0 yl
        fluid set visterm on
end_command
end

def set_ftime
ftime0 = time
end
```

```
; =================
; Run the simulation
; =================
def run_time
injCell_i = 9
injCell_j = 4
injCell_k = 4
crk_count = 0
loop qq (1,total_steps)
  if crk_num > crk_count + 10
    crk_count = crk_num
    myfilename = 'bitmap _angle15_' + 'crknum_'+ string(crk_num) +
'_injrate_' + string(inj_rate) + '.bmp'
command
          set output myfilename
          plot hardcopy 7
end_command
  end_if
inj_rate= inj_rate + inj_rate_gradient
inj_vel = -1*(inj_rate / inj_area)
command
          fluid boundary vel inj_vel 0 0 at injCell_i injCell_j injCell_k
end_command
loop ll(1,3000)
          command
            cycle 1
          end_command
  if crk_num > termination_crk_num then
exit
  end_if
```

```
end_loop
end_loop
end
; ==============================
; Calculate the volumetric time
; ==============================
def ftime_volumetric
volumetric_rate = 0.0
area_per_cell = (mv_Wz*mv_Hp)/(zsize*ysize)
loop j (1,ysize)
loop k (1,zsize)
volumetric_rate = volumetric_rate + fc_xvel(xsize,j,k)*area_per_cell*fc_por(xsize,j,k)
end_loop
end_loop
ftime_volumetric = time - ftime0
end
; ==============================
; Calculate the average input pressure
; ==============================
input_pres = 0
loop j (1, ysize)
          loop k (1,zsize)
             input_pres = input_pres + fc_pre(xsize,j,k)
          end_loop
end_loop
input_pres = input_pres / (ysize*zsize)
; ==============================
; Calculate the average output pressure
; ==============================
```

```
output_pres = 0
loop j (1, ysize)
          loop k (1,zsize)
             output_pres = output_pres + fc_pre(1,j,k)
          end_loop
end_loop
output_pres = output_pres / (ysize*zsize)
end
; ==============================
; Calculate quantities from cells
; ==============================
def quant_from_Cell
inj_press_Cell = fc_pre(injCell_i, injCell_j, injCell_k)
inj_vel_Cell = fc_xvel(injCell_i, injCell_j, injCell_k)
press_crk1_Cell333_start = fc_pre (3,3,3)
press_crk1_Cell343_start = fc_pre (3,4,3)
press_crk1_Cell353_start = fc_pre (3,5,3)
press_crk1_Cell363_start = fc_pre (3,6,3)
press_crk1_Cell334_start = fc_pre (3,3,4)
press_crk1_Cell344_start = fc_pre (3,4,4)
press_crk1_Cell354_start = fc_pre (3,5,4)
press_crk1_Cell364_start = fc_pre (3,6,4)
press_crk1_Cell634_end = fc_pre (6,3,4)
press_crk1_Cell644_end = fc_pre (6,4,4)
press_crk1_Cell654_end = fc_pre (6,5,4)
press_crk1_Cell664_end = fc_pre (6,6,4)
vel_crk1_Cell333_start = fc_xvel (3,3,3)
vel_crk1_Cell343_start = fc_xvel (3,4,3)
vel_crk1_Cell353_start = fc_xvel (3,5,3)
```

```
vel_crk1_Cell363_start = fc_xvel (3,6,3)
vel_crk1_Cell334_start = fc_xvel (3,3,4)
vel_crk1_Cell344_start = fc_xvel (3,4,4)
vel_crk1_Cell354_start = fc_xvel (3,5,4)
vel_crk1_Cell364_start = fc_xvel (3,6,4)
vel_crk1_Cell634_end = fc_xvel (6,3,4)
vel_crk1_Cell644_end = fc_xvel (6,4,4)
vel_crk1_Cell654_end = fc_xvel (6,5,4)
vel_crk1_Cell664_end = fc_xvel (6,6,4)
press_crk2_Cell734_end = fc_pre (7,3,4)
press_crk2_Cell744_end = fc_pre (7,4,4)
press_crk2_Cell754_end = fc_pre (7,5,4)
vel_crk2_Cell734_end = fc_xvel (7,3,4)
vel_crk2_Cell744_end = fc_xvel (7,4,4)
vel_crk2_Cell754_end = fc_xvel (7,5,4)
press_Cell034 = fc_pre (0,3,4)
vel_Cell034 = fc_xvel (0,3,4)
vel_Cell834 = fc_xvel (8,3,4)
end
; =============================
; Main routine - START
; =============================
make_fixed_balls
make_confinement
cycle 3000
SET echo off
wall prop fric 0.1
fluid_rate_grad
set plot bmp size 1024 780
```

```
make_bitmap_plot
set_fluid
set_ftime
history id=1 crk_num
history id=2 crk_num_cnf
history id=3 crk_num_csf
history id=4 crk_num_pnf
history id=5 crk_num_psf
history id=6 crk_num_snf
history id=7 crk_num_ssf
history id=8 et3_wexx                    ; wall-derived strains at xx plane
history id=9 et3_weyy                    ; wall-derived strains at yy plane
history id=10 et3_wezz                   ; wall-derived strains at zz plane
history id=11 et3_wevol
history id=12 et3_sexx                 ; specimen-derived strains at xx plane
history id=13 et3_seyy                 ; specimen-derived strains at yy plane
history id=14 et3_sezz                 ; specimen-derived strains at zz plane
history id=15 et3_sevol
history id=16 et3_wsxx                  ; wall-derived stresses at xx plane
history id=17 et3_wsyy                  ; wall-derived stresses at yy plane
history id=18 et3_wszz                  ; wall-derived stresses at zz plane
history id=19 et3_wsm
history id=20 et3_wsd
history id=21 et3_ssxx                ; specimen-derived stresses at xx plane
history id=22 et3_ssyy                ; specimen-derived stresses at yy plane
history id=23 et3_sszz                ;  specimen-derived stresses at zz plane
history id=24 et3_ssm
history id=25 et3_ssd
history id=26 et3_mexx                     ; averaged strain at xx plane
```

```
history id=27 et3_meyy                          ; averaged strain at yy plane
history id=28 et3_mezz                          ; averaged strain at zz plane
history id=29 et3_mevol
history id=30 et3_msxx                          ; averaged stress at xx plane
history id=31 et3_msyy                          ; averaged stress at yy plane
history id=32 et3_mszz                          ; averaged stress at zz plane
history id=33 et3_msm
history id=34 et3_msd
trace energy on
history id=35 energy body
history id=36 energy bond
history id=37 energy friction
history id=38 energy kinetic
history id=39 energy strain
history id=40 et3_e_delstrain         ; increment of total strain energy = strain + bond
history id=41 volumetric_rate
history id=42 ftime_volumetric
history id=43 pres_grad
history id=44 time_grad
history id=45 inj_rate
history id=46 measure s11 id = 4
history id=47 measure s22 id = 4
history id=48 measure s33 id = 4
history id=49 msm4 id = 4
history id=50 msd4 id = 4
history id=51 mexx_sphere4
history id=52 meyy_sphere4
history id=53 mezz_sphere4
history id=54 mevol4
```

```
history id=55 measure s11 id = 5

history id=56 measure s22 id = 5

history id=57 measure s33 id = 5

history id=58 msm5 id = 5

history id=59 msd5 id = 5

history id=60 mexx_sphere5

history id=61 meyy_sphere5

history id=62 mezz_sphere5

history id=63 mevol5

history id=64 measure s11 id = 6

history id=65 measure s22 id = 6

history id=66 measure s33 id = 6

history id=67 msm5 id = 6

history id=68 msd5 id = 6

history id=69 mexx_sphere6

history id=70 meyy_sphere6

history id=71 mezz_sphere6

history id=72 mevol6

history id=73 measure s11 id = 7

history id=74 measure s22 id = 7

history id=75 measure s33 id = 7

history id=76 msm5 id = 7

history id=77 msd5 id = 7

history id=78 mexx_sphere7

history id=79 meyy_sphere7

history id=80 mezz_sphere7

history id=81 mevol7

history id=82 measure s11 id = 8

history id=83 measure s22 id = 8
```

```
history id=84 measure s33 id = 8

history id=85 msm5 id = 8

history id=86 msd5 id = 8

history id=87 mexx_sphere8

history id=88 meyy_sphere8

history id=89 mezz_sphere8

history id=90 mevol8

history id=91 measure s11 id = 9

history id=92 measure s22 id = 9

history id=93 measure s33 id = 9

history id=94 msm5 id = 9

history id=95 msd5 id = 9

history id=96 mexx_sphere9

history id=97 meyy_sphere9

history id=98 mezz_sphere9

history id=99 mevol9

history id=100 measure s11 id = 10

history id=101 measure s22 id = 10

history id=102 measure s33 id = 10

history id=103 msm5 id = 10

history id=104 msd5 id = 10

history id=105 mexx_sphere10

history id=106 meyy_sphere10

history id=107 mezz_sphere10

history id=108 mevol10

history id=109 cal_tfrate

history id=110 quant_from_Cell

history id=111 inj_press_Cell

history id=112 inj_vel_Cell
```

```
history id=113 press_crk1_Cell333_start
history id=114 press_crk1_Cell343_start
history id=115 press_crk1_Cell353_start
history id=116 press_crk1_Cell363_start
history id=117 press_crk1_Cell334_start
history id=128 press_crk1_Cell344_start
history id=129 press_crk1_Cell354_start
history id=130 press_crk1_Cell364_start
history id=131 press_crk1_Cell634_end
history id=132 press_crk1_Cell644_end
history id=133 press_crk1_Cell654_end
history id=134 press_crk1_Cell664_end
history id=135 press_crk2_Cell734_end
history id=136 press_crk2_Cell744_end
history id=137 press_crk2_Cell754_end
history id=138 measure_forces
history id=139 avg_comp_force
history id=140 avg_tens_force
history id=141 tot_shear_xforce
history id=142 tot_shear_yforce
history id=143 tot_shear_zforce
history id=144 diagnostic muf
history id=145 _crk_x
history id=146 _crk_y
history id=147 _crk_z
history id=148 press_Cell034
history id=149 vel_Cell034
history id=150 vel_Cell834
oo = out('---- INFO: Starting fluid simulation')
```

```
SET fishcall 16 quant_from_Cell
set fishcall 3 measure_forces
run_time
draw_presgrad
ftime_volumetric
cal_tfrate                                  ; Calculate flow rate according to Darcy
crk_fil_all
crk_makeview
save Fluid_angle15_FLOWDONE.
oo = out('=====================================')
oo = out('The fluid flow configuration for this test was as follows:')
oo = out('Initial injection rate        (m3/sec) = '+string(inj_rate_init))
oo = out('Injection rate gradient       (m3/sec) = '+string(inj_rate_gradient))
oo = out('Duration of stable pressure   (sec)    = '+string(stable_pres_time))
oo = out('Duration of fluid experiment  (sec)    = '+string(final_time_secs))
oo = out('Results:')
oo = out('Total number of cracks                 = '+string(crk_num))
oo = out('=================================================')
oo = out('* Copyright (c) - 2013, PhD Marina Sousani *')
oo = out('* Have a nice day! *')
; ==============================
; Main routine - END
; ==============================
```

Bibliography

Abdeen, F., Khalil, M. (1995) *Origin of NORM in Ras Budran Oil Field*. Paper presented at the Middle East Oil Show, Bahrain,

Academia.edu (2013) Some Useful Numbers on the Engineering Properties of Materials (Geologic and Otherwise)

http://www.academia.edu/4156626/Some_Useful_Numbers_on_the_Engineering_Properties_of_Materials_Geologic_and_Otherwise_Angle_of_internal_friction. Accessed September 2013

Adachi, J., Siebrits, E., Peirce, A., Desroches, J. (2007) *Computer simulation of hydraulic fractures*. International Journal of Rock Mechanics and Mining Sciences 44 (5):739-757

Akram, M.S., Sharrock, G.B. (2009) *Physical and Numerical Investigation of a Cemented Granular Assembly under Uniaxial and Triaxial Compression*. Paper presented at the 43rd US Rock Mechanics Symposium and 4th US-Canada Rock Mechanics Symposium, Asheville,

Al-Busaidi, A., Hazzard, J.F., Young, R.P. (2005) *Distinct element modeling of hydraulically fractured Lac du Bonnet granite*. Journal of Geophysical Research: Solid Earth 110 (B6)

Almond, S., Clancy, S.A., Davies, R.J., Worrall, F. (2014) *The flux of radionuclides in flowback fluid from shale gas exploitation*. Environ Sci Pollut Res 21 (21):12316-12324

Anderson, T.L. (1991) *Fracture Mechanics: Fundamentals and Applications*. 3rd edn. CRC Press,

Areias, P.M.A., Belytschko, T. (2005) *Analysis of three-dimensional crack initiation and propagation using the extended finite element method*. International Journal for Numerical Methods in Engineering 63 (5):760-788

Assane Oumarou, T., Cottrell, B.E., Grasselli, G. *Contribution of Surface Roughness on the Shear Strength of Indiana Limestone Cracks-An Experimental study*. In: Rock joints and jointed rock masses, Tucson, AZ, USA, 2009.

ASTM, I. (2003) *E1820-01 Standard Tetst Method for Measurement of Fracture Toughness*.

Ayob, A.B., Tamin, M.N., Elbasheer, M.K. *Pressure limits of thick-walled cylinders*. In: International MultiConference of Engineers and Computer Scientists 2009, Hong Kong, March 18-20 2009.

Bachu, S., Bennion, B. (2008) *Effects of in-situ conditions on relative permeability characteristics of* CO_2*-brine systems*. Environmental Geology 54 (8):1707-1722

Baghbanan, A., Jing, L. (2008) *Stress effects on permeability in a fractured rock mass with correlated fracture length and aperture*. International Journal of Rock Mechanics and Mining Sciences 45 (8):1320-1334

Baird, A.F., McKinnon, S.D. (2007) *Linking stress field deflection to basement structures in southern Ontario: Results from numerical modelling*. Tectonophysics 432 (1–4):89-100

Bakun-Mazor, D., Hatzor, Y.H., Dershowitz, W.S. (2009) *Modeling mechanical layering effects on stability of underground openings in jointed sedimentary rocks*. International Journal of Rock Mechanics and Mining Sciences 46 (2):262-271

Belytschko, T., Black, T. (1999) *Elastic crack growth in finite elements with minimal remeshing*. International Journal for Numerical Methods in Engineering 45 (5):601-620

Benson, P.M., Vinciguerra, S., Meredith, P.G., Young, R.P. (2008) *Laboratory Simulation of Volcano Seismicity*. Science 322 (5899):249-252

Berkowitz, B. (2002) *Characterizing flow and transport in fractured geological media: A review*. Advances in Water Resources 25 (8–12):861-884

Bfer, G. (1985) *An isoparametric joint/interface element for finite element analysis*. International Journal for Numerical Methods in Engineering 21 (4):585-600

BGS, DECC (2013) *The Carboniferous Bowland Shale gas study: Geology and Resource Estimation*. Brirish Geological Survey (BGS), Department of Energy & Climate Change (DECC), London, UK

Bieniawski, Z.T. (1967) *Mechanism of brittle fracture of rock: Part I—theory of the fracture process*. International Journal of Rock Mechanics and Mining Sciences & Geomechanics Abstracts 4 (4):395-406

Bigoni, D., Radi, E. (1993) *Mode I crack propagation in elastic-plastic pressure-sensitive materials*. International Journal of Solids and Structures 30 (7):899-919

Blair, S.C., Thorpe, R.K., Heuze, F.E., Shaffer, R.J. (1989) *Laboratory Observations Of The Effect Of Geologic Discontinuities On Hydrofracture Propagation*. Paper presented at the 30th U.S. Symposium on Rock Mechanics (USRMS), Morgantown, West Virginia, 1989/1/1/

Bobet, A., Einstein, H. (1998) *Numerical modeling of fracture coalescence in a model rock material*. International Journal of Fracture 92 (3):221-252

Bocca, P., Carpinteri, A., Valente, S. (1990) *Size effects in the mixed mode crack propagation: Softening and snap-back analysis*. Engineering Fracture Mechanics 35 (1–3):159-170

Bortolan Neto, L., Kotousov, A. (2012) *Residual opening of hydraulically stimulated fractures filled with granular particles*. Journal of Petroleum Science and Engineering 100 (0):24-29

Bouteca, M.J., Sarda, J.P., Vincke, O. (2000) *Constitutive Law for Permeability Evolution of Sandstones During Depletion*. Paper presented at the SPE International Symposium on Formation Damage Control, Louisiana,

Boutt, D.F., Cook, B.K., McPherson, B.J.O.L., Williams, J.R. (2007) *Direct simulation of fluid-solid mechanics in porous media using the discrete element and lattice-Boltzmann methods*. Journal of Geophysical Research: Solid Earth 112 (B10):1-13

Brace, W.F., Paulding, B.W., Scholz, C. (1966) *Dilatancy in the fracture of crystalline rocks*. Journal of Geophysical Research 71 (16):3939-3953

Bruno, M.S. (1994) *Micromechanics of stress-induced permeability anisotropy and damage in sedimentary rock*. Mechanics of Materials 18 (1):31-48

Bryant, S., King, P., Mellor, D. (1993) *Network model evaluation of permeability and spatial correlation in a real random sphere packing*. Transp Porous Med 11 (1):53-70

Cai, Y., Zhuang, X., Augarde, C. (2010) *A new partition of unity finite element free from the linear dependence problem and possessing the delta property*. Computer Methods in Applied Mechanics and Engineering 199 (17–20):1036-1043

Carman, P.C. (1997) *Fluid flow through granular beds*. Chemical Engineering Research and Design 75, Supplement (0):S32-S48

Chan, H.C.M., Li, V., Einstein, H.H. (1990) *A hybridized displacement discontinuity and indirect boundary element method to model fracture propagation*. International Journal of Fracture 45 (4):263-282

Chen, G., Kemeny, J.M., Harpalani, S.H. *Fracture propagation and coalescence in marble plates with pre-cut notches under compression*.

In: Symposium in Fractured Jointed Rock Masses, Lake Tahoe, CA, 1995. pp 435-439

Chen, S., Doolen, G.D. (1998) *Lattice Boltzmann Method for Fluid Flows*. Annual Review of Fluid Mechanics 30:329-364. doi:10.1146

Cho, N., Martin, C.D., Sego, D.C. (2007) *A clumped particle model for rock*. International Journal of Rock Mechanics and Mining Sciences 44 (7):997-1010

Christianson, M., Board, M., Rigby, D. (2006) *UDEC simulation of triaxial testing of lithophysal tuff*. Paper presented at the The 41st U.S. Symposium on Rock Mechanics (USRMS), Golden, Colorado, 17-21/06/2006

COM (2014) *Exploration and production of hydrocarbons (such as shale gas) using high volume hydraulic fracturing in the EU* COMMUNICATION FROM THE COMMISSION TO THE EUROPEAN PARLIAMENT, THE COUNCIL, THE EUROPEAN ECONOMIC AND SOCIAL COMMITTEE AND THE COMMITTEE OF THE REGIONS vol 23. European Commission, Brussels

Cundall, P.A. *A computer model for simulating progressive, large-scale movements in blocky rock systems*. In: Symposium of International Society of Rock Mechanics, France, 1971. doi:citeulike-article-id:7797727

Cundall, P.A., Hart, D.R. (1992) *NUMERICAL MODELLING OF DISCONTINUA*. Engineering Computations 9 (2):101-113

Cundall, P.A., Strack, O.D.L. (1979) *Discrete numerical model for granular assemblies* Géotechnique 29 (1):47-65

Damjanac, B., Board, M., Lin, M., Kicker, D., Leem, J. (2007) *Mechanical degradation of emplacement drifts at Yucca Mountain—A modeling* *case study: Part II: Lithophysal rock*. International Journal of Rock Mechanics and Mining Sciences 44 (3):368-399

DECC (2011) *The Carbon Plan: Delivering our Carbon Future*. London

Deng, S., Li, H., Ma, G., Huang, H., Li, X. (2014) *Simulation of shale–proppant interaction in hydraulic fracturing by the discrete element method*. International Journal of Rock Mechanics and Mining Sciences 70 (0):219-228

Desroches, J., Thiercelin, M. (1993) *Modelling the propagation and closure of micro-hydraulic fractures*. International Journal of Rock Mechanics and Mining Sciences & Geomechanics Abstracts 30 (7):1231-1234

Diederichs, M.S. (1999) *Instability of Hard Rock Masses: The Role of Tensile Damage and Relaxation*. Univeristy of Waterloo, Waterloo, Ontario, Canada

Diederichs, M.S. (2003) *Manuel Rocha Medal Recipient Rock Fracture and Collapse Under Low Confinement Conditions*. Rock Mech Rock Eng 36 (5):339-381

Dong, S. (2007) *Direct numerical simulation of turbulent Taylor–Couette flow*. Journal of Fluid Mechanics 587:373-393

Donzé, V.F., Richefeu, V., Magnier, S.-A. (2008) *Advances in Discrete Element Method Applied to Soil, Rock and Concrete Mechanics*. EJGE Special Volume Bouquet 08

Duan, Q., Song, J.-H., Menouillard, T., Belytschko, T. (2009) *Element-local level set method for three-dimensional dynamic crack growth*. International Journal for Numerical Methods in Engineering 80 (12):1520-1543

Dullien, F.A.L. (1979) *Porous media: Fluid transport and pore structure*. 2nd edn. Academic Press, Inc, United States of America

Economic Affairs Committee, E. (2014) *The Economic Impact on UK Energy Policy of Shale Gas and Oil*. vol 3. Authority of the House of Lords, London, UK

Economides, M.J., Martin, T. (2007) *Modern Fracturing - Enhancing Natural Gas Production*. BJ Services Company, Houston

Edmiston, P.L., Keener, J., Buckwald, S., Sloan, B., Terneus, J. (2011) *Flow Back Water Treatment Using Swellable Organosilica Media*. Paper presented at the SPE Eastern Regional Meeting, Columbus, Ohio, USA,

Elkadi, A.S., van Mier, J.G.M. (2004) *Scaled Hollow-Cylinder Tests for Studying Size Effect in Fracture Processes of Concrete*. Paper presented at the Fracture Mechanics of Concrete Structures, U.S.A,

Enever, J., Bailin, W. *Scale effects in hollow cylinder tests*. In: ISRM International Symposium - 2nd Asian Rock Mechanics Symposium, Beijing, China, 2001. International Society for Rock Mechanics, pp 209-212

Ergun., S. (1952) *Fluid Flow Through Packed Columns*. Chemical Engineering Progress 48:89-94

Eshiet, K.I.-I., Sheng, Y. (2010) *Modelling Erosion Control in Oil Production Wells*. World Academy of Science, Engineering & Technology 70

Eshiet, K.I.-I., Sheng, Y. (2014a) *Investigation of geomechanical responses of reservoirs induced by carbon dioxide storage*. Environ Earth Sci 71 (9):3999-4020

Eshiet, K.I.-I., Sheng, Y., Jianqiao, Y. (2013) *Microscopic modelling of the hydraulic fracturing process*. Environ Earth Sci 68 (4):1169-1186. doi:10.1007/s12665-012-1818-5

Eshiet, K.I.I., Sheng, Y. (2014b) *Carbon dioxide injection and associated hydraulic fracturing of reservoir formations*. Environ Earth Sci 72 (4):1011-1024

Ewy, R.T., Cook, G.W., Myer, L.R. (1988) *Hollow cylinder tests for studying fracture around underground openings*. Paper presented at the The 29th U.S. Symposium on Rock Mechanics (USRMS), Minneapolis, MN, June 13-15

Falls, S.D., Young, R.P., Carlson, S.R., Chow, T. (1992) *Ultrasonic tomography and acoustic emission in hydraulically fractured Lac du Bonnet Grey granite*. Journal of Geophysical Research: Solid Earth 97 (B5):6867-6884

Fan, S.C., Jiao, Y.Y., Zhao, J. (2004) *On modelling of incident boundary for wave propagation in jointed rock masses using discrete element method*. Computers and Geotechnics 31 (1):57-66

Fang, Q., Li, Y. (2014) *Exhaustive brine production and complete CO2 storage in Jianghan Basin of China*. Environ Earth Sci 72 (5):1541-1553

Finlayson, A.B. (1990) *The Theory of Flow Through Packed Beds*. Fluid Mechanics for Fluidized Bed Reactors, vol 2013. University of Washington

Ghaboussi, J., Wilson, L.E., Isenberg, J. (1973) *Finite Element for Rock Joints and Interfaces*. Journal of the Soil Mechanics and Foundations Division 99 (10):849-862

Giamundo, V., Sarhosis, V., Lignola, G.P., Sheng, Y., Manfredi, G. (2014) *Evaluation of different computational modelling strategies for the analysis of low strength masonry structures*. Engineering Structures 73:160-169

Goodman, R.E. (1976) *Methods of geological engineering in discontinuous rocks.* . West Publishing Company, San Francisco

Goodman, R.E. (1989) *Introduction in Rock Mechanics*. 2nd edn. John Wiley & Sons Ltd, New York

Gordalla, B., Ewers, U., Frimmel, F. (2013) *Hydraulic fracturing: a toxicological threat for groundwater and drinking-water?* Environ Earth Sci 70 (8):3875-3893. doi:10.1007/s12665-013-2672-9

Green, A.S.P., Baria, R., Madge, A., Jones, R. (1988) *Fault-plane analysis of microseismicity induced by fluid injections into granite*. Geological Society, London, Engineering Geology Special Publications 5 (1):415-422

Grenon, M., Bruneau, G., Kapinga Kalala, I. (2014) *Quantifying the impact of small variations in fracture geometric characteristics on peak rock mass properties at a mining project using a coupled DFN–DEM approach*. Computers and Geotechnics 58 (0):47-55. doi:http://dx.doi.org/10.1016/j.compgeo.2014.01.010

Griffith, A.A. (1921) *The Phenomena of Rupture and Flow in Solids*. Philosophical Transactions of the Royal Society of London Series A, Containing Papers of a Mathematical or Physical Character 221 (582-593):163-198. doi:10.1098/rsta.1921.0006

Haimson, B.C. (2004) *Hydraulic fracturing and rock characterization*. International Journal of Rock Mechanics and Mining Sciences 41, Supplement 1 (0):188-194

Hallsworth, C.R., Knox, R.W.O.B. (1999) *British Geological Survey: Classification of sediments and sedimentary rocks*. vol 3. Nottingham

Hamidi, F., Mortazavi, A. (2013) *A new three dimensional approach to numerically model hydraulic fracturing process*. Journal of Petroleum Science and Engineering (0)

Hammah, R.E., Yacoub, T., Corkum, B., Corkum, B. (2008) *The Practical Modelling of Discontinuous Rock Masses with Finite Element Analysis*

Paper presented at the Proceedings of the 42nd US Rock Mechanics Symposium and 2nd US–Canada Rock Mechanics Symposium, San Francisco, USA, 29 June-02 July

Hammah, R.E., Yacoub, T., Corkum, B., Wibowo, F., Curran, J.H. (2007) *Analysis of blocky rock slopes with finite element Shear Strength Reduction analysis*. In: Rock Mechanics: Meeting Society's Challenges and Demands, Two Volume Set. Taylor & Francis, pp 329-334

Hanson, M.E., Anderson, G.D., Shaffer, R.J. (1980) *THEORETICAL AND EXPERIMENTAL RESEARCH ON HYDRAULIC FRACTURING*. Journal of Energy Resources Technology, Transactions of the ASME 102 (2):92-98

Hanson, M.E., Anderson, G.D., Shaffer, R.J., Thorson, L.D. (1982) *Some Effects of Stress, Friction, and Fluid Flow on Hydraulic Fracturing*. doi:10.2118/9831-PA

Harthong, B., Scholtès, L., Donzé, F.-V. (2012) *Strength characterization of rock masses, using a coupled DEM–DFN model*. Geophysical Journal International 191 (2):467-480

Hassani, B., Hinton, E. (1998) *A review of homegenization and topology optimization I-homogeneization theory for media with periodic structure*. Computers and Structures 69:707-717

Hatzor, Y.H., Benary, R. (1998) *The stability of a laminated Voussoir beam: Back analysis of a historic roof collapse using DDA*. International Journal of Rock Mechanics and Mining Sciences 35 (2):165-181

Hazzard, J.F., Young, R.P. (2000) *Simulating acoustic emissions in bonded-particle models of rock*. International Journal of Rock Mechanics & Mining Sciences 37:867-887

Hazzard, J.F., Young, R.P. (2002) *Moment tensors and micromechanical models*. Tectonophysics 356:181-197

Hazzard, J.F., Young, R.P. (2004) *Dynamic modelling of induced seismicity*. International Journal of Rock Mechanics and Mining Sciences 41 (8):1365-1376

Hertzberq, R.W. (1996) *Deformation and Fracture Mechanics of Engineering Materials*. 4th edn. John Wiley & Sons,

Hoek, E. (1983) *Strength of jointed rock masses*. Géotechnique 33 (3):187-223

Hoek, E. (2006) *Practical Rock Engineering*

Hoek, E., Brown, E.T. (1997) *Practical estimates of rock mass strength*. International Journal of Rock Mechanics and Mining Sciences 34 (8):1165-1186

Hoek, E., Carranza-Torres, C., Corkum, B. *Hoek-Brown failure criterion – 2002 edition*. In: Proceedings of the 5th North American Rock Mechanics Symposium, Toronto, Canada, 2002. pp 267-273

Hoek, E., Diederichs, M.S. (2006) *Empirical estimation of rock mass modulus*. International Journal of Rock Mechanics and Mining Sciences 43 (2):203-215

Hoek, E., Kaise, P.K., Bawden, W.F. (2000) *Support of underground excavations in hard rock*. CRS Press/ Balkema

Holt, R.M. (1990) *Permeability reduction induced by a non-hydrostatic stress field*. SPE Formation Evaluation 5 (4):444-448

Howard, G.C., Fast, C.R. (1970) *Hydraulic Fracturing*. Monograph series. Society of Petroleum Engineers, Texas

Huang, H., Lecampion, B., Detournay, E. (2013) *Discrete element modeling of tool-rock interaction I: rock cutting*. International Journal for Numerical and Analytical Methods in Geomechanics 37 (13):1913-1929

Huang, Y., Zhou, Z., Wang, J., Dou, Z. (2014) *Simulation of groundwater flow in fractured rocks using a coupled model based on the method of domain decomposition*. Environ Earth Sci 72 (8):2765-2777

Ingraffea, A.R., Heuze, F.E. (1980) *Finite element models for rock fracture mechanics*. International Journal for Numerical and Analytical Methods in Geomechanics 4 (1):25-43

Ishida, T. (2001) *Acoustic emission monitoring of hydraulic fracturing in laboratory and field*. Construction and Building Materials 15 (5–6):283-295

Ishida, T., Aoyagi, K., Niwa, T., Chen, Y., Murata, S., Chen, Q., Nakayama, Y. (2012) *Acoustic emission monitoring of hydraulic fracturing laboratory experiment with supercritical and liquid CO2*. Geophysical Research Letters 39 (16):L16309

Ishida, T., Chen, Q., Mizuta, Y., Roegiers, J.-C. (2004) *Influence of Fluid Viscosity on the Hydraulic Fracturing Mechanism*. Journal of Energy Resources Technology, Transactions of the ASME 126 (3):11

Ishida, T., Sasaki, S., Matsunaga, I., Chen, Q., Mizuta, Y. *Effect of grain size in granitic rocks on hydraulic fracturing mechanism*. In: (GSP) GSP (ed) Trends in Rocks Mechanics: Proceedings of sessions of Geo-Denver 2000 Denver, Colorado, 2000. American Society of Civil Engineers (ASCE), pp 128-139

Itasca-Consulting-Group (2008a) *FISH in PFC3D 3: PFC FishTank*. 4 edn. ICG, Minneapolis, MN

Itasca-Consulting-Group (2008b) *User's Guide 1: Introduction*. 4 edn. ICG, Minneapolis, MN.

Itasca Consulting Group (2005) *Lagrangian Analysis of Continua (FLAC)*. 5.0 edn. ICG, Minneapolis, MN

Itasca Consulting Group (2008a) *Basic Fluid Analysis Option*. 4 edn. ICG, Minneapolis, MN

Itasca Consulting Group (2008b) *Example's Application 9: Incorporation of Fluid Coupling in PFC3D*. 4 edn. ICG, Minneapolis, MN

Itasca Consulting Group (2008c) *FISH in PFC3D 3: PFC FishTank*. 4 edn. ICG, Minneapolis, MN

Itasca Consulting Group (2008d) *Particle Flow Code in 3 Dimensions (PFC3D)*. 4 edn. ICG, Minneapolis, MN

Itasca Consulting Group (2008e) *Theory and Background 1: General Formulation*. 4 edn. ICG, Minneapolis, MN

Itasca Consulting Group (2008f) *Theory and Background 2: Contact models*. ICG, Minneapolis, MN

Itasca Consulting Group (2008g) *Theory and Background 3: Implementation Issues*. ICG, Minneapolis, MN

Itasca Consulting Group (2008h) *User's Guide 3: Problem Solving with PFC3D*. 4 edn. ICG, Minneapolis, MN

Itasca Consulting Group Inc (2013) *Universal Distinct Element Code (UDEC)*. Minneapolis, USA

Jaeger, J.C., Cook, N.G.W., Zimmerman, R.W. (2007) *Fundamentals of rock mechanics*. 4th edn. Wiley-Blackwell, Oxford

Jia, Y., Li, Y., Hlavka, D. (2009) *Flow through Packed Beds*. University-of-Rochester,

Jiang, Y., Li, B., Yamashita, Y. (2009) *Simulation of cracking near a large underground cavern in a discontinuous rock mass using the expanded* *distinct element method*. International Journal of Rock Mechanics and Mining Sciences 46 (1):97-106

Jiefan, H., Ganglin, C., Yonghong, Z., Ren, W. (1990) *An experimental study of the strain field development prior to failure of a marble plate under compression*. Tectonophysics 175 (1–3):269-284

Jing, L. (1998) *Formulation of discontinuous deformation analysis (DDA) — an implicit discrete element model for block systems*. Engineering Geology 49 (3–4):371-381

Jing, L., Hudson, J.A. (2002) *Numerical methods in rock mechanics*. International Journal of Rock Mechanics and Mining Sciences 39 (4):409-427

Jing, L., Ma, Y., Fang, Z. (2001) *Modeling of fluid flow and solid deformation for fractured rocks with discontinuous deformation analysis (DDA) method*. International Journal of Rock Mechanics and Mining Sciences 38 (3):343-355

Jing, L., Stephansson, O. (1997) *Network Topology and Homogenization of Fractured Rocks*. In: Jamtveit B, Yardley BD (eds) Fluid Flow and Transport in Rocks. Springer Netherlands, pp 191-202

Kazerani, T. (2013) *Effect of micromechanical parameters of microstructure on compressive and tensile failure process of rock*. International Journal of Rock Mechanics and Mining Sciences 64 (0):44-55

Kazerani, T., Yang, Z.Y., Zhao, J. (2012) *A Discrete Element Model for Predicting Shear Strength and Degradation of Rock Joint by Using Compressive and Tensile Test Data*. Rock Mech Rock Eng 45 (5):695-709

Kemeny, J. (2005) *Time-dependent drift degradation due to the progressive failure of rock bridges along discontinuities*. International Journal of Rock Mechanics and Mining Sciences 42 (1):35-46

Khanna, A., Kotousov, A., Sobey, J., Weller, P. (2012) *Conductivity of narrow fractures filled with a proppant monolayer*. Journal of Petroleum Science and Engineering 100 (0):9-13

Kim, B.S., Park, S.W., Kato, S. (2012) *DEM simulation of collapse behaviours of unsaturated granular materials under general stress states*. Computers and Geotechnics 42 (0):52-61. doi:http://dx.doi.org/10.1016/j.compgeo.2011.12.010

Kissinger, A., Helmig, R., Ebigbo, A., Class, H., Lange, T., Sauter, M., Heitfeld, M., Klünker, J., Jahnke, W. (2013) *Hydraulic fracturing in unconventional gas reservoirs: risks in the geological system, part 2*. Environ Earth Sci 70 (8):3855-3873

Knill, J.L., Cratchley, C.R., Early, K.R., Gallois, R.W., Humphreys, J.D., Newbery, J., Price, D.G., Thurrell, R.G. (1970) *The logging of rock cores for engineering purposes.*, vol 3. Geological Society Engineering Group Working Party Report,

Kozicki, J., Donzé, F.V. (2008) *A new open-source software developed for numerical simulations using discrete modeling methods*. Computer Methods in Applied Mechanics and Engineering 197 (49–50):4429-4443

Kozicki, J., Donzé, F.V. (2009) *YADE‐OPEN DEM: an open‐source software using a discrete element method to simulate granular material*. Engineering Computations 26 (7):786-805

Krajcinovic, D. (2000) *Damage mechanics: accomplishments, trends and needs*. International Journal of Solids and Structures 37 (1–2):267-277

Kresse, Weng, X., Chuprakov, D., Prioul, R., Cohen, C. (2013) *Effect of Flow Rate and Viscosity on Complex Fracture Development in UFM Model*. Effective and Sustainable Hydraulic Fracturing.

Lajtai, E.Z. (1974) *Brittle fracture in compression*. International Journal of Fracture 10 (4):525-536

Lange, T., Sauter, M., Heitfeld, M., Schetelig, K., Brosig, K., Jahnke, W., Kissinger, A., Helmig, R., Ebigbo, A., Class, H. (2013) *Hydraulic fracturing in unconventional gas reservoirs: risks in the geological system part 1*. Environ Earth Sci 70 (8):3839-3853

Lewis, D., Corin, T. (2012) *Britain's Shale Gas Potential*. Infrastructure for Business, vol 3. Institute of Directors (IoD),

Li, C., Xie, L., Ren, L., Xie, H., Wang, J. (2013) *Evaluating the Applicability of Fracture Criteria to Predict the Crack Evolution Path of Dolomite Based on SCB Experiments and FEM*. Mathematical Problems in Engineering 2013:13

Li, W.-Y., Lv, B., Ouyang, H., Du, J., Zhou, H., Wang, D. (2014) *A Hybrid Finite Element-Fourier Spectral Method for Vibration Analysis of Structures with Elastic Boundary Conditions*. Mathematical Problems in Engineering 2014:11

Li, Y.-P., Chen, L.-Z., Wang, Y.-H. (2005) *Experimental research on pre-cracked marble under compression*. International Journal of Solids and Structures 42 (9–10):2505-2516

Lisjak, A., Figi, D., Grasselli, G. (2014) *Fracture development around deep underground excavations: Insights from FDEM modelling*. Journal of Rock Mechanics and Geotechnical Engineering 6 (6):493-505

Lisjak, A., Grasselli, G. (2014) *A review of discrete modeling techniques for fracturing processes in discontinuous rock masses*. Journal of Rock Mechanics and Geotechnical Engineering 6 (4):301-314

Lockner, D.A., Byerlee, J.D., Kuksenko, V., Ponomarev, A., Sidorin, A. (1991) *Quasi-static fault growth and shear fracture energy in granite*. Nature 350 (6313):39-42

Lorig, L.J., Cundall, P.A. (1989) *Modeling of Reinforced Concrete Using the Distinct Element Method*. In: Shah S, Swartz S (eds) Fracture of Concrete and Rock. Springer New York, pp 276-287

Lu, X., Wu, W.-l. (2006) *A subregion DRBEM formulation for the dynamic analysis of two-dimensional cracks*. Mathematical and Computer Modelling 43 (1–2):76-88

Manouchehrian, A., Marji, M. (2012) *Numerical analysis of confinement effect on crack propagation mechanism from a flaw in a pre-cracked rock under compression*. Acta Mech Sin 28 (5):1389-1397

Martin, C.D. (1997) *Seventeenth Canadian Geotechnical Colloquium: The effect of cohesion loss and stress path on brittle rock strength*. Canadian Geotechnical Journal 34 (5):698-725

Martinez, A.R. (1999) *Fracture coalescence in natural rock*. Massachusetts Institute of Technology,

Martinez, D. (2012) *Fundamental Hydraulic Fracturing Concepts for Poorly Consolitated Formations*. Dissertation/Thesis, University of Oklahoma, Ann Arbor, US

Mas Ivars, D. (2010) *Bonded Particle Model for Jointed Rock Mass*. Stockolm, Sweden

Mas Ivars, D., Pierce, M.E., Darcel, C., Reyes-Montes, J., Potyondy, D.O., Paul Young, R., Cundall, P.A. (2011) *The synthetic rock mass approach for jointed rock mass modelling*. International Journal of Rock Mechanics and Mining Sciences 48 (2):219-244

Matsunaga, I., Kobayashi, H., Sasaki, S., Ishida, T. (1993) *Studying hydraulic fracturing mechanism by laboratory experiments with acoustic emission monitoring*. International Journal of Rock Mechanics and Mining Sciences & Geomechanics Abstracts 30 (7):909-912

McKinnon, S.D., Garrido de la Barra, I. (2003) *Stress field analysis at the El Teniente Mine: evidence for N–S compression in the modern Andes*. Journal of Structural Geology 25 (12):2125-2139

Moës, N., Dolbow, J., Belytschko, T. (1999) *A finite element method for crack growth without remeshing*. International Journal for Numerical Methods in Engineering 46 (1):131-150

Moin, P., Mahesh, K. (1998) *Direct Numerical Simulation: A Tool in Turbulence Research*. Annual Review of Fluid Mechanics 30:539-578

Moon, T., Nakagawa, M., Berger, J. (2007) *Measurement of fracture toughness using the distinct element method*. International Journal of Rock Mechanics and Mining Sciences 44 (3):449-456

Mughieda, O., Alzo'ubi, A. (2004) *Fracture mechanisms of offset rock joints-A laboratory investigation*. Geotechnical and Geological Engineering 22 (4):545-562

Munjiza, A., Andrews, K.R.F., White, J.K. (1999) *Combined single and smeared crack model in combined finite-discrete element analysis*. International Journal for Numerical Methods in Engineering 44 (1):41-57

Munjiza, A.A. (2004) *The Combined Finite-Discrete Element Method*. John Wiley & Sons Ltd, Chichester, UK

Nagel, N., Gil, I., Sanchez-nagel, M., Damjanac, B. (2011) *Simulating Hydraulic Fracturing in Real Fractured Rocks - Overcjavascript:iterm()oming the Limits of Pseudo3D Models*. Paper presented at the SPE Hydraulic Fracturing Technology Conference, The Woodlands, Texas, USA, 2011/1/1/

Neuman, S.P. (2005) *Trends, prospects and challenges in quantifying flow and transport through fractured rocks*. Hydrogeol J 13 (1):124-147

Nield, A.D., Bejan, A. (2006) *Convection in Porous Media*, vol 3rd Edition. Springer,

Olsson, O., Weichgrebe, D., Rosenwinkel, K.-H. (2013) *Hydraulic fracturing wastewater in Germany: composition, treatment, concerns*. Environ Earth Sci 70 (8):3895-3906

Owen, D.R.J., Feng, Y.T. (2001) *Parallelised finite/discrete element simulation of multi-fracturing solids and discrete systems*. Engineering Computations 18 (3/4):557-576

Panel of Experts (2012) *Hydrofracking Risk Assessment*. ExxonMobil Production Deutschland GmbH,

Papanastasiou, P. (2000) *Hydraulic fracture closure in a pressure-sensitive elastoplastic medium*. International Journal of Fracture 103 (2):149-161

Petit, J.-P., Barquins, M. (1988) *Can natural faults propagate under Mode II conditions?* Tectonics 7 (6):1243-1256

Potyondy, D., Autio, J. (2000) *Bonded-Particle Simulations of the In-Situ Failure Test At Olkiluoto*. Paper presented at the The 38th U.S. Symposium on Rock Mechanics (USRMS), Washington, D.C., 2001/1/1/

Potyondy, D., Cundall, P. (1998) *Modeling notch-formation mechanisms in the URL Mine-by Test Tunnel using bonded assemblies of circular particles*. International Journal of Rock Mechanics and Mining Sciences 35 (4-5):510-511

Potyondy, D.O. (2012) *A Flat-Jointed Bonded-Particle Material For Hard Rock*. Paper presented at the 46th U.S. Rock Mechanics/Geomechanics Symposium, Chicago, Illinois, 2012/1/1/

Potyondy, D.O., Cundall, P.A. (2004) *A bonded-particle model for rock*. International Journal of Rock Mechanics & Mining Sciences:1329-1364. doi:10.1016

Potyondy, D.O., Cundall, P.A., Lee, C.A. (1996) *Modelling Rock Using Bonded Assemblies of Circular Particles*. Paper presented at the 2nd North American Rock Mechanics Symposium, Montreal, Canada, 19-21 June

Rabczuk, T., Bordas, S.P.A., Zi, G. (2014) *Computational Methods for Fracture*. Mathematical Problems in Engineering 2014:2

Riahi, A., Curran, J.H., Hammah, R.E. (2012) *Application of continuum-interface computational methods in analysis of jointed rock problems*. In: Innovative Numerical Modelling in Geomechanics. CRC Press, pp 317-332

Riedl, J., Rotter, S., Faetsch, S., Schmitt-Jansen, M., Altenburger, R. (2013) *Proposal for applying a component-based mixture approach for ecotoxicological assessment of fracturing fluids*. Environ Earth Sci 70 (8):3907-3920

Rockfield Software Ltd (2004) *ELFEN 2D/3D numerical modelling package*. Rockfield Software Ltd,, Swansea, UK

Royal Society, R. (2012) *Shale gas extraction in the UK: A review of hydraulic fracturing*. The Royal Society, The Royal Academy of Engineering, London

Rutqvist, J., Birkholzer, J., Cappa, F., Tsang, C.F. (2007) *Estimating maximum sustainable injection pressure during geological sequestration of CO2 using coupled fluid flow and geomechanical fault-slip analysis*. Energy Conversion and Management 48 (6):1798-1807

Sarhosis, V., Sheng, Y. (2014) *Identification of material parameters for low bond strength masonry*. Engineering Structures 60 (0):100-110

SCCS (2009) *Opportunities for CO2 Storage around Scotland: an integraded research study*. Scottish Centre for Carbon Storage, Edinburgh

Schlangen, E., Garboczi, E.J. (1997) *Fracture simulations of concrete using lattice models: Computational aspects*. Engineering Fracture Mechanics 57 (2–3):319-332

Schmidt, R.A. (1976) *Fracture-toughness testing of limestone*. Experimental Mechanics 16 (5):161-167

Schmidt, R.A., Huddle, C.W. (1977) *Effect of confining pressure on fracture toughness of Indiana limestone*. International Journal of Rock Mechanics and Mining Sciences & Geomechanics Abstracts 14 (5–6):289-293

Scholtès, L., Donzé, F.-V. (2012) *Modelling progressive failure in fractured rock masses using a 3D discrete element method*. International Journal of Rock Mechanics and Mining Sciences 52:18-30

Scholtès, L., Donzé, F.-V. (2013) *A DEM model for soft and hard rocks: Role of grain interlocking on strength*. Journal of the Mechanics and Physics of Solids 61 (2):352-369

Scholtès, L., Donzé, F.-V., Khanal, M. (2011) *Scale effects on strength of geomaterials, case study: Coal*. Journal of the Mechanics and Physics of Solids 59 (5):1131-1146

Shi, G.h., Goodman, R.E. (1988) *Discontinuous Deformation Analysis - A New Method for Computing Stress, Strain And Sliding of Block Systems*. Paper presented at the The 29th U.S. Symposium on Rock Mechanics (USRMS), Minneapolis, Minnesota,

Shie, Y. (2014) *Dynamic Fracture in Thin Shells Using Meshfree Method*. Mathematical Problems in Engineering 2014:8

Shimizu, H., Murata, S., Ishida, T. (2009) *The Distinct Element Analysis For Hydraulic Fracturing Considering The Fluid Viscosity*. Paper presented at the 43rd U.S. Rock Mechanics Symposium & 4th U.S. - Canada Rock Mechanics Symposium, Asheville, North Carolina, US, 28 June-1 July

Shimizu, H., Murata, S., Ishida, T. (2011) *The distinct element analysis for hydraulic fracturing in hard rock considering fluid viscosity and particle size distribution*. International Journal of Rock Mechanics and Mining Sciences 48 (5):712-727

Shimizu, H., Murata, S., Ito, T., Ishida, T. (2012) *The Distinct Element Analysis for Hydraulic Fracturing in Unconsolidated Sand Considering Fluid Viscosity*. 2012/1/1/

Sitharam, T.G., Latha, G.M. (2002) *Simulation of excavations in jointed rock masses using a practical equivalent continuum approach*. International Journal of Rock Mechanics and Mining Sciences 39 (4):517-525

Sitharam, T.G., Sridevi, J., Shimizu, N. (2001) *Practical equivalent continuum characterization of jointed rock masses*. International Journal of Rock Mechanics and Mining Sciences 38 (3):437-448

Song, J.-H., Lea, P., Oswald, J. (2013a) *Explicit Dynamic Finite Element Method for Predicting Implosion/Explosion Induced Failure of Shell Structures*. Mathematical Problems in Engineering 2013:11

Song, J.-H., Menouillard, T., Tabarraei, A. (2013b) *Explicit Dynamic Finite Element Method for Failure with Smooth Fracture Energy Dissipations*. Mathematical Problems in Engineering 2013:12

Sousani, M. *Modelling of the Hydraulic Fracturing of Rocks: A Multi Scale and a Multiphase Approach*. In: Papanikos GT (ed) 1st Annual International Conference on Earth and Environmental Sciences, Athens, 14-17 July 2014.

Sousani, M., Eshiet I-I, K., Ingham, D., Pourkashanian, M., Sheng, Y. (2014) *Modelling of hydraulic fracturing process by coupled discrete element and fluid dynamic methods*. Environ Earth Sci 72 (9):3383-3399. doi:10.1007/s12665-014-3244-3

Sousani, M., Ingham, D., Pourkashanian, M., Sheng, Y., Eshiet I-I, K. (2015) *Simulation of the hydraulic fracturing process of fractured rocks by the discrete element method*. Environ Earth Sci:1-19. doi:10.1007/s12665-014-4005-z

Stefanou, I., Vardoulakis, I. (2005) *Stability Assessment of SE/E Rock Corner Slope of the Acropolis Hill in Athens*. Paper presented at the 5th GRACM International Congress on Computational Mechanics, Limassol, Cyprus, 29June-1July

Tang, C. (1997) *Numerical simulation of progressive rock failure and associated seismicity*. International Journal of Rock Mechanics and Mining Sciences 34 (2):249-261

Tang, C.A., Hy, L. (2013) *The DDD method based on combination of RFPA and DDA*. In: Guangqi Chen YO, Lu Zheng and Takeshi Sasaki (ed) Frontiers of Discontinuous Numerical Methods and Practical Simulations in Engineering and Disaster Prevention. CRC Press, pp 105-112

Tarokh, A., Fakhimi, A. (2014) *Discrete element simulation of the effect of particle size on the size of fracture process zone in quasi-brittle materials*. Computers and Geotechnics 62 (0):51-60. doi:http://dx.doi.org/10.1016/j.compgeo.2014.07.002

Taylor, C., Lewis, D. (2013) *Getting shale gas working*. Infrastructure for Business, vol 6. Institue of Directors (IoD),

The Economist (2011) *Shale gas in Europe and America*. The Economist,, vol Is this really the end?

Timoshenko, S. (1941) *Strength of Materials Part II: Advanced Theory and Problems*. 2nd edn. Lancaster Press, Inc., Palo Alto, California

Tsuji, Y., Kawaguchi, T., Tanaka, T. (1993) *Discrete particle simulation of two-dimensional fluidized bed*. Powder Technology 77 (1):79-87

V. Šmilauer, E. Catalano, B. Chareyre, S. Dorofeenko, J. Duriez, A. Gladky, J. Kozicki, C. Modenese, L. Scholtès, L. Sibille, J. Stránský, Thoeni, K. (2010) *The YADE Project*. Yade - Open Source Discrete Element Method, vol 1st.

Valko, P., Economides, M.J. (1995) *Hydraulic Fracture Mechanics*. John Wiley & Sons,

van Dam, D.B., de Pater, C.J., Romijn, R. (2000a) *Analysis of Hydraulic Fracture Closure in Laboratory Experiments*. SPE 151-158

van Dam, D.B., de Pater, C.J., Romijn, R., Romijn, R. (2000b) *Analysis of Hydraulic Fracture Closure in Laboratory Experiments*. SPE Production & Facilities 15 (3):151-158

Vincent, M.C. (2002) *Proving It - A Review of 80 Published Field Studies Demonstrating the Importance of Increased Fracture Conductivity*. Paper presented at the SPE Annual Technical Conference and Exhibition, San Antonio, Texas,

Vinciguerra, S., Meredith, P.G., Hazzard, J. (2004) *Experimental and modeling study of fluid pressure-driven fractures in Darley Dale sandstone*. Geophysical Research Letters 31 (9)

Walton, K. (1987) *The effective elastic moduli of a random packing of spheres*. Journal of the Mechanics and Physics of Solids 35 (2):213-226

Wang, H., Wang, E., Tian, K. (2004) *A model coupling discrete and continuum fracture domains for groundwater flow in fractured media*. Journal of Hydraulic Research 42 (sup1):45-52

Wang, T., Zhou, W., Chen, J., Xiao, X., Li, Y., Zhao, X. (2014) *Simulation of hydraulic fracturing using particle flow method and application in a coal mine*. International Journal of Coal Geology 121 (0):1-13

Warpinski, N.R.F., Branagan, P.T.F., Mahrer, K.D.F., Wolhart, S.L.F., Moschovidis, Z.A.F. (1999) *Microseismic monitoring of the Mounds drill cuttings injection tests*. Paper presented at the The 37th U.S. Symposium on Rock Mechanics (USRMS), Vail, Colorado,

Wong, L.N.Y., Einstein, H. (2006) *Fracturing Behavior of Prismatic Specimens Containing Single Flaws*. Paper presented at the The 41st U.S. Symposium on Rock Mechanics (USRMS), Golden, Colorado, 2006/1/1/

Wong, L.N.Y., Einstein, H.H. (2007) *Coalescence behavior in Carrara marble and molded gypsum containing artificial flaw pairs under uniaxial compression*. In: Rock Mechanics: Meeting Society's Challenges and Demands, Two Volume Set. Taylor & Francis, pp 581-589

Wong, L.N.Y., Einstein, H.H. (2009a) *Crack Coalescence in Molded Gypsum and Carrara Marble: Part 1. Macroscopic Observations and Interpretation*. Rock Mech Rock Eng 42 (3):475-511

Wong, L.N.Y., Einstein, H.H. (2009b) *Crack Coalescence in Molded Gypsum and Carrara Marble: Part 2—Microscopic Observations and Interpretation*. Rock Mech Rock Eng 42 (3):513-545

Wong, L.N.Y., Einstein, H.H. (2009c) *Systematic evaluation of cracking behavior in specimens containing single flaws under uniaxial compression*. International Journal of Rock Mechanics and Mining Sciences 46 (2):239-249

Wong, R.H.C., Chau, K.T. (1998) *Crack coalescence in a rock-like material containing two cracks*. International Journal of Rock Mechanics and Mining Sciences 35 (2):147-164

Woodbury, A., Zhang, K. (2001) *Lanczos method for the solution of groundwater flow in discretely fractured porous media*. Advances in Water Resources 24 (6):621-630

Wright, P., J., F. (1955) *Comments on an indirect tensile test in concrete cylinders*. Magazine of Concrete Research 7 (20):87-96

Wu, Q., Liu, Y., Liu, D., Zhou, W. (2011) *Prediction of Floor Water Inrush: The Application of GIS-Based AHP Vulnerable Index Method to Donghuantuo Coal Mine, China*. Rock Mech Rock Eng 44 (5):591-600

Xu, B.H., Yu, A.B. (1997) *Numerical simulation of the gas-solid flow in a fluidized bed by combining discrete particle method with computational fluid dynamics*. Chemical Engineering Science 52 (16):2785-2809

Xu, C., Fowell, R.J. (1994) *Stress intensity factor evaluation for cracked chevron notched brazilian disc specimens*. International Journal of Rock Mechanics and Mining Sciences & Geomechanics Abstracts 31 (2):157-162

Yoon, J.S., Zang, A., Stephansson, O. (2014) *Numerical investigation on optimized stimulation of intact and naturally fractured deep geothermal reservoirs using hydro-mechanical coupled discrete particles joints model*. Geothermics 52 (0):165-184

Zeidouni, M., Nicot, J.-P., Hovorka, S. (2014) *Monitoring above-zone temperature variations associated with CO2 and brine leakage from a storage aquifer*. Environ Earth Sci 72 (5):1733-1747

Zhang, X.-P., Wong, L. (2012) *Cracking Processes in Rock-Like Material Containing a Single Flaw Under Uniaxial Compression: A Numerical*

Study Based on Parallel Bonded-Particle Model Approach. Rock Mech Rock Eng 45 (5):711-737

Zhang, X.-P., Wong, L. (2013) *Crack Initiation, Propagation and Coalescence in Rock-Like Material Containing Two Flaws: a Numerical Study Based on Bonded-Particle Model Approach*. Rock Mech Rock Eng 46 (5):1001-1021

Zhang, X., Last, N., Powrie, W., Harkness, R. (1999) *Numerical modelling of wellbore behaviour in fractured rock masses*. Journal of Petroleum Science and Engineering 23 (2):95-115

Zhao, X.B., Zhao, J., Cai, J.G., Hefny, A.M. (2008) *UDEC modelling on wave propagation across fractured rock masses*. Computers and Geotechnics 35 (1):97-104

Zhu, B., Wu, Q., Yang, J., Cui, T. (2014) *Study of pore pressure change during mining and its application on water inrush prevention: a numerical simulation case in Zhaogezhuang coalmine, China*. Environ Earth Sci 71 (5):2115-2132

Zhu, H., Zhuang, X., Cai, Y., Ma, G. (2011) *High Rock Slope Stability Analysis Using the Enriched Meshless Shepard and Least Squares Method*. International Journal of Computational Methods 08 (02):209-228

Zhuang, X., Augarde, C., Bordas, S. (2011) *Accurate fracture modelling using meshless methods, the visibility criterion and level sets: Formulation and 2D modelling*. International Journal for Numerical Methods in Engineering 86 (2):249-268

Zhuang, X., Augarde, C.E., Mathisen, K.M. (2012) *Fracture modeling using meshless methods and level sets in 3D: Framework and modeling*. International Journal for Numerical Methods in Engineering 92 (11):969-998

Zhuang, X., Huang, R., Liang, C., Rabczuk, T. (2014) *A Coupled Thermo-Hydro-Mechanical Model of Jointed Hard Rock for Compressed Air Energy Storage*. Mathematical Problems in Engineering 2014:11

Zi, G., Belytschko, T. (2003) *New crack-tip elements for XFEM and applications to cohesive cracks*. International Journal for Numerical Methods in Engineering 57 (15):2221-2240